

# **FINAL TECHNICAL REPORT**

## **Asia Pacific Research Initiative for Sustainable Energy Systems**

**Office of Naval Research**

**Grant Award Number N00014-15-1-0028**

**January 1, 2015 through June 30, 2019**



**HNEI**

**Hawai'i Natural Energy Institute**

University of Hawai'i at Mānoa

**September 2019**

## Table of Contents

<b>EXECUTIVE SUMMARY .....</b>	<b>2</b>
<b>TASK 1: PROGRAM MANAGEMENT AND OUTREACH.....</b>	<b>5</b>
<b>TASK 2: FUEL CELL &amp; HYDROGEN RESEARCH .....</b>	<b>5</b>
2.1 Fuel Cell Testing .....	5
2.2 Contamination Mitigation: Air Filtration Materials Development .....	25
2.3 Hydrogen Refueling Support .....	33
2.4 Materials for Solar Fuels .....	38
<b>TASK 3 BIOFUELS .....</b>	<b>40</b>
3.1 Bioenergy Systems .....	40
3.2 High-Rate Anaerobic Digestion .....	41
3.3 Liquid Fuels from Syngas .....	44
3.4 Bio-Contamination of Fuels .....	51
3.5 Oxygen-Enhanced Flash-Carbonization .....	69
<b>TASK 4: METHANE HYDRATES .....</b>	<b>70</b>
<b>TASK 5: SECURE MICROGRIDS .....</b>	<b>90</b>
<b>TASK 6: OCEAN ENERGY .....</b>	<b>132</b>
<b>TASK 7: ENERGY EFFICIENCY .....</b>	<b>138</b>
7.1 Data Collection First Generation Project Frog Buildings .....	138
7.2 High Wind Energy Generator Testing .....	154

**Final Technical Report**  
**Asia Pacific Research Initiative for Sustainable Energy Systems**  
**Grant Award Number N00014-15-1-0028**  
**January 1, 2015 through June 30, 2019**

## **EXECUTIVE SUMMARY**

This report summarizes work conducted under Grant Award Number N00014-15-1-0028 the Asia Pacific Research Initiative for Sustainable Energy Systems 2014 (APRISES14), funded by the Office of Naval Research (ONR) to the Hawaii Natural Energy Institute (HNEI) of the University of Hawaii at Manoa (UH). The overall objective of APRISES14 was to develop, test, and evaluate distributed energy systems, emerging technologies and power grid integration using Hawaii as a model for applicability throughout the Pacific Region. APRISES14 encompassed fuel cell research, contaminant mitigation and evaluation; seafloor methane hydrates destabilization, microbial degradation and reservoir mapping; synthetic fuels processing and production to accelerate the use of biofuels for Navy needs; alternative energy systems for electric power generation and integration into smart microgrids, and energy efficient building platforms. Testing and evaluation of alternative energy systems included Ocean Thermal Energy Conversion (OTEC), development of several microgrid test projects, and wind energy generation.

Under Task 1, Program Management and Outreach, HNEI provided overall program management and coordination, developed and monitored partner and subcontract agreements, and developed outreach materials for both technical and non-technical audiences. Additionally, HNEI continued to collaborate closely with ONR and NRL to identify high-priority areas requiring further detailed evaluation and analysis.

Under Task 2, Fuel Cell Testing, HNEI continued to develop and apply fuel cell diagnostics, contributed to the development of fuel cell contamination mechanisms and mitigation strategies and applied this knowledge to design novel water purification technologies, and also to synthesize lower cost fuel cell catalysts. Contaminant Mitigation focused on development of syntheses and characterization techniques of advanced metallo ionic liquids and molten salts air purification materials to enable efficient use of fuel cells in harsh environmental conditions. Hydrogen Refueling Support involved the commissioning of hydrogen production and compression equipment, recertification of Hydrogen Transport Trailers (HTT), and the installation of improved design Thermal Pressure Relief Devices on hydrogen cylinders. Low-Cost Material for Solar Fuels Production continued to develop novel thin film materials for low-cost photovoltaic applications using scalable “printing” processing.

Efforts under Task 3, Biofuels, focused on the development, testing and evaluation of alternative fuels and technologies, and included activities in the areas of Bioenergy Systems, High-Rate Anaerobic Digestion, Liquid Fuels from Syngas, Bio-contamination of Fuels, and Oxygen-enhanced Flash-Carbonization. For Bioenergy Systems, yields and fatty acid profiles of oils derived from the *Milletia pinnata* seed were determined to support development of alternative fuels and higher value products. A final system design was completed for demonstration scale High-Rate Anaerobic Digestion reactors, with an initial mixing tank followed by an up-flow packed-bed anaerobic digester filled with biochar-based biofilm supports, with optional follow-on reactors. Liquid Fuels from Synthesis Gas research revealed the reaction routes of catalytic reforming a polymer into hydrocarbon oil and demonstrated bio-oil formation from residual microbial biomass. To control biofuel contamination, a eukaryotic metabolic pathway for biofuel degradation has been proposed based on proteome and genome data, and biological inhibition has also been examined. The effects of Constant-volume carbonization processing conditions on product yields and properties were determined to support the development of novel materials.

Methane Hydrates Task 4 primary accomplishments were: 1) using 3D seismic profiles and borehole data was used to calculate volumetric gas-in-place estimates for hydrate reservoirs in the Kumano Basin offshore of the Kii Peninsula, Japan; 2) laboratory experiments were completed to evaluate the effectiveness of environmentally-benign glycerol solutions to destabilize methane hydrate; and 3) continued the investigation of microbial degradation of methane and heavier hydrocarbons in marine environments through benchtop experiments and metagenomics techniques.

Secure Microgrids, Task 5 included a range of projects to develop, test and integrate secure microgrid technology including distributed energy resources. The Molokai Load Bank project analyzed performance and of a controllable load bank as an energy safety valve to provide a near-term solution for interconnection and a longer-term grid management asset for this small island grid and other microgrid applications. The Coconut Island DC Microgrid project progressed efforts to demonstrate the performance and resilience of a DC microgrid designed to serve loads within two buildings on the island, including reliable power to critical loads during interruptions of grid supplied power, and to provide the island with clean electrified transportation options powered primarily by the sun. The Load and PV Synthesis project focused on validating synthesized load and PV data by injecting it along with field measurements into a simulated electrical model of the Maui Meadows feeder, with the overall objective to synthesize PV and load data from a limited number of field measurements in order to enable realistic distribution feeder modeling with high distributed PV penetration. Under the Power Grid Monitoring and Controls project, a low-cost, fully integrated and highly flexible device and system were developed for distributed electrical measurement, real-time analysis, and controls to help solve grid operational issues with high penetrations of distributed energy resources.



Under the Conservation Voltage Reduction (CVR) Demonstration project, a distribution circuit was selected for the demonstration. This circuit supplies the Plaza Housing complex at USMC Camp Foster in Okinawa, Japan. Hardware-in-the-loop testing was performed to validate the proposed CVR control algorithm and the associated communications between the field meters and the CVR controller. A user-interface was also developed to provide USMC Okinawa personnel with information regarding the status of the voltage and HNEI-controller. Under the Solar Forecasting project HNEI significantly expanded the long-term database to study regional irradiance patterns and variability, and utilized the observations within the database to calibrate and validate several components of the solar forecasting system, generate a new regional turbidity product for clear sky irradiance modeling, and evaluate the effects of the new turbidity product on the accuracy of satellite image derived irradiance. Under the Advanced Power Systems Laboratory project, a conceptual design was developed and HNEI collaborated with a local electrical engineering firm to produce design drawings necessary for laboratory build-out, based on a highly flexible architecture incorporating state-of-the-art grid test and simulation equipment.

Task 6, Ocean Energy focused on development of advanced heat exchangers for Ocean Thermal Energy Conversion (OTEC) through a subaward to Makai Ocean Engineering. Makai's work continued development, fabrication, and testing Thin-Foil Heat Exchangers (TFHX), in addition to corrosion testing and biofouling prevention. In order to compare the TFHXs to the previously tested heat exchangers, twelve 1.2-m long TFHX plates were fabricated, and each configuration was tested as both a condenser and an evaporator. When evaluated in terms of heat exchanger operating pressure, at 2MW duty, the TFHXs have both a better operating pressure at the same seawater pumping power and a higher energy density compared to the previously tested heat exchangers. Funding for the Wave Energy Testing planned for Task 6 was reallocated to other areas of the program as approved by ONR.

Under Energy Efficiency Task 7, HNEI resumed monitoring the three first generation Project Frog buildings, (constructed and instrumented under previous ONR funding), to compare performance to second generation FROGs constructed at UH Manoa. Secondly, HNEI contracted with a manufacturer, HEWS Technology, Inc., to install, test, and report on performance of their novel "High Wind Energy Generator".

This report describes the work that has been accomplished under each of these tasks, along with summaries of task efforts that are detailed in journal and other publications, including reports, conference proceedings, presentations and a patent application. **Publications produced through these efforts are listed and available, or linked, on HNEI's website at <https://www.hnei.hawaii.edu/publications/project-reports#APRISES14>.**

## **TASK 1: PROGRAM MANAGEMENT AND OUTREACH**

This program-wide task provided management and coordination of all research, test, development and evaluation efforts under APRISES14. Partner and subcontract agreements were developed and monitored, and outreach materials for both technical and non-technical audiences were developed. In close collaboration with ONR, high-priority needs requiring further detailed evaluation and analysis were identified for application of emerging energy technologies, with a focus on Hawaii and the Asia-Pacific region. Additional detail for partner, subcontract and outreach activities are included in the following task summaries.

## **TASK 2: FUEL CELL & HYDROGEN RESEARCH**

Under Task 2, HNEI conducted research, testing and evaluation to advance fuel cell systems, developed air filtration materials to mitigate air contaminants in harsh environments, supported hydrogen refueling infrastructure on the Big Island of Hawaii, and developed new materials and devices for solar fuels production.

### **2.1 Fuel Cell Testing**

Fuel cell testing activities included single cell testing in support of the Naval Research Laboratory (NRL) efforts to develop fuel cells for unmanned aerial vehicles; testing to validate new methods to measure and separate mass transfer coefficients into fundamental contributions for the design of high power fuel cells, synthesis of potentially low cost and durable transition metal carbide (TMC) catalysts applicable to a variety of technologies including fuel cells, water electrolyzers for hydrogen production, and flow batteries; continued contaminant characterization to support develop of recovery strategies for fuel cells exposed to sulfur and halogen species present in air; exploratory experiments to assess the potential of fuel cell materials for water desalination and wastewater treatment; and development of a new diagnostics methodology to characterize non-uniform current density distribution.

Key accomplishment and details of the work conducted in each of these areas are described below. Publications and presentations are referenced at the end of this section.

## Support to NRL

Under APRISES14, HNEI continued its collaboration with NRL, evaluating NRL's use of additive manufacturing to tune PEMFC electrode structures fabricated using ultrasonic spray deposition to create graded electrodes with stacked layers of different properties. The micro-porosity of catalyst layers has been shown to play a significant role on water management [1, 2]. However, a clear understanding of the preferred spatial distribution of meso- and micro-pores does not exist and is needed to optimize gas and water transport and achieve maximum performance. NRL investigated the impact of ionomer, carbon support materials, and various graded catalyst layers on PEMFC performance using several diagnostic techniques. HNEI supported this work by performing experiments to establish the dependence of the oxygen mass transfer coefficient on catalyst layer properties using an original procedure developed at HNEI, which was recently extended and deconvolutes the overall oxygen mass transport coefficient into several fundamental contributions.

The average limiting current density  $i_{ave}$  ( $A\ m^{-2}$ ) was first measured with low oxygen concentrations to obtain an overall oxygen mass transfer coefficient  $k$  ( $m\ s^{-1}$ ) [3].

$$i_{ave} = i_e (1 - e^{-nFkp_r/RTi_{ef}}) \quad [2.1.1]$$

with  $i_e$  the inlet reactant flow rate equivalent current density ( $A\ m^{-2}$ ),  $n$  the number of electrons exchanged in the electrochemical reaction,  $F$  the Faraday constant ( $96,500\ C\ mol^{-1}$ ),  $p_r$  the dry inlet reactant stream pressure (Pa),  $R$  the ideal gas constant ( $8.3143\ J\ mol^{-1}\ K^{-1}$ ),  $T$  the temperature (K), and  $f$  the inert gas to reactant fraction in the dry inlet reactant stream. Equation 2.1.1 accounts for the uneven current density distribution occurring at low stoichiometries. The overall mass transfer coefficient  $k$  is subsequently separated into molecular diffusion ( $k_m$ ), Knudsen diffusion ( $k_K$ ) and ionomer permeability ( $k_e$ ) contributions with changes in gas diluent molecular mass  $M$  and oxygen concentration  $c$  [3].

$$\frac{1}{k} = \frac{1}{k_m(M)} + \frac{1}{k_{e+K}(c)} = \frac{1}{k_m(M)} + \frac{1}{k_e(c)} + \frac{1}{k_K} \quad [2.1.2]$$

Recent in situ PEMFC data obtained from another project has shown that the catalyst layer ionomer mass transfer resistance depends on the oxidant stream oxygen concentration. This aspect is novel, expands the method that was previously developed [3], and will be reported under APRISES15. Figure 2.1.1 illustrates exemplary Equation 2.1.1 plots whereas Figure 2.1.2 shows the sequential mass transfer coefficient separation process based on Equation 2.1.2. Average current density data is first fitted to Equation 2.1.1 to extract the overall mass transfer coefficient (Figure 2.1.1). Subsequently, the overall mass transfer coefficient is plotted as a function of the gas diluent molecular mass (Figure 2.1.2, left). An extrapolation to a zero molecular mass yields a lumped mass transfer coefficient, which includes Knudsen diffusion and ionomer permeability contributions (Figure 2.1.2, left). The following use of Equation 2.1.2 leads to the molecular

diffusion mass transfer coefficient (Figure 2.1.2, right). The lumped mass transfer coefficient is graphed as a function of the oxygen concentration (Figure 2.1.2, center), which provides an estimate of the Knudsen diffusion at a zero oxygen concentration. The re-use of Equation 2.1.2 finally gives the ionomer permeability mass transfer coefficient.

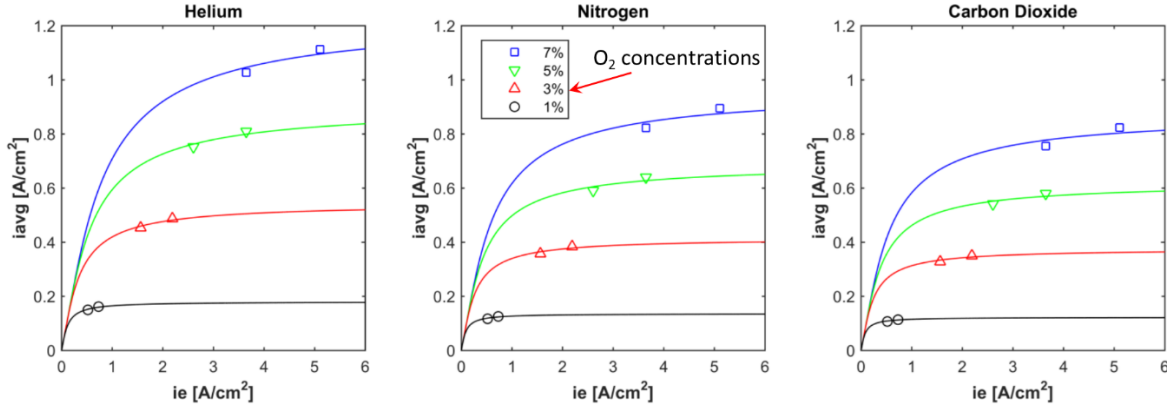


Figure 2.1.1. Plots of the average limiting current as a function of the inlet reactant flow rate equivalent current density for different oxygen concentrations and gas diluents.

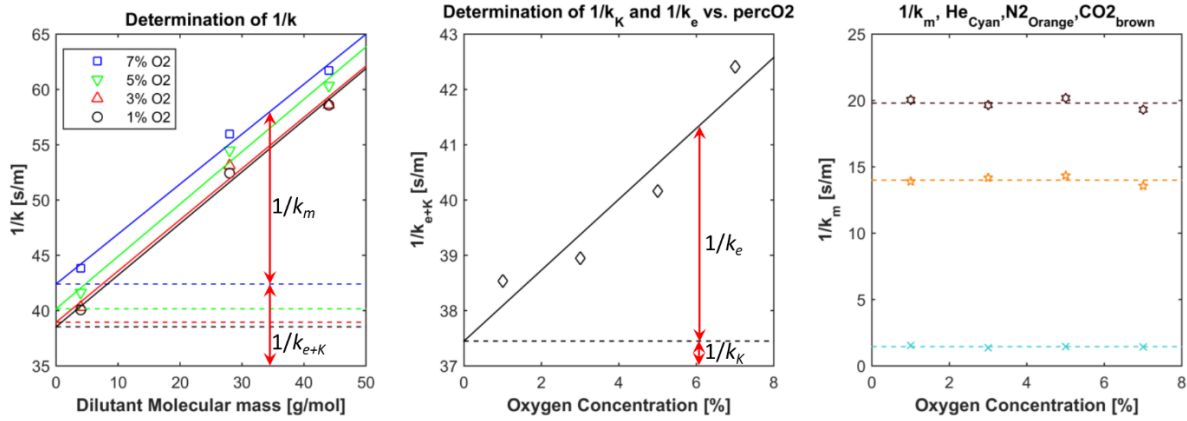


Figure 2.1.2. Overall oxygen mass transfer resistance (the inverse of the mass transfer coefficient) as a function of the gas diluent molecular mass for different oxygen concentrations (left). The lumped mass transfer resistance (gas phase Knudsen diffusion, solid phase ionomer permeability) as a function of the oxygen concentration (center). Gas phase molecular diffusion resistance as a function of the oxygen concentration for different gas diluent molecular masses (right).

The mass transfer separation method embodied by Equations 2.1.1 and 2.1.2 is different than other methods. For instance, operation at high stoichiometries and low oxygen concentrations is generally used to avoid local variations in current densities but likely overemphasizes the forced convection contribution in porous gas diffusion electrodes [4]. As a result, parameter values do

not necessarily apply to practical operating conditions. Subsequently, the overall mass transfer coefficient is separated, for example, using diluent molecular mass and temperature variations [4].

In this work, HNEI evaluated 8 different cathode catalyst layer formulations produced by NRL. Each formulation was tested in a single cell and subjected to 60 different combinations of diluent gas ( $\text{C}_3\text{F}_8$ ,  $\text{CO}_2$ ,  $\text{N}_2$ , He), gas flow rates, and oxygen concentrations (1-7 %). Each test series of 60 different combinations was repeated at least 6 times to increase the statistical accuracy. Data were analyzed using Equations 2.1.1 and 2.1.2 (Figures 2.1.1 and 2.1.2). As results have not been approved for public release, they are not presented in this report. For more information contact Karen Swider-Lyons [karen.lyons@nrl.navy.mil](mailto:karen.lyons@nrl.navy.mil).

Future NRL support at HNEI will focus on expanding the database detailing oxygen mass transfer contributions using a commercially relevant range of platinum catalyst loading. This activity will assist validation of the overall mass transfer coefficient separation method and the existence of a dependence between the ionomer permeability mass transfer coefficient and oxygen concentration, particularly for low platinum loadings, which impacts the catalyst loading selection tradeoff. In addition, the expanded database will serve as a basis for comparison to other oxygen mass transport coefficient measurement and separation methods. For the next phase of the study, state of the art membrane/electrode assemblies with a commercially relevant range in platinum cathode catalyst loading will be provided by General Motors (3 different catalyst loadings covering the 0.05 to 0.15 mg Pt  $\text{cm}^{-2}$  range). The future work will also support one international graduate student.

## Mass Transfer Analysis

This objective of this activity was to develop a local impedance model (LIM) to validate an overall cell impedance model (CIM) created under APRISES12 [5] that provides local information, including impedances and kinetic and transport parameters. The CIM brings local diagnostic capabilities to anyone without access to a segmented cell system. This work is also important to validate a HNEI diagnostic method to determine and separate mass transfer coefficients, valuable for optimization of electrode structures for high power operation. This work was completed in collaboration with the Institute of Energy and Climate Research, Jülich, Germany and is supported by other federal funds provided by the Army Research Office.

Figure 2.1.3 presents a comparison between kinetic and transport parameters derived from the LIM fitted to segmented cell data and the CIM fitted to the overall cell data. Generally, both parameter sets are fairly consistent. However, several apparent irregularities were noted. For instance, both LIM and CIM derived parameters show a decrease of the cathode catalyst layer proton conductivity along the flow field length for current densities of 0.4 and 0.6 A  $\text{cm}^{-2}$ . This is a counter-intuitive observation because the accumulation of product water at this location is expected to increase ionomer conductivity. It was hypothesized that the oxidation of acidic species attached to the

carbon surface at lower cell potentials [6] is hindered by the accumulation of liquid water near the cathode outlet. Additionally, both parameter sets demonstrate an unexplained large increase of the cathode oxygen diffusivity along the channel length for both current densities. Again, the accumulation of product water is expected to prevent such an occurrence. The origin of these effects requires supplementary investigations. More details are provided in the published manuscript (item 1 in the Publications and presentations section).

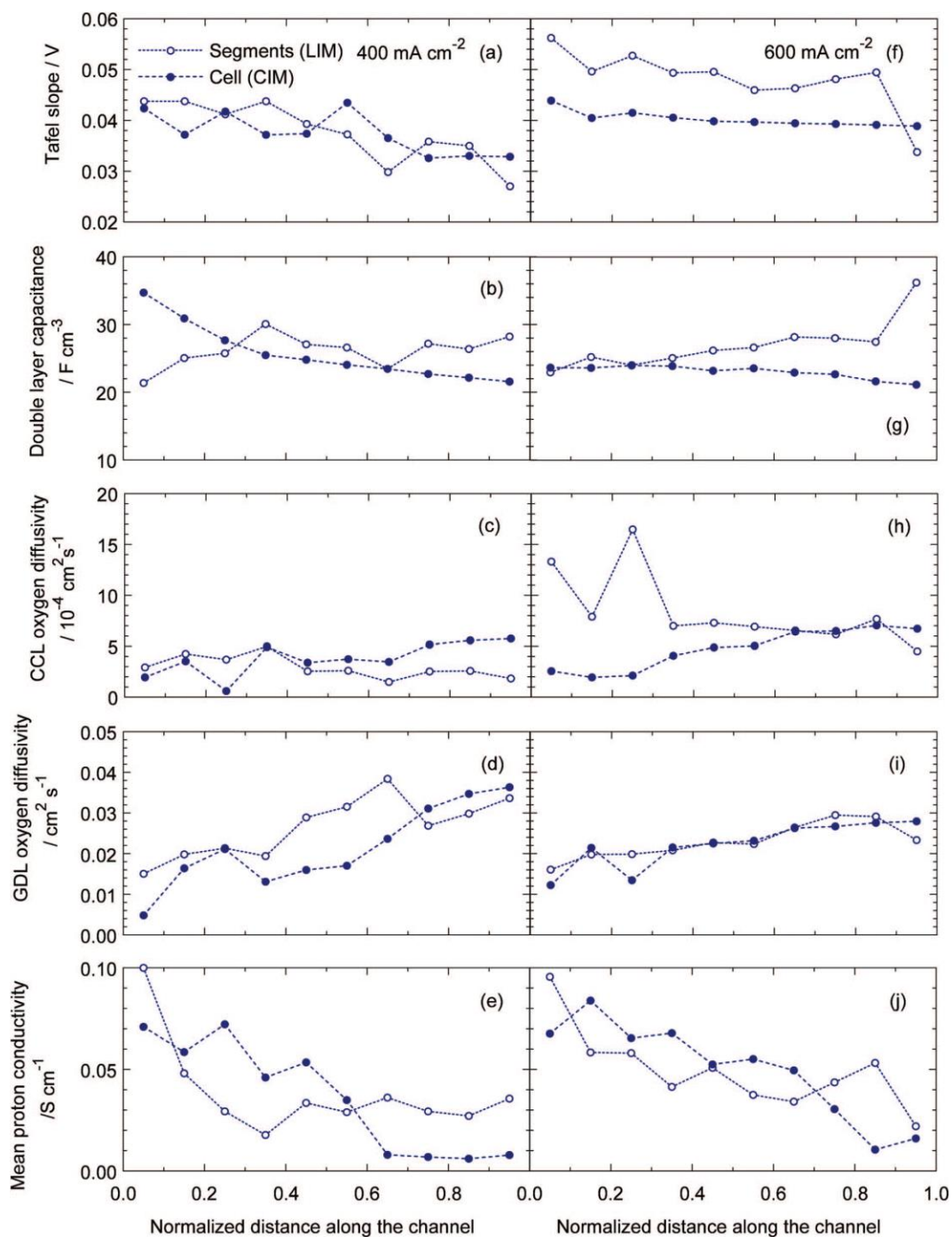


Figure 2.1.3. Oxygen reduction Tafel slope (a, f), cathode double layer capacitance (b, g), cathode catalyst layer oxygen diffusivity (c, h), gas diffusion layer oxygen diffusivity (d, i), and mean proton conductivity (e, j) obtained by fitting local impedance spectra (open points) and the whole cell spectrum (solid points). 0.4 (a to e) and 0.6 (f to j) A cm<sup>-2</sup>.

## Transition Metal Carbide Catalysts

This new activity focused on the synthesis of low cost and durable transition metal carbide (TMC) catalysts applicable to technologies such as fuel cells, water electrolyzers for hydrogen production, and flow batteries. In comparison, state-of-the-art platinum catalysts for fuel cell and water electrolysis are expensive. TMCs are attractive because they possess an electronic structure similar to platinum that promotes high catalyst activities and outstanding thermal and chemical stabilities. The novel TMC catalyst morphology in this work was designed to have a large active area that decreases kinetic voltage losses and a stronger bond between catalysts particles and support to delay aging. The composition of TMC catalysts is also tunable by varying the carbon concentration and transition metal, which is an advantage to improve activity.

Catalyst synthesis equipment was identified, procured and commissioned (rotary evaporator, tube furnace, vacuum filtration system, vacuum oven). Subsequently, TMC catalysts were synthesized using two different carbons; graphite (a baseline material) and a carbon derived from coconut husk decomposed in an argon atmosphere at high temperature. For each carbon, TMC catalysts were synthesized in two sequential steps, which brings into contact a carbon or a carbon containing material and a vanadium species at high temperatures under an argon atmosphere to avoid oxidation. Key synthesis and catalyst structure details are avoided to protect the intellectual property.

Catalysts were first characterized by X-ray diffraction to ensure that the synthesis was successful and TMCs were obtained. Figure 2.1.4 shows X-ray diffraction patterns (signal intensity versus X-ray reflection angle) of the vanadium carbides using coconut husk ( $\text{TMC}_{\text{coconut}}$ ) and graphite ( $\text{TMC}_{\text{graphite}}$ ) as carbon sources. The peaks represent distinct signatures that enables species identification with a library of X-ray diffraction patterns for reference materials. As shown in Figure 2.1.4a, the carbon obtained from coconut husk carburization ( $\text{Carbon}_{\text{coconut}}$ ) is amorphous (peaks are relatively wide in comparison to crystalline materials). The dominating phase for  $\text{TMC}_{\text{coconut}(1)}$  obtained after the first step is  $\text{V}_8\text{C}_7$ . That material contains a small amount of vanadium oxide  $\text{V}_2\text{O}_3$ , which is removed by a sulfuric acid leaching step ( $\text{TMC}_{\text{coconut}(1)\text{-acid}}$ ). After the second synthesis step ( $\text{TMC}_{\text{coconut}(2)}$ ), the amount of  $\text{V}_2\text{O}_3$  is larger than after the first step.  $\text{TMC}_{\text{coconut}(2)}$  was leached in sulfuric acid to remove the oxide and an X-ray diffraction pattern is planned to confirm its composition.

For graphite, similar results were obtained with the exception of graphite itself (Figure 2.1.4b). Graphite, a crystalline material, is characterized by significantly narrower peaks than the amorphous carbon derived from coconut husk (Figure 2.1.4a). Otherwise, the  $\text{TMC}_{\text{graphite}(1)}$  also shows the presence of  $\text{V}_8\text{C}_7$  and a small amount of  $\text{V}_2\text{O}_3$  that is removed by sulfuric acid ( $\text{TMC}_{\text{graphite}(1)\text{-acid}}$ ). After the second synthesis step,  $\text{V}_2\text{O}_3$  is still present in the catalyst ( $\text{TMC}_{\text{graphite}(2)}$ ).  $\text{TMC}_{\text{graphite}(2)}$  was exposed to sulfuric acid to remove the oxide and an X-ray



diffraction pattern is planned to confirm its composition. The average size of  $V_8C_7$  crystals for  $TMC_{coconut(1)}$ ,  $TMC_{coconut(2)}$ ,  $TMC_{graphite(1)}$ , and  $TMC_{graphite(2)}$  is approximately 50, 42, 46, and 59 nm, respectively.

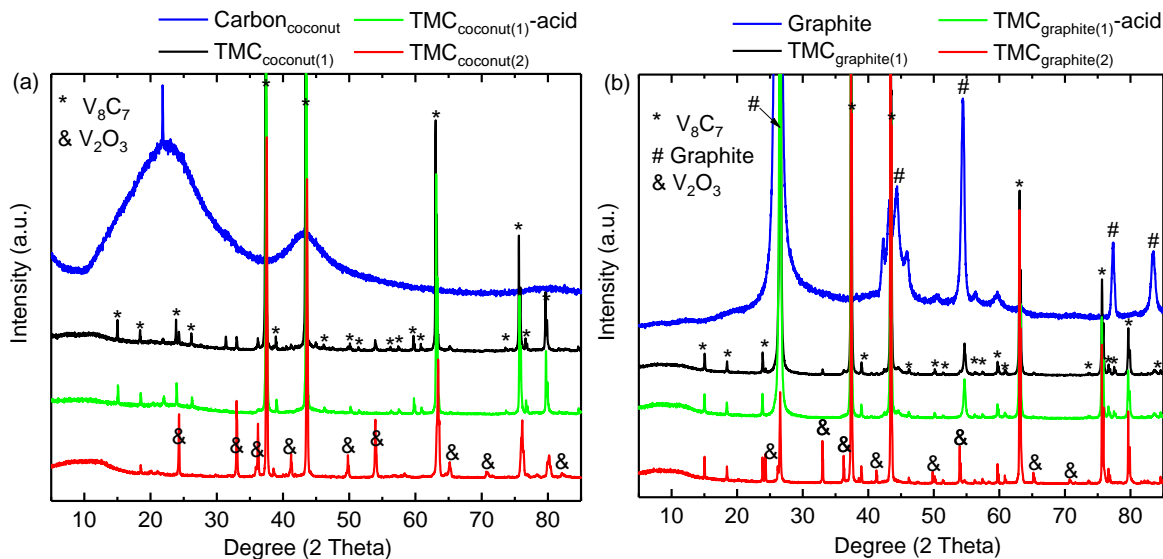


Figure 2.1.4. X-ray diffraction patterns of vanadium carbides obtained from carburization of (a) coconut husk and (b) graphite as carbon sources.

After the catalyst composition was confirmed, the catalytic activity of vanadium carbides for fuel cell, water electrolyzer and vanadium flow battery reactions was measured. Benefits were observed only for the vanadium reactions. Reactions involving vanadium ions in their 5+ and 4+ oxidation states ( $VO_2^+$  and  $VO^{2+}$ ) were evaluated by cyclic voltammetry and are shown in Figure 2.1.5. Electrochemical parameters are given in Table 2.1.1. The carbon samples were also leached with sulfuric acid and labeled as “-acid” for comparison with the carbide samples. The reversibility and catalytic activity toward  $VO_2^+/VO^{2+}$  redox reactions is evaluated on the basis of the potential separation between peaks ( $\Delta E_p$ ), the peak currents ratio ( $I_{pa}/I_{pc}$ ) and peak currents. Values of 0.059 V for  $\Delta E_p$  and 1 for  $I_{pa}/I_{pc}$  correspond to a reversible one-electron process (ideal case) [7]. Smaller  $\Delta E_p$  and higher peak current values indicate a relatively better reversibility and catalytic activity toward  $VO_2^+/VO^{2+}$  redox reactions. As shown in Figure 2.1.5a and Table 2.1.1, the  $TMC_{coconut(1)}$ -acid sample has marginally better reversibility and catalytic activity than the  $Carbon_{coconut}$ -acid sample (carbon is the common catalyst for vanadium flow batteries). However, for the graphite samples (Figure 2.1.5b), an improvement is not observed for the  $TMC_{graphite(1)}$ -acid sample (larger  $\Delta E_p$  and smaller peak current values). For TMC samples obtained after the second synthesis step ( $TMC_{coconut(2)}$  and  $TMC_{graphite(2)}$ ), the catalyst performance is lowered in comparison to TMC samples that resulted from the first synthesis step ( $TMC_{coconut(1)}$  and  $TMC_{graphite(1)}$ ). This

observation partly led to a planned change for the second synthesis step to avoid this issue as discussed below.

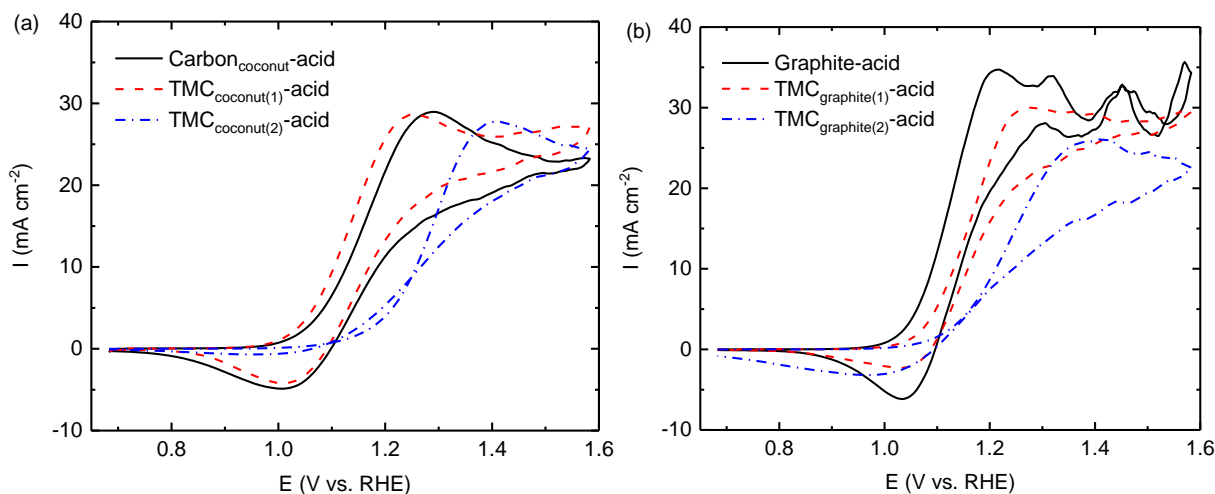


Figure 2.1.5.  $\text{VO}_2^+/\text{VO}^{2+}$  redox reactions on various electrodes recorded at  $10 \text{ mV s}^{-1}$  in  $\text{N}_2$  saturated  $3 \text{ M H}_2\text{SO}_4 + 1 \text{ M VOSO}_4$  at  $25^\circ\text{C}$ . (a) coconut husk and (b) graphite as carbon sources.

Table 2.1.1. Electrochemical data obtained from the cyclic voltammograms recorded in Figure 2.1.5.

Sample	$E_{pa}$ /V	$E_{pc}$ /V	$I_{pa}$ /mA cm <sup>-2</sup>	$I_{pc}$ /mA cm <sup>-2</sup>	$\Delta E_p$ /V	$I_{pa}/I_{pc}$
Carbon <sub>coconut</sub>	1.29	1.01	29.07	27.79	0.28	1.05
TMC <sub>coconut(1)</sub>	1.25	1.01	28.78	29.96	0.24	0.96
TMC <sub>coconut(2)</sub>	1.41	1.01	27.75	25.21	0.40	1.10
Graphite	1.21	1.04	34.67	34.64	0.17	1.00
TMC <sub>graphite(1)</sub>	1.27	1.04	29.98	30.31	0.23	0.99
TMC <sub>graphite(2)</sub>	1.41	1.03	26.19	28.14	0.38	0.93

Figure 2.1.6 shows similar information as Figure 2.1.5 for redox reactions involving vanadium ions in their 3+ and 2+ oxidation states ( $\text{V}^{3+}$  and  $\text{V}^{2+}$ ). The TMC<sub>coconut(1)</sub>-acid and TMC<sub>graphite(1)</sub>-acid show higher redox current densities than Carbon<sub>coconut</sub>-acid and Graphite-acid, respectively, indicating that vanadium carbide exhibits a better reversibility and a higher catalytic activity toward  $\text{V}^{3+}/\text{V}^{2+}$  redox reactions with smaller  $\Delta E_p$  and higher peak current values.

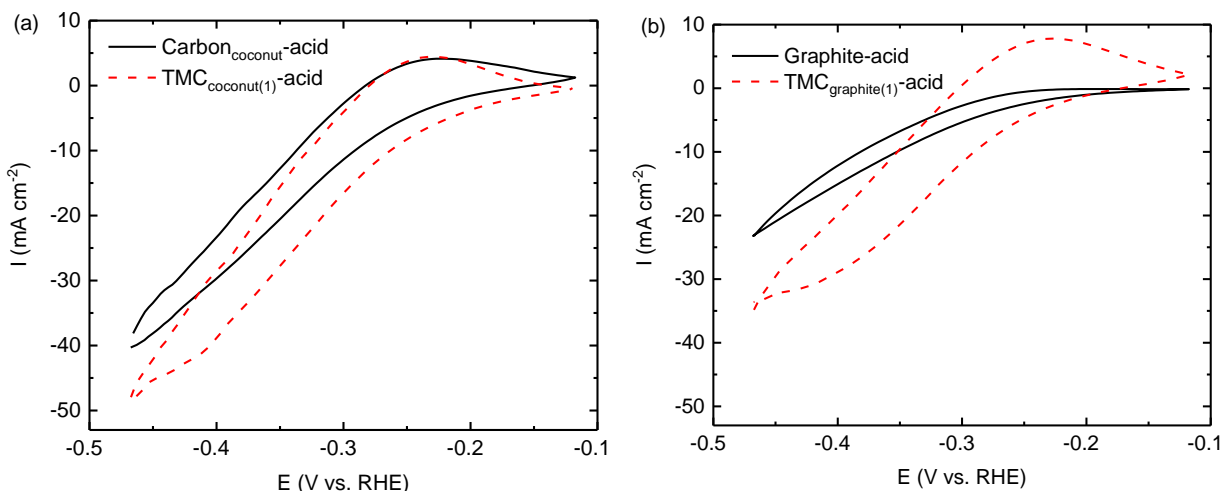


Figure 2.1.6.  $V^{3+}/V^{2+}$  redox reactions on various electrodes recorded at  $10 \text{ mV s}^{-1}$  in  $N_2$  saturated  $3 \text{ M H}_2\text{SO}_4 + 1 \text{ M } (V^{3+}+V^{2+})$  at  $25^\circ\text{C}$ . (a) coconut husk and (b) graphite as carbon sources.

Future activities will include modifications to the catalyst synthesis approach because Figure 2.1.5 results indicate that the second step diminish the catalyst activity. Furthermore, a small amount of oxide was detected after each synthesis step (Figure 2.1.4). A small amount of hydrogen will be added to the gas circulating during the synthesis to maintain reducing conditions and minimize the formation of oxides. This change also has the advantage of decreasing the synthesis temperature, which will minimize particle coalescence and favor the formation of small particles that are desirable for a high exposed surface area. Subsequently, the activity of the catalysts will be re-evaluated for reactions relevant to fuel cells, water electrolyzers and flow batteries, which may include changes in compositions to increase activity by tuning the catalyst particle structure, morphology and size. Additional characterization methods will also be used with the objective to create predictive correlations between catalyst activity and particle characteristics (energy dispersive X-ray spectroscopy, scanning electron microscopy, transmission electron microscopy, X-ray photoelectron spectroscopy). A few of these characterization activities will be jointly carried out with Kyushu University.

## Fuel Cell Contamination Mechanisms

Under APRISES14, a fuel cell contaminated with sulfur dioxide ( $\text{SO}_2$ ) was characterized with a segmented cell system and a mechanism and mathematical model were developed to facilitate the development of performance loss mitigation and recovery strategies. Sulfur dioxide is a particularly important contaminant due to its various anthropogenic (fossil fuel combustion) and natural (volcanic eruptions) sources and persistent voltage losses after exposure is interrupted [8-13]. This work was completed in collaboration with Technische Universität Braunschweig, Germany.

Figure 2.1.7 depicts local fuel cell voltage and normalized current density transients before, during and after exposure to 2 ppm sulfur dioxide, which demonstrate a significant voltage loss (70 and 295 mV at steady state for respectively 0.2 and 1 A cm<sup>-2</sup>). Although differences in local cell voltage are minimal (Figure 2.1.7a and c), local current densities are significantly and differentially affected (Figure 2.1.7b and d). Moreover, the local current density redistribution is dependent on the overall current density and is more complex for the 1 A cm<sup>-2</sup> case.

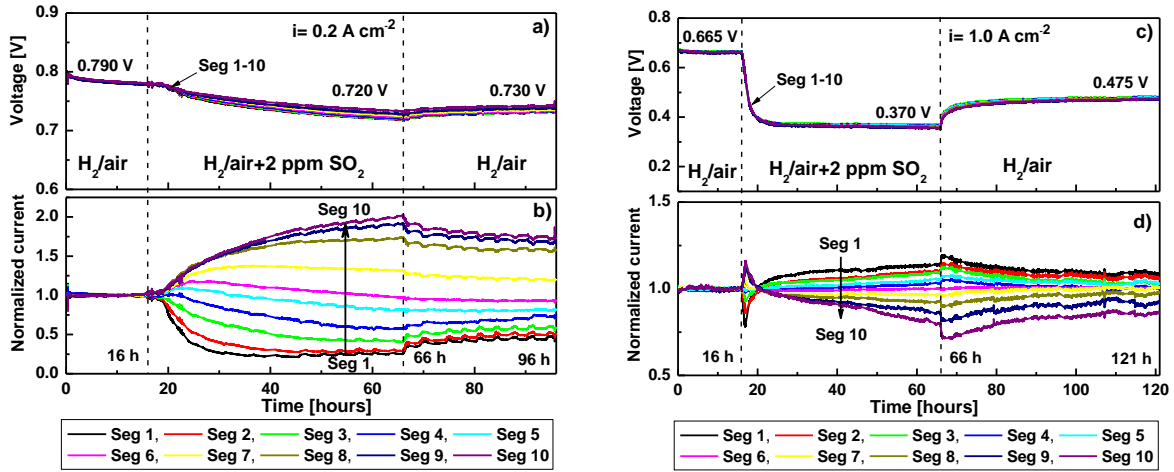


Figure 2.1.7. Cell voltage (a, c) and normalized current density (b, d) transients resulting from a segmented fuel cell temporarily contaminated by 2 ppm SO<sub>2</sub> in air for overall current densities of 0.2 (a, b) and 1 A cm<sup>-2</sup> (c, d).

Figure 2.1.7 data are attributed to electrochemical sulfur dioxide reactions that are cathode potential dependent. For a low current density of 0.2 A cm<sup>-2</sup>, the cell voltage remains in a relatively narrow range of 0.72 to 0.78 V (Figure 2.1.7), values that are close to the oxidation potential of SO<sub>2</sub> on platinum. Adsorption and possible slow oxidation of SO<sub>2</sub> [14-16] progresses from the cathode inlet, forming various strongly and weakly bonded SO<sub>x</sub> species blocking the Pt surface, which impacted segments 1 to 4 with concurrent decreases in current density and cell voltage (Figure 2.1.7a and b). At 1.0 A cm<sup>-2</sup>, a similar pattern is initially observed but with a larger decrease in cell voltage. After the cell voltage reached 0.5 to 0.55 V, an inflection point in the voltage transients is observed (not visible in Figure 2.1.7c) and a drastic change in current density redistribution occurs (Figure 2.1.7d). These observations and the appearance of a low frequency inductance in impedance spectra (not shown) indicated the presence of an additional electrochemical process involving an electron transfer. Sulfur dioxide reduction to SO begins at a potential of 0.45 V versus the hydrogen reference electrode [17, 18], which is consistent with an uncorrected 0.5 to 0.55 V cell voltage.

After the contaminant injection was interrupted, the cell voltage is not restored to its initial value due to strongly adsorbed leftover species on the catalyst surface;  $\text{SO}_x$  species for  $0.2 \text{ A cm}^{-2}$  and  $\text{S}^0$  for  $1 \text{ A cm}^{-2}$ . The formation of  $\text{S}^0$  was detected by X-ray photoelectron spectroscopy (not shown) not only on the cathode electrode but also on the cathode gas diffusion layer. Fuel cell performance can only be restored by removing these leftover sulfur species from the Pt surface, which can be achieved by bringing the cathode potential to a value greater than 1 V versus the hydrogen reference electrode. From a practical point of view, any recovery procedure is restricted to the use of system components including the fuel cell stack, the limited gas supply (hydrogen and air), pumps, humidifiers, and power electronics.

All fuel cell diagnostic results provided the information needed to develop a contamination mechanism and mathematical model, which accounts for oxygen reduction and sulfur dioxide electrochemical and chemical reactions as well as species adsorption and desorption processes. Figure 2.1.8a shows a good agreement between model simulation results and experimental cell voltage data during both contamination and recovery periods. Figure 2.1.8b details species coverages on the catalyst surface. More details are provided in the published manuscript (item 2 in the Publications and presentations section).

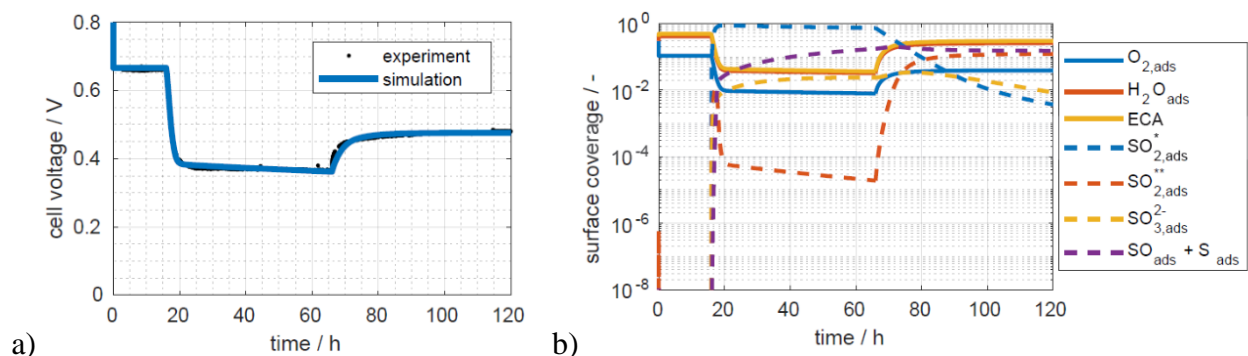


Figure 2.1.8. Cell voltage (a) and surface coverages (b) as a function of time before, during, and after contamination by 2 ppm  $\text{SO}_2$  at a current density of  $1 \text{ A cm}^{-2}$ .

### Performance Recovery for Contaminated Fuel Cells

Under APRISES11 and 13, recovery strategies using 2 oxidant gases (nitrous oxide,  $\text{N}_2\text{O}$  and ozone,  $\text{O}_3$ ) were evaluated at HNEI to restore PEMFCs poisoned by traces of sulfur dioxide (emitted by volcanoes), bromomethane (emitted by oceans), and hydrogen chloride (emitted by volcanoes and oceans) in air. Both oxidants were expected to bring the cathode potential above 1.6 V versus the hydrogen reference electrode, a value that is sufficiently high to oxidize sulfur dioxide, bromomethane and hydrogen chloride products (respectively, sulfur, bromide and chloride) and produce species (respectively, sulfate, bromine and chlorine) that are more easily entrained and eliminated by the gas stream and liquid water. Unfortunately, experimental results

indicated that  $\text{N}_2\text{O}$  is inefficient to oxidize adsorbates due to the low open circuit voltage (OCV) of  $\sim 0.75$  V versus the hydrogen reference electrode with pure  $\text{N}_2\text{O}$ . In contrast,  $\text{O}_3$  is too potent (the OCV reaches 1.51 V versus the hydrogen reference electrode with 1000 ppm  $\text{O}_3$  in air), causes permanent damage to the catalyst layer, and adds cell voltage losses.

Under APRISES14, new methods were conceived that are based on changes in operating conditions to recover cell performance losses resulting from sulfur dioxide, bromomethane and hydrogen chloride exposure. These in situ methods were effective for single cells. For example, Figures 2.1.9 and 2.1.10 illustrate cell performance transients and polarization curves, including degradation and recovery phases from a temporary bromomethane and sulfur dioxide exposure. Figure 2.1.9a shows that the cell voltage that is initially constant before the introduction of 50 ppm bromomethane at approximately 7 h, is gradually reduced by approximately 50 % over a period of 20 h. At approximately 26 h, neat air circulation is restored, which leads to a small cell voltage recovery after 6 h of operation. However, after the recovery operation (period marked as “recovery”), the initial cell voltage was reestablished to its initial value. Figure 2.1.9b polarization curves also indicate that the cell performance completely recovered for all current densities. The situation for 10 ppm sulfur dioxide contamination is qualitatively identical. Figure 2.1.10a successively depicts a steady cell voltage (up to  $\sim 8$  h), a progressive cell voltage reduction of  $\sim 45$  % (from  $\sim 8$  to  $\sim 16$  h), and an increase in cell voltage with neat air to a value equal to 70 % of the initial cell performance (from  $\sim 16$  to  $\sim 24$  h). Subsequently, recovery operations for the cathode and anode (periods marked as “recovery”), which brought the cell voltage to respectively 90 and 99 % of its initial value. Cell polarization curves in Figure 2.1a.10b show a similar stepwise and almost complete recovery for all current densities up to  $\sim 1.6 \text{ A cm}^{-2}$ . Key recovery method details are avoided to protect the intellectual property.

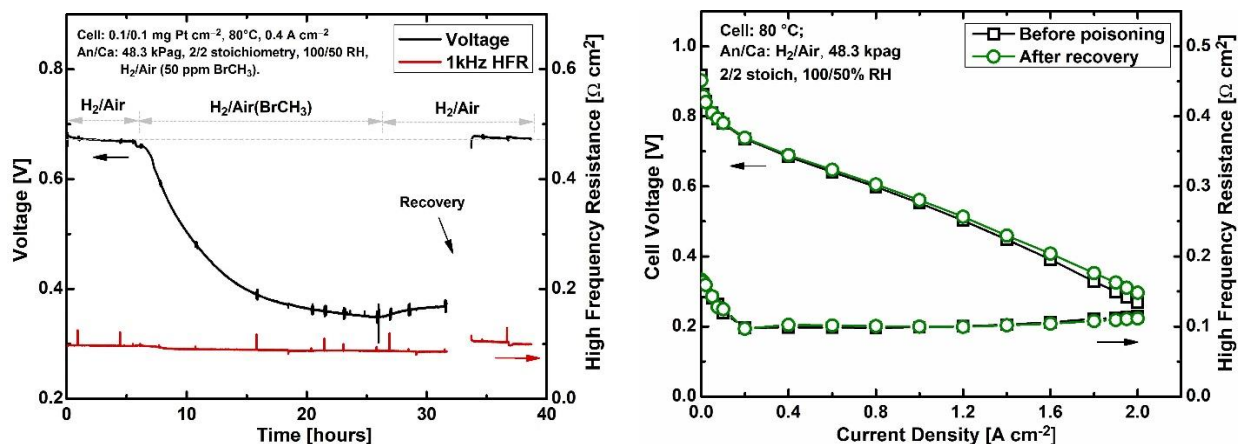


Figure 2.1.9. Cell voltage response (black curve) to a temporary bromomethane exposure followed by recovery periods with neat air and changes in operating conditions (a). Polarization curves (2 curves at the top) before contamination (PaBOT) and after recovery periods (PaEOT) (b). HFR: high frequency resistance, An/Ca: anode/cathode, stoich: stoichiometry, RH: relative humidity.

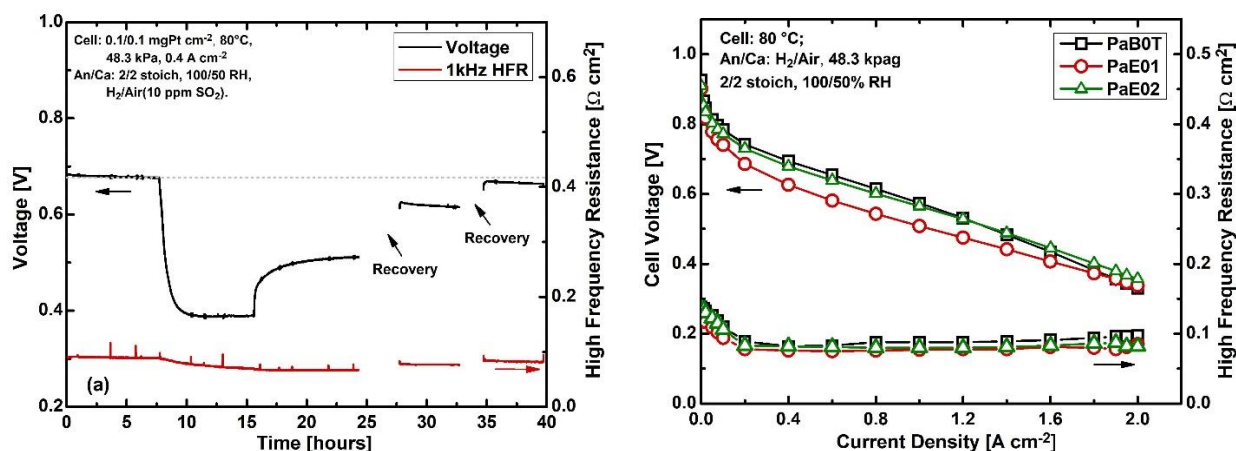


Figure 2.1.10. Cell voltage response (black curve) to a temporary sulfur dioxide exposure followed by recovery periods with neat air and changes in operating conditions (a). Polarization curves (3 curves at the top) before contamination (PaBOT) and after recovery periods (PaEOT, PaE02) (b). HFR: high frequency resistance, An/Ca: anode/cathode, stoich: stoichiometry, RH: relative humidity.

Under a future APRISES award, the contamination recovery work will resume to evaluate the methods' effectiveness with commercially relevant fuel cell stacks and further assess the need to protect that intellectual property. Stack compatible, in situ recovery methods are preferable to increase system robustness (the air intake filter may fail) and avoid the need for electrical connections to each cell for electrode potential control (contaminant oxidation or reduction). An

invention disclosure will be filed if single cell results are successfully duplicated with fuel cell stacks for sulfur dioxide, bromomethane and hydrogen chloride.

### **Novel Water Purification Process**

Under this new activity PEMFC materials and designs were adapted to evaluate their potential as a low energy technology for water desalination and wastewater purification. PEMFCs produce water, which is managed in part by taking advantage of the membrane water transport properties to avoid flooding within the cells. Membrane water treatment processes, one of the leading market segments, share similarities with PEMFC materials and designs, including separated compartments with a water permeable membrane. The raw water is introduced in one compartment. The selective membrane subject to a specific driving force (pressure gradient, temperature gradient, etc.) lets the water permeate to the other compartment as the clean water stream (the permeate). The water that contains undesirable contaminants bypasses the membrane and flows out as a waste stream (the retentate or concentrate).

Under APRISES14, a PEMFC was modified and operated as a membrane water treatment process to assess the prospects of PEMFC materials and designs. Operating conditions were selected to exploit membrane water transport properties and minimize the energy consumption associated with the water transport driving force.

Seawater desalination and wastewater treatment tests were conducted with a modified 50 cm<sup>2</sup> active area PEMFC. The seawater was locally obtained from a nearby beach and a wastewater sample was acquired from a municipal Oahu water treatment plant. The seawater and wastewater were fed to the cell at a 2.1 g min<sup>-1</sup> flow rate. The other side of the cell was swept by N<sub>2</sub> at a 0.3 standard L min<sup>-1</sup> flow rate to push the permeate water out of the cell. The permeate flow rate through the membrane structure was measured resulting in values of 0.72 and 0.81 g min<sup>-1</sup> for the seawater and wastewater, respectively. These values represent water recoveries of 34 and 39 % and water productivities of 7.8 and 8.8 kg μm h<sup>-1</sup> m<sup>-2</sup> kPa<sup>-1</sup>, respectively. Seawater, wastewater, permeate, and concentrate water samples were analyzed by several methods: total organic carbon, total organic nitrogen, ion chromatography, and inductively coupled plasma. Results are given in Figure 2.1.11. The following 7 ions, Cl<sup>-</sup>, Na<sup>+</sup>, SO<sub>4</sub><sup>2-</sup>, Br<sup>-</sup>, K<sup>+</sup>, Mg<sup>2+</sup>, Ca<sup>2+</sup>, have a concentration that is typical of seawater (Figure 2.1.11, top). The concentration of all seawater components in the permeate was reduced by a factor of at least 100 (>99 % ion rejection) with the exception of total organic carbon and nitrogen which have low concentration levels in seawater. For the wastewater (Figure 2.1.11, bottom), the concentration of all components in the permeate was reduced by a factor of at least 10 (>90 % ion rejection) with the exception of total organic nitrogen, fluoride, and ammonium. The larger decrease in species concentration for seawater is partly attributed to the lower concentration driving force for wastewater (more dilute stream). Both permeate water qualify as freshwater on a salt content basis (<500 mg L<sup>-1</sup>). These results obtained



with a sub-optimal cell favorably compare to a water productivity of  $4.6 \text{ kg } \mu\text{m h}^{-1} \text{ m}^{-2} \text{ kPa}^{-1}$  for a vacuum multi-effect membrane distillation with enhanced heat recovery water desalination pilot plant (an increase of 70 %) with otherwise similar ion rejection of 99.98 % and water recovery of 36 % [19]. The energy consumption for the HNEI water treatment process, another key comparative metric, was not accessible with the experimental setup used.

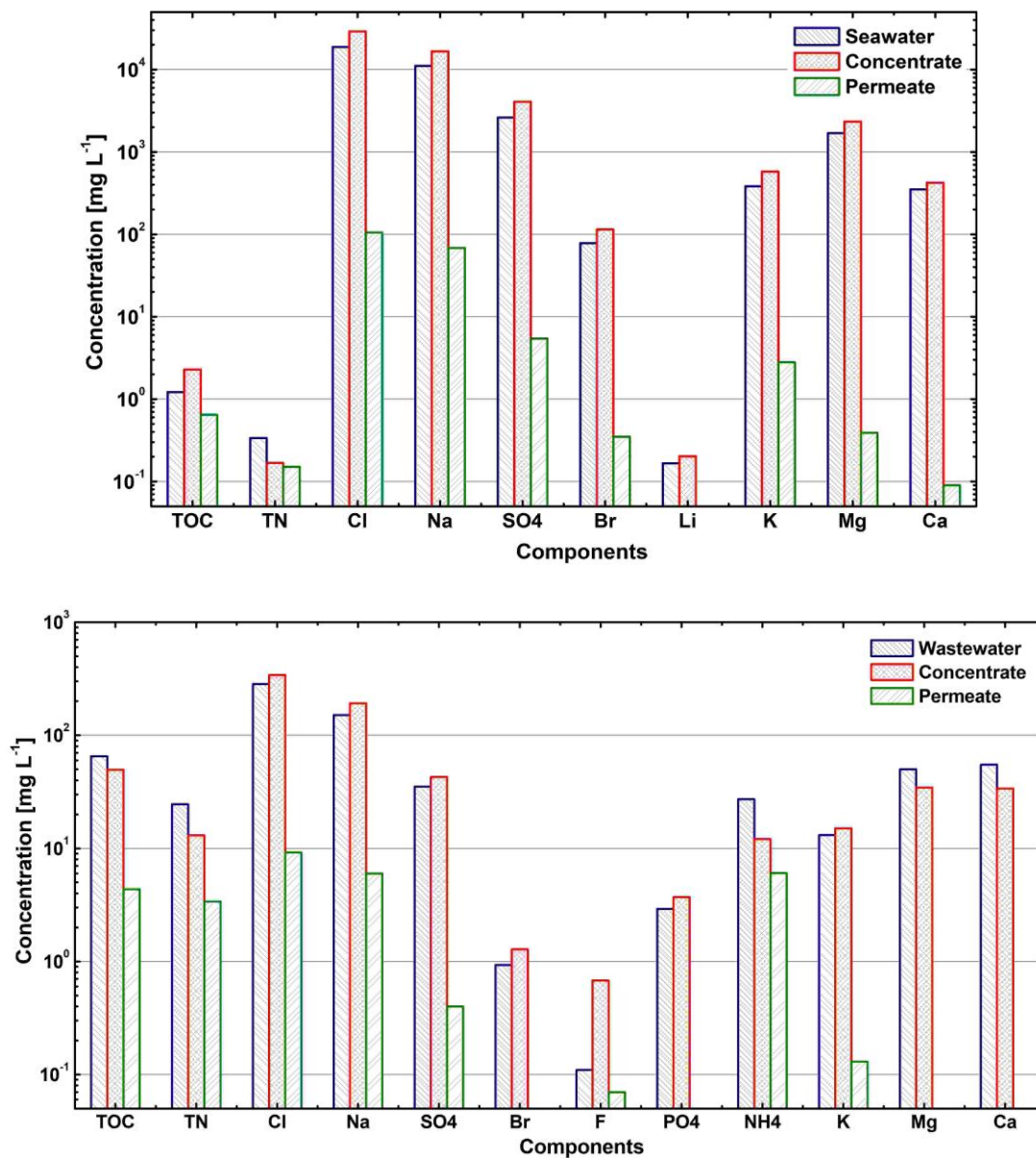


Figure 2.1.11. Concentration of dissolved seawater (top) and wastewater (bottom) species for unaltered, concentrate and permeate samples.

An invention disclosure was filed and proposals were submitted to the Department of the Interior and the Department of Energy to accelerate development of the HNEI water treatment process.

Additionally, under a future APRISES award, the energy consumption for water pumping will be estimated to more clearly define benefits. Furthermore, modifications will be introduced to further improve water productivity and recovery, species selectivity, and energy consumption.

### **Current Density Distribution Analysis**

Under APRISES14, a fuel cell mathematical model was constructed to predict the current density distribution using polarization curve parameters and ohmic resistances that are more easily measured and that do not require a complex segmented cell system. The model is of interest to designers because an uneven current distribution may locally accelerate material degradation. This work was completed in collaboration with the Institute of Energy and Climate Research, Jülich, Germany.

An analytical solution was derived for the case of a relatively small cell resistance by modifying a previously published framework [20]. The unmodified framework was also used to create a numerical algorithm for validation of the analytical solution. A Python code for the analytical solution can be downloaded from [https://github.com/akulikovsky/Local-current/blob/master/Local\\_current\\_solver.py](https://github.com/akulikovsky/Local-current/blob/master/Local_current_solver.py). Figure 2.1.12a indicates that the first order analytical solution matches the numerical solution as long as the ohmic resistance is relatively small, which occurs for overall current densities equal or below  $0.2 \text{ A cm}^{-2}$ . More details are provided in the published manuscript (item 3 in the Publications and presentations section).

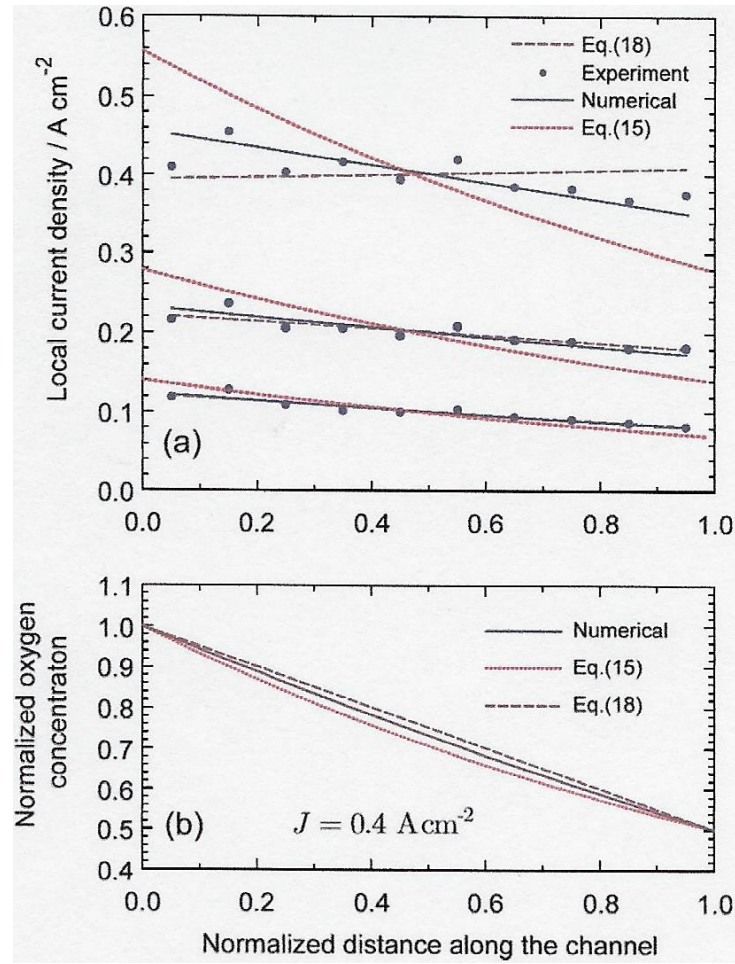


Figure 2.1.12. Experimental (points) and model current density distributions (lines) for an air flow field channel (a). Zero (zero ohmic resistance, red dash line) and first (relatively small ohmic resistance, purple dash line) order approximations. Numerical solution (solid black line). Corresponding numerical (solid line) and analytical (red and purple dash lines) normalized oxygen concentration profiles (b).

## Publications and Presentations

### *Peer Reviewed Publications*

1. Reshetenko, T. and Kulikovskiy, A. 2019. A Model for Local Impedance: Validation of the Model for Local Parameters Recovery from a Single Spectrum of PEM Fuel Cell. J. Electrochem. Soc., 166, pp F431-F439.
2. Reshetenko, T., Laue, V., Krewer, U., and Artyushkova, K. 2019. Poisoning Effects of  $\text{SO}_2$  in an Air Stream on Spatial PEMFC Performance. J. Power Sources, 438, article 226949.

3. Reshetenko, T. and Kulikovskiy, A. 2019. On the Distribution of Local Current Density along a PEM Fuel Cell Cathode Channel. *Electrochem. Commun.*, 101, 35-38.
4. Zhai, Y. and St-Pierre, J. 2019. Acetonitrile Contamination in Cathode of Proton Exchange Membrane Fuel Cells and the Cell Performance Recovery. *Appl. Energy*, 242, pp 239-247.
5. Qi, J., Zhai, Y., and St-Pierre, J. 2019. Effect of Contaminant Mixtures in Air on Proton Exchange Membrane Fuel Cell Performance. *J. Power Sources*, 413, 86-97.

#### *Conference Proceedings and Posters*

1. Reshetenko, T. and Ben, B. L. 2018. Effects of Structural and Textural Properties of GDL on Oxygen Mass Transport Coefficient in PEMFC, Gordon Research Conference (Fuel Cells), July 29 to August 3, 2018, Bryant University, Smithfield, RI, USA.
2. Reshetenko, T. and Ben, B. L. 2018. Effect of NO<sub>2</sub> as Air Pollution on Spatial Performance of High- and Low-Pt Loaded PEM Fuel Cells. 69<sup>th</sup> Annual Meeting of the International Society of Electrochemistry, September 2-7, 2018, Bologna, Italy, ise181180.
3. St-Pierre, J. 2019. Protecting Proton Exchange Membrane Fuel Cells from Contaminants in Reactant Streams. AFS Filtcon 2019 conference, April 1-3, 2019, Cherry Hill, NJ, USA, abstract S3.1.1.
4. Severa, G., Dubarry, M., Higgins, S., St-Pierre, J., Sun, R., Dulai, H., Lee, J. H., Uspal, W., Shin, S., Qu, W., and Kim, A. S. 2019. 'Pacific-Islands' Consilience Desalination Aiming for Zero-Discharge: Concepts, Designs, and Feasibility', in 2019 International Conference on Smart Cities (2019 ICSC) Proceedings, International Society for Maintenance and Rehabilitation of Transportation Infrastructures (iSMARTi), accepted.

#### **References**

- [1] Chi, B., Hou, S., Liu, G., Deng, Y., Zeng, J., Song, H., Liao, S., and Ren, J. 2018. Tuning Hydrophobic-Hydrophilic Balance of Cathode Catalyst Layer to Improve Cell Performance of Proton Exchange Membrane Fuel Cell (PEMFC) by Mixing Polytetrafluoroethylene (PTFE). *Electrochim. Acta*, 277, pp 110-115.
- [2] Chen, L., Kang, Q., and Tao, W. 2019. Pore-Scale Study of Reactive Transport Processes in Catalyst Layer Agglomerates of Proton Exchange Membrane Fuel Cells. *Electrochim. Acta*, 306, pp 454-465.
- [3] Reshetenko, T. and St-Pierre, J. 2014. Separation Method for Oxygen Mass Transport Coefficient in Gas and Ionomer Phases in PEMFC GDE. *J. Electrochem. Soc.*, 161, pp F1089-F1100.

- [4] Nonoyama, N., Okazaki, S., Weber, A. Z., Ikogi, Y., and Yoshida, T. 2011. Analysis of Oxygen-Transport Diffusion Resistance in Proton-Exchange-Membrane Fuel Cells. *J. Electrochem. Soc.*, 158, pp B416-B423.
- [5] Reshetenko, T. and Kulikovsky, A. 2018. A Model for Extraction of Spatially Resolved Data from Impedance Spectrum of a PEM Fuel Cell. *J. Electrochem. Soc.*, 165, pp F291-F296.
- [6] Modestov, A. D., Kapustin, A. V., Avakov, V. B., Landgraf, I. K., and Tarasevich, M. R. 2014. Cathode Catalyst Layers with Ionomer to Carbon Mass Ratios in the Range 0–2 Studied by Electrochemical Impedance Spectroscopy, Cyclic Voltammetry, and Performance Measurements. *J. Power Sources*, 272, pp 735-742.
- [7] Bard, A. J. and Faulkner, L. R. 2011. *Electrochemical Methods - Fundamentals and Applications*, 2<sup>nd</sup> edition, Wiley, New York.
- [8] Pressler, V. and Ige, D. Y. 2016. State of Hawaii Annual Summary 2015 Air Quality Data. State of Hawaii Department of Health, Honolulu.
- [9] Sutton, A. J., Elias, T., and Navarrete, R. 1994. Volcanic Gas Emissions and their Impact on Ambient Air Character at Kilauea Volcano, Hawaii. United States Department of the Interior and United States Geological Survey, Open-File Report 94-569.
- [10] Angelo, M. S. and St-Pierre, J. 2014. The Effect of Common Airborne Impurities and Mixtures on PEMFC Performance and Durability. *ECS Trans.*, 64 (3), pp 773-788.
- [11] Garsany, Y., Baturina, O. A., and Swider-Lyons, K. E. 2007. Impact of SO<sub>2</sub> on the Oxygen Reduction Reaction at Pt/Vulcan Carbon Electrocatalysts. *J. Electrochem. Soc.*, 154, pp B670-B675.
- [12] Baturina, O. A. and Swider-Lyons, K. E. 2009. Effect of SO<sub>2</sub> on the Performance of the Cathode of a PEM Fuel Cell at 0.5-0.7 V. *J. Electrochem. Soc.*, 156, pp B1423-B1430.
- [13] Zhai, Y., Bender, G., Dorn, S., and Rocheleau, R. 2010. The Multiprocess Degradation of PEMFC Performance due to SO<sub>2</sub> Contamination and its Recovery. *J. Electrochem. Soc.*, 157, pp B20-B26.
- [14] Loučka, T. 1971. Adsorption and Oxidation of Sulphur and of Sulphur Dioxide at the Platinum Electrode. *Electroanal. Chem. Interf. Electrochem.*, 31, pp 319-332.
- [15] Appleby, A. J. and Pichon, B. 1979. The Mechanism of the Electrochemical Oxidation of SO<sub>2</sub> in Sulfuric Acid Solutions. *J. Electroanal. Chem.*, 95, pp 59-71.
- [16] Korzeniewski, C., McKenna, W., and Pons, S. 1987. An In Situ Infrared Study of the Oxidation of Sulfur Dioxide on Platinum Electrodes. *J. Electroanal. Chem.*, 235, pp 361-368.
- [17] Contractor, A.Q. and Lal, H. 1978. The Nature of Species Adsorbed on Pt from SO<sub>2</sub> Solutions. *J. Electroanal. Chem.*, 93, pp 99-107.
- [18] Baturina, O., Gould, B. D., Korovina, A., Garsany, Y., Stroman, R., Northrup, P. A. 2011. Products of SO<sub>2</sub> Adsorption on Fuel Cell Electrocatalysts by Combination of Sulfur K-Edge XANES and Electrochemistry. *Langmuir*, 27, pp 14930-14939.
- [19] Andrés-Mañas, J. A., Ruiz-Aguirre, A., Acién, F. G., and Zaragoza, G. 2018. Assessment of a Pilot System for Seawater Desalination Based on Vacuum Multi-Effect Membrane Distillation with Enhanced Heat Recovery, *Desalination*, 443, pp 110-121.

- [20] Chevalier, S., Josset, C., and Auvity, B. 2018. Analytical Solutions and Dimensional Analysis of Pseudo 2D Current Density Distribution Model in PEM Fuel Cells. *Renew. Energy*, 125, pp 738-746.

## 2.2 Contamination Mitigation: Air Filtration Materials Development

Under this task advanced metallo ionic liquids and molten salts air purification materials were synthesized and characterized to enable efficient use of fuel cells in harsh environmental conditions.

The key accomplishments of this subtask included: syntheses of advanced manganese (Mn), iron (Fe) and zinc (Zn) based acetate/thiocyanate metallo ionic liquids and molten salts; development of fundamental understanding of the structural aspects of the novel materials using alternate funding in collaboration with Dr. Dera from HIGP; preliminary SO<sub>2</sub> gas absorption studies of the Mn compounds with FT-ATR analyses indicating interaction of the SO<sub>2</sub> with the Mn compound, [Mn<sub>4</sub>(OAc)<sub>10</sub>[EMIM]<sub>2</sub>]<sub>n</sub>; successful development syntheses techniques for MOFs in our laboratory to enable development of high surface area hybrid MOFs-activated carbon sorbents specific for fuel cell air purification.

Our previous laboratory experiments and complimentary density functional theoretical calculations have shown the acetate anion as critical to the absorption of SO<sub>2</sub> by supported [EMIM][Ac] ionic liquid. [1, 2] These studies indicated that the gas contaminants preferentially interact with the oxygen atoms of the acetate anion of the ionic liquid compared to the imidazole cation. Consequently, in APRISES14 we focused on designing a class of advanced acetate and thiocyanate based metallo ionic liquids and molten salts with a high content of the small, highly charged basic anions as well as containing alkaline earth or transitional metal ions with expandable coordinative environment, with the aim of increasing acidic gas air purification breakthrough and saturation capacity compared to the state of the art. Our approach of combining ionic liquids and ionic solids presents opportunities to tailor the physico-chemical properties of the resulting metallo ionic liquids and molten salts. This approach can plausibly enhance or create new liquid salts with optimized properties for other applications such as battery electrolytes and thermally or magnetically responsive, high flux draw solutes for forward osmosis water purification.

Generally, an ionic liquid is a salt in the liquid state, however, liquid salts have been divided into two separate categories by virtue of their melting temperatures. Ionic liquids are designated as salts whose melting point is below 100 °C, whilst molten salts are salts with a melting temperature above 100 °C. This differentiation is arbitrary, and does not reflect any fundamental differences between the two classes of materials. Ionic liquids have recently received considerable attention in numerous applications due to their negligible volatility, large liquidus range, and tunable

chemical properties. [3-7] [5-11] Traditional ionic liquids contain large asymmetric organic cations and small inorganic anions with short-lived ion pairs. Under APRISES14 we successfully designed and synthesized novel metallo ionic liquids and molten salt materials and confirmed their syntheses utilizing X-ray diffraction, infrared vibrational spectroscopy and thermal analyses techniques as discussed in detail below for the novel manganese compounds.

The X-ray studies of the synthesized materials were performed utilizing alternate funding in collaboration with Dr. Dera at HIGP. Figure 2.2.1. shows the crystal structure of the metallo ionic liquid compound  $[\text{EMIM}][\text{Fe}]_2[\text{Ac}]_5\text{H}_2\text{O}$  with onset melting point of  $\sim 95^\circ\text{C}$  and a molten salt,  $[\text{Mn}_4(\text{OAc})_{10}[\text{EMIM}]_2]_n$ , with onset melting point of about  $123^\circ\text{C}$ .

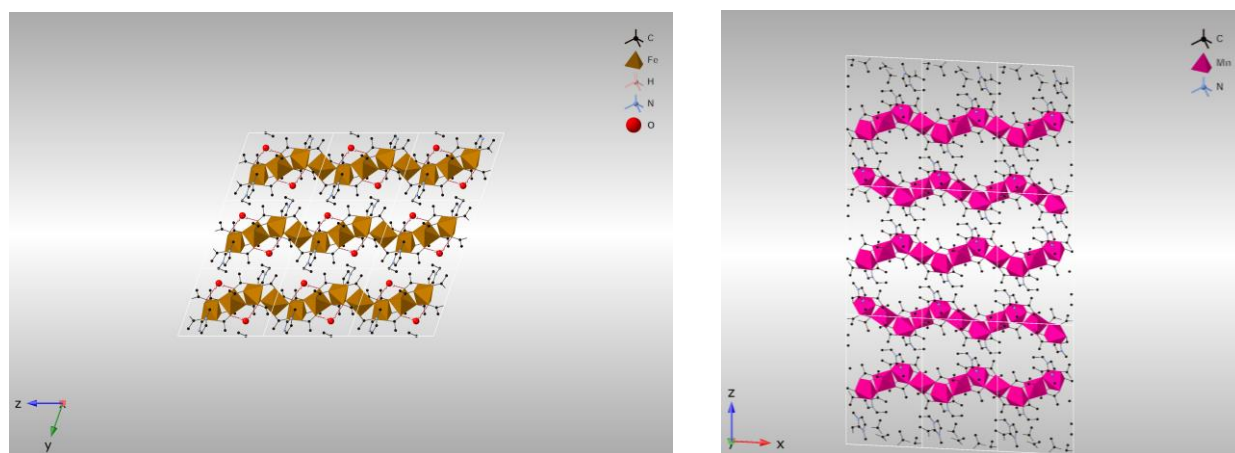


Figure 2.2.1. Crystal structure of metallo ionic liquid, Fe compound  $[\text{EMIM}][\text{Fe}]_2[\text{Ac}]_5\text{H}_2\text{O}$  and molten salt Mn compound I,  $[\text{Mn}_4(\text{OAc})_{10}[\text{EMIM}]_2]_n$ .

Figure 2.2.2. shows the topology of the anhydrous and hydrated  $[\text{Mn}_4(\text{OAc})_{10}[\text{C}_2\text{mim}]_2]_n$  materials. The  $[\text{EMIM}]$  cation moieties do not participate in the coordination of the Mn ions, but are hydrogen bonded to the acetates. Three manuscripts are under preparation on the synthesis, crystal structure and properties of the novel crystalline Mn, Fe, Sc and Zn compounds.



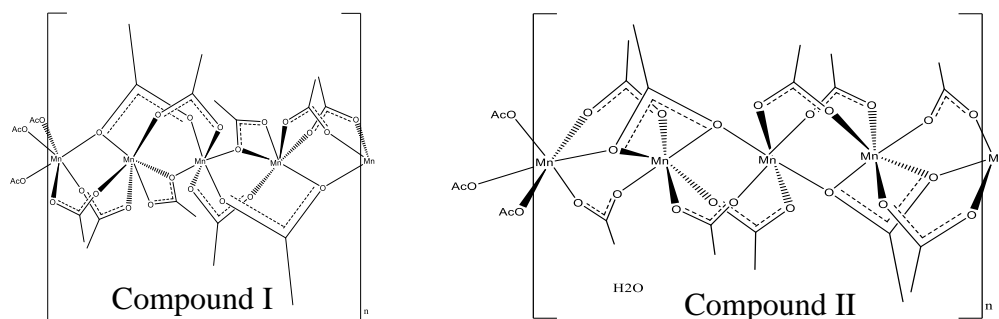


Figure 2.2.2. Different topology and stereochemistry observed depending on water content in Mn materials; anhydrous compound I ( $[\text{Mn}_4(\text{OAc})_{10}[\text{C}_2\text{mim}]_2]_n$ ) is monoclinic whilst the hydrous compound II  $[\text{Mn}_4(\text{OAc})_{10}[\text{EMIM}]_2 \cdot 2\text{H}_2\text{O}]_n$  is triclinic.

### Thermal Analyses of Novel Manganese Compounds

Thermogravimetric (TGA) and Differential Scanning Calorimetry (DSC) of the reactants and synthesized materials was performed using a TA Instruments Q600 SDT employing a temperature ramp of 10 °C/min and argon flow of 100 mL/min up to 600°C. Comparison of the TGA and DSC spectra of Mn compounds with that of reactants ( $\text{Mn}(\text{OAc})_2$  and  $[\text{EMIM}][\text{OAc}]$ ) clearly confirms formation of the new products. The TGA spectra of the  $[\text{EMIM}][\text{OAc}]$  is observed to have mass loss of about 96 % around 250 °C corresponding to the decomposition of the ionic liquid, whilst the manganese acetate is seen to decompose in a single step at 320 °C.

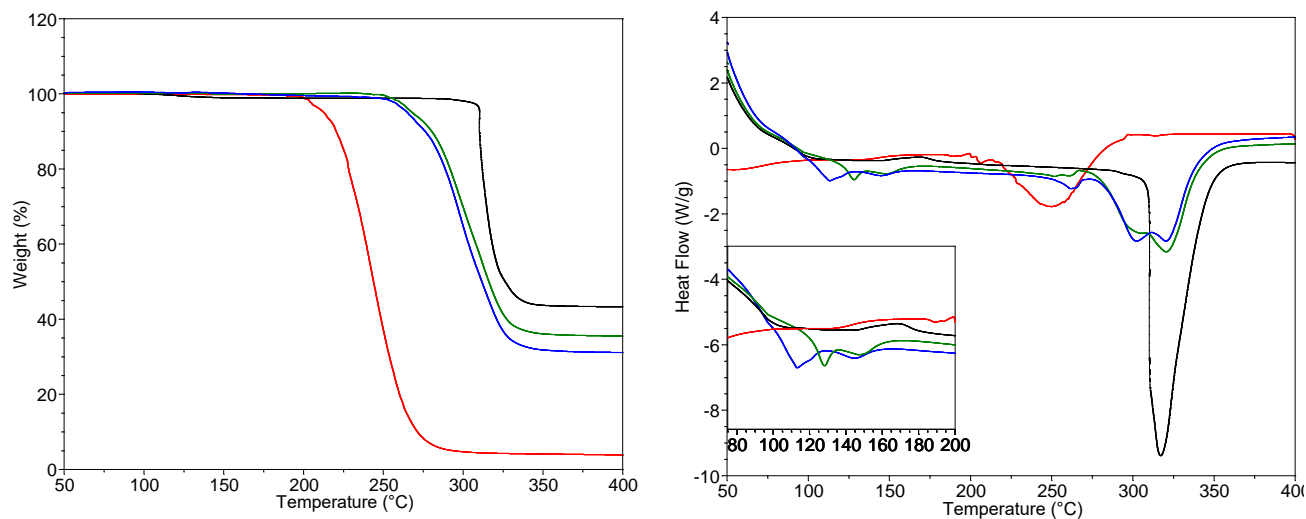


Figure 2.2.3. Thermogravimetric analyses and Differential Scanning Calorimetry of compound I and II at 10 °C/min under Argon flow of  $[\text{EMIM}][\text{OAc}]$  (red),  $\text{Mn}(\text{OAc})_2$  (black), Compound I:  $[\text{Mn}_4(\text{OAc})_{10}[\text{C}_2\text{mim}]_2]_n$  (green) and Compound II:  $[\text{Mn}_4(\text{OAc})_{10}[\text{EMIM}]_2 \cdot 2\text{H}_2\text{O}]_n$  (blue).



The Mn compounds (compounds I and II) have a higher thermal stability compared to the [EMIM][OAc], decomposing around 300-320 °C with a total weight loss of 65-69 %. The similarity in the TGA/DSC decomposition profile of both compounds confirms their structural resemblance. The higher thermal stability can be attributed to the increased ionic bonding and lattice ordering in the novel materials compared to [EMIM][OAc]. It can be anticipated that further altering of the metal ion charge, size or type; and functional groups on the EMIM cation, or anion will result in further tuning of the physical and chemical properties of these novel compounds resulting in materials with unique properties for multiple applications. The DSC spectra shows endothermic peaks below 130 °C which are attributed to melting and water loss. The solid to liquid transformation of compounds I and II was visually confirmed using an SRS Digimelt apparatus, which shows both compounds melting in the temperature range of 120-130 °C. The endothermic peaks at 301 and 321 °C are attributable to the multi-step decomposition of the materials.

### **Vibrational Spectroscopy of the Novel Manganese Compounds**

IR spectra were recorded with a spectral resolution of 2 cm<sup>-1</sup>, with 30 or 64 scans in the range 600 – 4000 cm<sup>-1</sup>. The spectra were either recorded at 25 °C in our lab with a Nicolet iS10 FTATR or with our collaborators at University of Geneva using variable temperature Biorad Excalibur Instrument equipped with a portable Specac Golden Gate heatable ATR setup, which allowed us to prepare samples in the glovebox. The IR frequency modes of [EMIM][OAc] have been assigned from the literature. Particularly, the interaction between the anion and the cation is shown by the following frequencies: 630 cm<sup>-1</sup> (OCO bending + CC stretching), 896 cm<sup>-1</sup> (OCO bending + CC stretching), 995 and 1035 cm<sup>-1</sup> (CH<sub>3</sub> bending), 1322 cm<sup>-1</sup> (symmetric CO stretching), 1373 and 1425 cm<sup>-1</sup> (CH<sub>3</sub> bending), 1567(br) cm<sup>-1</sup> (antisymmetric CO stretching), 702 cm<sup>-1</sup> (in plane ring deformation + C<sub>Et</sub>N stretching + C<sub>Me</sub>N stretching), 1171 cm<sup>-1</sup> (In plane C<sub>Im</sub>H bending). The room temperature IR of Mn(OAc)<sub>2</sub> has two strong carboxylate modes at 1388 and 1566 cm<sup>-1</sup> which suggests a bridging connection in the solid state: Mn--O--C(CH<sub>3</sub>)-O-Mn (i.e. the acetate connects 2 Mn<sup>2+</sup> ions).[12-15] The [Mn<sub>4</sub>(OAc)<sub>10</sub>[EMIM]<sub>2</sub>]<sub>n</sub> (red spectrum) and [Mn<sub>4</sub>(OAc)<sub>10</sub>[EMIM]<sub>2</sub>·2H<sub>2</sub>O]<sub>n</sub> (black spectrum) show a similar behavior in-line with the XRD results. The presence of [EMIM]<sup>+</sup> cation is displayed by the peaks at 1170 and 1010 cm<sup>-1</sup>. Two new sharp bands at 844 and 761 cm<sup>-1</sup> appear. According to the theoretical decomposition of the IR spectrum of [EMIM][OAc], most of the spectral intensities below 1000 cm<sup>-1</sup> arise from the acetate ion. It is therefore possible that these two sharp bands are characteristic for these new Mn materials.

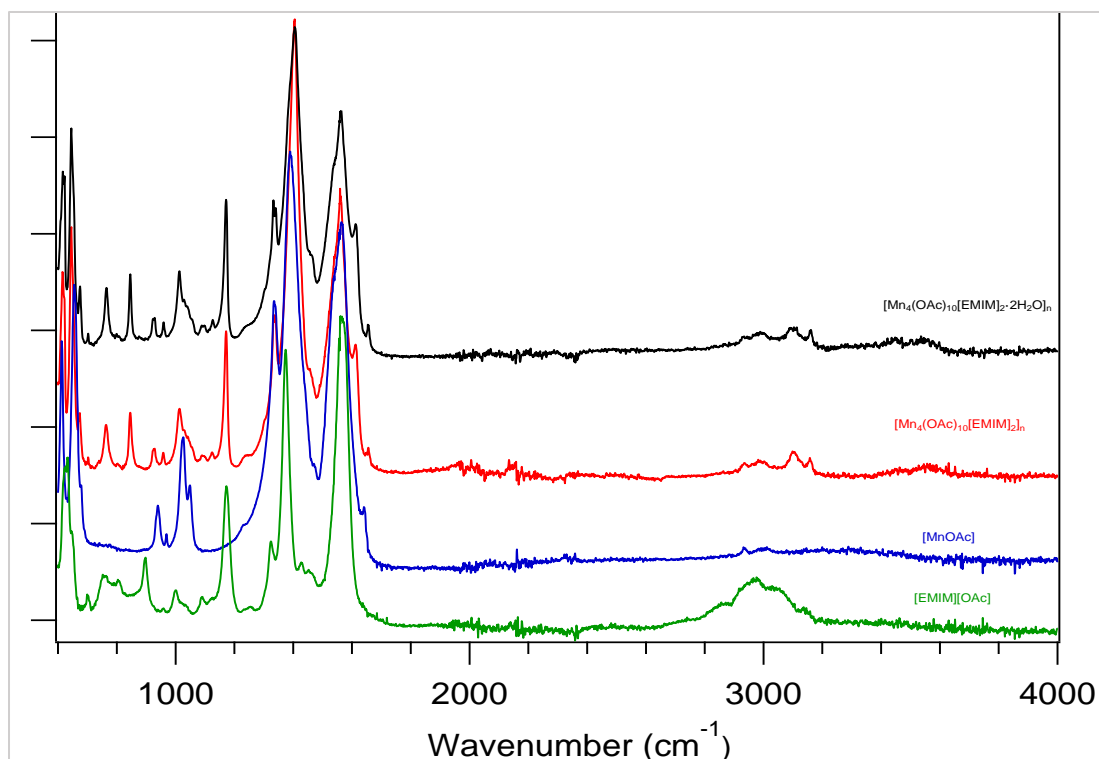


Figure 2.2.4. Comparative FTIR spectra of the [EMIM][OAc] (green line), the [MnOAc] (blue line), the  $[\text{Mn}_4(\text{OAc})_{10}[\text{EMIM}]_2]_n$  (red line), and the  $[\text{Mn}_4(\text{OAc})_{10}[\text{EMIM}]_2 \cdot 2\text{H}_2\text{O}]_n$  (black line).

Variable temperature FTIR were performed by heating compounds I and II from 30°C to 280°C with a step of 10°C. Then, the samples were cooled down to 30°C in order to collect the IR spectrum. The  $[\text{Mn}_4(\text{OAc})_{10}[\text{EMIM}]_2]_n$  sample shows some phase transitions while heating. At 120°C, the doublet at 671  $\text{cm}^{-1}$  is convoluted in one peak. The two signals at 763 and 844  $\text{cm}^{-1}$  disappear at 160°C. The two peaks at 925 and 957  $\text{cm}^{-1}$  become one peak at 160°C, which is still present after cooling the sample. Interestingly, the frequency at 1174  $\text{cm}^{-1}$  is shifted at 1158  $\text{cm}^{-1}$  when the temperature is 120°C. The latter is shifted at 1166  $\text{cm}^{-1}$  at 160°C. The signals at 1336, 1405, 1558  $\text{cm}^{-1}$  are broader at 160°C. Further, the peak at 1611  $\text{cm}^{-1}$  disappears at 160°C.

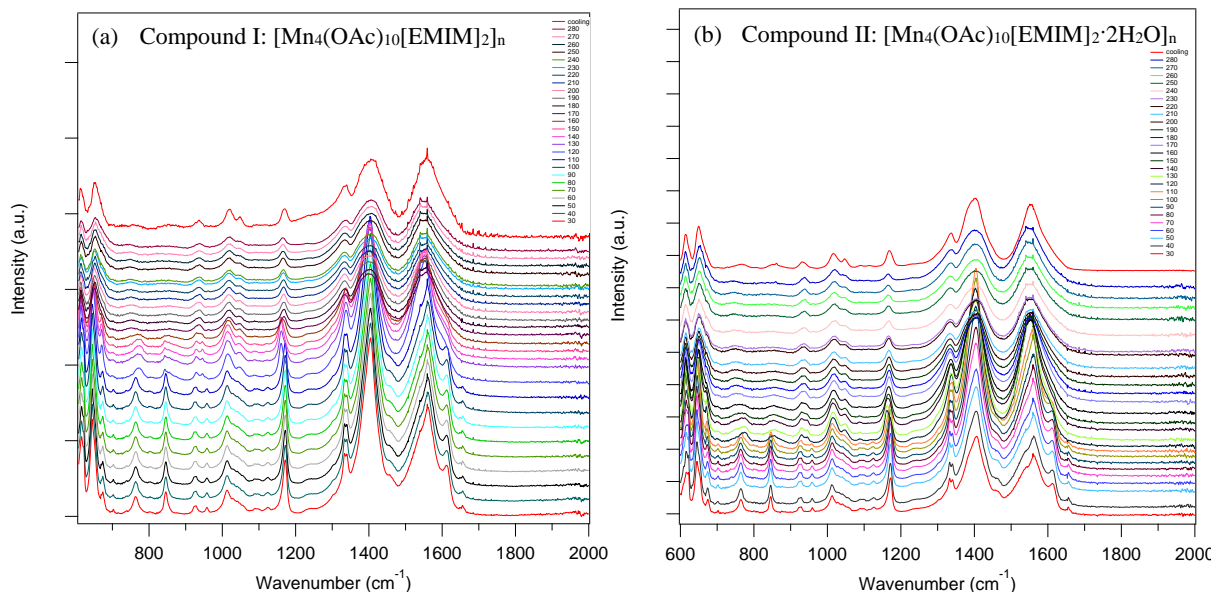


Figure 2.2.5. In situ High temperature-FTIR of compound I,  $[\text{Mn}_4(\text{OAc})_{10}[\text{EMIM}]_2]_n$  and compound II,  $[\text{Mn}_4(\text{OAc})_{10}[\text{EMIM}]_2 \cdot 2\text{H}_2\text{O}]_n$ .

The  $[\text{Mn}_4(\text{OAc})_{10}[\text{EMIM}]_2 \cdot 2\text{H}_2\text{O}]_n$  compound's weak O-H stretching of water around  $3500 \text{ cm}^{-1}$  is observed to disappear while heating the sample at  $100^\circ\text{C}$ . Besides this signal the FTIR spectra are similar to that of the water free sample eluding to the similarity in structure of the two compounds that is observed by XRD.

### Preliminary $\text{SO}_2$ and $\text{H}_2\text{S}$ Gas Absorption

Preliminary gas sorption measurements of the interaction of  $\text{SO}_2$  with the novel Mn compounds were performed using a Paar Inc. reactor system. The acidic gas sorption reactions were performed at  $25\text{--}170^\circ\text{C}$ . Initial activation of the Mn absorbents by heat treatment to  $170^\circ\text{C}$ , to open up coordination sites for acidic gas in the absorbents, similar to the activation of MOFs was explored. The FTATR analyses indicate the sorption of  $\text{SO}_2$  by the novel Mn compound,  $[\text{Mn}_4(\text{OAc})_{10}[\text{EMIM}]_2]_n$  as seen in Figure 2.2.6. New vibrational peaks are observed in FTATR spectra of  $\text{SO}_2$  reacted sample in  $800\text{--}1000 \text{ cm}^{-1}$  region, which are attributed to sulfur oxide species.

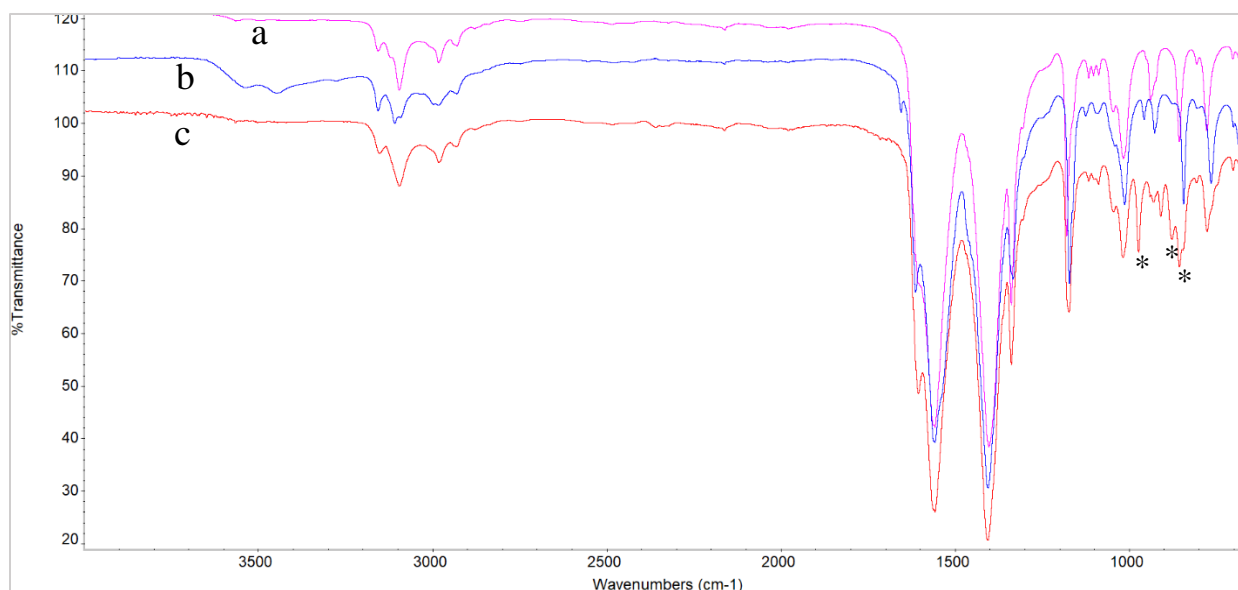


Figure 2.2.6. Comparative FTIR spectra of; (a) pure  $[\text{Mn}_4(\text{OAc})_{10}[\text{EMIM}]_2]_n$  at 25 °C, (b) pure  $[\text{Mn}_4(\text{OAc})_{10}[\text{EMIM}]_2]_n$  heat treated at 170 °C and (c)  $[\text{Mn}_4(\text{OAc})_{10}[\text{EMIM}]_2]_n$  treated with  $\text{SO}_2$  between 25-170 °C.

Under APRISES16 we will nano-confine the novel acetate and thiocyanate metallo ionic liquid and molten salt materials in granulated nanoporous activated carbon and determine their acidic gas sorption performance under simulated harsh air environments. Due to the high chemical tunability, surface area and gas capture potential of MOFs and LDHs derived mixed metal compounds, we will perform syntheses and testing of acid gas sorption performance of hybrid MOFs/LDH-nanoconfined activated carbons. Complimentary, Theoretical Density Functional Theory (DFT) calculations using dispersion corrected B3LYPd functional [16-19] and a 6-311(d,p) basis set [20, 21] will be performed with the GAMESS [22] software package in collaboration with Department of Chemistry to gain an understanding of the thermodynamic properties and the favored binding interactions between acidic gas contaminants and, the metallo ionic liquids and molten salts. We will also begin research on draw solutes with potential for forward osmosis seawater desalination for drinking water and agriculture and explore the potential of the novel metallo ionic liquids and molten salts as high flux, reversible energy efficient draw solutes.

## Publications and Presentations

### *Contributed Presentations*

1. Godwin Severa, John Head, Keith Bethune, Scott Higgins and Richard Rocheleau, *Advances in Gas Filtration Materials Research: Fuel Cell Air Purification Challenge?* American

## References

- [1] Severa, G., et al., *SO<sub>2</sub> sorption by activated carbon supported ionic liquids under simulated atmospheric conditions*. Chemical Engineering Journal, 2015. 265: p. 249-258.
- [2] Severa, G., et al., *Comparative studies of low concentration SO<sub>2</sub> and NO<sub>2</sub> sorption by activated carbon supported [C2mim][Ac] and KOH sorbents*. Journal of Environmental Chemical Engineering, 2018. 6(1): p. 718-727.
- [3] Wasserscheid, P. and T. Welton, *Ionic liquids in synthesis*. 2003, Weinheim: Wiley-VCH Verlag.
- [4] Kirchner, B., ed. *Topics in current chemistry*. Ionic liquids, ed. B. Kirchner. Vol. 290. 2009, Springer-Verlag new york. 40.
- [5] Lei, Z., C. Dai, and B. Chen, *Gas Solubility in Ionic Liquids*. Chemical Reviews, 2013. 114(2): p. 1289-1326.
- [6] MacFarlane, D.R., et al., *Energy applications of ionic liquids*. Energy & Environmental Science, 2014. 7(1): p. 232-250.
- [7] Smiglak, M., et al., *Ionic liquids for energy, materials, and medicine*. Chemical Communications, 2014. 50(66): p. 9228-9250.
- [8] Rogers, R.D. and K.R. Seddon, *Ionic Liquids--Solvents of the Future?* Science, 2003. 302(5646): p. 792-793.
- [9] Ghandi, K., *A Review of Ionic Liquids, Their Limits and Applications*. Green and Sustainable Chemistry, 2014. 4: p. 44-53.
- [10] Irge, D.D., *Ionic Liquids: A Review on Greener Chemistry Applications, Quality Ionic Liquid Synthesis and Economical Viability in a Chemical Processes*. American Journal of Physical Chemistry, 2016. 5: p. 74-79.
- [11] Meng, T., et al., *Ionic Liquid-Based Non-Aqueous Electrolytes for Nickel/Metal Hydride Batteries*. Batteries, 2017. 3(1): p. 4.
- [12] Nakamoto, K., *Infrared and Raman Spectra of Inorganic and Coordination Compounds, Part A: Theory and Applications in Inorganic Chemistry*. 6th ed. 2009: John Wiley and Sons.
- [13] Alcock, N.W., V.M. Tracy, and T.C. Waddington, *Acetates and acetato-complexes. Part 2. Spectroscopic studies*. Journal of the Chemical Society, Dalton Transactions, 1976(21): p. 2243-2246.
- [14] Deacon, G.B. and R.J. Phillips, *Relationships between the carbon-oxygen stretching frequencies of carboxylato complexes and the type of carboxylate coordination*. Coordination Chemistry Reviews, 1980. 33(3): p. 227-250.
- [15] Ito, K. and H.J. Bernstein, *THE VIBRATIONAL SPECTRA OF THE FORMATE, ACETATE, AND OXALATE IONS*. Canadian Journal of Chemistry, 1956. 34(2): p. 170-178.
- [16] Becke, A.D., *Density-functional exchange-energy approximation with correct asymptotic behavior*. Physical Review A, 1988. 38(6): p. 3098-3100.

- [17] Lee, C., W. Yang, and R.G. Parr, *Development of the Colle-Salvetti correlation-energy formula into a functional of the electron density*. Physical Review B, 1988. 37(2): p. 785-789.
- [18] Becke, A.D., *Density-functional thermochemistry. III. The role of exact exchange*. The Journal of Chemical Physics, 1993. 98(7): p. 5648-5652.
- [19] Grimme, S., et al., *A consistent and accurate ab initio parametrization of density functional dispersion correction (DFT-D) for the 94 elements H-Pu*. J Chem Phys, 2010. 132(15): p. 154104.
- [20] Krishnan, R., et al., *Self-consistent molecular orbital methods. XX. A basis set for correlated wave functions*. The Journal of Chemical Physics, 1980. 72(1): p. 650-654.
- [21] Frisch, M.J., J.A. Pople, and J.S. Binkley, *Self-consistent molecular orbital methods 25. Supplementary functions for Gaussian basis sets*. The Journal of Chemical Physics, 1984. 80(7): p. 3265-3269.
- [22] Schmidt, M.W., et al., *General atomic and molecular electronic structure system*. Journal of Computational Chemistry, 1993. 14(11): p. 1347-1363.

## 2.3 Hydrogen Refueling Support

Hydrogen refueling activities are focused on two locations: the hydrogen production and fueling station located at the Natural Energy Laboratory Hawaii Authority (NELHA) in Kailua-Kona, and the hydrogen fueling dispenser station located at Hawaii Volcanoes National Park (HAVO), both on the Island of Hawaii (Figure 2.3.1). APRISES14 funding supported the commissioning of hydrogen production and compression equipment at the NELHA site, repairs to the high tensile steel frame of one of our three Hydrogen Transport Trailers (HTT), and the installation of improved design Thermal Pressure Relief Devices on all HTT hydrogen composite cylinders. This was a recertification requirement specified by the cylinder manufacturer. The first HTT trailer was delivered to the NELHA facility in December 2018 and was purged with nitrogen. The County of Hawaii Hele-On bus was delivered in December 2018 to the US Hybrid facility on Oahu where it commenced final commissioning and testing.

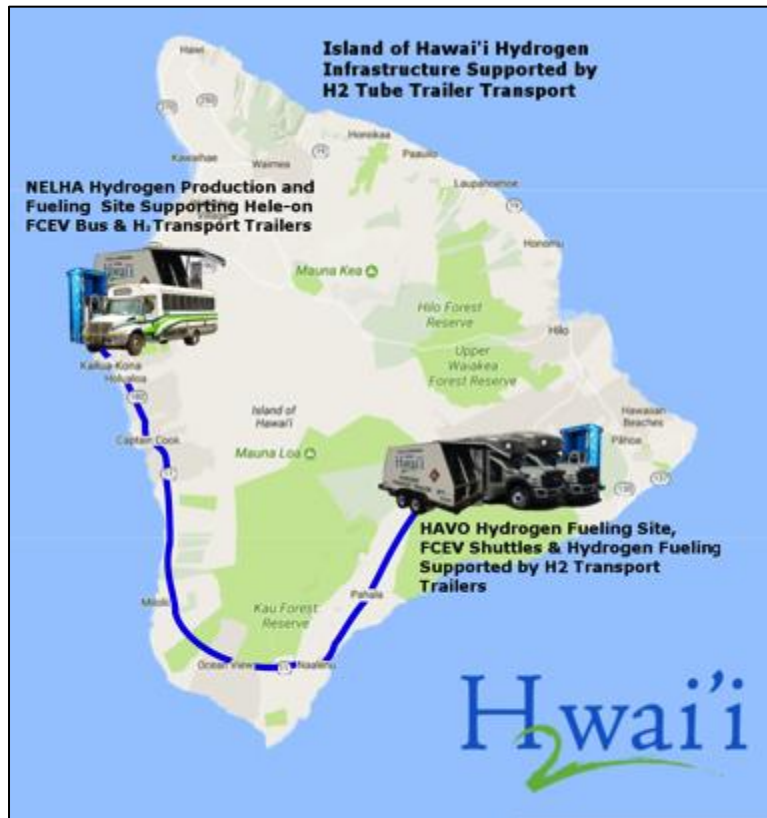


Figure 2.3.1 Central Site Production/Distributed Dispensing.

As illustrated in Figure 2.3.1, the overall hydrogen fueling concept was to deliver hydrogen from the hydrogen production facility in Kona to HAVO to support the operation of two (2) HAVO Fuel Cell Electric Buses (FCEBs) illustrated in Figure 2.3.2. The HTT (Figure 2.3.3) filled with 105 kg of hydrogen at 450 bar, would be dropped off and used to cascade fill the buses. The empty HTT would be picked up and delivered back to the Kona site to be refilled (Figure 2.3.4).



Figure 2.3.2 HAVO Fuel Cell Electric Bus.





Figure 2.3.3 Hydrogen Transport Trailer.



Figure 2.3.4: NELHA Hydrogen Production and Dispensing Station.

HNEI worked with HAVO to design the site improvements for the installation of a hydrogen dispensing station to support fueling the two (2) HAVO hydrogen buses. HNEI prepared a contract with an architecture and engineering firm to prepare the detailed design and site drawings. A rendering of the site conceptual design is provided in Figure 2.3.5. Unfortunately, the Kilauea volcano erupted on the very day the contract was to be signed and the contract was not signed. Subsequently after a prolonged eruption event, it was determined that the damage to HAVO infrastructure was very severe and the HAVO installation effort was stopped.





Figure 2.3.5: HAVO 350 Bar dispensing station.

The Hydrogen Transport Trailers purchased for this work had not been shipped to Hawaii and were approaching their five-year certification expiration date. Since there is no capability in Hawaii to recertify composite cylinders of the size used in these trailers, it was decided to recertify the trailers before delivering them to Hawaii.

The trailers were disassembled by Powertech and the hydrogen storage cylinders were shipped to Luxfer, the cylinder manufacturer located in Calgary, Alberta. Luxfer tested and recertified the cylinders. To meet new safety requirements, the Thermal Pressure Relief Device (TPRD) valves installed inside the cylinders were replaced with an upgraded valve.



Figure 2.3.6: Composite Cylinder with TPRD Removed.

During the inspection of the trailer frames, a crack caused by water freezing inside one of the structural steel tubing components was discovered. This required the frame to be repaired and recertified. The frame repair was completed and the HTTs were reassembled by Powertech (Figure 2.3.7).



Figure 2.3.7: HTT Frame and Cylinder

### **Relocation of the HAVO Buses and Hydrogen Fueling Equipment**

Based on the decision to cancel the HAVO bus project due to the eruption, the County of Hawaii Mass Transit Agency requested the National Park Service to donate the HAVO buses to the county. The HAVO park superintendent approved the request and the buses were transferred to the County. It is planned to relocate the HAVO hydrogen fueling equipment to a site that will support the operation of the HAVO buses by the county. The most likely location will be at the County MTA's new maintenance facility in Hilo.

### **Publications and Presentations**

#### *Conference Presentations*

1. J.M. Ewan, *Supporting a Hawaii Hydrogen Economy*, 1<sup>st</sup> Costa Rica International Hydrogen Conference, August 13, 2018, San Jose, Costa Rica.
2. J.M. Ewan, *Hydrogen – What will it take in Hawaii?*, Germany-Hawaii Clean Energy Symposium, 30 October, 2018, Honolulu, HI.

3. J.M. Ewan, *Hydrogen Energy Systems as a Grid Management Tool*, 2018 NELHA Energy Storage Conference, Natural Energy Laboratory Hawaii Authority, December 6, 2018 Kailua-Kona, HI.

#### *Briefings*

1. J.M. Ewan, *HNEI Big Island Hydrogen Projects – CTE Brief*, Natural Energy Laboratory Hawaii Authority, July 26, 2018, Kailua-Kona, HI.
2. J.M. Ewan, *MCBH Hydrogen Presentation*, Marine Corps Base Hawaii Elementary School, November 29, 2018, Kaneohe Bay, HI.
3. J.M. Ewan, *MTA Hydrogen Bus Brief*, Natural Energy Laboratory Hawaii Authority, December 4, 2018, Kailua-Kona, HI.
4. J.M. Ewan, *The Magic of Hydrogen*, Young Professionals in Energy Monthly Meeting, UH Manoa, January 28, 2019, Honolulu, HI.
5. J.M. Ewan, *Hele-On Zero Emission Bus*, County of Hawaii Transportation Hui, February 1, 2019, Hilo, HI.
6. J.M. Ewan, *ASU Hydrogen Brief*, HNEI, February 4, 2019, Honolulu, HI.

## **2.4 Materials for Solar Fuels**

The task continues previous ONR-funded efforts (APRISSES11-13) to develop novel thin film materials, primarily  $\text{Cu}_2\text{ZnSn}(\text{S},\text{Se})_4$  and CZTSSe, for solar energy conversion using a potentially low-cost and scalable liquid-based process. With this approach, printable inks containing all the necessary components to form the solar absorbers can be easily coated on various substrates using high-throughput techniques, including spin coating and inkjet printing. Under past ONR funding, our group first developed a technology to form CZTSSe thin films using nano-crystalline “inks” made of CZTS (sulfide) nanoparticles with controlled composition, size and morphology. Printed inks were subsequently heated with elemental selenium to form polycrystalline CZTSSe absorbers with power conversion efficiency (PCE) of approximately 2.3% (as measured with fully integrated CZTSSe-based solar cells). Although promising, this technique was not reproducible, as nanoparticles tended to agglomerate quickly in the inks after initial dispersion, making the printing step difficult. In subsequent work, the nanoparticle-based inks were replaced with ones containing only molecular complexes of copper, zinc and tin ( $\text{SnCl}_2$ ,  $\text{CuCl}$  and  $\text{ZnCl}_2$ ) and thiourea (sulfur source) dissolved in methanol (Figure 2.4.1a). The resulting CZTS solutions are very stable and easy to process. After heating under selenium atmosphere, CZTS ink is converted into CZTSSe absorbers with exceptional crystallinity and void-free (Figure 2.4.1b). Fully integrated CZTSSe solar cells made with this new technique reached PCE up to 7% (Figure 2.4.1c).

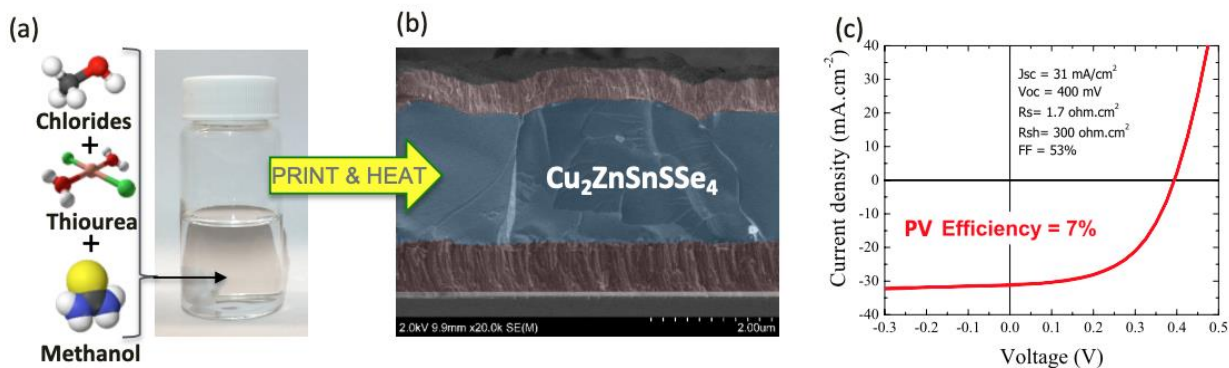


Figure 2.4.1 (a) Picture of a stable molecular ink containing metal chlorides, thiourea and methanol. (b) Scanning electron microscopy cross-sectional view and (c) current-voltage characteristic of a printed CZTSSe solar cell.

The effort under APRISES14, focused on the post-printing heating step to further understand how CZTS molecular inks are converted into crystalline CZTSSe thin films. In a typical CZTSSe thin film synthesis protocol, 10 layers of ink are successively coated onto a substrate with a short 3-minute heating treatment on a hot plate in air at 250°C between each layer. The newly formed precursor is then placed in a vacuum furnace with elemental selenium and heated at 550°C for 30 minutes to form the absorber. Raman spectroscopy measurements were first performed on precursors and after either a 20-minute or a 30-minute long heating stage under selenium atmosphere (Figure 2.4.2a). We can observe that the Raman spectrum measured on the precursors (black curve) reach a maximum at 340  $\text{cm}^{-1}$ , consistent with the value reported for  $\text{Cu}_2\text{ZnSnS}_4$ . Thus, we conclude that the 3-minute long hot plate treatment performed after each printing step is sufficient to induce a chemical reaction between the metal chlorides and thiourea to form CZTS. Although Raman spectroscopy is usually used for qualitative analysis (i.e. phase identification), studies have shown direct correlations between broadening of Raman peaks and absorber crystal quality, concluding that the more “defective” the material, the broader the Raman peak. Thus, we conclude that the broad Raman peak observed on the precursor is an indicator of “poor” crystallographic ordering. This conclusion is supported by the scanning electron microscopy (SEM) cross-sectional view in Figure 2.4.2b showing a precursor made of small grains 50 nm in diameter or less. The Raman spectra measured after a 20-minute long heating step at 550°C in presence of selenium vapor evidences a clear change in microstructure (Figure 2.4.2a, blue curve). A significant reduction in the CZTS peak intensity is observed, along with the presence of a small, yet sharp CZTSe signal at 198  $\text{cm}^{-1}$ . As the heating dwell time is increased to 30 minutes (Figure 2.4.2a, red curve), the intensity of the CZTS peak at 340  $\text{cm}^{-1}$  is further reduced, while that of CZTSe at 198  $\text{cm}^{-1}$  increased. We therefor conclude that the resulting thin film is predominantly CZTSe. Further analysis, including energy dispersive X-ray spectroscopy, revealed indeed that CZTSSe films contains on average about 95% selenium and 5% sulfur.

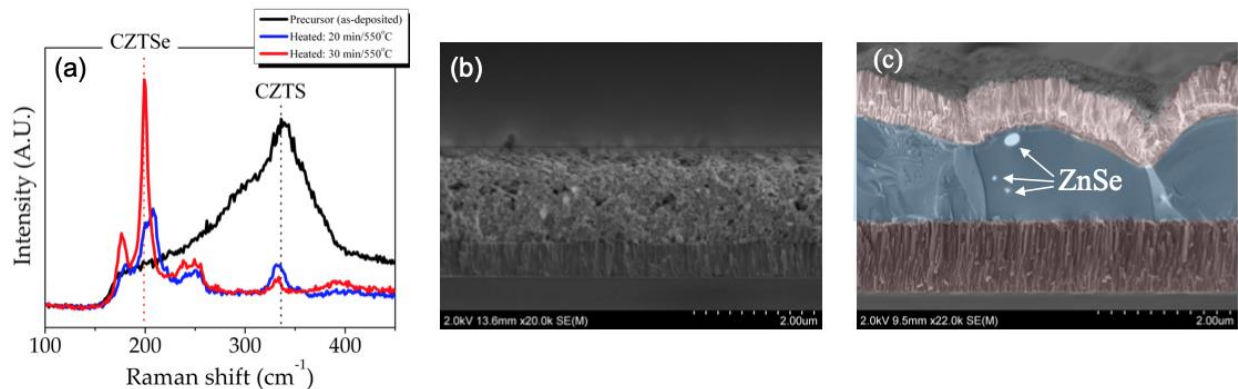


Figure 2.4.2. (a) Raman shift measured on printed CZTS molecular ink before (black curve) and after heating under selenium atmosphere (blue curve: 20 min at 550°C, red curve: 30 min at 550°C). Scanning electron microscopy cross-sectional views of (b) an as-deposited CZTS precursor and (c) a CZTSSe film with ZnSe segregated phase.

It should be noted that single phase CZTSSe absorbers are not always achieved with our process. In fact, SEM cross-sectional analyses have evidenced the presence of undesirable ZnSe phase near the top part of some of our thin films (Figure 2.4.2c). We have not identified which experimental conditions are responsible for such phase segregation, yet we have found it to be responsible for significant reduction in PCE, from 6-7% on average down to 2%. Future work under APRISES15 will be focused on further analyzing the exact chemical composition of these isolated phases and pinpoint which of the temperature, dwell time or selenium vapor pressure is responsible for this phenomena.

## TASK 3 BIOFUELS

Task 3 continued research supporting the development of technologies for the production and use of synthetic fuels. Fuel properties of Pongamia seeds and pods grown in Hawaii were determined, anaerobic digestion and technology was advanced to produce liquid fuel from syngas, and research was conducted to prevent fuel degradation from bio-contamination.

### 3.1 Bioenergy Systems

Pongamia (*Milletia pinnata*), a nitrogen fixing tree, is a potential resource for renewable fuel production. The present work utilizes reproductive material (seeds and pods) from pongamia trees growing under different environments on the Island of Oahu, Hawaii, USA. Proximate and



ultimate analysis, heating value, and elemental composition of the seeds, pods, and de-oiled seed cake were determined. The oil content of the seeds and the properties of the oil were determined using the ASTM and AOCS methods. Seed oil contents were measured in a range from 19 to 25 %wt. Oleic was the fatty acid present in greatest abundance (47 to 52 %wt) and unsaturated fatty acids accounted for 77 to 82 %wt of the oil. Pongamia oil was found to have similar characteristics as jatropha oil. Complete details can be found in the publication submitted to the journal Fuel and currently under review.

## **Publications and Presentations**

### *Peer Reviewed Publications*

Fu, J., Morgan, T., Summers, S., Turn, S. 2019. Fuel properties of *Milletia pinnata* seeds and pods grown in Hawaii. Fuel. Submitted and in review.

## **3.2 High-Rate Anaerobic Digestion**

The objective of this activity was to design and evaluate novel biofilm support media for use in high-rate anaerobic digestion systems to treat high strength wastewater as rapidly as possible. Under past funding, the efficacy of these systems to treat high strength wastewater were investigated and advanced. These systems utilized biochar as a medium to support growth of methanogenic microbial biofilm communities. These systems proved successful at demonstration scale. However, biochar is a material that is rather bulky and can occupy much of the reactor bulk volume. This leads to lower reactor efficiency. To improve efficiency, biofilm support materials that provide more active catalytic surface area is needed.

To that end various biofilm support materials (novel chitosan – biochar supports, novel biochar – PVC supports) were developed and evaluated under this funding. In addition, an aerobic tricking filter was added as a downstream unit operation to improve treatment efficiency. The efficacy of this biofilm based anaerobic-aerobic treatment process was then tested for its ability to remove chemical contaminants of emerging concern (CEC's, such as caffeine (CAE), carbamazepine (CBZ), and three estrogens) as well as key pathogen indicator organisms (*Escherichia coli* (CN-13) and F+ specific coliphage (MS-2 bacteriophage)) from wastewater. CEC's were spiked into synthetic reactor feed to overall concentrations of 500 µg/L and the system showed no observable reduction in CBZ over a 51-day evaluation period, while after 74 days, CAE showed an 11.09% reduction in effluent from the anaerobic digester (AD) stage and a 91.90% reduction in the effluent from the trickling filter (TF). Estrogens 17β-estradiol (E2) and 17α-ethinylestradiol (EE2) were spiked and their concentrations (including the E2 degradation byproduct—estrone E1) were

monitored. After 90-days of observation, combined concentrations of E1 and E2 showed virtually no reduction in the AD but a 99.67% reduction in the TF; while EE2 showed a 1.62% reduction in the AD stage and 20.36% after the TF stage. These results suggest the combined anaerobic-aerobic biofilm-based reactor system is capable of treating wastewaters highly concentrated with caffeine, estrone, and  $17\beta$ -estradiol but less so with those contaminated with CBZ and  $17\alpha$ -ethinylestradiol. Indicating pathogens *E. coli* CN-13 and F+ specific coliphage (MS-2 bacteriophage) were spiked in the feed to overall concentrations of  $1 \times 10^8$  MPN/L and  $1 \times 10^6$  PFU/L, respectively. Across the overall reactor system, *E. coli* (CN-13) achieved an average of 3-log reductions and F+ Specific Coliphage (MS-2 bacteriophage) achieved an average of 1-log reduction.

Under this and past funding cycles, long term testing of novel chitosan – biochar supports at laboratory scale was completed. While the results were positive in terms of achieving biofilm supports that hosted thin-film biofilm communities of methanogenic microbial communities, the chitosan biopolymer absorbed excess water and as a consequence filled void volumes and contributed to gas holdup. This led to the alternate design of thin filamentous thin ribbon carbon supports where in biochar bits were embedded onto the surface of a thin strip of polyvinyl chloride film. The testing of these materials was a key work product of this funding cycle.

The reactor system is presented in Figure 3.2.1. The system consists of an upflow anaerobic packed bed biofilm reactor (UAnPBBR) followed by a trickling filter (TF). Additional tertiary unit operations were added to mimic units used in industry to meet extremely stringent effluent requirements. The biofilm support materials tested were biochar embedded on PVC strips.

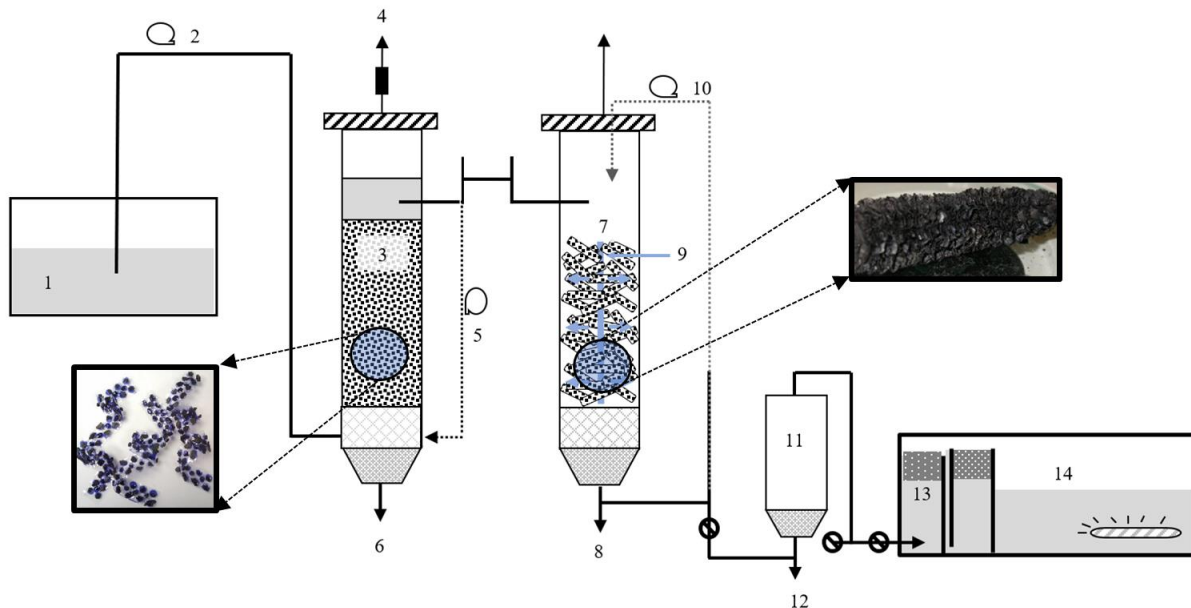


Figure 3.2.1. High rate anaerobic-aerobic digestion (HRAAD) reactor system. Legend: 1) chilled feed tank; 2) feed dosing pump; 3) UAnPBB, 4) biogas; 5) UAnPBBR recycle; 6, 8, 12) solids discharge line; 7) TF; 9) inlet air stream; 10) TF recycle; 11) settling tank; 13) reticulated sponge foam filters; 14) final holding tank with submerged UV light lamp pump system.

In trials using straight biochar in the anaerobic column the combined anaerobic-aerobic system treated high strength wastewater feed successfully. The system achieved total chemical oxygen demand (TCOD) and total suspended solids (TSS) reductions of 97.8 and 97.5%, respectively and produced a pH neutral effluent. The system also produced methane rich biogas gas at a yield of 0.3105 m<sup>3</sup> methane per kg-1 TCOD reduced. In trials using biochar imbedded on PVC strips (Figure 3.2.1) in the anaerobic column, the designed biofilm based anaerobic-aerobic treatment process, the efficacy to reduce the liquid phase concentrations of contaminants of concern as well as key pathogen indicator organisms from wastewater was investigated. Results showed this treatment process duplicated state of the art literature findings for the reduction of CAE (91.90%) and CBZ. The removal of E1 and E2 (99.67%) from the liquid phase, however, showed higher efficiency than previously reported findings (Luo et al. 2014, Falas et al. 2016, Joss et. al 2004, Gonzalez-Gil et al. 2016). In addition, the biofilm-based reactor system demonstrated a strong ability to buffer a one-time spike in the concentration of a CEC that was found difficult to degrade (EE2), suggesting biofilm-based reactors possess an ability to absorb and buffer against periodic surges in CEC, even when they are not readily degraded in the reactor. While the system appears to be effective in removing bacterial pathogens such as tested *E. coli*, persistence of F+ coliphages to the treatment signals the need to add additional tertiary treatment unit operations.



In total, this work led to a final system design decision for demonstration scale reactors for fabrication and installation. It comprises an initial mixing tank followed by an up-flow packed bed anaerobic digester filled with biochar-based biofilm supports. Follow on reactors can be additional anaerobic up-flow packed bed anaerobic digesters or down-flow trickling filters. In future funding cycles this design will be developed to support full fabrication and installation at commercial scale.

Detailed method and results are published in the journal articles listed below.

## **Publications**

### *Peer Reviewed Publications*

1. Lamichhane, K., Furukawa, D., and M. J. Cooney. 2017. Co-digestion of glycerol with municipal wastewater. *Journal of Chemical Engineering & Process Technology*. 3(1): 1034.
2. Lamichhane, K, Lewis, K., Rong, K., Babcock, R., and M. J. Cooney. 2017. Treatment of high strength acidic wastewater using passive pH control. *Journal of Water Process Engineering*. 18:198-201.
3. Cooney, M. J., Lamichhane, K. and K. Rong. 2019. Cross comparative analysis of liquid phase anaerobic digesters. *Journal of Water Process Engineering*. *Journal of Water Process Engineering*. Volume 29, June, 100765.

## **3.3 Liquid Fuels from Syngas**

The aim of this subtask was to develop a technology for production of liquid fuels from syngas ( $H_2$ , CO, and  $CO_2$ ). The process included two steps: (a) formation of polyhydroxybutyrate (PHB) by using a chemoautotrophic bacterium from the gas substrates, and (b) conversion of PHB into liquid fuels. In this work, we investigated the reaction routes of catalytic reforming of PHB into hydrocarbon oil and formation of bio-oil from the residual microbial biomass. As a result, we demonstrated new conversion routes to produce high-grade hydrocarbon oil as well as bio-oil. The

full details are provided in peer-reviewed publications [1, 2] and the major results and discoveries are summarized as follows.

Crotonic acid (CA,  $\text{CH}_3\text{CH}=\text{CHCO}_2\text{H}$ ) and 3-hydroxybutyric acid (3HB,  $\text{CH}_3\text{CHOHCH}_2\text{CO}_2\text{H}$ ) were two major monomeric intermediates of PHB degradation. Under pyrolysis conditions, PHB was primarily decomposed into CA via a  $\beta$ -elimination six-member ring structure [3]. Under acidic hydrolysis conditions, both 3HB and CA were formed [4]. The molar ratio of 3HB to CA reflects the relative extent of hydrolysis versus pyrolysis of PHB [1]. Figure 3.3.1A & B show the same hydrocarbon compounds formed from PHB and CA, respectively. It was also found that 3HB was first converted into CA and then into the hydrocarbon compounds [1]. CA was therefore the key monomeric intermediate in PHB reforming. Four representative compounds in the hydrocarbon oil were identified with GC-MS analysis as shown in Figure 3.3.1A. They were 1,2,3,4-tetramethyl-5-(1-methylethyl)-benzene (*Compound 1* thereafter), 1,2,3,4-tetramethylbenzene (*Compound 2* thereafter), 1,2,3,5-tetramethylbenzene (*Compound 3* thereafter), and 1-indanone,3,3,4,5,7-pentamethyl-benzene (*Compound 4* thereafter). *Compound 1* was the predominant compound and had a similar chemical structure of *Compounds 2* and *3*, probably involving the same reaction intermediate and route.

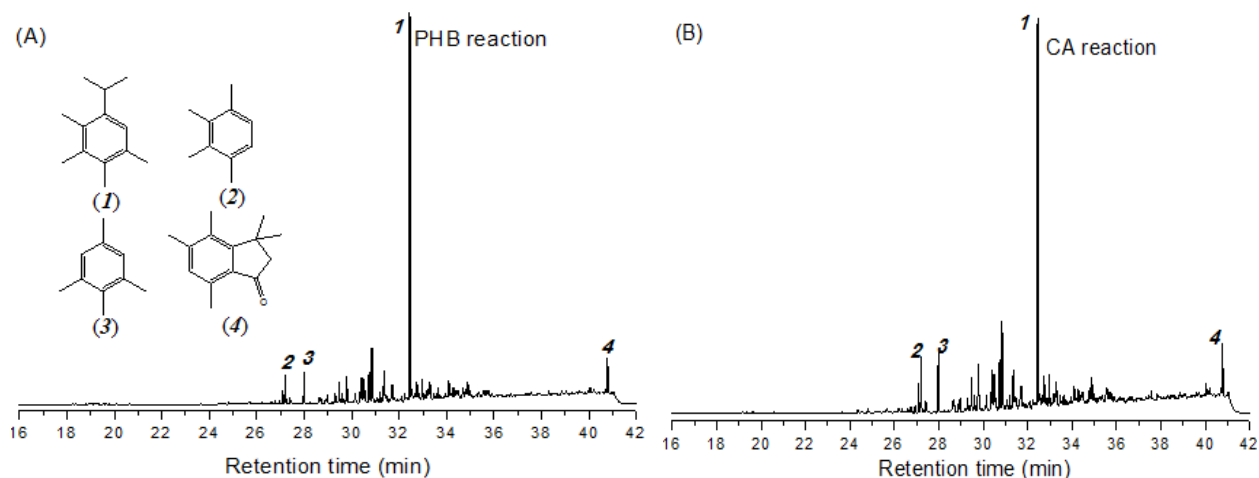


Figure 3.3.1. (A) GC-MS spectrum of hydrocarbon oil from PHB reforming and the chemical structures of representative compounds; (B) GC-MS spectrum of hydrocarbon oil from CA under the same reaction conditions.

CO<sub>2</sub> and propylene (C<sub>3</sub>H<sub>6</sub>) were the major gaseous products formed in PHB or CA reforming. Little CO was detected in the gas phase, indicating negligible decarbonylation of PHB or CA. According to the stoichiometry of CA decarboxylation (C<sub>4</sub>H<sub>6</sub>O<sub>2</sub> → C<sub>3</sub>H<sub>6</sub> + CO<sub>2</sub>), equal molar concentrations of C<sub>3</sub>H<sub>6</sub> and CO<sub>2</sub> were expected, but the actual molar ratio of CO<sub>2</sub> to C<sub>3</sub>H<sub>6</sub> ranged from 5.5 to 17.1, depending on the reaction conditions [1]. It was attributed to further conversion of propylene into hydrocarbon compounds since propylene was an active reagent under the reaction conditions. In a controlled experiment with propylene as the initial reagent, propylene was oligomerized to C<sub>6</sub>-C<sub>12</sub> alkenes as determined with GC-MS analysis (Figure 3.3.2B), but no aromatic compounds were formed. The alkenes from propylene were quite similar to those formed (a, b, c) in PHB reaction as shown in Figure 3.3.2A. This fact indicated that alkenes in hydrocarbon oil were formed from propylene oligomerization. In addition, when propylene and toluene were reacted under the same reaction conditions, propylene participated in alkylation of toluene to form several substituted aromatic compounds [1]. However, propylene alone did not form aromatics. Compounds 1-4 must be formed via other reaction routes, so decarboxylation of CA into propylene was not the only reaction route of PHB deoxygenation.

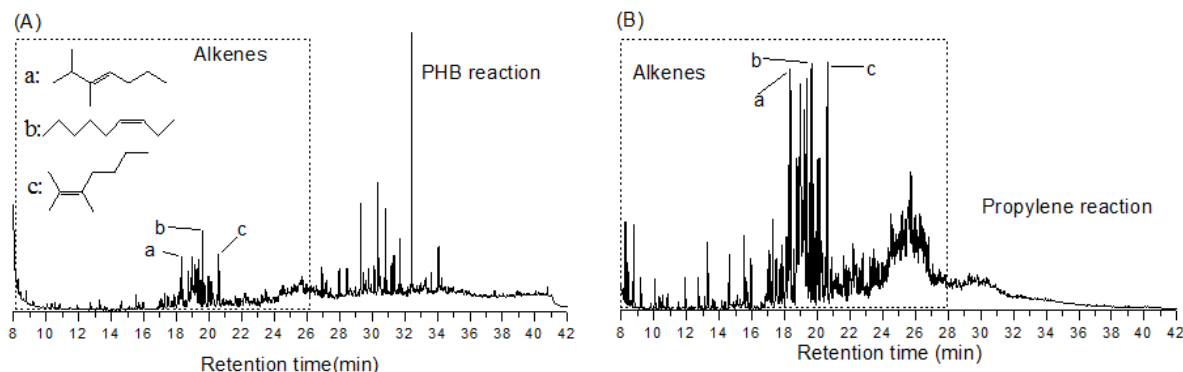


Figure 3.3.2. (A) GC-MS spectrum of hydrocarbon oil from PHB reaction and the chemical structures of representative alkenes; (B) GC-MS spectrum of hydrocarbon oil from propylene under the same reaction conditions.

In previous work, we found that water, in addition to CO<sub>2</sub>, was also formed from CA deoxygenation [5]. Ketonization of CA was a possible reaction, in which two molecules of carboxylic acids (CA) were converted into one ketone, one CO<sub>2</sub>, and one water [6]. According to the theory of unsaturation degree of reagents and products, two CAs with total four unsaturation degrees may be ketonized into one C<sub>7</sub>H<sub>10</sub>O compound (three unsaturation degrees), one CO<sub>2</sub> (one unsaturation degree) and one H<sub>2</sub>O (zero unsaturation degree). We checked the compounds formed in the early stage of PHB and CA reforming, respectively, and found two unsaturated seven-carbon compounds: 2,3-dimethyl-2-cyclopenten-1-one (C<sub>7</sub>H<sub>10</sub>O, *Compound 5* thereafter) and 3-methyl-2-cyclohexenone (C<sub>7</sub>H<sub>10</sub>O, *Compound 6* thereafter) as shown in Figure 3.3.3A. They were

confirmed with pure chemicals obtained from a supplier (Sigma-Aldrich). *Compounds 5* and *6* were quite reactive and quickly converted into stable aromatic compounds (benzenes and naphthalenes) as revealed by GC-MS analysis (Figure 3.3.3B). Although the detailed mechanism of *Compounds 5* and *6* from CA was not clear yet, the presence of these compounds confirmed the ketonization reaction of CA. Importantly, the CA ketonization provided a route to formation of aromatic compounds.

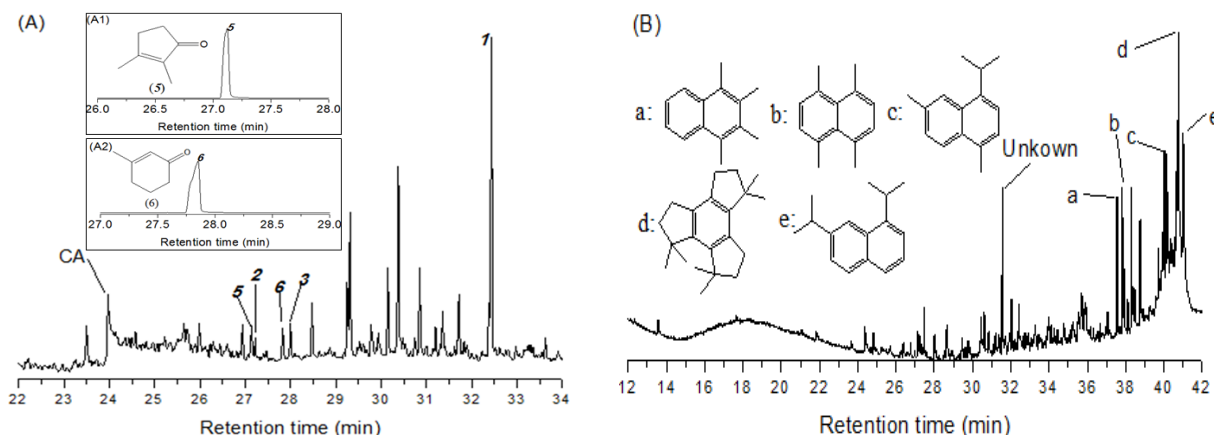


Figure 3.3.3. (A) GC-MS spectrum of hydrocarbon oil formed in the early stage of CA reforming and *Compounds 5* and *6*; (B) GC-MS spectrum of aromatic compounds formed from *Compound 5*.

*Compound 5* was an unsaturated ketone and a key intermediate in the formation of the aromatics from PHB or CA. When *Compound 5* was used as an initial reagent under the typical reaction conditions, the products were much dependent on propylene. In the absence of propylene, naphthalenes (*Compounds a-e* in Figure 3.3.3B) were the main products. In the presence of propylene, however, *Compounds 1-3* were formed as shown in Figure 3.3.4. Some naphthalenes (*Compounds a-e*), however, were also formed in the reaction of *Compound 5* with propylene. This was attributed to poor contact between *Compound 5* (in a liquid solution) and propylene (in gas phase). The separation of two reagents favored the formation of naphthalenes. To check this hypothesis, we replaced propylene with 2-propanol in the reaction with compound 5, considering that 2-propanol was dissolved in the liquid solution and could be quickly converted into propylene in the acid catalytic conditions [7]. Interestingly, naphthalenes were significantly reduced while compounds *1-3* were increased. The aromatics distribution in Figure 3.3.4C was quite similar to those of aromatics formed from CA or PHB (Figure 3.3.1). These results indicated that both *Compound 5* and propylene were the key intermediates in the formation of main alkyl benzenes

(*Compounds 1-3*). Aromatic compounds were also formed from *Compound 6*, but none of them were the main *Compounds 1-4*.

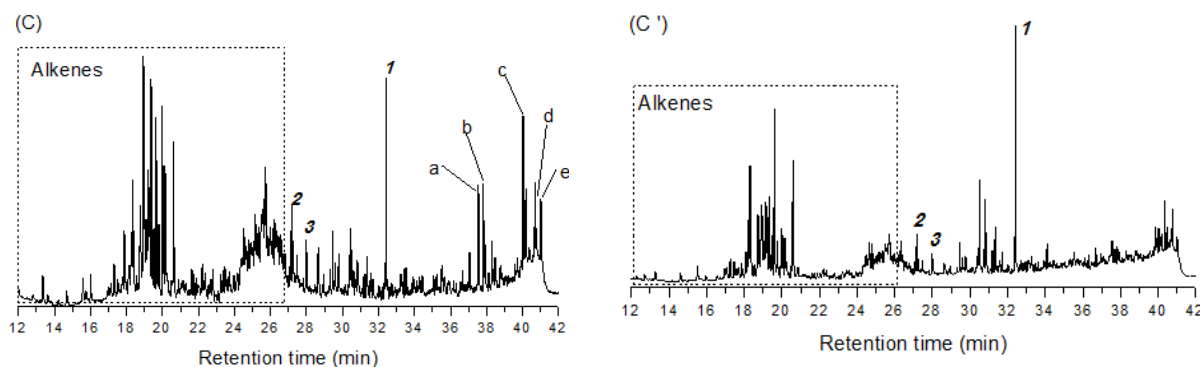


Figure 3.3.4. (C) GC-MS spectrum of hydrocarbons from reaction of *Compound 5* and propylene; (C') GC-MS spectrum of hydrocarbons from reaction of *Compound 5* and 2-propanol.

It was concluded that both decarboxylation and ketonization of CA occurred under the reaction conditions, the former generated propylene and the latter provided *Compound 5* and other active ketones. The competition of decarboxylation and ketonization determined the final composition of hydrocarbon oil, which was affected by the reaction conditions. *Compound 4* was a representative oxygen-containing aromatic compound in the hydrocarbon oil, but was not formed in the reactions of ketones with propylene. It might be formed from acylation of the aromatic compounds with CA [8]. In a controlled experiment, we found that toluene was acylated with CA to form H-inden-1-one,2,3-dihydro-3,3-dimethyl- as a main product [1], an evidence of acylation of aromatic compounds with CA.

Based on the results above, the reaction routes of PHB reforming into hydrocarbon oil are summarized in Figure 3.3.5. The main sequential reactions are divided into three stages: (1) degradation of PHB to crotonic acid (CA), (2) deoxygenation of crotonic acid into propylene and unsaturated ketones, and (3) combination of the deoxygenated small molecules into final hydrocarbons. In the first stage,  $H_3PO_4$  is an effective catalyst in PHB hydrolysis and degradation (steps 1-3) and CA is the key intermediate. Deoxygenation of CA occurs in the second stage, including decarboxylation of CA into propylene and ketonization of CA into unsaturated ketones such as *compound 5* (steps 4 and 5). In the third stage, multiple reactions occur among propylene and ketones, including oligomerization of propylene into alkenes (step 6), aromatic cyclization of propylene with *Compound 5* to form *Compounds 2* and *3* (steps 7 and 8), alkylation of propylene with *Compound 2* to form *Compound 1* (step 9), and acylation of *Compound 3* with CA to form *Compound 4* (step 10). In addition, deoxygenation of the O-containing ketones (*Compounds 5* and

6) leads to naphthalenes (step 11). Crotonic acid, propylene and *Compound 5* are the key intermediates that determine the final composition of hydrocarbon oil.

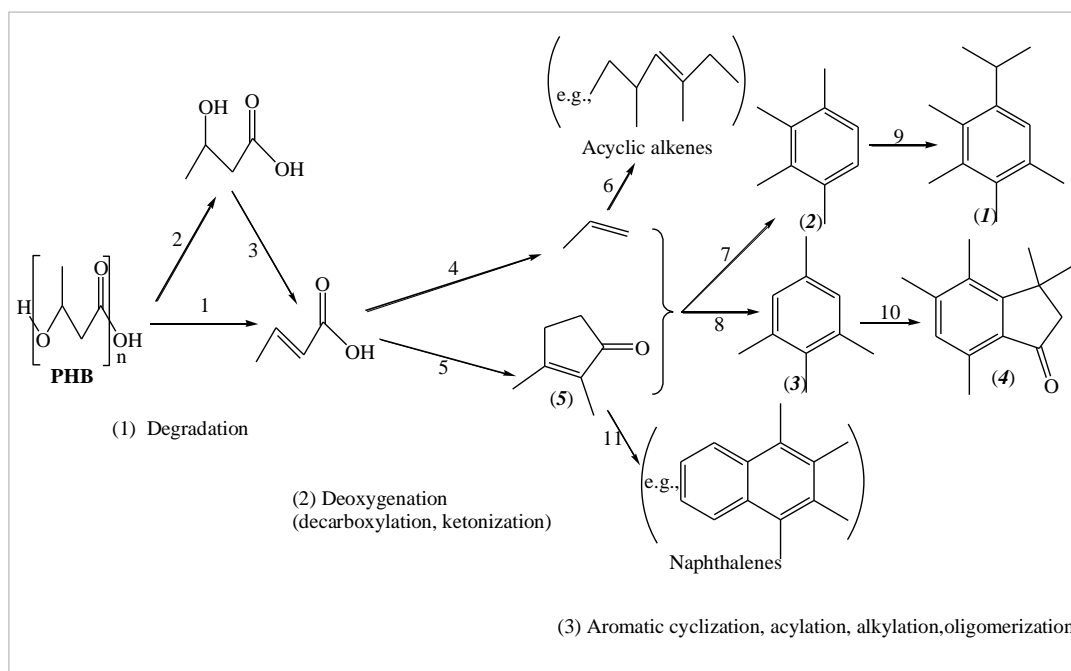


Figure 3.3.5. Proposed reaction routes of catalytic PHB reforming into hydrocarbon compounds.

In addition to PHB, the new process also generated residual microbial biomass that contained C (45.1% w/w), H (5.6% w/w), O (27.8% w/w) and N (12.9% w/w). The high heating value (HHV) of the bacterial biomass was c.a.  $20 \text{ MJ kg}^{-1}$ , similar to those of microalgal and cellulosic biomass ( $17\text{--}22 \text{ MJ kg}^{-1}$ ) [2]. A bio-oil was generated through a simple thermal liquefaction of the biomass in hot water ( $300^\circ\text{C}$ ). The bio-oil contained various hydrophobic compounds, including hydrocarbons (benzene and long chain alkane), nitrogen-containing compounds (pyridines, pyrroles and indoles), and oxygen-containing compounds (esters and ketones) [2]. Table 3.3.1 compares the bio-oil with those derived from cellulosic biomass and microalgae through hydrothermal liquefaction. Compared with the elemental composition of the original microbial

biomass, the C and H contents of bio-oil were significantly increased while O and N reduced. The bio-oil has a quite high HHV (34.6 MJ kg<sup>-1</sup>) and is a good oil for biodiesel production.

Table 3.3.1. Bio-oils generated from different biomass through hydrothermal liquefaction

Biomass Type	Species	Temp (°C)	Elemental content (% w/w)				HHV (MJ kg <sup>-1</sup> )	Reference
			C	H	O	N		
Bacteria	<i>C. necator</i>	300	70.9	9.4	11.8	7.9	34.6	This work
Microalgae	<i>Spirulina</i>	350	68.3	8.3	16.4	6.2	31.5	[9]
Cellulosic	Corn cob	280	63	6.9	28.8	0.4	25.4	[10]

## Publications and Presentations

### *Peer Reviewed Publications*

1. S. Kang, J. Yu. Reaction routes in catalytic reforming of poly(3-hydroxybutyrate) into renewable hydrocarbon oil, *RSC Advances*, 2015, 5, 30005–30013. DOI: 10.1039/c5ra03195h.
2. S. Kang, J. Yu. Hydrophobic organic compounds from hydrothermal liquefaction of bacterial biomass, *Biomass and Bioenergy*, 2015, 74, 92-95. DOI: 10.1016/j.biombioe.2015.008.
3. J. Yu, Pradeep Munasinghe. Gas fermentation enhancement for chemolithotrophic growth of *Cupriavidus necator* on carbon dioxide, *Fermentation*, 2018, 4, 63-77. DOI: 10.3390/fermentation4030063.

### *Contributed Presentations*

1. Jian Yu (2019) Drop-in transportation fuels from renewable hydrogen and carbon dioxide. World Hydrogen Technologies Convention 2019, June 2-7, Tokyo, Japan.
2. Jian Yu (2017) Bioplastics and drop-in transportation fuels from carbon dioxide and solar hydrogen. Environmental and Energy Resource Management Summit 2017, November 9-11, Washington DC.

## References

- [1] S. Kang, J. Yu. Reaction routes in catalytic reforming of poly(3-hydroxybutyrate) into renewable hydrocarbon oil, *RSC Advances*, 2015, 5, 30005–30013. DOI: 10.1039/c5ra03195h
- [2] S. Kang, J. Yu. Hydrophobic organic compounds from hydrothermal liquefaction of bacterial biomass, *Biomass and Bioenergy*, 2015, 74, 92-95. DOI: 10.1016/j.biombioe.2015.008.

- [3] H. Ariffin, H. Nishida, Y. Shirai, M. A. Hassan. Determination of multiple thermal degradation mechanisms of poly(3-hydroxybutyrate), *Polymer Degradation and Stability*, 2008, 93, 1433-1439.
- [4] J. Yu, D. Plackett, L. X. L. Chen. Kinetics and mechanism of the monomeric products from abiotic hydrolysis of poly[(R)-3-hydroxybutyrate] under acidic and alkaline conditions, *Polymer Degradation and Stability*, 2005, 89, 289-299.
- [5] S. Kang, J. Yu. One-pot production of hydrocarbon oil from poly(3-hydroxybutyrate), *RSC Advances*, 2014, 4, 14320-14327.
- [6] T. N. Pham, T. Sooknoi, S. P. Crossley, D. E. Resasco. Ketonization of carboxylic acids: mechanisms, catalysts, and implications for biomass conversion, *ACS Catalysis*, 2013, 3, 2456-2473.
- [7] J. Bedia, R. Ruiz-Rosas, J. Rodriguez-Mirasol, T. Cordero. A kinetic study of 2-propanol dehydration on carbon acid catalysts, *Journal of Catalysis*, 2010, 271, 33-42.
- [8] C. Castro, A. Corma, J. Primo. On the acylation reactions of anisole using  $\alpha,\beta$ -unsaturated organic acids as acylating agents and solid acids as catalysts: a mechanistic overview, *Journal of Molecular Catalysis A: Chemical*, 2002, 177, 273-280.
- [9] U. Jena, N. Vaidyanathan, S. Chinnasamy, K.C. Das. Evaluation of microalgae cultivation using recovered aqueous co-product from thermochemical liquefaction of algal biomass, *Bioresource Technology*, 2011, 102(3), 3380–3387.
- [10] J. Gan, W. Yuan. Operating condition optimization of corn cob hydrothermal conversion for bio-oil production, *Applied Energy*, 2013, 103: 350–357.

### 3.4 Bio-Contamination of Fuels

Evidence suggests that all fuels are susceptible to bio-contamination resulting in microbial induced corrosion of fuel system components and fuel degradation. These problems are often associated with the presence of water. Furthermore, tactical fuels often have specific purity requirements, subjecting them to higher standards. For this reason, comparisons of tactical fuels with other blends of fuels are not universally applicable. Also, the recent trend toward blending of fuels from renewable resources has the potential to introduce contamination issues not previously seen, ranging from biological contamination to chemical stability. Under this task, research was performed that is applicable toward the further development of (1) rapid detection methodologies for the presence of microbial populations in fuels, especially those associated with fuel degradation, and (2) designing inhibitors to combat fuel degradation.

The first part of this subtask utilized the previously isolated biofuel contaminant *Moniliella wahieum* (ATCC MYA-4962) as a model organism. This fungi has the demonstrated capacity to metabolize biodiesel as a carbon source for growth. Characterization of the eukaryotic degradation pathways will be used to expand the database of genetic information that will serve as the



fundamental basis for rapid-detection methodologies and also to provide useful considerations related with biofuel degradation.

To determine this metabolic pathway, we performed a comprehensive genome analysis for *M. wahieum*, its gene annotation, and a proteomic analysis. While ONR support for this project is ending, a differential mRNA analysis will be completed through a collaborative effort with Kyongpook University, Korea.

While the biodegradation of petroleum and other hydrocarbons have been previously studied, the microorganisms described were from environments other than from contaminated biodiesel [1-4]. *M. wahieum* is a model organism for studying biodiesel degradation metabolism since it was isolated from an in-use and contaminated storage tank.

The *M. wahieum* genome was characterized by single molecule real-time sequencing and proteomics. Genome assembling and annotation have found the genes related to  $\beta$ -oxidation and the citric acid cycle. *M. wahieum* can uptake and metabolize biodiesel as a carbon source, which is consistent with previous observations from cell culture. A biodiesel degradation pathway for *M. wahieum* has been proposed based upon the genome annotation results, further analysis will look at RNA expression profiles. Furthermore, 22 stress-response genes from exposure to starvation, hypoxia, and acidity were found from the genome annotation and proteome analysis. These genes promote the survival of *M. wahieum* in the harsh biodiesel environment.

Table 3.4.1 Genome assembling and annotation results from *M. wahieum* MYA-4962.

Genome sequencing		Genome annotation	
<b>Total output (bp)</b>	5,179,292,893	<b>No. of mRNA</b>	16,579
<b>Preassembled base (bp)</b>	1,913,435,278	<b>No. of coding sequence</b>	49,296
<b>No. of contigs</b>	223	<b>No. of exon</b>	51,007
<b>Total length of contigs</b>	69,496,977	<b>No. of tRNA</b>	1,189
<b>Coverage</b>	73.594	<b>No. of rRNA</b>	1,650
<b>N50 (bp)</b>	620,520	<b>No. of UTR region</b>	118

The isolated genomic DNA was first sent to the Duke Center for Genomic and Computational Biology and sequenced using a Pacbio Sequel platform and two SMRT cells (Pacific Biosciences, MenloPark, CA). The long-read sequences were assembled using FALCON open source software [5, 6]. Statistics from the genome assembly were also calculated using FALCON. The MAKER genome annotation pipeline program, was used and analysis was done with gene prediction methodology [7]. The reference genome used for annotation was from the Basidiomycota phylum, and BLASTX used for gene prediction [8]. A KOG analysis was performed with the WebMGA program using the genome annotation results for the classification of orthologous proteins [9].

The proteome analysis was previously performed and has been briefly described in the Asia Pacific Research Initiative for Sustainable Energy Systems (APRISES2013). The translated proteins that were specifically expressed and identified during biodiesel metabolism were used along with the genome data to identify the degradation pathway.

The KEGG Automatic Annotation Server (KAAS) was used to develop a proposed catabolic pathway for biodiesel metabolism [10]. The genomes from *Cryptococcus*, *Ustilago*, and *Moniliophthora* are the model organisms used for the catabolic pathway determination. These results were then compared with the proteome data.

Total genome sequence and annotation of *M. wahliae* ATCC MYA-4962 was determined to have a genome having approximately 69.4 Mb. The sequencing resulted in the generation of 223 contigs having 73.6 times of coverage. The sequence data has been deposited into the NCBI database (Accession No. RSEE000000000). A total of 16,579 genes and 49,296 genes were annotated from mRNA and DNA coding sequences, respectively (Table 3.4.1).

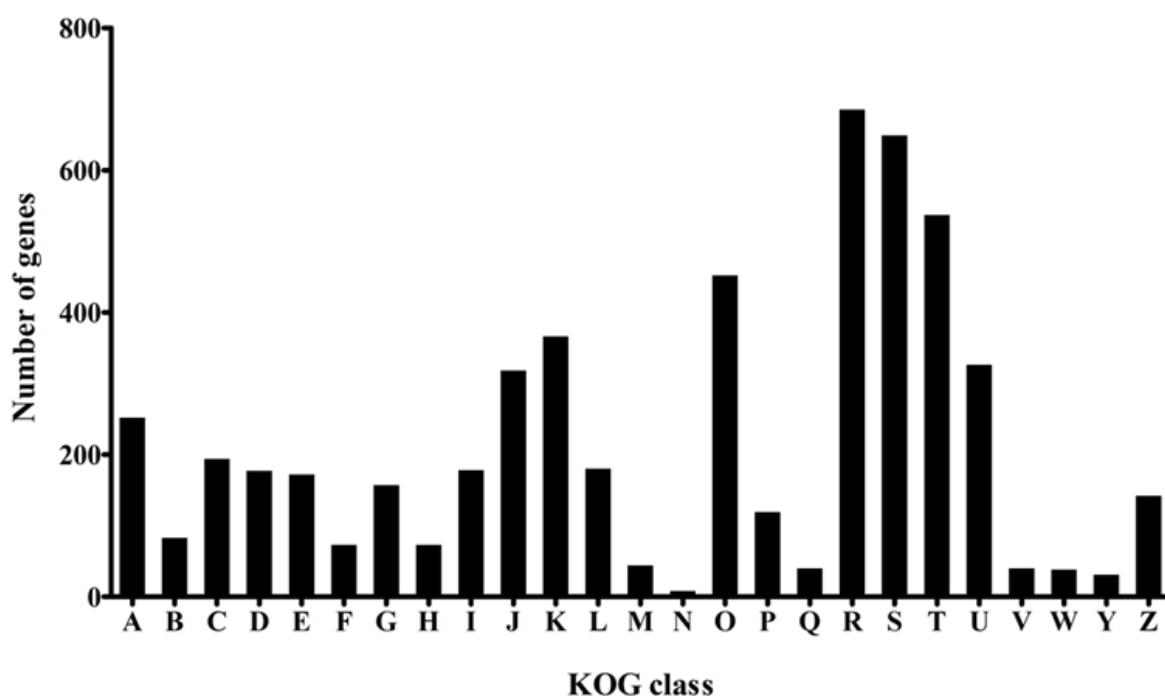


Figure 3.4.1. KOG analysis of all proteins from *M. wahieum* ATCC MYA-4962. A, RNA processing and modification; B, Chromatin structure and dynamics; C, Energy production and conversion; D, Cell cycle control, cell division, chromosome partitioning; E, Amino acid transport and metabolism; F, Nucleotide transport and metabolism; G, Carbohydrate transport and metabolism; H, Coenzyme transport and metabolism; I, Lipid transport and metabolism; J, Translation, ribosomal structure and biogenesis; K, Transcription; L, Replication, recombination and repair; M, Cell wall/membrane/envelope biogenesis; N, Cell motility; O, Posttranslational modification, protein turnover, chaperones; P, Inorganic ion transport and metabolism; Q, Secondary metabolites biosynthesis, transport and catabolism; R, General function prediction only; S, Function unknown; T, Signal transduction mechanisms; U, Intracellular trafficking, secretion, and vesicular transport; V, Defense mechanisms; W, Extracellular structures; Y, Nuclear structure; Z, Cytoskeleton.

EuKaryotic Orthologous Groups (KOG) tool was used to determine approximately 5,800 proteins that were mostly categorized by general functional prediction. Coding genes having been classified with lipid (180 proteins) or carbohydrate (159 proteins) metabolisms were determined (Figure 3.4.1).

Genes involved with  $\beta$ -oxidation and the TCA cycle were determined from the annotation results and the KOG analysis. Proteins thought to be associated with the metabolism of biodiesel that

were both found in the annotated genome and in the protein analysis are shown in Table 3.4.2. The results suggest that biodiesel is metabolized by  $\beta$ -oxidation.

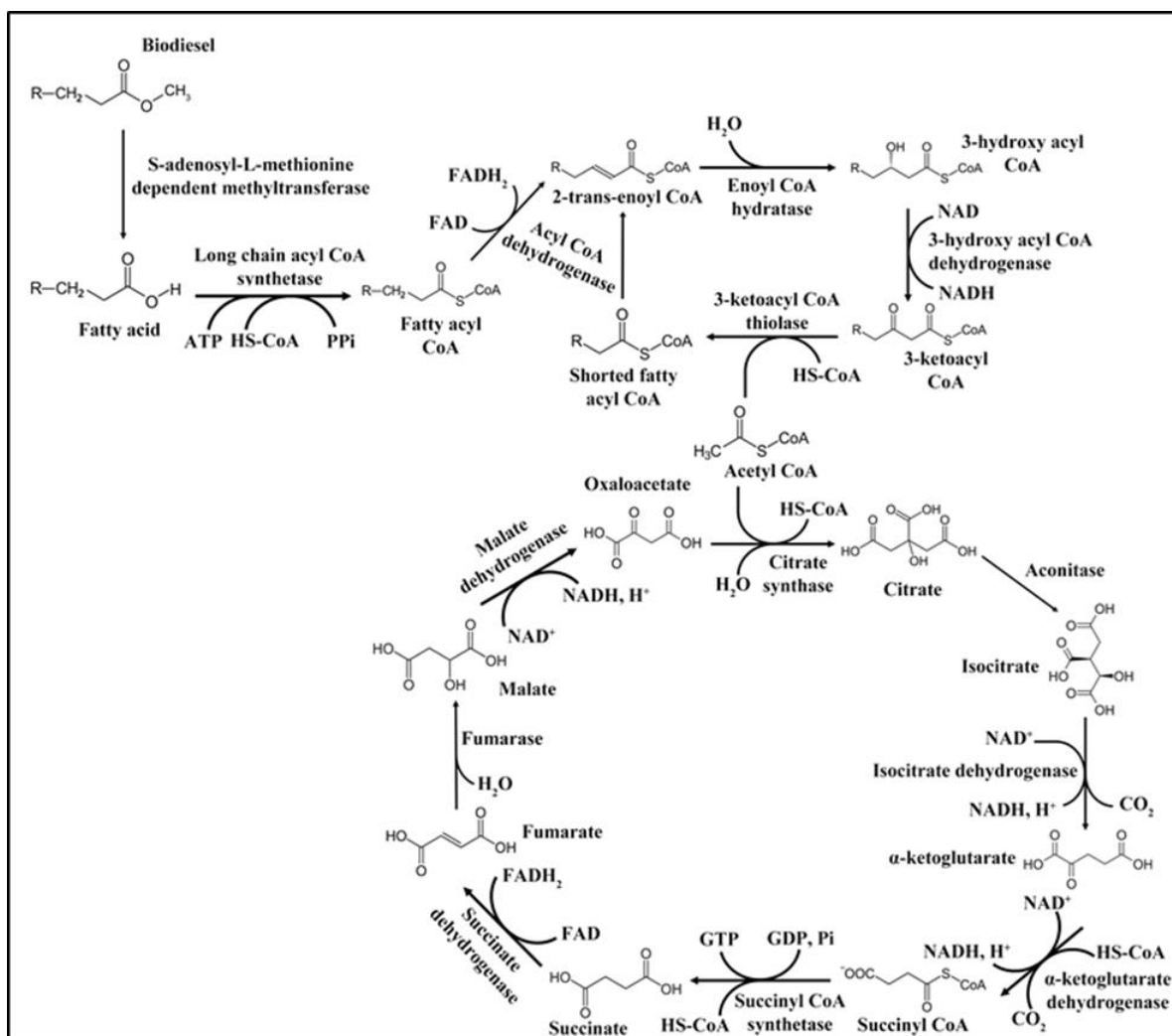


Figure 3.4.2. Proposed biodiesel metabolic pathway of *M. wahieum* ATCC MYA-4962. Arrows indicate the direction of the reaction. All enzymes in this figure were detected in genome annotation and proteome analysis.

A catabolic pathway for the metabolism of biodiesel for *M. wahieum* ATCC MYA-4962 is proposed in Figure 3.4.2. Biodiesel is principally composed from fatty acid methyl esters. During catabolic degradation, the methyl group is first transferred from the ester, and is mediated by a S-adenosyl-L-methionine dependent methyltransferase. The resultant fatty acids are transported to the interior of the mitochondria by membrane associated long chain fatty acid transporters. In the mitochondria, the fatty acids are then metabolized via  $\beta$ -oxidation producing Acetyl-CoA that is

further metabolized by the TCA cycle.  $\beta$ -Oxidation has been previously found related to the decomposition of fatty acid methyl ester (FAMES) [11-12].

Table 3.4.2 The list of detected genes that are related with biodiesel degradation based upon the genome annotation for *M. wahlbergii*.

Function	Enzyme	E-value*
Hydrolysis of methyl esters to fatty acids	s-Adenosyl-l-methionine-dependent methyltransferase	1.10E-109
Transport of fatty acids into mitochondria	Long chain fatty acid transporter	8.30E-146
$\beta$ -oxidation	Long chain acyl-CoA Synthetase	1.80E-159
	Acyl-CoA oxidase	5.24E-75
	Acyl-CoA dehydrogenase	7.94E-21
	Enoyl-CoA hydratase	2.10E-82
	3-hydroxyl-CoA dehydrogenase	7.59E-114
	3-ketocacyl-CoA thiolase	2.69E-160
TCA cycle	Citrate synthase	0
	Aconitase	0
	Isocitrate dehydrogenase	0
	$\alpha$ -ketoglutarate dehydrogenase	0
	Succinyl-CoA synthetase	8.51E-148
	Succinate dehydrogenase	0
	Fumarase	0
	Malate dehydrogenase	5.08E-112

The biodiesel environment is biologically stressful, and many stress-related proteins were found to be expressed. A total of 22 genes that are related to stress-response were differentially expressed between different carbon sources (Figure 3.4.3). A total of 15 genes related to nutrition starvation, 4 genes associated with hypoxia, and 2 genes expressed in response to an acidic environment (Table 3.4.3). During hyperosmotic stress, a signal protein was activated stimulating a mitogen-

activated kinase. The mitogen-activated kinase is a transcription factor that causes apoptosis under stress including osmotic pressure and heat shock, influencing the expression of glycerol-3-phosphate dehydrogenase. The glycerol-3-phosphate dehydrogenase stimulates the synthesis of glycerolipids facilitating glycerol accumulation [13-15]. The heat shock protein, HSP70, was selectively expressed when grown using biodiesel. HSP70 is a housekeeping protein, minimizing structural and conformation damage to other proteins [16, 17].

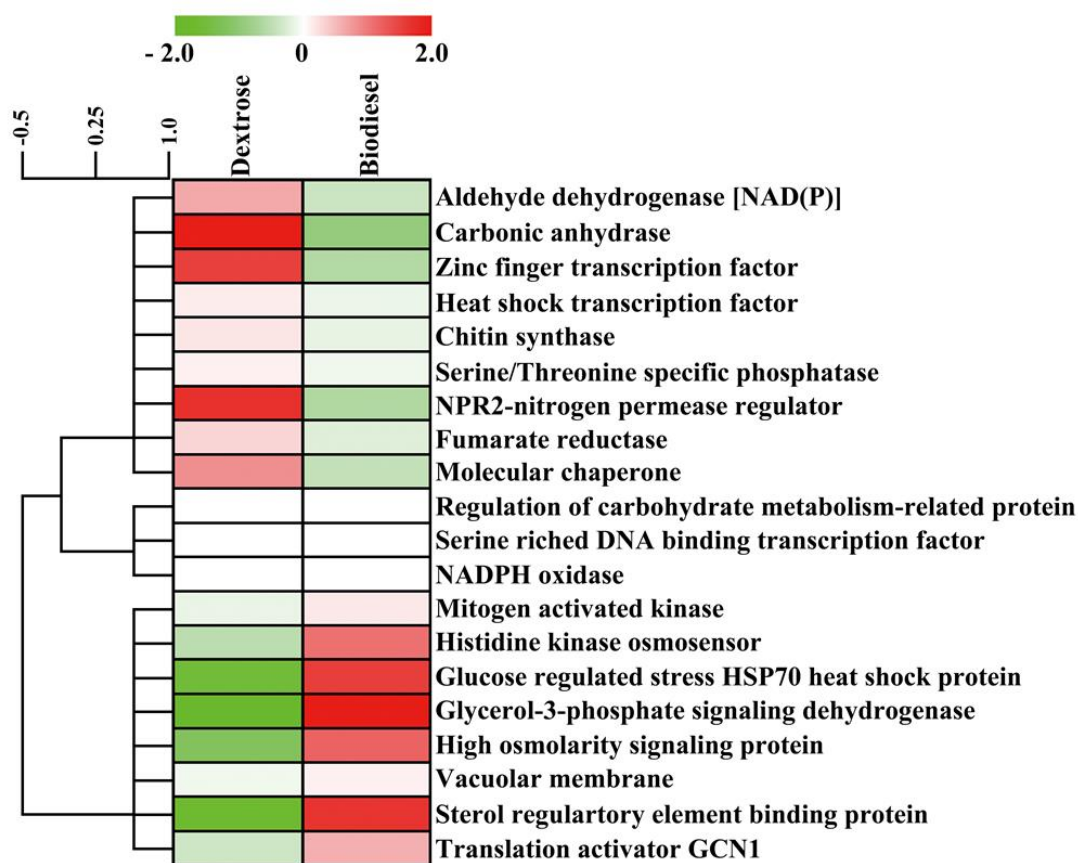


Figure 3.4.3. Stress-response proteins (genes) in *M. wahlbergii* ATCC MYA-4962. Three protein clusters were generated by hierarchical clustering with the Pearson correlation. A value such as -2, 0, and 2 indicate fold change. From up to down, the three clusters are consisted of highly expressed proteins in glucose, similarly expressed proteins, and highly expressed proteins in biodiesel.

Although there were no significant differences between expressions of vacuolar membrane-associated proteins, they are typically selectively expressed during times of nutrient deficiency [18]. Sterol regulatory binding proteins are transcriptional factors expressed during hypoxia. Fungi such as *Cryptococcus*, *Aspergillus* are known to have adaptation mechanisms related with hypoxia

[19]. Proteins that are related to primary metabolism including aldehyde dehydrogenase, carbonic anhydrase, zinc finger transcription factor, NPR2-nitrogen permease regulator, and fumarate reductase are differentially expressed when grown in YM media. These results are expected, considering the availability of an easily metabolized carbon source.

This genome sequence is currently the most comprehensive for the genus. Furthermore, while the proposed biodiesel degradation pathway requires additional validation from RNA expression, it is the most relevant to date information that describes the catabolism of biodiesel.

The second part of this subtask utilized again the previously isolated biofuel contaminant *M. wahieum* as a model organism to experiment with different nanoparticle inhibitors. Broad spectrum antimicrobial activity was determined by comparing the effects of synthesized nanoparticles with the prokaryotic *E. coli*. The activities of the nanoparticles were found by characterization of the physical damage that occurred to the cell membrane, and metabolic effects. These results and the information provided here are applicable toward bio-inhibitor development for use in fuels.

There have been numerous antimicrobial investigations performed using metal and metal oxide nanoparticles that have described toxicity against both gram positive and gram-negative bacteria [20-25]. Iron oxide nanoparticles ( $\text{Fe}_3\text{O}_4$ ) and copper oxide ( $\text{CuO}$ ) have been previously used for the elimination of biological contaminants, and in industry as catalysts [21, 26, 27]. Silver ( $\text{Ag}$ ) nanoparticles are known to generate free ions and have radical activities making them efficient antimicrobial agents. However, the production of pure silver particle is challenging. Therefore, the use of silver-based nanoparticles, such as  $\text{AgO-Fe}_3\text{O}_4$ ,  $\text{AgO-Fe}_3\text{O}_4$ -graphene oxide,  $\text{AgO-Fe}_3\text{O}_4$ -cellulose has been investigated [28, 29]. Lanthanum oxide ( $\text{La}_2\text{O}_3$ ), has a strong ionic charge, and was found to be effective against fungi [30]. The antimicrobial activity of the nanoparticle is determined by its chemical composition and surface characteristics [31]. Nanoparticles can damage the cell membrane and impact metabolic activity [32]. Understanding the effects of nanoparticle concentration, cell membrane disruption, and transport into the intracellular environment are critical for toxicity determinations. Nanoparticles composed from silver, copper, iron and graphene or their binary mixtures were examined as inhibitors against the fungus *M. wahieum* ATCC MYA-4962.

Table 3.4.3 Stress-response genes differentially expressed by *M. wahieum* when grown using biodiesel as a carbon source.

Stress	Protein	E-value
Nutrition starvation	Mitogen activated kinase	2.24E-60
	Histidine kinase osmosensor	1.25E-101
	Aldehyde dehydrogenase [NAD(P)]	3.13E-77
	Carbonic anhydrase	9.48E-59
	Zinc finger transcription factor	1.91E-20
	Heat shock transcription factor	6.96E-31
	Glucose regulated stress HSP70 Heat shock protein	2.00E-173
	Chitin synthase	1.80E-126
	Glycerol-3-phosphate dehydrogenase	2.29E-43
	Serine/Threonine specific phosphatase	7.41E-24
Hypoxia (oxygen deficiency)	High osmolarity signaling protein	4.85E-32
	Regulation of carbohydrate metabolism-related protein	9.89E-14
	NPR2-nitrogen permease regulator	5.44E-81
	Vacuolar membrane	1.07E-83
Acidic environment	Sterol regulatory element binding protein	7.05E-41
	Serine riched DNA binding transcription factor	8.74E-13
	Fumarate reductase	9.98E-156
	Molecular chaperone	8.73E-88
	NADPH oxidase	8.63E-18
	Translation activator GCN1	3.90E-112

The nanoparticles that were synthesized for this experiment (AgO, AgO-Fe<sub>3</sub>O<sub>4</sub>, La<sub>2</sub>O<sub>3</sub> and CuO) were determined to be crystalline and spherical, having a diameter respectively in AgO (10-40 nm), AgO-Fe<sub>3</sub>O<sub>4</sub> (10-50 nm), La<sub>2</sub>O<sub>3</sub> (60-80 nm), CuO (40-70 nm) (Figure 3.4.4). The smaller AgO nanoparticles have approximately 2.4, and 1.9 times greater surface area in comparison with the La<sub>2</sub>O<sub>3</sub> and CuO nanoparticles.

Aggregates are intuitively larger than the nominal particle and many studies emphasize the importance of a well-dispersed suspension. Inhibition of *E. coli* and *M. wahieum* Y12<sup>T</sup> after exposure to varying doses of nanoparticles were determined (Table 3.4.4).



*E. coli* and *M. wahieum* Y12<sup>T</sup> were inhibited by low concentrations of silver (from 0.01 to 0.05 mg mL<sup>-1</sup>) [30]. The EC<sub>50</sub> value of La<sub>2</sub>O<sub>3</sub> on *E. coli* was 379 times greater when compared with *M. wahieum* Y12<sup>T</sup>. While the AgO was the most effective at eliminating *E. coli* and *M. wahieum* Y12<sup>T</sup>, followed by AgO-Fe<sub>3</sub>O<sub>4</sub>, AgO-graphene and CuO nanoparticles. Silver nanoparticles and other silver compounds are known to have toxic effects on both bacteria and fungi [32-34]. AgO-Fe<sub>3</sub>O<sub>4</sub> and CuO have been previously shown to inhibit select-microorganisms [35]. Exposure to La<sub>2</sub>O<sub>3</sub> nanoparticles inhibited the growth of *M. wahieum* Y12<sup>T</sup> [30], whereas no obvious effects on *E. coli* were observed at high concentration (1 mg mL<sup>-1</sup>). The La<sub>2</sub>O<sub>3</sub> has been reported to be inhibitory to gram-positive bacteria that results from interactions with the peptidoglycan cell wall. Since *E. coli* lacks a prominent cell wall, this might be a reason for its ineffectiveness against *E. coli*. Reduced efficacy of the La<sub>2</sub>O<sub>3</sub> might also result from aggregation at higher concentrations. Aggregates greatly reduce the amount of surface area and can impact inhibit its passing through the cell membrane [20]. In comparison, the positively charged AgO-Fe<sub>3</sub>O<sub>4</sub> exhibited enhanced antimicrobial activity that are the direct result of ionic interactions between the negatively charged cell surfaces [27]. Relative to the AgO nanoparticles, the next highest toxicity was observed with CuO and AgO-Fe<sub>3</sub>O<sub>4</sub> on an equal mass basis (Table 3.4.5).

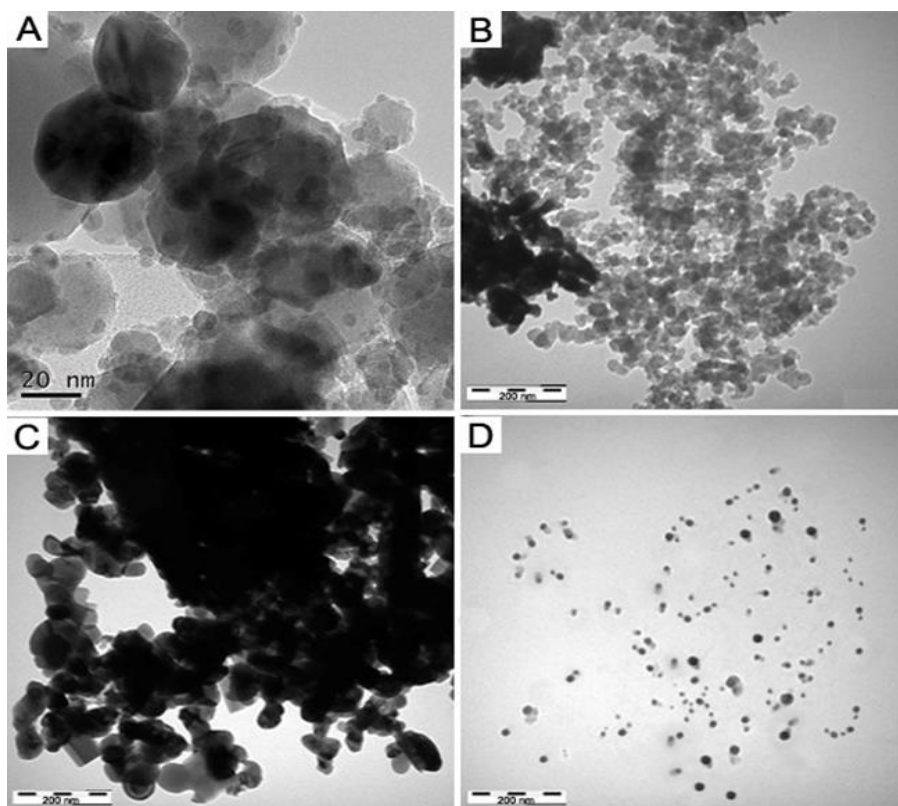


Figure 3.4.4. Transmission Electron Microscope images of the nanoparticle AgO-Fe<sub>3</sub>O<sub>4</sub> (A), La<sub>2</sub>O<sub>3</sub> (B), CuO (C) and AgO (D). A Hitachi S-3400 N TEM was used.

The changes in FDA activity after exposure to the nanoparticles are shown in Figures 3.4.5 and 6. The AgO nanoparticles are still more effective at inhibiting the metabolism of both *M. wahieum* Y12<sup>T</sup> and *E. coli* (Zhang *et al.* 2018) and was more effective at doing so relative to the other examined silver containing compounds. At a concentration of 0.5 mg mL<sup>-1</sup>, CuO minimally reduced FDA activity. Compared with *E. coli*, *M. wahieum* Y12<sup>T</sup> was more susceptible to inhibition from AgO-Fe<sub>3</sub>O<sub>4</sub> and GO-Cu-AgO nanoparticles. Exposing *M. wahieum* Y12<sup>T</sup> to 0.01 mg mL<sup>-1</sup> of AgO-Fe<sub>3</sub>O<sub>4</sub> resulted in a 75% reduction in growth rate, and inhibited growth 4 times more when compared with *E. coli* at that concentration. The EC<sub>50</sub> was also 15 times lower (0.02 mg mL<sup>-1</sup>).

Table 3.4.4. Median effective concentrations (EC<sub>50</sub>), half maximal inhibitory concentrations (IC<sub>50</sub>), no-observed-effect concentrations (NOEC), lowest-observed-effect concentrations (LOEC), and susceptibility constants (Z) for *E. coli* and *M. wahieum* Y12<sup>T</sup> exposed to the metal oxide nanoparticles on LB and MS for 24 h. Unit is mg/mL.

Microbe	Nanoparticle	EC <sub>50</sub>	IC <sub>50</sub>	NOEC	LOEC	Z
<i>E. coli</i>	La <sub>2</sub> O <sub>3</sub>	190	1.62	< 0.75	1.00	0.058
	AgO	0.005	0.027	< 0.05	0.05	263
	CuO	0.050	0.121	< 0.50	0.50	7.41
	AgO-Fe <sub>3</sub> O <sub>4</sub>	0.006	0.008	< 0.02	0.02	268
	Ag-graphene	0.011	0.014	< 0.01	0.05	79.7
<i>M. wahieum</i> Y12 <sup>T</sup>	La <sub>2</sub> O <sub>3</sub>	0.501	0.826	< 1.00	2.50	0.98
	AgO	0.005	0.006	0.005	0.01	288
	CuO	0.074	0.165	0.10	0.50	6.82
	AgO-Fe <sub>3</sub> O <sub>4</sub>	0.011	0.121	< 0.02	0.03	232
	Ag-graphene	0.033	0.038	< 0.02	0.05	30.5

Table 3.4.5. Toxicity comparisons for AgO, CuO and Ag-Fe<sub>3</sub>O<sub>4</sub> nanoparticles exposed to *E. coli* and *M. wahieum* Y12<sup>T</sup>.

AgO (mg/mL)	CFU/mL					CuO (mg/mL)	CFU/mL					AgO- Fe <sub>3</sub> O <sub>4</sub> (mg/mL)	CFU/mL				
	<i>E. coli</i>		Y12 <sup>T</sup>				<i>E. coli</i>		Y12 <sup>T</sup>				<i>E. coli</i>		Y12 <sup>T</sup>		
	0 h	24 h	0 h	24 h			0 h	24 h	0 h	24 h			0 h	24 h	0 h	24 h	
0.00	1.4×10 <sup>6</sup>	6.1×10 <sup>9</sup>	0.0	2.5×10 <sup>5</sup>	3.9×10 <sup>7</sup>	0	1.4×10 <sup>6</sup>	6.1×10 <sup>9</sup>	0.0	2.1×10 <sup>5</sup>	1.0×10 <sup>7</sup>	0.0	3.0×10 <sup>6</sup>	8.0×10 <sup>8</sup>	0.0	1.1×10 <sup>6</sup>	3.3×10 <sup>7</sup>
0.05	1.4×10 <sup>6</sup>	1.2×10 <sup>4</sup>	0.005	2.5×10 <sup>5</sup>	2.1×10 <sup>7</sup>	0.1	1.4×10 <sup>6</sup>	1.5×10 <sup>9</sup>	0.1	2.1×10 <sup>5</sup>	3.9×10 <sup>6</sup>	0.005	3.0×10 <sup>6</sup>	3.8×10 <sup>8</sup>	0.005	1.1×10 <sup>6</sup>	1.9×10 <sup>7</sup>
0.10	1.4×10 <sup>6</sup>	0	0.01	2.5×10 <sup>5</sup>	2.2×10 <sup>5</sup>	0.5	1.4×10 <sup>6</sup>	1.5×10 <sup>8</sup>	0.5	2.1×10 <sup>5</sup>	3.3×10 <sup>5</sup>	0.01	3.0×10 <sup>6</sup>	2.6×10 <sup>8</sup>	0.01	1.1×10 <sup>6</sup>	1.7×10 <sup>7</sup>
0.15	1.4×10 <sup>6</sup>	0	0.015	2.5×10 <sup>5</sup>	1.2×10 <sup>2</sup>	1.0	1.4×10 <sup>6</sup>	8.0×10 <sup>7</sup>	1.0	2.1×10 <sup>5</sup>	1.9×10 <sup>5</sup>	0.015	3.0×10 <sup>6</sup>	2.1×10 <sup>8</sup>	0.015	1.1×10 <sup>6</sup>	1.6×10 <sup>7</sup>
0.20	1.4×10 <sup>6</sup>	0	0.02	2.5×10 <sup>5</sup>	8.6×10 <sup>2</sup>	1.5	1.4×10 <sup>6</sup>	3.0×10 <sup>7</sup>	1.5	2.1×10 <sup>5</sup>	1.5×10 <sup>5</sup>	0.02	3.0×10 <sup>6</sup>	3.8×10 <sup>6</sup>	0.02	1.1×10 <sup>6</sup>	1.0×10 <sup>7</sup>
			0.03	2.5×10 <sup>5</sup>	5.9×10 <sup>2</sup>	2.0	1.4×10 <sup>6</sup>	4.0×10 <sup>7</sup>	2.0	2.1×10 <sup>5</sup>	4.9×10 <sup>4</sup>	0.03	3.0×10 <sup>6</sup>	1.3×10 <sup>3</sup>	0.03	1.1×10 <sup>6</sup>	3.1×10 <sup>4</sup>
			0.04	2.5×10 <sup>5</sup>	0							0.04	3.0×10 <sup>6</sup>	0	0.04	1.1×10 <sup>6</sup>	1.2×10 <sup>4</sup>
			0.05	2.5×10 <sup>5</sup>	0							0.05	3.0×10 <sup>6</sup>	0	0.05	1.1×10 <sup>6</sup>	90

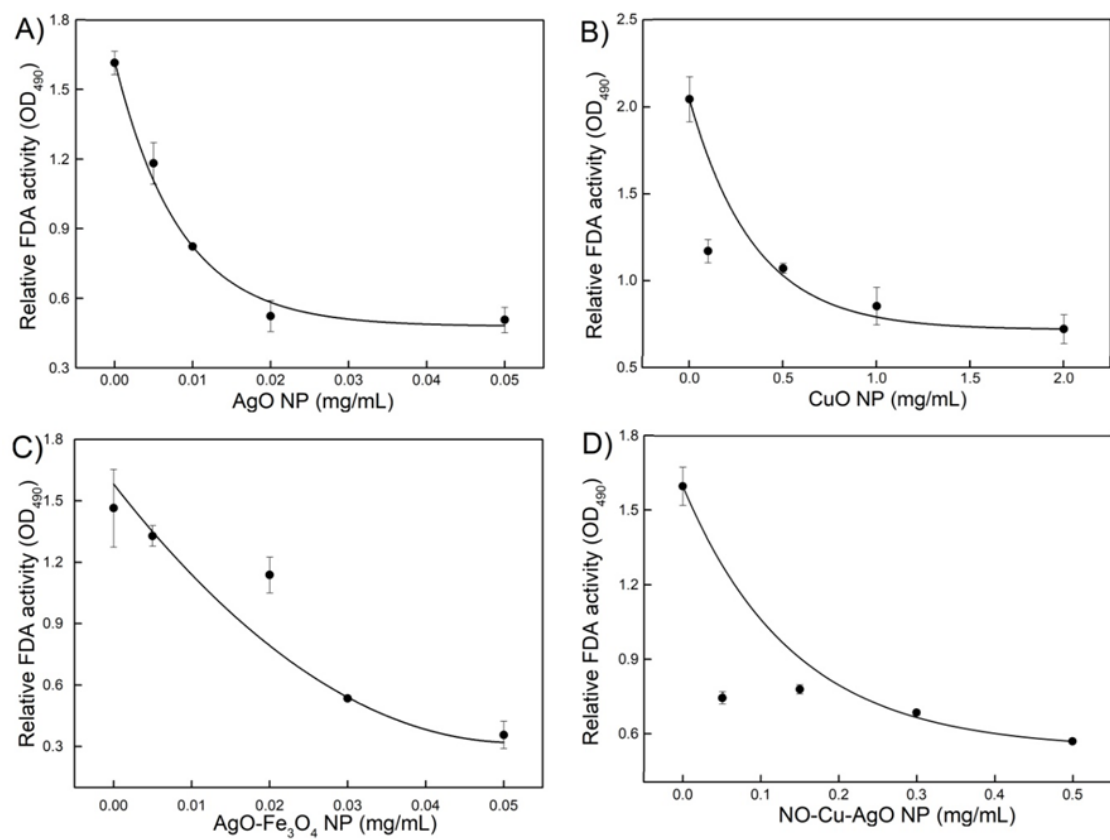


Figure 3.4.5. Relative changes in FDA activity (OD<sub>490</sub>) for *E. coli*. Bars represent one standard deviation of the mean three replicates.

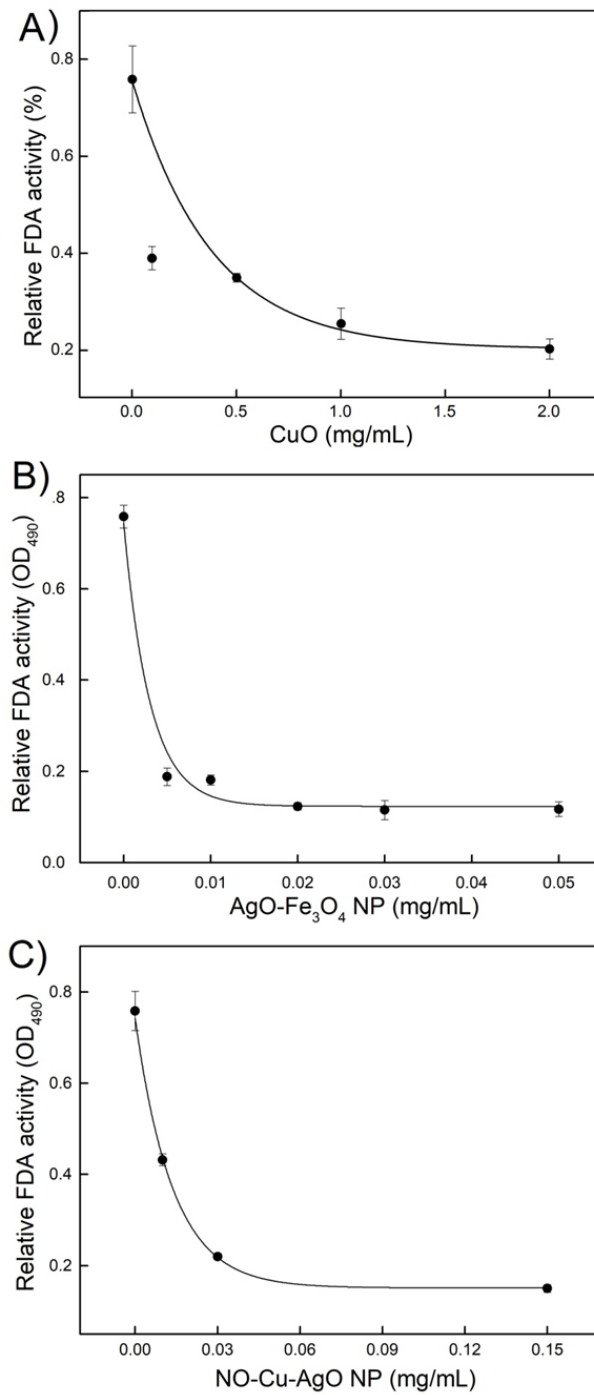


Figure 3.4.6. Relative changes in FDA activity (OD<sub>490</sub>) for *M. wahieum* Y12<sup>T</sup>. Bars represent one standard deviation of the mean three replicates.

According to cell membrane stability examinations, all of the nanoparticles caused damage to both *E. coli* and *M. wahieum* Y12<sup>T</sup> (Figure 3.4.7). The AgO nanoparticles reduced cell membrane

stability at a concentration that was 20 times lower compared with CuO. A positive relationship between efficacy and dose was observed only between AgO and *E. coli*.

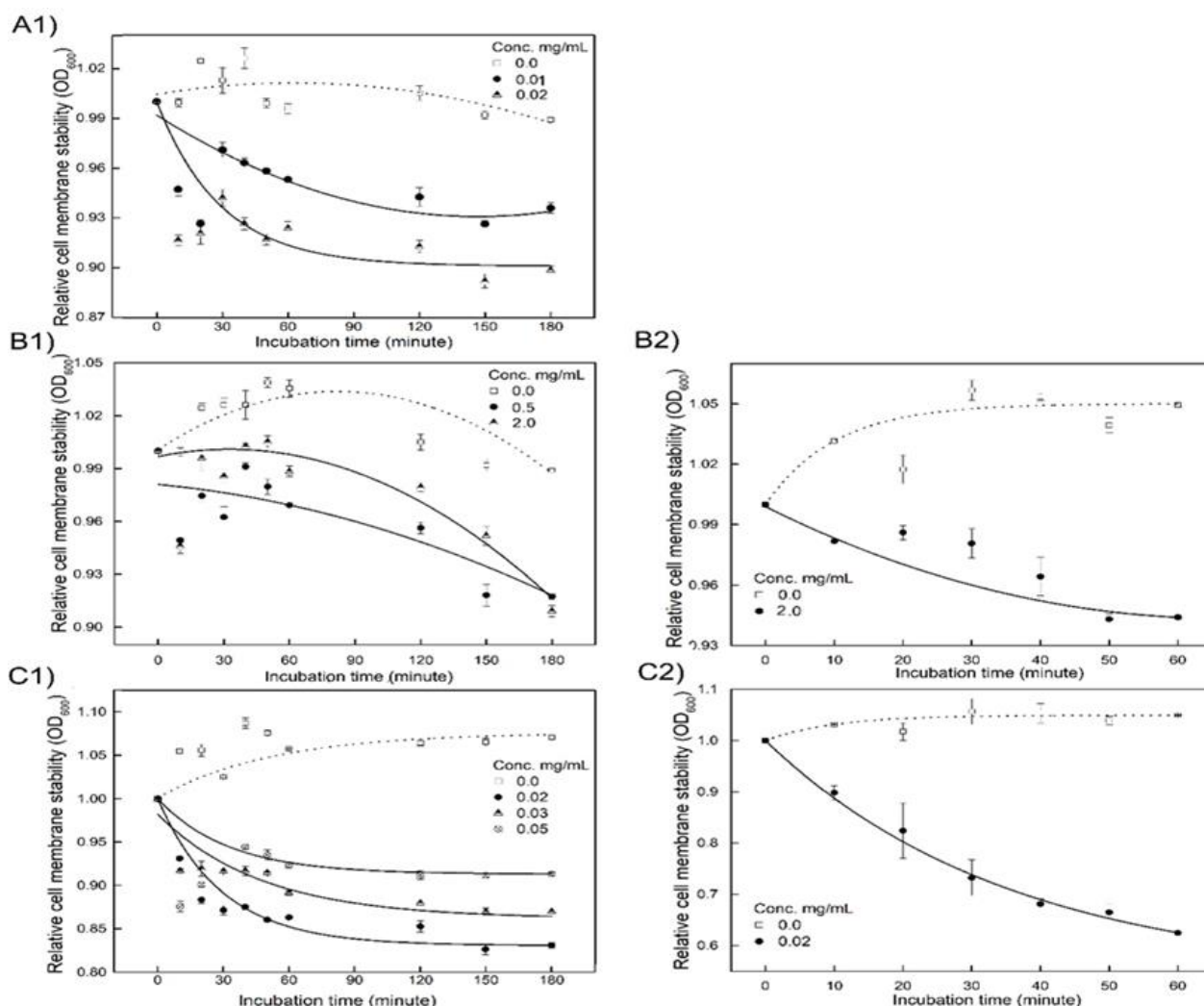


Figure 3.4.7. Changes in the relative cell membrane stability of *E. coli* (A1, B1 and C1) and *M. wahieum* Y12<sup>T</sup> (B2 and C2) after exposure to different concentrations of, CuO (B), Ag-Fe<sub>3</sub>O<sub>4</sub> (C) nanoparticles and the subsequent growth in YM medium containing 1% SDS. Bars represent one standard deviation of the mean three replicates.

To investigate the impact that the nanoparticles have on cell surfaces, electron microscopy was performed (Figures 3.4.8 and 9). Smaller particles have high surface area to volume ratios and have higher free energy [36-38]. Dispersion and aggregation are compound dependent, therefore those that are both small and maintain dispersion in fluid suspension have the potential for enhanced antimicrobial activity. As determined by SEM, *M. wahieum* Y12<sup>T</sup> and *E. coli* cells are

normally columnar and have a smooth surface, the average diameters were 0.5-1  $\mu\text{m}$ . After exposure to the metal nanoparticles, the cells developed irregular pits on the membrane surface. Damage to the cell wall and membrane from ionic and free radical reactions are facilitated by certain nanoparticles, including those that are metallic [22, 24, 39, 40]. Cells that are exposed to nanoparticles have been previously shown to developed wrinkles on the cell surface following their internalization. The surface chemistry of the nanoparticle governs the interfacial reactions that occur at its surface [41].

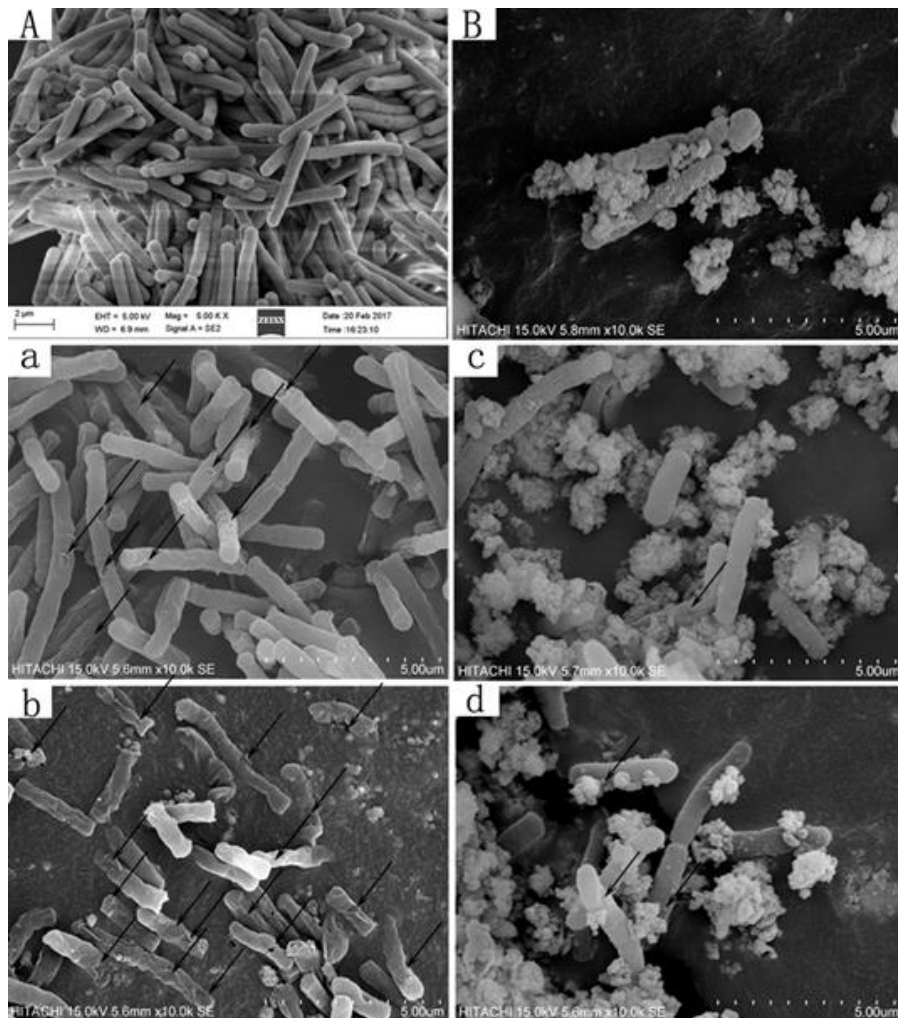


Figure 3.4.8. SEM images of *E. coli* untreated (A) and treated with AgO nanoparticles (a. 0.01 mg/L; b. 0.04 mg/L) and  $\text{La}_2\text{O}_3$  nanoparticles (B. 5.0 mg/mL; c. 2.5 mg/mL; d. 5.0 mg/mL) for 6 h.

The electrostatic interactions that occur between the positively charged silver nanoparticle and the negatively charged membrane can mechanically damage the membrane and then more easily cross into the cell [42]. After entering the cell, the nanoparticle interacts with DNA, proteins, lipids,

flavonoids, and polysaccharides. The interaction inhibits respiration and electron transfer, collapsing the proton motive force due to leakage, that ultimately result in gradient dysfunction and cell death [20, 43]. The use of metallic nanoparticles having antimicrobial mechanisms similar that also have favorable bulk characteristics have potential applications as biological inhibitors in biofuels. The manuscript containing this data has been submitted for publication and is currently under peer review.

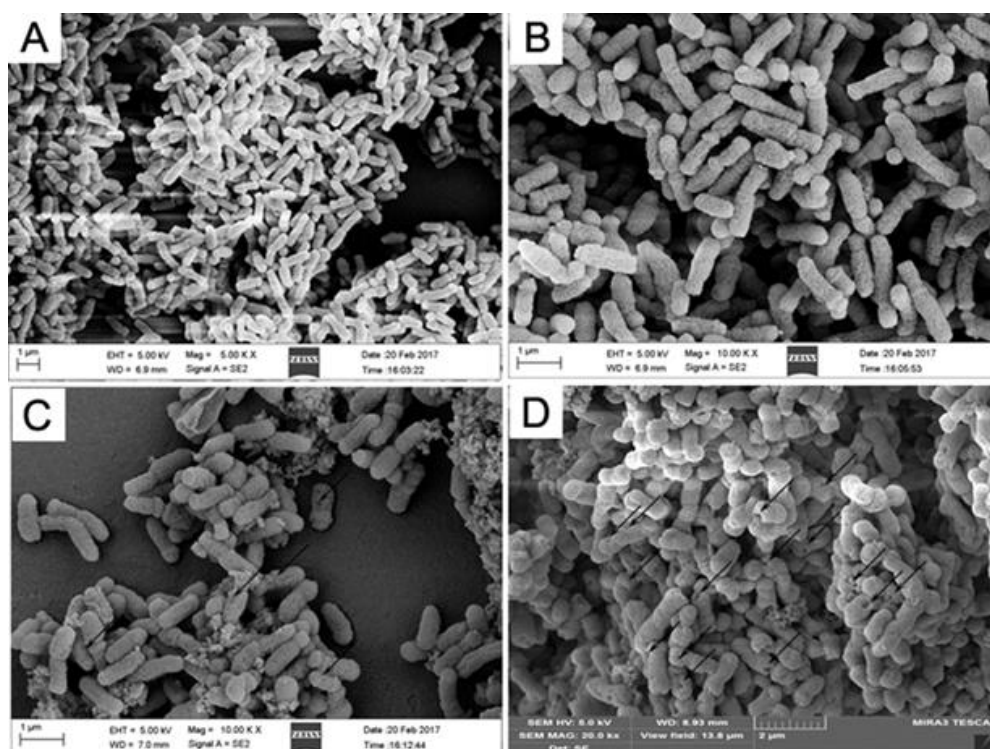


Figure 3.4.9. SEM images of *M. wahieum* Y12<sup>T</sup> untreated (A, B) and treated with  $\text{La}_2\text{O}_3$  (C) nanoparticles (5.0 mg/L) and  $\text{AgO-Fe}_3\text{O}_4$  (D) nanoparticles (0.1 mg/mL) for 6 h.

## References

- [1] Purwasena I., Astuti D., Fatmawati R., Afinanisa, Q. 2018. Isolation and Characterization of Oil-Degrading Bacteria from One of South Sumatera's Oilfield, In *IOP Conference Series: Materials Science and Engineering*, IOP Publishing, p 012123.
- [2] Geetha S., Joshi S. J., Kathrotiya S. 2013. Isolation and characterization of hydrocarbon degrading bacterial isolate from oil contaminated sites. *APCBEE procedia*, 5, 237-241.
- [3] Macchi M., Martinez M., Tauil R. N., Valacco M., Morelli I., Coppotelli B. 2018. Insights into the genome and proteome of *Sphingomonas paucimobilis* strain 20006FA involved in the regulation of polycyclic aromatic hydrocarbon degradation. *World Journal of Microbiology and Biotechnology*, 34 (1), 7.



- [4] Atashgahi S., Hornung B., Waals M. J., Rocha U. N. Hugenholtz F., Nijse B., Molenaar, D., Spanning R., Stams, A. J., Gerritse, J. 2018. A benzene-degrading nitrate-reducing microbial consortium displays aerobic and anaerobic benzene degradation pathways. *Scientific reports*, 8 (1), 4490.
- [5] Chin C.-S., Alexander D. H., Marks P., Klammer A. A., Drake J., Heiner C., Clum A., Copeland A., Huddleston J., Eichler E. E. 2013. Nonhybrid, finished microbial genome assemblies from long-read SMRT sequencing data. *Nature methods*, 10 (6), 563.
- [6] Chin C.-S., Peluso P., Sedlazeck F. J., Nattestad M., Concepcion G. T., Clum A., Dunn C., O'Malley R., Figueroa-Balderas R., Morales-Cruz A. 2016. Phased diploid genome assembly with single-molecule real-time sequencing. *Nature methods*, 13 (12), 1050.
- [7] Cantarel B. L., Korf I., Robb S. M., Parra G., Ross E., Moore, B., Holt, C., Alvarado A. S., Yandell M. 2008. MAKER: an easy-to-use annotation pipeline designed for emerging model organism genomes. *Genome research*, 18 (1), 188-196.
- [8] Altschul, S. F., Madden, T. L., Schäffer, A. A., Zhang, J., Zhang, Z., Miller, W., Lipman, D. J. 1997. Gapped BLAST and PSI-BLAST: a new generation of protein database search programs. *Nucleic acids research*, 25 (17), 3389-3402.
- [9] Wu S., Zhu Z., Fu L., Niu B., Li W. 2011 WebMGA: a customizable web server for fast metagenomic sequence analysis. *BMC genomics*, 12 (1), 444.
- [10] Moriya, Y., Itoh, M., Okuda, S., Yoshizawa, A. C., Kanehisa, M. 2007 KAAS: an automatic genome annotation and pathway reconstruction server. *Nucleic acids research*, 35 (suppl\_2), W182-W185.
- [11] Campbell, J. W., Morgan-Kiss R. M., E. Cronan Jr, J. 2003. A new *Escherichia coli* metabolic competency: growth on fatty acids by a novel anaerobic  $\beta$ -oxidation pathway. *Molecular microbiology*, 47 (3), 793-805.
- [12] Peralta-Yahya P. P., Zhang F., Del Cardayre S. B., Keasling J. D. 2012 Microbial engineering for the production of advanced biofuels. *Nature*, 488 (7411), 320.
- [13] Hohmann S. 2009. Control of high osmolarity signalling in the yeast *Saccharomyces cerevisiae*. *FEBS letters*, 583 (24), 4025-4029.
- [14] Pearson G., Robinson F., Beers Gibson T., Xu B.-e., Karandikar M., Berman K., Cobb M. H. 2001. Mitogen-activated protein (MAP) kinase pathways: regulation and physiological functions. *Endocrine reviews*, 22 (2), 153-183.
- [15] Driver T., Trivedi D. K., McIntosh O. A., Dean A. P., Goodacre R., Pittman J. K. 2017. Two glycerol-3-phosphate dehydrogenases from *Chlamydomonas* have distinct roles in lipid metabolism. *Plant physiology*, pp. 00491.2017.
- [16] Papadopoulos M. C., Sun X. Y., Cao J., Mivechi N. F., Giffard R. G. 1996. Over-expression of HSP-70 protects astrocytes from combined oxygen-glucose deprivation. *Neuroreport*, 7 (2), 429-432.
- [17] Mayer M., Bukau B. 2005. Hsp70 chaperones: cellular functions and molecular mechanism. *Cellular and molecular life sciences*, 62 (6), 670.



- [18] Li S. C., Kane P. M. 2009. The yeast lysosome-like vacuole: endpoint and crossroads. *Biochimica et Biophysica Acta (BBA)-Molecular Cell Research*, 1793 (4), 650-663.
- [19] Bien C. M., Espenshade P. J. 2010. Sterol regulatory element binding proteins in fungi: hypoxic transcription factors linked to pathogenesis. *Eukaryotic cell*, 9 (3), 352-359.
- [20] Djurišić A B, Leung Y H, Ng A M, et al. 2015. Toxicity of Metal Oxide Nanoparticles: Mechanisms, Characterization, and Avoiding Experimental Artefacts. *Small* 11(1),26-44.
- [21] Baek Y.W., An Y.J. 2011. Microbial toxicity of metal oxide nanoparticles (CuO, NiO, ZnO, and Sb<sub>2</sub>O<sub>3</sub>) to *Escherichia coli*, *Bacillus subtilis*, and *Streptococcus aureus*. *Sci. Total. Environ.*, 409, 1603-1608.
- [22] Kim, J.S., Kuk, E., Yu K.N., Kim, J.H., Park, S.J., Lee, H.J., Kim, S.H., Park, Y.K., Hwang, C.Y., Kim, Y.K., Lee, Y.S., Jeong, D.H., Cho, M.H. 2007. Antimicrobial effects of silver nanoparticles. *Nanomed-Nanotechnol* 3, 95-101.
- [23] Tamboli D.P., Lee Dae S. 2013. Mechanistic antimicrobial approach of extracellularly synthesized silver nanoparticles against gram positive and gram negative bacteria. *J. Hazard. Mater.* 260, 878-884.
- [24] Arakha M, Pal S, Samantarrai D, et al. 2015. Antimicrobial activity of iron oxide nanoparticle upon modulation of nanoparticle-bacteria interface. *Scientific Reports*, 5:14813.
- [25] Abramenko N.B., Demidova T.B., Abkhalimov E.V., et al. 2017. Ecotoxicity of different-shaped silver nanoparticles: Case of zebrafish embryos. *J. Hazard. Mater.*, 347:89.
- [26] Kasemets, K., Ivask, A., Dubourguier, H.C., Kahru, A. 2009. Toxicity of nanoparticles of ZnO, CuO and TiO<sub>2</sub> to yeast *Saccharomyces cerevisiae*. *Toxicol. In Vitro*, 23,1116-1122.
- [27] Khan, M., Lo I.M.C. 2017. Removal of ionizable aromatic pollutants from contaminated water using nano  $\gamma$ -Fe<sub>2</sub>O<sub>3</sub> based magnetic cationic hydrogel, sorptive performance, magnetic separation and reusability. *J. Hazard. Mater.* 322, 195-204.
- [28] Yang Y., Ren S., Zhang X., Yu Y., Liu C., Yang J., Miao L. 2018. Safety and efficacy of PLGA (Ag-Fe<sub>3</sub>O<sub>4</sub>)-coated dental implants in inhibiting bacteria adherence and osteogenic inducement under a magnetic field, *Int. J. Nanomed.* 13, 3751-3762.
- [29] Peng S., Gao F., Zeng D., Peng C., Chen Y., Li M. 2018. Synthesis of Ag-Fe<sub>3</sub>O<sub>4</sub> nanoparticles supported on polydopamine-functionalized porous cellulose acetate microspheres: catalytic and antibacterial applications, *Cellulose*, 25, 4771-4782.
- [30] Zhang L, Zhou L, Li Q X, et al (2018). Toxicity of lanthanum oxide nanoparticles to the fungus *Moniliella wahieum* Y12<sup>T</sup> isolated from biodiesel. *Chemosphere*, 199:495-501.
- [31] Berean K. J., Adetutu E.M., Ou J.Z., Nour M., Nguyen E.P., Paull D., ... Bishop-Hurley G.J. 2015. A unique in vivo approach for investigating antimicrobial materials utilizing fistulated animals, *Sci. Rep.*, 5 11515.
- [32] Sun, X., Shi, J., Zou, X., Wang, C., Yang, Y., Zhang, H. 2016. Silver nanoparticles interact with the cell membrane and increase endothelial permeability by promoting VE-cadherin internalization. *J. Hazard. Mater.*, 317, 570-578.
- [33] Prabhu S., Poulouse E.K. 2012. Silver nanoparticles: mechanism of antimicrobial action, synthesis, medical applications, and toxicity effects. *International Nano Letters* 2, 32.

- [34] Shrivastava, S., Bera, T., Roy, A., Singh, P., Ramachandrarao, D. 2007. Characterization of enhanced antibacterial effects of novel silver nanoparticles. *Nanotechnology*, 18, 225103-225112.
- [35] Zheng X., Y. Su, Y. Chen, R. Wan, M. Li, H. Huang, X. Li. 2016. Carbon nanotubes affect the toxicity of CuO nanoparticles to denitrification in marine sediments by altering cellular internalization of nanoparticle, *Sci. Rep.* 6, 27748.
- [36] Vilela P, Liu H, Lee S C, et al 2018. A systematic approach of removal mechanisms, control and optimization of silver nanoparticle in wastewater treatment plants. *Sci. Total. Environ.*, 633, 989-998.
- [37] Shang L., Nienhaus K., Nienhaus G.U. 2014. Engineered nanoparticles interacting with cells: size matters. *J. Nanobiotechnol.*, 12, 5.
- [38] Rizwan M., Ali S., Qayyum M.F., Ok Y.S., Adrees M., Ibrahim M., Zia ur Rehman M., Farid M., Abbas F. 2017. Effect of metal and metal oxide nanoparticles on growth and physiology of globally important food crops: A critical review. *J. Hazard. Mater.*, 322,2-16.
- [39] Fabrega, J., Fawcett, S.R., Renshaw, J.C., Lead, J.R. 2009. Silver nanoparticle impact on bacterial growth: effect of pH, concentration, and organic matter. *Environ. Sci. Technol* 43:7285-7290.
- [40] Lopes, S., Pinheiro, C., Soares, A.M., Loueiro, S. 2016. Joint toxicity prediction of nanoparticles and ionic counterparts: Simulating toxicity under a fate scenario. *J. Hazard. Mater.*, 320, 1-9.
- [41] Metch J W, Burrows N D, Murphy C J, et al 2018. Metagenomic analysis of microbial communities yields insight into impacts of nanoparticle design. *Nature Nanotechnol* 13(3).
- [42] Leroueil, P.R., Hong, S., Mecke, A., Baker, J.R., Orr, B.G., Banaszak Holl, M.M. 2007. Nanoparticle interaction with biological membranes: does nanotechnology present a Janus face. *Accounts Chem. Res.*, 40, 335-342.
- [43] Kubo A L, Capjak I, Vrček I V, et al 2018. Antimicrobial potency of differently coated 10 and 50 nm silver nanoparticles against clinically relevant bacteria *Escherichia coli*, and *Staphylococcus aureus*. *Colloids & Surfaces B Biointerfaces* 170:401-410.

### 3.5 Oxygen-Enhanced Flash-Carbonization

Under this subtask the effects of processing conditions (closed versus open reactor, pressure, temperature, soaking time, biomass loading, heating rate and fuel particle size) on product yields and char properties from constant-volume carbonization were studied. Increasing the pretest, inert-gas, system pressure from 0 to 2.17 MPa did not significantly affect product yields or char proximate analysis results. Increasing the reaction time from 30 to 190 minutes and the temperature in a 300-550°C range improved fixed-carbon contents and reduced volatile matter while maintaining or slightly increasing the fixed-carbon yields. In contrast to flash-carbonization or

traditional carbonization observations where larger particles produce beneficial effects, constant-volume carbonization produced equal or higher fixed-carbon contents and yields from smaller biomass particles. This offers possibilities that smaller size, lower-grade biomass can be used to produce high, fixed-carbon yield charcoal. Under certain processing conditions, the particulate biomass underwent a transient plastic phase transition that produced a single solid piece of final char. Complete details can be found in the publication listed below including a discussion of the role of processing conditions in the formation of the transient plastic phase.

## **Publications and Presentations**

### *Peer Reviewed Publications*

1. Legarra, M., Morgan, T., Turn, S., Wang, L., Skreiberg, O., Antal, M. 2019. Effect of processing conditions on the constant volume carbonization of biomass. *Energy & Fuels*. 33, pp 2219-2235.

### *Conference Proceedings and Posters*

1. Arizaleta, M. S. Turn, T. Morgan, O. Skreiberg, L. Wang, M. Gronli. 2018. Carbonization of Biomass in Constant-Volume Reactors. Presented at Pyro2018, 22<sup>nd</sup> International Symposium on Analytical and Applied Pyrolysis. June 3-8, 2018. Kyoto, Japan.
2. Arizaleta, M., T. Morgan, S. Turn, O. Skreiberg, L. Wang. 2018. Manufacturing charcoal in sealed vessels. Presented at the 26th European Biomass Conference and Exhibition. May 14-17, 2018, Copenhagen, Denmark.
3. Arizaleta, M., T. Morgan, S. Turn, O. Skreiberg, L. Wang. 2018. Manufacturing charcoal in sealed vessels. Presented at the 255th American Chemical Society National Meeting. March 18-22, 2018, New Orleans, LA.

## **TASK 4: METHANE HYDRATES**

The Methane Hydrates activities under APRISES14 comprised four areas of focus: Hydrate Exploration, Hydrate Energy, Environmental Impacts of Methane Release from Hydrates, and International Collaborative R&D.

National R&D programs on methane hydrates were initiated in Japan and India in the mid-1990's with the goal of commercial gas production within a 20 year time horizon [1]. The U.S. established its own program in May 2000. The Methane Hydrate Research and Development Act of 2000

(Public Law 106-193) included seven technical areas of focus: (1) identification, exploration, assessment, and development of methane hydrate as a source of energy; (2) technology development for efficient and environmentally sound recovery of methane from hydrates; (3) transport and storage of methane produced from methane hydrates; (4) education and training related to methane hydrate resource R&D; (5) assessment and mitigation of environmental impacts of natural and purposeful hydrate degassing; (6) development of technologies to reduce the risks of drilling through methane hydrates; and (7) support of exploratory drilling projects.

The objectives of the Methane Hydrates Task of the APRISES initiative align closely with the priorities of P.L. 106-193, but emphasize those areas of particular relevance to the ONR and which are consistent with the overall goals of APRISES. Specifically, the development of hydrates and related sources of seafloor methane as logistical fuels for Naval applications, and related marine environmental issues, have been the principal areas of interest; exploratory drilling projects and seafloor stability/safety to date have received limited attention. Work also was performed to explore engineering applications of hydrates such as hydrogen fuel storage. Task objectives were devised to leverage fully the hydrate R&D expertise and infrastructure that had been developed at HNEI during previous research programs on CO<sub>2</sub> ocean sequestration and deep oil spills.

For APRISES14, the goals of the Methane Hydrates Task were to:

- Support development of tools to identify hydrate reservoirs in seafloor sediments and arctic permafrost.
- Pursue development of practicable methods to recover methane gas from hydrates.
- Investigate environmental impacts of methane hydrates on the marine environment.
- Promote international collaborative research on methane hydrates.

Specific technical initiatives that were pursued to attain the above goals included:

- Investigate methods to map seafloor methane hydrate reservoirs and estimate the volume of gas-in-place contained in these reservoirs based on 3D seismic profiles and borehole data.
- Continue laboratory experiments on hydrate destabilization by chemical inhibitors.
- Conduct benchtop experiments to investigate microbial degradation of methane and heavier hydrocarbons in marine and estuarine environments.
- Organize the 10<sup>th</sup> International Workshop of Methane Hydrate R&D.

Technical accomplishments for each of the four areas of emphasis are described below.

## Detection of Seafloor Methane Hydrate

Currently, there are no unambiguous methods to detect the location and extent of methane hydrate deposits in the seafloor sediment. Bottom simulating reflections (BSRs) appearing in seismic surveys are considered to be the best indicators of the presence of gas hydrates. Despite several decades of research, the nature of BSRs including their occurrence, distribution patterns, amplitude strength, continuity, and phase characteristics continues to present a challenge to seismic interpretations.

In an effort to address this shortcoming, we analyzed three-dimensional seismic data collected previously during surveys of the Kumano Forearc Basin in the Nankai Trough, offshore of the Kii Peninsula, Japan, which is located ~100 km southwest of the Daini Atsumi Knoll. The Daini Atsumi Knoll is the site of the first offshore gas hydrate production trial [1]. These seismic records were interpreted using borehole data to map the hydrate reservoir and estimate the volume of methane gas-in-place. The results of this analysis were published in a peer-review journal [2]. A succinct summary of these results is provided below. Complete details can be found in a publication by Taladay *et al.* [2] which is posted on the HNEI website.

Seismic imaging is an important tool for identifying gas hydrate (GH) because both GH and free gas alter the physical properties of marine sediments, which will, in turn, affect the travel path and attenuation of the seismic wavelet [3–5]. Concentrated hydrate deposits tend to form at and just above the base of the GH stability zone (BGHS) in the seafloor sediment. At depths below this base, the geothermal gradient results in temperatures that melt the hydrate. A sharp change occurs in sediment mechanical properties at the phase boundary between GH saturated layers overlying a zone where free gas, water, and potentially non-cementing hydrate occupy the pore space [6]. This discontinuity in physical properties is expressed in seismic data as BSRs, and BSRs remain our strongest remotely sensed indicator to infer the presence of gas hydrate [7]. Constraints from wells and pressure core samples are essential checks to confirm the presence of hydrates and to estimate the amount of gas present in a hydrate reservoir [8].

The present study employed high-resolution, three dimensional seismic reflection data combined with Integrated Ocean Drilling Program (IODP) borehole data collected through the Kumano Basin offshore of the Kii Peninsula, Japan, to: (1) identify and map potential zones of concentrated gas hydrate; and (2) calculate a volumetric gas-in-place estimate for these newly mapped reservoirs using constraints from the borehole data. It is the first study of its kind for this region.

Gas proxies were identified beneath the main BSR observed in the seismic records of the site, which allowed us to infer the gas migration mechanisms in the basin. Gas charged fluids are believed to migrate into basin sediments from anticlinal features in the underlying accretionary prism and move through the sediments as diffuse fluid flow which updip permeable sands

sandwiched by less permeable clays. This occurs episodically through faults and fractures and through gas hydrate recycling following perturbation to the BGHS from uplift and rapid sedimentation. Clear signs of active fluid advection were not indicated by the current BSR character. Given the previously published geochemical data, and our observed seismic indicators in lower basin sediments, it is likely that deep fluids are episodically charging the two zones of concentrated gas hydrate deposits identified above the primary BSR. Hydrate recycling at the BSR is also evidenced by closely stacked BSRs in the center of the basin. A thick GH layer acting as a seal for gas below provides a trap for gas to accumulate and then later be incorporated into new GHs following perturbations to the base of hydrate stability conditions.

Our analysis of the seismic records and borehole data indicate that there is a high probability of two distinct zones of concentrated gas hydrate which are 10–90 m thick. We estimate that the amount of gas-in-place potentially locked up in these reservoirs is 1.9–46.3 trillion cubic feet with a preferred estimate of 15.8 trillion cubic feet.

## **Hydrate Energy**

Practicable and environmentally acceptable methods to destabilize hydrate reservoirs in seafloor sediments and arctic permafrost must be developed in order to release and collect the methane gas for energy applications. Hydrate destabilization strategies also are of critical importance to the operation of natural gas transport pipelines, which are vulnerable to blockage by solid hydrate plugs. Under prior ONR awards, significant progress was made by HNEI in elucidating the mechanisms by which various chemical reagents destabilize pure methane hydrate [9-11].

For APRISES14, we continued our experimental studies of hydrate destabilization by reagent injection. Specifically, we focused on extending the earlier work by Kinoshita [9] which quantified the effectiveness of various alcohols and a diol in destabilizing methane hydrate. By application of Mobile Order Thermodynamics Theory, Kinoshita [9] and Nihous *et al.* [10], we're able to explain the observed effectiveness of these reagents based on induced changes in the activity of water. They posited that the addition of alcohols and glycols causes hydrate decomposition by binding to water molecules in the quasi-liquid layer on the solid hydrate surface. This disrupts the dynamic equilibrium between hydrate decomposition and re-crystallization. It was proposed that the activity of water decreased (which results in a reduction in hydrate destabilization effectiveness) with increasing alkyl group size and decreasing number of hydroxyl groups.

Experiments were performed to test Kinoshita's hypothesis by investigating the effectiveness of glycerol to decompose methane hydrate. Glycerol is a triol (i.e., has three hydroxyl groups) with a relatively large alkyl group. It is produced industrially in large quantities and is non-toxic. This makes it an attractive alternative to conventional hydrate inhibitors such as methanol.

The primary accomplishment under this task was completion of an experimental study to determine the effectiveness of glycerol solutions to destabilize methane hydrate. At the time that this report was written, a manuscript was being prepared for submittal for publication in a peer review journal. A summary of key findings follows.

Glycerol (Propane-1,2,3-triol;  $C_3H_8O_3$ ; MW = 92.02 g/mol) is produced in relatively large quantities from plant and animal sources. It is not toxic and is used extensively in the food industry and in medical and personal care products. Glycerol is a waste product of biodiesel production. Overproduction of glycerol has resulted in its very low price: over the past few years, crude glycerol price has remained well less than 1 U.S. \$/kg.

Glycerol is a triol with three hydroxyl groups. The structure of glycerol is shown in Figure 4.1.

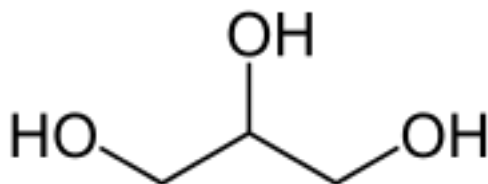


Figure 4.1. Glycerol structure.

On the basis of its low cost and excellent toxicity profile, glycerol presents itself as an attractive alternative to alcohols and diols which have been employed by the oil and gas industry to prevent hydrate blockage of natural gas pipelines. Its effectiveness as a hydrate inhibitor, however, has not been assessed. Toward this end, benchtop experiments were performed, following the previously-reported methods developed by at HNEI by Kinoshita [9], in which solutions of glycerol were injected at elevated pressure onto methane hydrate samples in a Calvet-Tien calorimeter.

Figure 4.2 presents a schematic diagram of the experimental facility. Methane hydrate was formed in the sample cell of a Setaram BT2.15 calorimeter at a constant pressure of 7.00 MPa (1000 psi).

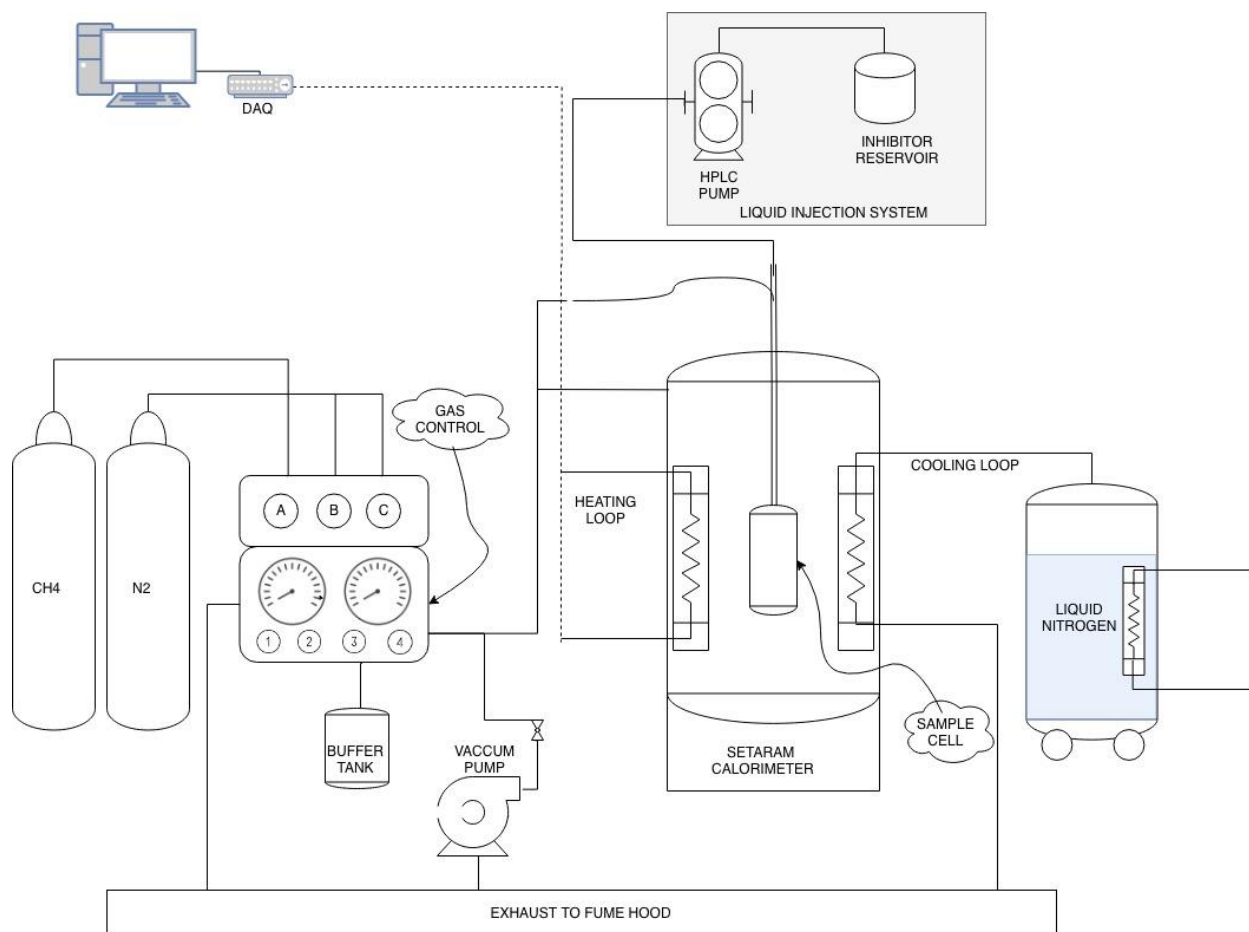


Figure 4.2. Schematic diagram of the experimental facility.

A typical thermogram of the hydrate synthesis process, which includes the temperature history of the sample and measured heat flow, is shown in Figure 4.3.

Unlike the alcohols and diol tested previously, at ambient pressure, pure glycerol exists as a solid at temperatures below approximately 17.8°C. Increasing pressure to keep the glycerol from freezing at temperatures where methane hydrate is stable was not an option, since these pressures exceeded the 10.4 MPa upper operating limit of the calorimeter. In order to be able to inject glycerol as a liquid into the calorimeter sample cell with our HPLC (High Performance Liquid Chromatography) pump, the only feasible alternative was to dissolve the glycerol in water. Doing this, however, complicates interpretation of the results, since the activity of the water component of the aqueous glycerol solution would have to be accounted for in effectiveness calculations.

An additional problem emerged during trial tests when it was determined that, with the exception of dilute solutions, the viscosity of the glycerol-water mixtures was excessively high at low temperatures (e.g., <~15°C). The HPLC pump was unable to operate at these high levels of fluid



viscosity. The solutions were therefore injected at 25 °C, which was about 20 °C higher than the sample temperature. The associated thermal energy input of the warm fluid was estimated and subtracted from the total energy absorbed by the sample which was measured with the calorimeter during the injection process.

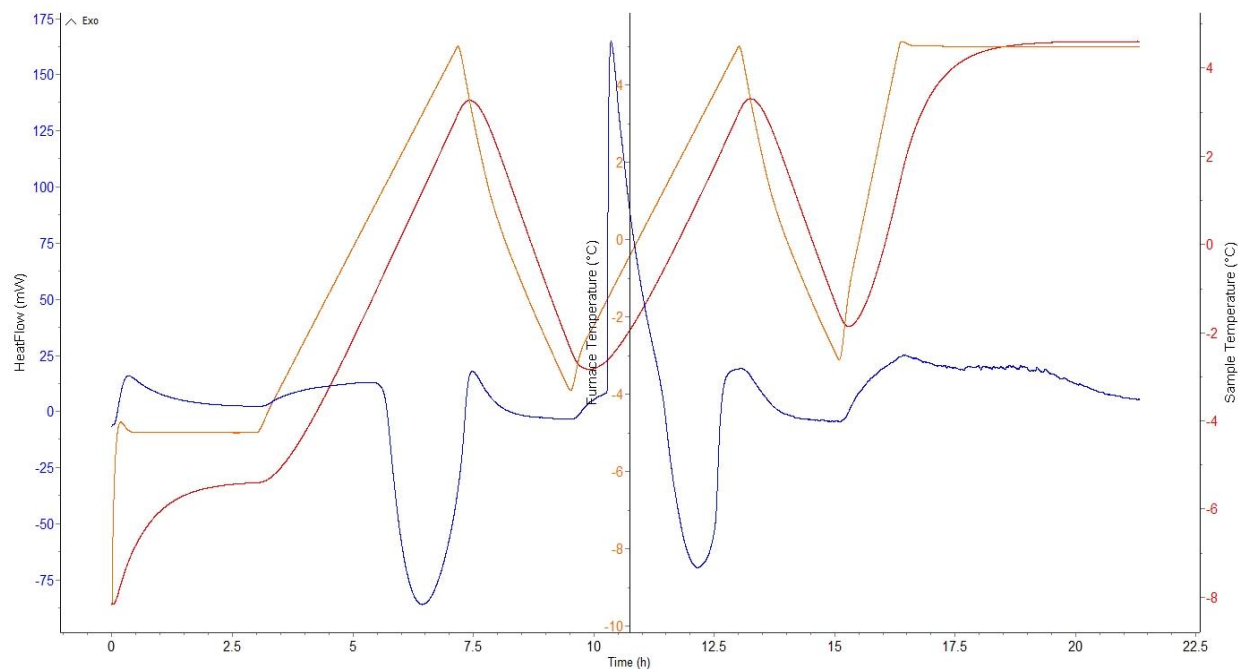


Figure 4.3. Thermogram of hydrate synthesis process. Orange line is the calorimeter furnace temperature; red line is the sample temperature; blue line is the measured heat flow to/from the sample. During the hydrate synthesis process, temperature is cycled repeatedly above and below the freezing point of water.

It was decided to employ glycerol-water mixtures of 50% and 80% glycerol by mass in these experiments. The masses of reagent grade glycerol and distilled water were determined with an analytical balance and combined in a beaker. A programmable HPLC pump was used to inject small volumes of these solutions onto the methane hydrate in the calorimeter sample cell. A detailed description of the experimental methods can be found in Kinoshita [9].

Figure 4.4 shows a representative thermogram of the reagent injection/hydrate destabilization process. In this test, 50 w% glycerol solution was injected and the sample energy transfers were monitored for about four hours. During this period, the temperature of the sample was maintained at a nearly constant value; temperature varied by less than 0.1 °C. The sharp negative peak in the heat flow record indicates energy being absorbed by the sample in mW. The yellow area in the figure corresponds to the total amount of energy that was absorbed.

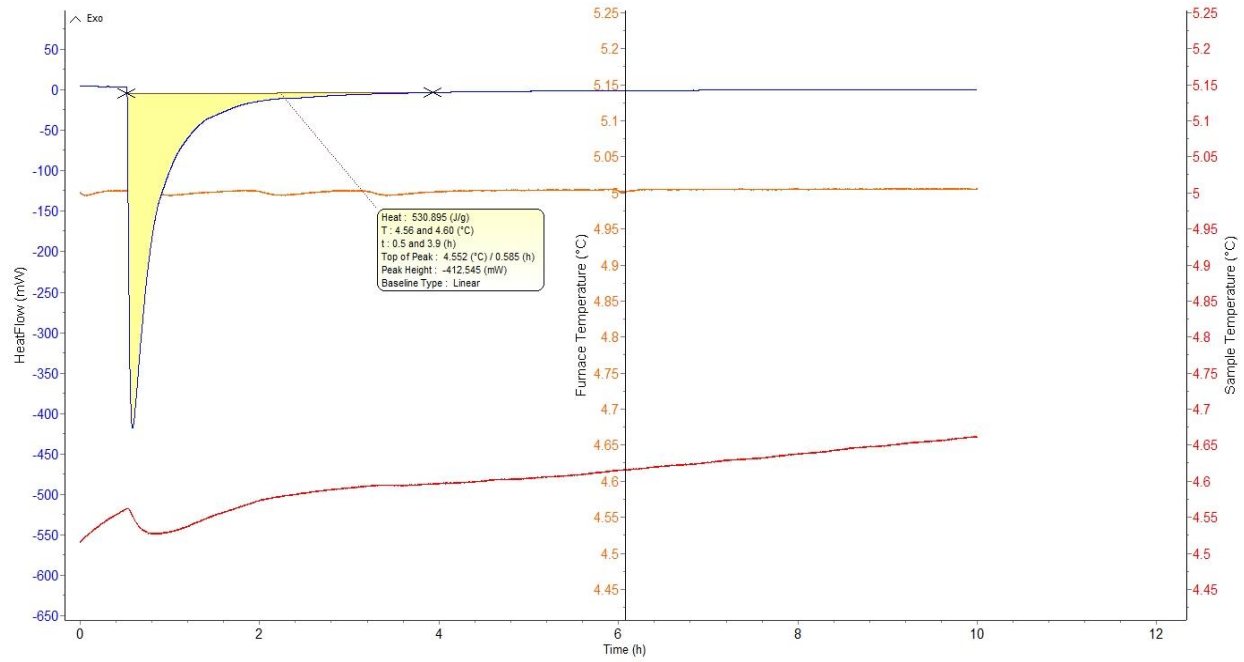


Figure 4.4. Thermogram of 50 wt% glycerol-water solution injection onto methane hydrate held at 5 °C and 7.0 MPa. Orange line is the calorimeter furnace temperature; red line is the sample temperature; blue line is the measured heat flow [mW] to/from the sample. The yellow area represents the total energy absorbed by the sample during this process.

The measured thermal energy absorbed by the sample comprises three primary components: 1) heating of the sample due to non-isothermal injection (i.e., energy absorbed to cool the 25 °C glycerol solution to the sample temperature of about 4.55 °C); 2) energy released as a result of mixing of produced water (due to hydrate dissociation) with glycerol; and 3) energy absorbed as solid hydrate dissociates by contact with glycerol. The non-isothermal injection component was estimated using the following equation:

$$\text{Energy due to non – isothermal injection} = C_{p(50w.\% \text{ glycerol})} \times (\Delta T) \quad (4.1)$$

Where  $\Delta T$  = Injection temperature of the glycerol solution – Sample temperature, and the heat capacity of 50 wt% glycerol-water solution was estimated by extrapolating the property data [12] shown in Figure 4.4. Similar property data exist for the 80 wt% case.

The energy of mixing was estimated using the approach employed previously by Kinoshita [9]:

$$\text{Energy of Mixing} = f(X_{final}) - f(X_{initial}) = \text{mol} \times (h_{final} - h_{initial}) \quad (4.2)$$

Where  $h$ , the enthalpy of solution per mole of glycerol, is a function of the molar ratio  $X$  of glycerol to water and is obtained by extrapolating the data in Figure 4.5.

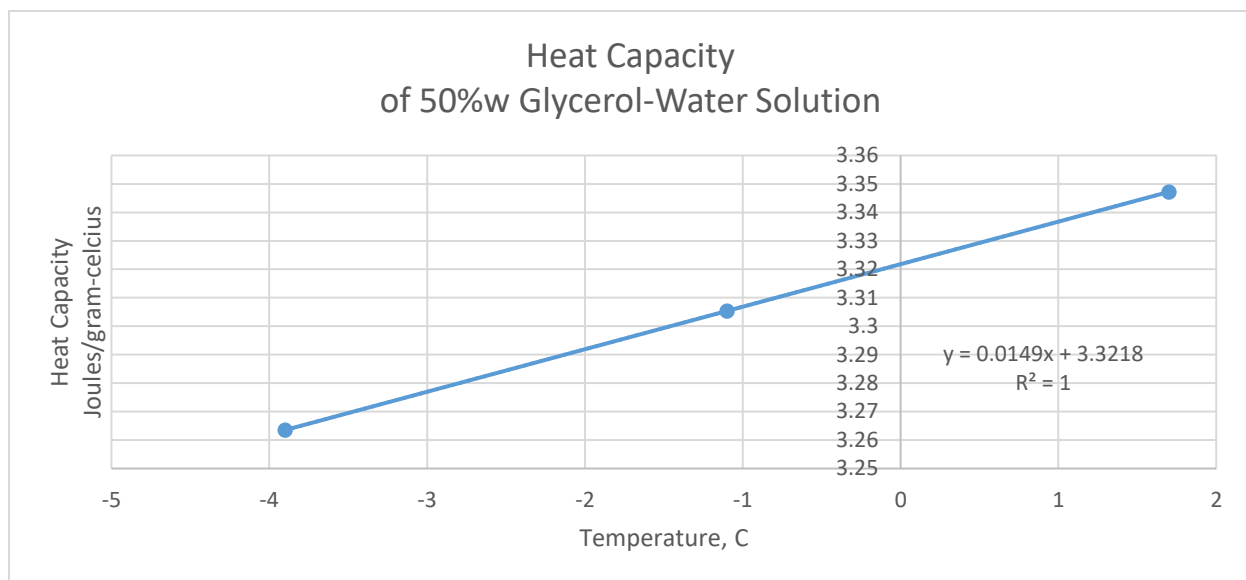


Figure 4.5. Heat capacity of 50 wt% glycerol-water solution. Data from “Physical Properties of Glycerin and its Solutions” [12].

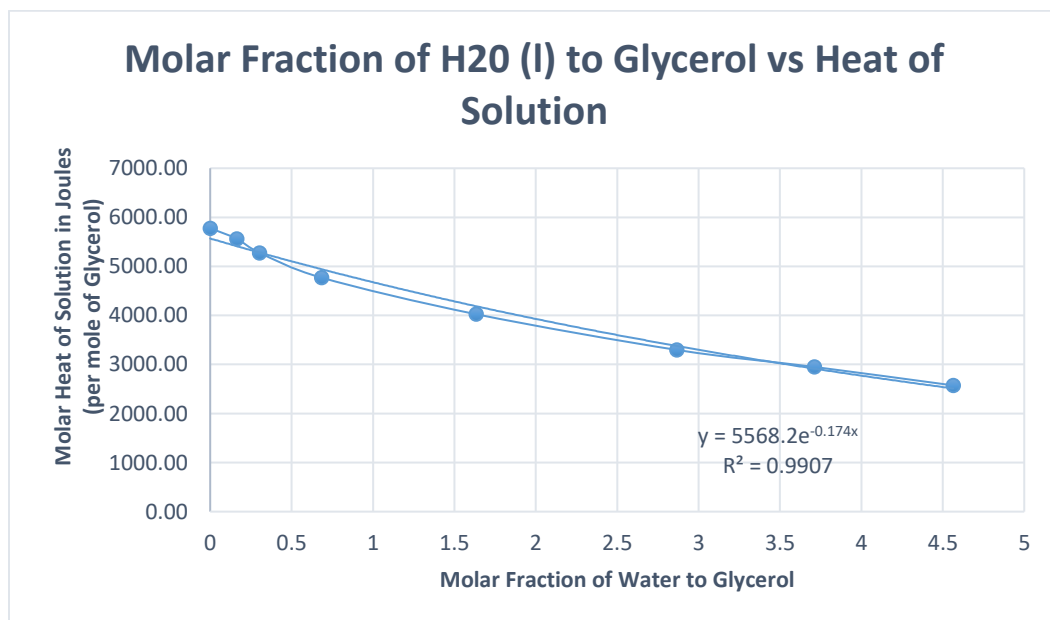


Figure 4.6. Enthalpy of solution as a function of molar fraction of H<sub>2</sub>O to glycerol. Data from “Physical Properties of Glycerin and its Solutions” [12].

By application of equations 4.1 and 4.2, the heat flows associated with non-isothermal injection and mixing of produced water were estimated and subtracted from the calorimeter data. The resulting value, hereinafter referred to as the Destabilization Energy Fraction, is assumed to be the energy absorbed to dissociate a portion of the hydrate sample. The total number of moles of methane hydrate that decomposed is then determined by:

$$M_{hydrate} = \text{Destabilization Energy Fraction} / h_{dissociation} \quad (4.3)$$

Here,  $M_{hydrate}$  is the number of moles of hydrate that dissociates due to contact with glycerol and  $h_{dissociation}$  is the molar enthalpy of dissociation. In this study we employed the value of  $h_{dissociation} = 54,490 \text{ J/mol}$  reported by Ota *et al.* [13].

Unfortunately, the relationship for the energy of mixing (Equation 4.2) requires the amount of produced water from hydrate dissociation, so the system of equations (4.1-4.3) must be solved implicitly.

Table 4.1 provides preliminary results from the glycerol injection experiments.

Table 4.1 Effectiveness of Glycerol to Decompose Methane Hydrate.

Glycerol weight%	Mass of H <sub>2</sub> O in Sample (g)	Mass of Injected Glycerol Solution (g)	Heat Absorbed by Sample (J)	Mol Glycerol Injected Ng	Mol Hydrate Dissociated Nh	Effectiveness (Nh/Ng)
80%	2.000	1.581	536.9	0.0137	0.0148	1.08
80%	1.826	1.396	622.8	0.0121	0.0136	1.12
50%	2.356	1.113	478.6	0.00604	0.0103	1.70
50%	2.206	1.709	719.1	0.00928	0.0148	1.60

The data suggest that aqueous solutions of glycerol are effective at dissociating hydrates. To provide some context, Kinoshita [9] estimated the effectiveness of ethylene glycol (diol), methanol, ethanol, and 2-propanol to be approximately 0.92, 0.71, 0.58, and 0.11, respectively.

The reason for the increase in effectiveness as the concentration of glycerol decreases is not clear, but may be related to changes in the activity of the water phase. Analysis of the present data using Mobile Order Thermodynamics is ongoing. When this is completed, the results will be submitted for publication in a peer review journal.

### Environmental Impacts of Methane Release from Hydrates

The presence of hydrocarbons, including methane, are known to stimulate biological activity

within the ocean water column [14-16]. To advance our understanding of the metabolic processes associated with natural and accidental hydrocarbon release in marine and estuarine environments, microbiological community determinations in seawater were performed during APRISES14.

Sequencing of microbial community DNA using Next-Generation Sequencing techniques (NGS) allow for rapid assessments of biodiversity. These metagenomic studies increase the sensitivity of detection and allow for the identification of species that would be overlooked using traditional methods. Moreover, NGS can be utilized to detect the presence of functional genes. The combination of functional genomics along with community information provide insight into biogeochemical processes [17].

For this investigation, surface seawater was collected at the Ala Wai Boat Harbor in Honolulu, Hawaii. The harbor waters are already influenced by hydrocarbons and likely have an indigenous biological community with bio-degradation capabilities. The indigenous biological communities in the collected seawater were enriched with either: 1) B-100 biodiesel; 2) F76 diesel; or 3) crude oil from the Texas-Louisiana shelf in the Gulf of Mexico that was mixed with 1.5% v/v Corexit 9500 surfactant. The enriched seawater and controls were periodically sampled, and the biological communities were determined after DNA extraction and Illumina NGS.

Table 4.2 presents a summary of the experimental results. These results are estimates of the total phylogeny and represent only a 5% subsample. Geneious<sup>TM</sup> software was used for the phylogenetic determinations. The incubation period for the experiment was 28 days. The biodiesel results are reported on the 14<sup>th</sup> day when the maximum reduction of hydrocarbon was observed. Populations exhibiting an increase in percentage compared with the controls are highlighted in yellow.

Community comparisons focused on the Alpha and Gammaproteobacteria classes of bacteria. Hydrocarbon and oxygen-dependent methane oxidation are often associated with microorganisms included within these two classes of Proteobacteria [18, 19]. As seen in Table 4.2, Proteobacteria comprise greater than 93% of the total bacteria detected in the hydrocarbon containing samples, compared to only 78% in the controls. Bacteroides also were determined to constitute a significant portion of the community and are known to have hydrocarbon degradation metabolisms [20]. Bacteroides levels were found to be lower in the enriched samples than in the controls. The Alphaproteobacteria community in samples with added hydrocarbons were significantly elevated while the Gammaproteobacterial population decreased when biodiesel was added, but was largely unaffected by the presence of diesel fuel and crude oil.

During the 2010 Deepwater Horizon oil spill in the Gulf of Mexico, large quantities of Corexit 9500 dispersant was applied both on the surface and directly to the contaminant plume issuing from the broken riser at 1500 m depth. It subsequently was determined that populations of Oceanospiralles, Rhodobacterales, Pseudoalteromonas, and some other species increased

significantly over baseline values [21]. In the present study, adding crude oil and Corexit to the Ala Wai seawater appeared to have a similar—albeit less dramatic--effect: the relative percentage of these organisms increased above levels measured in the final controls, but were only modestly elevated over levels in the initial controls.

As mentioned previously, the Ala Wai Boat Harbor suffers from a constant presence of petroleum hydrocarbons. The relatively high percentages of Oceanospiralles, Rhodobacterales, and Pseudoalteromonas found in the initial controls may reflect a biological adaptation to hydrocarbons that are chronically present in that environment. In addition to the Rhodobacterales Oceanospiralles orders whose populations increased relative to the final (incubated) seawater control samples, elevated levels of *Hyphomonadaceae* and the *Rhodospirillaceae* families were detected in seawater with added crude oil. Both of these families of microbes have been associated with crude oil degradation [22, 23]. While Sphingomondales also may have hydrocarbon degradation capabilities [24], they were not detected in the crude oil seawater samples, but were identified in the other test samples.

Table 4.2 Distribution of Proteobacteria in seawater after enrichment with different hydrocarbons.

Seawater Initial	Seawater Final	Biodiesel Final (after 14 days)	Diesel Final	BP-Crude oil with Corexit
<b>Proteobacteria – 75%</b>	<b>Proteobacteria – 78%</b>	<b>Proteobacteria – 96%</b>	<b>Proteobacteria – 93%</b>	<b>Proteobacteria-93%</b>
<b>Alphaproteobacteria – 26%</b>	<b>Alphaproteobacteria – 38%</b>	<b>Alphaproteobacteria – 58%</b>	<b>Alphaproteobacteria – 54%</b>	<b>Alphaproteobacteria- 60%</b>
	Sphingomonadales – 0.9%	Sphingomonadales – 3%	Sphingomonadales – 2%	
	Sphingomonadaceae- 0.6%	Sphingomonadaceae – 2%	Sphingomonadaceae – 1%	
Rhodobacterales – 26%	Rhodobacterales – 14%	Rhodobacterales – 10%	Rhodobacterales – 21%	Rhodobacterales-19%
Rhodobacteraceae – 15%	Rhodobacteraceae 14%	Rhodobacteraceae – 10%	Rhodobacteraceae – 21%	Rhodobacteraceae-19%
Rhodospirillales – 8%	Rhodospirillales – 14%	Rhodospirillales – 24%	Rhodospirillales – 19%	Rhodospirillales- 20%
Rhodospirillaceae – 7%	Rhodospirillaceae – 12%	Rhodospirillaceae – 24%	Rhodospirillaceae – 19%	Rhodospirillaceae- 20%
		Caulobacteriales 18%		Caulobacteriales-19%
		Hyphomonadaceae-17%		Hyphomonadaceae-19%
<b>Gammaproteobacteria – 45%</b>	<b>Gammaproteobacteria – 37%</b>	<b>Gammaproteobacteria – 25%</b>	<b>Gammaproteobacteria – 36%</b>	<b>Gammaproteobacteria-33%</b>
Pseudomonadales – 0.9%	Pseudomonadales – 0.6%	Pseudomonadales – 2%	Pseudomonadales – 0.3%	Pseudomonadales- 2%
Pseudomonadaceae – 0.9%	Pseudomonadaceae 0.6%	Pseudomonadaceae – 1%	Pseudomonadaceae – 0.3%	
Oceanospirillales – 18%	Oceanospirillales – 6%	Oceanospirillales – 5%	Oceanospirillales – 5%	Oceanospirillales- 19%
Alcanivoracaceae – 0.2%	Oceanospirillaceae – 1%	Alcanivoracaceae – 0.2%	Alcanivoracaceae – 0.6%	Oceanospirillaceae-19%
Oceanospirillaceae – 14%		Oceanospirillaceae – 4%	Oceanospirillaceae – 4%	
Alteromonadales – 11%	Alteromonadales – 10%	Alteromonadales – 14%	Alteromonadales – 11%	Alteromonadales- 11%
Alteromonadaceae – 10%	Alteromonadaceae – 9%	Alteromonadaceae – 6%	Alteromonadaceae – 10%	Alteromonadaceae-6%
		Pseudoalteromonadaceae-5%		Pseudoalteromonadaceae-3%
<b>Bacteroidetes</b>	<b>Bacteroidetes</b>	<b>Bacteroidetes</b>	<b>Bacteroidetes</b>	<b>Bacteroidetes</b>
Bacteroidetes – 9%	Bacteroidetes – 8%	Bacteroidetes – 2%	Bacteroidetes – 3%	Bacteroides 1%

The B-100 biodiesel has the most uniform composition and is the most susceptible to biodegradation [25]. B-100 contains linear hydrocarbons, and the fatty acid portion is easily metabolized by many microorganisms. Compared with the control seawater, the percentages of Sphingomonadales, Rhodospirillales, Caulobacteriales (which includes the *Hyphomonadaceae* family), Pseudomonadales, and Alteromonadales were elevated by the addition of biodiesel. In the diesel sample, Sphingomonadales, Rhodobacterales, and Rhodospirillales were enriched.

Diversity indices were determined using the National Institute of Health's Nephel platform [26]. The 16S amplicon data was analyzed with Napehele using the Mothur v1.40.5 pipeline and standard-setting [27]. Differences and changes in biological diversity were estimated using Shannon and Chao1 indices (Figure 4.6) and rarefaction (Figure 4.7). The Shannon index is commonly used to determine bacterial diversity based upon the operational taxonomic units (OTUs). Rarefaction and the Chao1 index are both measures of species richness [28].

The results from the Shannon Index suggest that the different incubations were similar in species richness and evenness based upon the observed OTUs; however, when comparing the results of the Chao1 index, which estimates species numbers based upon abundance, the diesel and crude oil enriched samples have greater biological diversity when compared with the biodiesel. This may reflect a competitive advantage by a smaller group of microorganisms that can rapidly utilize the biodiesel hydrocarbon. Many microorganisms have the potential to metabolize the fatty acid component of biodiesel [29]. The compositions of diesel and crude oil, on the other hand, are complex and contain recalcitrant aromatic hydrocarbons. The range of hydrocarbons and the potential need for specialized metabolisms would prompt the establishment of a more diverse biological community.

The observed changes in OTUs shown in Figure 4.7 are consistent with the Chao1 diversity results. The biodiesel enriched seawater had the least amount of OTUs and was the only hydrocarbon that reduced the diversity over the experimental period. Furthermore, the number of different OTUs was the lowest when compared with the other hydrocarbon-containing seawater samples.



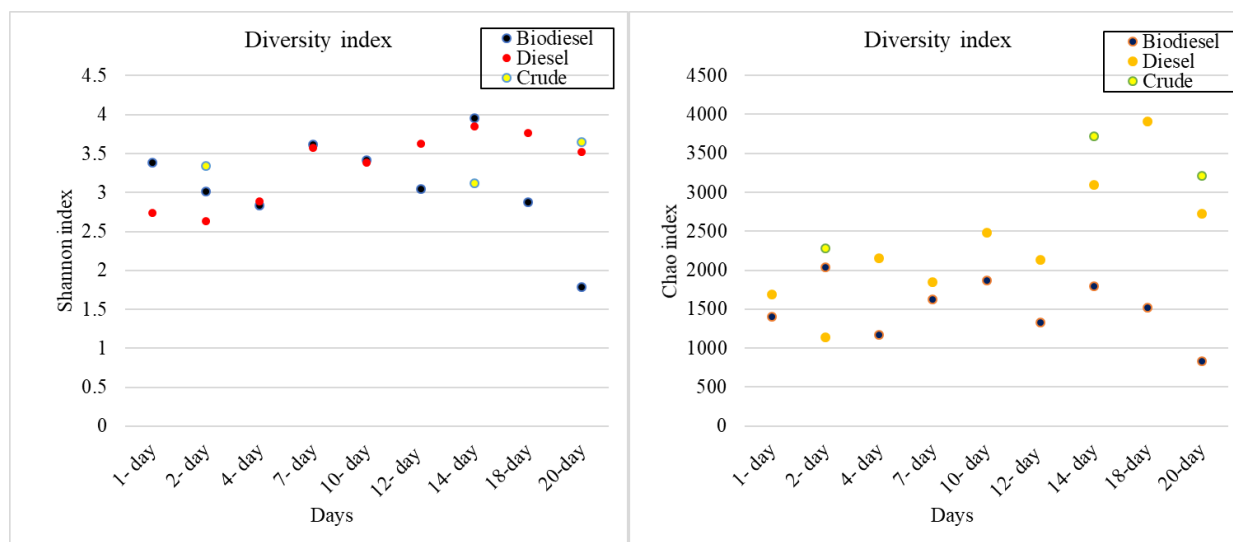


Figure 4.7. Seawater diversity indices for incubations using different hydrocarbons. The Shannon and Chao1 indices for the initial seawater were 3.3506 and 1624.9, respectively. The Shannon and Chao1 indices for the incubated seawater without hydrocarbon were 4.564 and 2178, respectively, after 20 days.

The results of a Principal Coordinates Analysis (PCoA) using binomial distances are shown in Figure 4.8. These results indicate that the established microbial communities in the hydrocarbon-supplemented seawater have become largely dissimilar when compared with the initial seawater control. Following incubation of the control, this difference persists, albeit to a lesser degree. The distances between the different seawater communities exposed to the hydrocarbons are distinct but more closely related. Among all the tested samples, the crude and diesel communities are the most related to the other.

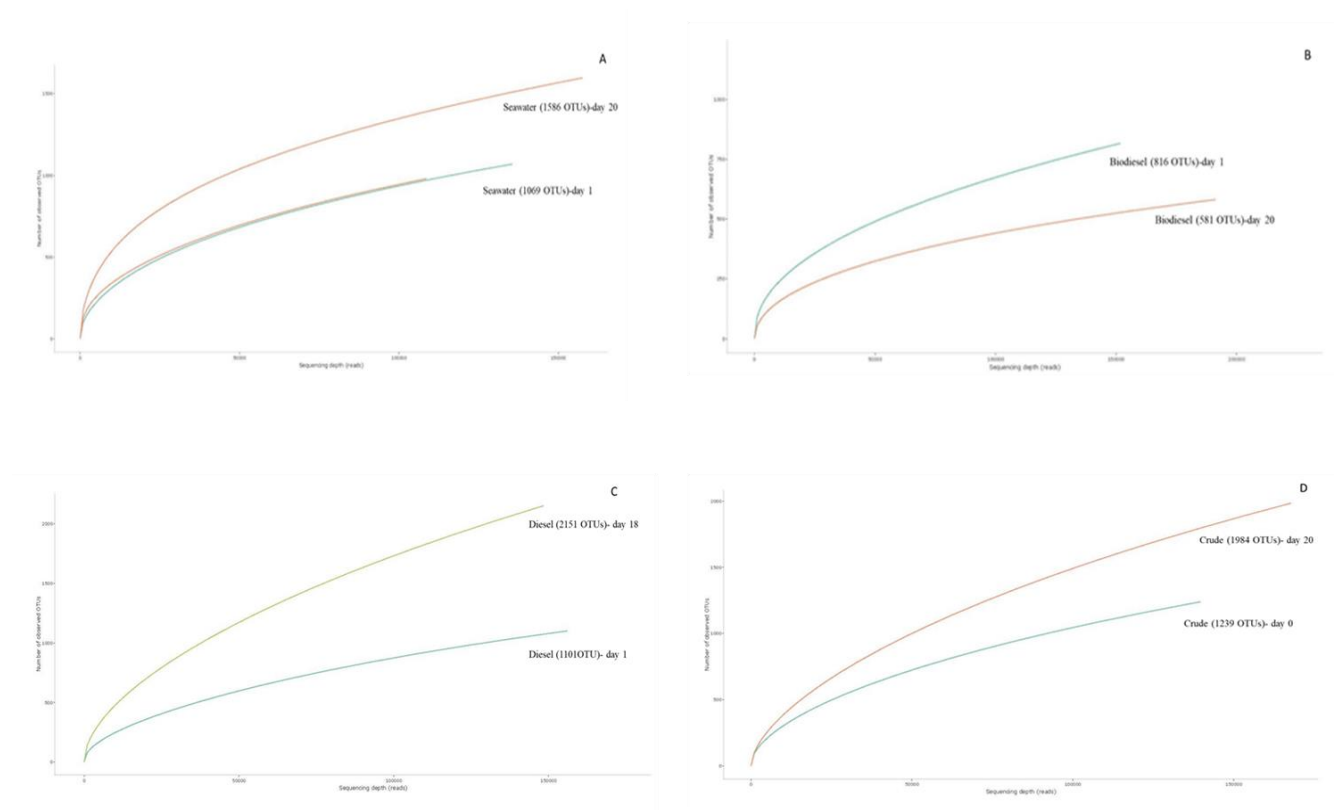


Figure 4.8. Rarefaction curves showing the changed diversity in seawater upon exposure to the different hydrocarbons. Maximum changes in OTUs are shown: A) Seawater- 1069, 1586 OTUs B) Biodiesel- 816, 581 OTUs C) Diesel 1101, 2151 OTUs D) Crude-1239, 1984 OTUs.

The present investigation provides insight into the seawater microbial communities that develop when different types of hydrocarbons are metabolically available. Diesel consists largely of aliphatic and aromatic hydrocarbons, while biodiesel is composed of long-chain alkyl esters made from fatty acids and generally includes no aromatics nor sulfur. The PCoA analysis shows that the diesel and crude oils have communities that are more closely related, likely due to the presence of microorganisms that can also utilize aromatics. The distributions of Proteobacteria, however, suggest distinct compositions.

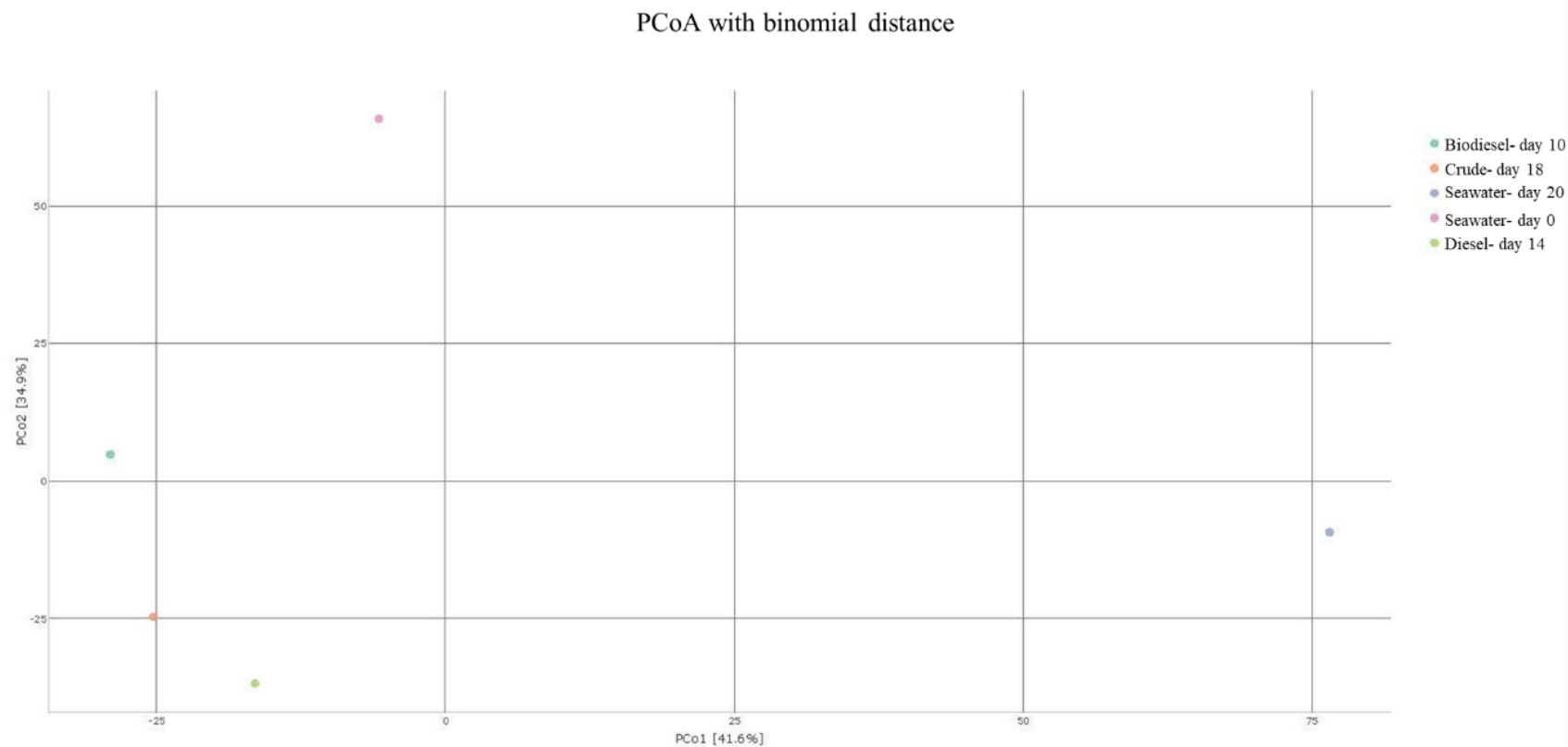


Figure 4.9. PCoA binomial distance analysis. These results compare the seawater controls with those supplemented by the addition of the different hydrocarbons. The samples selected for the comparison are based upon the maximum observed OTUs.

The chemical composition of diesel is more closely related to biodiesel than crude oil. It was expected that populations in seawater exposed to biodiesel would be more similar to those found in diesel enriched samples than in samples with added crude oil. The PCoA distance for the biodiesel community is farther from the other hydrocarbons samples and appears to be more closely related to communities exposed to crude oil than diesel. This result is unexpected and warrants further study.

Additional community investigations that examine response of the microbial assemblage in seawater to other categories of hydrocarbons would contribute to our understanding of marine hydrocarbon degradation. Subsequent inclusion of functional genetic targets could then allow for clearer definition of the biogeochemical processes involved.

### **International Collaborative Research and Development**

Pursuant to the goal of promoting international R&D cooperation on methane hydrates, that was a cornerstone of the methane hydrate task of the previous HEET program proposal, HNEI organized the 10th International Fiery Ice Workshop on methane hydrates in 2016. Fiery Ice 2016 The 10<sup>th</sup> International Workshop on Methane Hydrate Research and Development was held in Honolulu, Hawaii, on June 15<sup>th</sup> to 17<sup>th</sup> 2016 at the Imin Conference Center. A total of 60 registrants from United States, Japan, China, Germany, India, New Zealand, Norway, and the Republic of Korea attended the workshop. The 2.5-day workshop included 7 national reports, 5 breakout sessions, and 20 oral and 25 poster presentations. The key theme of the workshop was “15 Years of Progress and Future Directions”. It highlighted accomplishments and changes in hydrate science and engineering since the first workshop in 2001, and identified directions for the future. The national reports described the present status of gas hydrate research in the United States, China, Korea, Japan, Norway, New Zealand, and Germany. Five breakout sessions were organized around five topics including: 1) Fundamental laboratory and modeling studies; 2) Exploration and resource assessment; 3) Reservoir and production modeling; 4) The path forward: key areas for future R&D; and 5) The impact of cheap fossil fuels on methane hydrate R&D.

### **Publications and Presentations**

#### *Peer Reviewed Publications*

Taladay, K., Boston, B. and Moore, G.E. 2017. Gas-in-place estimate for potential gas hydrate concentrated zone in the Kumano Basin, Nankai Trough Forearc, Japan. *Energies* 10 (10), 152. doi: 10.3390/en10101552.

## References

- [1] Oyama, A. and Masutani, S.M. 2017. A review of the methane hydrate program in Japan. *Energies* 10(10), 1447. doi:10.3390/en10101447.
- [2] Taladay, K., Boston, B. and Moore, G.E. 2017. Gas-in-place estimate for potential gas hydrate concentrated zone in the Kumano Basin, Nankai Trough Forearc, Japan. *Energies* 10(10), 1552. doi: 10.3390/en10101552.
- [3] Riedel, M., Collett, T.S., Kumar, P., Sathe, A.V. and Cook, A. 2010. Seismic imaging of a fractured gas hydrate system in the Krishna-Godavari Basin offshore India. *Mar. Pet. Geol.* 27, 1476–1493.
- [4] Tamaki, M., Suzuki, K., Fujii, T. and Sato, A. 2016. Prediction and validation of gas hydrate saturation distribution in the eastern Nankai Trough, Japan: Geostatistical approach integrating well-log and 3D seismic data. *Interpretation* 4, SA83–SA94.
- [5] Kroeger, K.F., Crutchley, G.J., Hill, M.G. and Pecher, I.A. 2017. Potential for gas hydrate formation at the northwest New Zealand shelf margin—New insights from seismic reflection data and petroleum systems modelling. *Mar. Pet. Geol.* 83, 215–230.
- [6] Burwicz, E., Reichel, T., Wallmann, K., Rottke, W., Haeckel, M. and Hensen, C. 2017. 3-D basin-scale reconstruction of natural gas hydrate system of the Green Canyon, Gulf of Mexico. *Geochem. Geophys. Geosyst.* 18, 1959–1985.
- [7] Hillman, J.I.T., Cook, A.E., Sawyer, D.E., Kucuk, H.M. and Goldberg, D.S. 2017. The character and amplitude of ‘discontinuous’ bottom simulating reflections in marine seismic data. *Earth Planet. Sci. Lett.* 459, 157–169.
- [8] Santamarina, J.C., Dai, S., Terzariol, M., Jang, J., Waite, W.F., Winters, W.J., Nagao, J., Yoneda, J., Konno, Y., Fujii, T. et al. 2015. Hydro-bio-geomechanical properties of hydrate-bearing sediments from Nankai Trough. *Mar. Pet. Geol.* 66, 1–17.
- [9] Kinoshita, C.K. 2008. An experimental investigation employing combined calorimetry and raman spectroscopy of thermodynamic inhibitors used to decompose methane hydrates. M.S. thesis. University of Hawaii, Honolulu, Hawaii. Available from: [https://scholarspace.manoa.hawaii.edu/bitstream/10125/20686/HAWN\\_Q111.H3\\_4320\\_r.pdf](https://scholarspace.manoa.hawaii.edu/bitstream/10125/20686/HAWN_Q111.H3_4320_r.pdf)
- [10] Nihous, G.C., C.K. Kinoshita, and Masutani S.M. 2009. A determination of the activity of water-alcohol mixtures using mobile order thermodynamics. *Chem. Eng. Sci.* 64(11), 2767-2771. doi: 10.1016/j.ces.2009.02.047.
- [11] Sylva, T.Y., Kinoshita, C.K., and Masutani. S.M. 2016. Inhibiting effects of transition metal salts on methane hydrate stability. *Chem. Eng. Sci.* 155 doi: 10.1016/j.ces.2016.06.028.
- [12] Physical properties of glycerine and its solutions. 1963. New York: Glycerine Producers Association.
- [13] Ota, M. Abe, Y. Watanabe, M. Smith, R.L. and Inomata, H. 2005. Methane recovery from methane hydrate using pressurized CO<sub>2</sub>. *Fluid Phase Equilib.* 228, 553–559.

- [14] Hazen, T.C., Dubinsky, E.A., DeSantis, T.Z., Andersen, G.L., Piceno, Y.M., Singh, N., et al. 2010. Deep-sea oil plume enriches indigenous oil-degrading bacteria. *Science* 330, 204–208. doi: 10.1126/science.1195979.
- [15] Hazen, T.C., Prince, R.C. and Mahmoudi, N. 2016. Marine oil biodegradation. *Environ. Sci. Technol.* 50, 2121–2129. doi: 10.1021/acs.est.5b03333.
- [16] Steinle L., Graves C.A., Treude T., Ferre B., Biastoch A., Bussman I., Berndt C., Krastel S. James R.H., Behrens E., Boning C.W., Greinert J., Sapart C.J., Scheinert M., Sommer S., Lehmann M.F. and Niemann H. 2015. Water column methanotrophy controlled by a rapid oceanographic switch. *Nature Geo.* 8; 378-382.
- [17] Zak D.R., Blackwood C.B. and Waldrop M.P. 2006. A molecular dawn for biogeochemistry. *Trends Ecol Evol.* 21, 288–295. doi: 10.1016/j.tree.2006.04.003.
- [18] Liu Z. and J. Liu. 2013. Evaluating bacterial community structures in oil collected for the sea surface and sediment in the northern Gulf of Mexico after the Deepwater Horizon oil spill. *Microbiol. Open* 2(3), 492- 504. doi: 10.1002/mbo3.89.
- [19] Kalyuzhnaya M.G., Gomez O.A. and Murrell J.C. 2019. The Methane-Oxidizing Bacteria (Methanotrophs). In: McGenity T. (eds) *Taxonomy, Genomics and Ecophysiology of Hydrocarbon-Degrading Microbes. Handbook of Hydrocarbon and Lipid Microbiology.* Springer.
- [20] Rolling W.F.M., Milner M.G., Jones D.M., Lee K., Danial F., Swannell R.J. and Head I.M. 2002. Robust hydrocarbon degradation and dynamics of bacterial communities during nutrient enhanced oil spill bioremediation. *Appl. Environ. Microbiol.* 68(11), 5537-5548. doi: 10.1128/AEM.68.11.5537-5548.2002.
- [21] Chakraborty R., Borglin S.E., Dubinsky E.A., Anderson G.L.H and Hazen T.C. 2012. Microbial response to the MC-252 oil and Corexit 9500 in the Gulf of Mexico. *Front. Microbiol.* doi: 10.3389/fmicb.2012.00357.
- [22] Doyle S.M., Whitaker E.A., De Pascuale V., Wade T.L., Knap A.H., Santschi P.H., Quigg A. and Sylvan J.B. 2018. Rapid formation of microbe oil aggregates and changes in community composition in coastal surface water following exposure to oil and the dispersant Corexit. *Front. Microbiol.* doi: 10.3389/fmicb.2018.00689.
- [23] Berry D. and T. Gutierrez. 2017. Evaluating the detection of hydrocarbon degrading bacteria in 16S rRNA gene sequencing surveys. *Front. Microbiol.* doi: 10.3389/fmicb.2017.00896.
- [24] Ghosal D., Ghosh S., Dutta T.K. and Ahn Y. 2016. Current state of knowledge in microbial degradation of polycyclic aromatic hydrocarbons (PAHs): a review. *Front Microbiol.* 7, 1369.
- [25] Ching T.H., Yoza B.A., Wang R., Masutani S., Donachie S., Hihara L. and Li Q. 2016. Biodegradation of biodiesel and microbiologically induced corrosion by *Moniliella* sp. Y12. *Intern. Biodeter. Biodegrad.* 108, 122-126.
- [26] Weber N., Liou D., Dommer J., MacMenamin P., Quinones M., Misner I., Oler A.J., Wan J., Kim L., Coakley McCarthy M., Ezeji S., Noble K. and Hurt D.E. 2018. *Nephele*: a cloud

- platform for simplified standardized and reproducible microbiome data analysis. *Bioinformatics* 34(8), 1411-1431.
- [27] Schloss P.D., Westcott S.L., Ryabin T., Hall J.R., Hartmann M., Hollister E.B., Lesniewski R.A., Oakley B.B., Parks D.H., Robinson C.J., Sahl J.W., Stres B., Thallinger G.G., Van Horn D.J. and Weber C.F. 2009. Introducing mothur: Open-source, platform-independent, community-supported software for describing and comparing microbial communities. *Appl Environ Microbiol.* 75(23), 7537-7541.
- [28] Kim B.R., Shin J., Guevarra R.B., Lee J.H., Kin D.W., Seol K-H., Lee J-H., Kim H.B. and Isaacson R.E. 2017. Deciphering diversity indices for a better understanding of microbial communities. *J. Microbiol. Biotechnol.* 27(12), 2089-2093.
- [29] DeMello J.A., Carmichael C.A., Peacock E.E., Nelson R.K., Samuel Arey J. and Reddy C.M. 2007. Biodegradation of environmental behavior of biodiesel mixtures in the sea: an initial study. *Mar. Pollut. Bull.* 54(7), 894-904.

## TASK 5: SECURE MICROGRIDS

Task 5 included a range of projects to develop, test and integrate secure microgrid technology including distributed energy resources.

### **Molokai Load Bank**

Molokai is the fourth smallest of the Hawaiian Islands in the central Pacific. Its power system is small and isolated serving a rural population of approximately 7,300 residents, making it an inherent micro-grid. The island's system peak demand is 5.7 MW with an evening minimum demand as low as 2.2 MW. At the start of 2019, the island had approximately 2.3 MW of distributed solar photovoltaic (PV) generation installed and approved for installation; predominantly behind-the-meter systems located on the rooftops of residential homes and a small number of commercial or public buildings on island. A 100kW hydro project is also grid-tied.

In March 2015, Maui Electric Company, Ltd. informed customers that the Molokai grid had reached its system-level PV hosting capacity limit. Since that time, most interconnection requests have been delayed pending implementation of a solution to address the grid constraint. As a result, customer applications for an additional 665 kW of distributed PV systems were held in a queue pending interconnection approval by the utility. In total, there is in excess of 3 MW of distributed generation installed, approved or in the queue on the Molokai system, which has a minimum daytime load of only 3.7 MW.

The system-level PV hosting constraint is a function of the limited load on the island being inadequate at times during the day to accommodate the energy production from the existing and proposed new grid-tied PV systems in the queue, and the minimum reliable operating points of the must-run diesel generation on island. Further, the high penetration of PV on the grid can exacerbate system stability challenges during foreseeable contingency events, such as a sudden loss of a generating unit or a power line fault, causing the system frequency to drop below 57 Hz in a few cycles. Sudden drops in frequency in turn cause distributed PV systems to trip offline, with a cascade effect leading to system-wide blackout.

Figure 5.1 illustrates the primary system level constraint of energy oversupply during periods of low demand and high PV output. If the net load (load minus PV) falls below the minimum diesel generation dispatch level of 1.3 MW, the system can no longer be operated in compliance with its downward regulating reserve requirement, which is an operating reliability criteria to address sudden load loss due to unplanned, but anticipated system contingencies such as line faults. The dark brown line in Figure 5.1 shows that the net load in 2015 was close to the minimum generation dispatch level for the system and thus, the system-level PV hosting capacity had been reached.



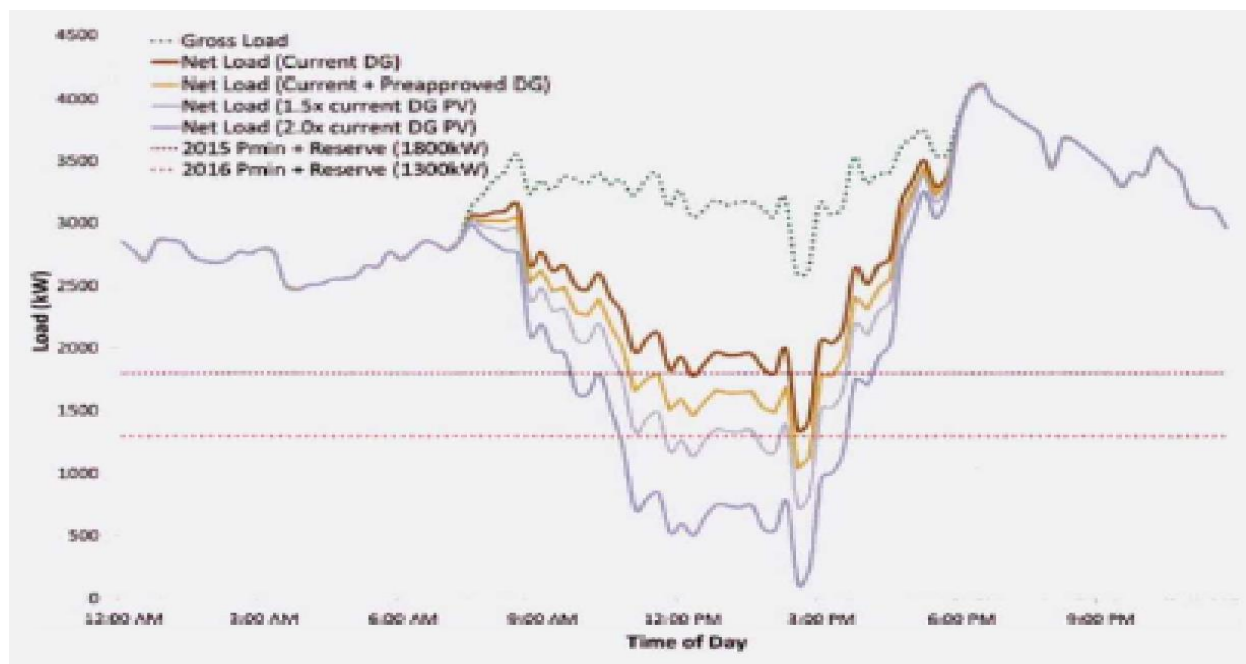


Figure 5.1. System-Level Hosting Capacity on Molokai

Source: E3 Interconnection Potential Analysis – Molokai, October 8, 2015.<sup>1</sup>

Figure 5.2 illustrates an analysis using hourly system load data from 2009 for Molokai. In 2009, there was only a negligible amount of distributed PV tied to the electric grid on the system. With system demand having grown little since then, the 2009 recorded system demand is a very good proxy for the gross load on the island today. The calculated 2,942 kW of distributed PV (2,144 kW installed, 133 kW PV approved and 665 kW in the queue) and 100 kW of hydro production was subtracted from the 2009 load data to generate a prospective net load profile to be served by thermal generation in Figure 5.2. The excess energy periods are indicated by the areas where the blue line (net load profile) dips below the orange minimum generation line.

<sup>1</sup> *Instituting a proceeding to investigate distributed energy resource policies*, Docket No. 2014-0192, Compliance Filing – System Level Hosting Capacity, (December 11, 2015), Exhibit 3, Page 13 of 19.

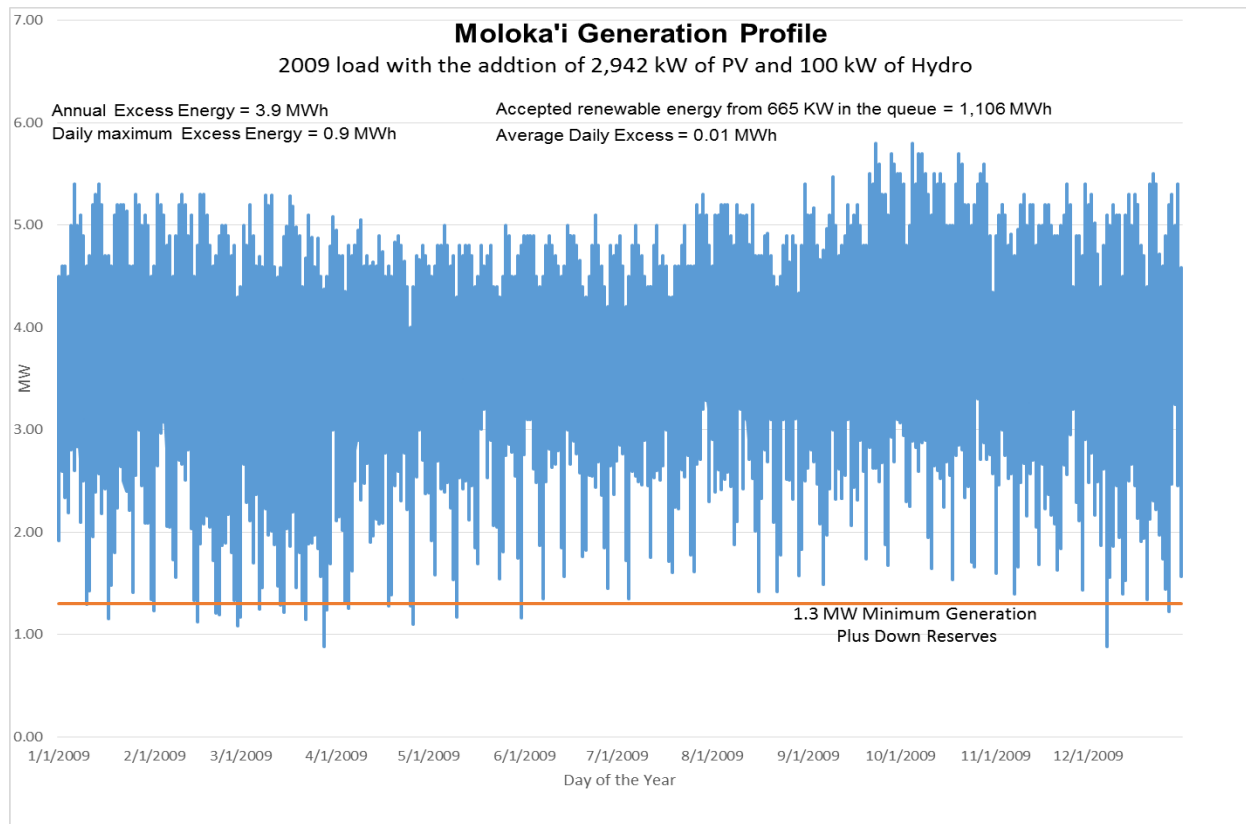


Figure 5.2. Prospective Molokai Net Load Profile with Added PV.

Two solutions that have been among those considered to address this near-term constraint are the development of direct control capabilities on distributed generation (DG) systems and the installation of energy storage. Conceptually, both of these solutions could address the relative energy imbalance but both have some limitations or drawbacks, particularly in the near-term.

Implementing controls on DG systems would provide grid operators a direct ability to manage the output of distributed PV systems and balance energy supply on the Molokai grid. However, this option is likely to require time to implement acceptable and effective communication and control protocols to a fleet of customer-owned DG systems, particularly if the protocols are expected to have a level of commercial interoperability and security commensurate with that of utility-scale renewable energy and conventional plants. Furthermore, customers will have to understand and accept these new requirements for interconnection, and existing customers would require system retrofits and likely require compensation for curtailment of production. Thus, implementing this option alone was unlikely to provide an immediate integration solution to the current backlog of interconnection requests.

Energy storage systems, both utility-scale and distributed, could be used to shift energy supplied from PV systems in high output periods in the mid-day to peak periods in the evening. Energy storage solutions could also be used as a possible solution to reduce the minimum generation constraint and down-reserve requirements. For the energy shifting storage application, while energy storage prices continue to fall in the market, preliminary estimates indicate this may be a costly integration solution at today's storage prices.

Both of these integration options (and others<sup>2</sup>) are potentially promising, and possibly necessary, as Molokai moves towards a 100% renewable system. However, for the reasons discussed above they do not appear to be rapidly implementable near-term solutions<sup>3</sup> that would effectively address the immediate near-term constraint on DG interconnection.

This project analyzes the performance and effectiveness of a controllable load bank as an energy safety valve to provide a near-term solution for interconnection and longer-term grid management asset for small island grid and microgrid applications. In this application, the load bank would add load to the Molokai system, using secure communications within the power plant, when needed as a near-term solution to balance the grid during infrequent periods of excess energy supplied to the grid. While this excess energy would be literally burned off as heat, enabling the interconnection of all 665 kW of distributed PV in the queue results in a significant increase in renewable energy accepted on the grid in exchange for a relatively small amount of excess energy per year.

Figure 5.3 illustrates that a projected 1,106 MWh of additional renewable energy is utilized by the grid while a mere 4 MWh of excess energy is dissipated as non-productive heat loss if the 665 kW of distributed PV in the queue were allowed to interconnect to the Molokai grid as a direct result of the new load bank operation.

---

<sup>2</sup> Another possible solution is implementation of aggressive time of use rates and demand response programs to encourage higher demand during daytime hours with high solar output. These solutions will also require time and significant cost and resource to implement at scale, particularly on a small rural island such as Molokai.

<sup>3</sup> In this context, near-term is considered as a solution that could be implemented within a year.

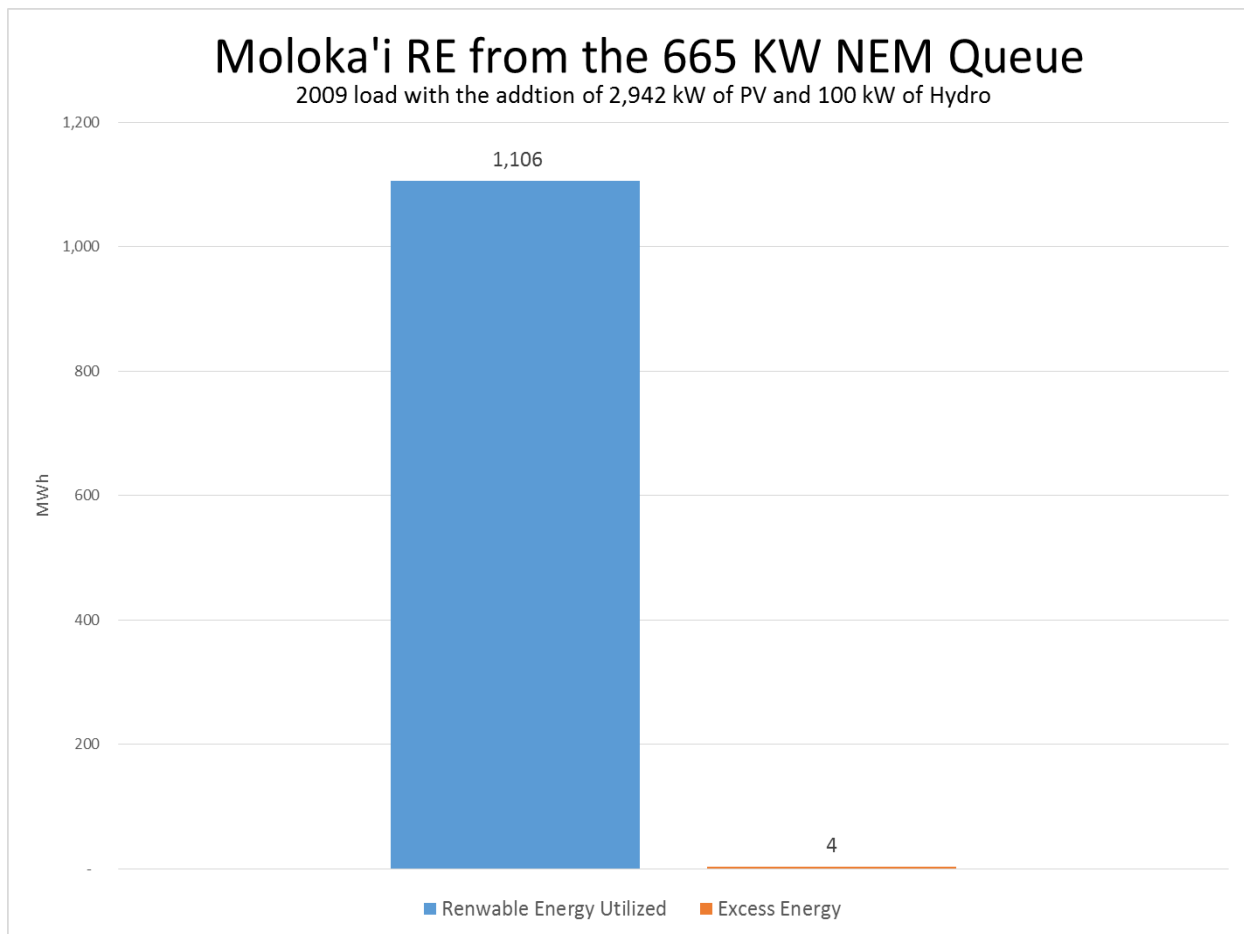


Figure 5.3. Additional renewable energy from PV held in the queue.

Under APRISES12 funding, an agreement was executed with the utility to collaborate on the integration and installation of the load bank, including algorithm and control development, and data sharing. Figure 5.4 depicts the ASCO 4800, 750 kA resistive load bank and associated step-up transformer installed and commissioned by the utility at its Palaa Power Station on Molokai.



Figure 5.4. Installed load bank and step-up transformer.

Work in collaboration with the utility has continued on this project under APRISES14 to design and test algorithms and controls to automate the load bank's primary use case of managing excess distributed PV energy on the grid. In November 2018, upon load bank operational commissioning and implementation of automated controls, the utility was able to allow the interconnection of an additional 725 kW of distributed PV capacity onto the system, exceeding the original 665 kW held in the queue. Figure 5.5 below depicts the PV hosting capacity for Hawaiian Electric Company's power systems, including Molokai, that are filed quarterly with the Hawaii Public Utilities commission. It shows that an additional 0.7 MW of capacity was added to the system following the installation of the load bank and its automated controls.

# Alternatives to Storage

## Dynamic Load Bank (Energy Safety Valve)

A 750kW Load bank was placed into service in November of 2018

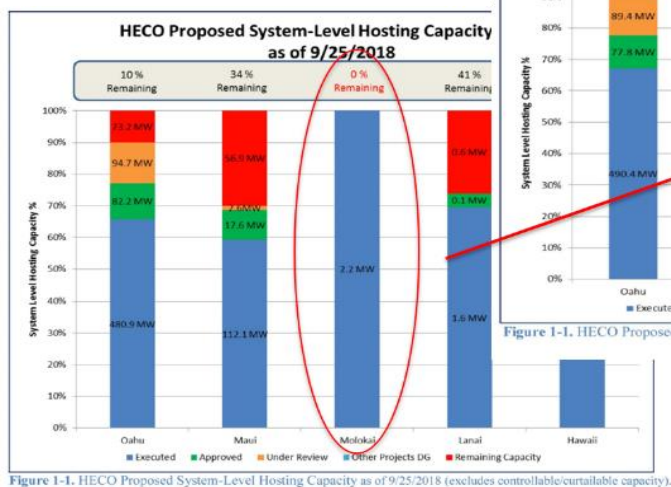


Figure 1-1. HECO Proposed System-Level Hosting Capacity as of 9/25/2018 (excludes controllable/curtailable capacity).

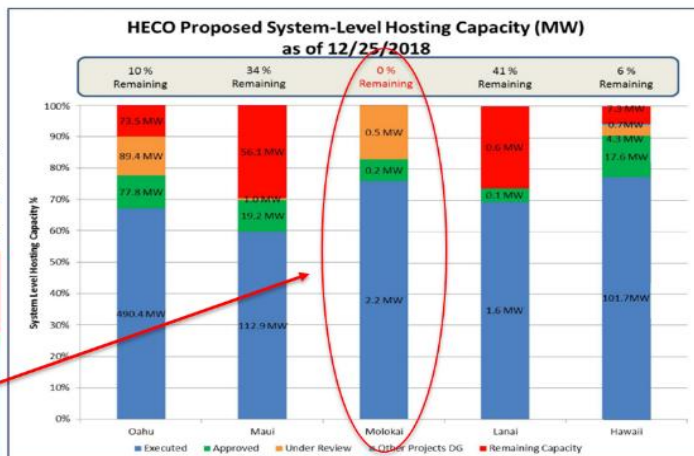


Figure 1-1. HECO Proposed System-Level Hosting Capacity as of 12/25/2018 (excludes controllable/curtailable capacity).

An 725kW of additional DGPV was then allowed to connect to the system.

Figure 5.5. Increase in Molokai system-level PV hosting capacity.

Under APRISES14, HNEI further developed additional use cases and implemented test plans to investigate additional system benefits that the load bank may support beyond the management of excess distributed PV energy. These use cases include very rapid response to system over and under frequency dynamic events due to system disruptions and the provision of downward regulating reserves, all of which hold the potential for enhancing grid security and reliability, while integrating increased levels of renewable energy. These additional potential use cases are described below in Table 5.1.

Table 5.1. Additional use cases.

<b>Contingency Event Response (Under-Frequency and Over-Frequency)</b>		
<b>Under-Frequency</b>		
<ul style="list-style-type: none"> <li>• <b>Line Fault Event</b> (early stage subsequent to the event);</li> <li>• <b>Generator Trip Event</b></li> </ul>		
<b>Line Fault Event</b>		
No response (Generators and Battery will respond to the event)		
<b>Generator Trip Event</b>		
<b>Load Bank State</b>	<b>Load Bank Response/Control</b>	<b>Event Detection</b>
Load Bank <b>Not Active</b> prior to the event	<ul style="list-style-type: none"> <li>• No response (Generators and Battery will respond to the event)</li> </ul>	
Load Bank <b>Active</b> prior to the event	<ul style="list-style-type: none"> <li>• Load Bank response similar to an under-frequency load shed (UFLS) kicker block <ul style="list-style-type: none"> <li>○ 57.75 (TBD) Hz</li> <li>○ Time Delay = 2 (TBD) sec</li> </ul> </li> <li>• Shed the Load Bank prior to the last two kicker blocks (avoid customer load shed)</li> </ul>	<ul style="list-style-type: none"> <li>• Monitor frequency measurement of existing BESS PMU meter every 200 msec.</li> </ul>
<b>Over-Frequency</b>		
<ul style="list-style-type: none"> <li>• <b>Line Fault Event</b> (final stage subsequent to the event- post breaker operation)</li> </ul>		
<b>Load Bank State</b>	<b>Load Bank Response/Control</b>	<b>Event Detection</b>
Load Bank <b>Not Active</b> prior to the event	<ul style="list-style-type: none"> <li>• Load Bank added to the grid if the frequency exceeds 60.5 (TBD) Hz <ul style="list-style-type: none"> <li>○ Time Delay = 2 (TBD) sec</li> <li>○ R = 500 kW</li> </ul> </li> </ul> <p>(Note: system freq. bias = 100 kW/0.1 Hz)</p>	<ul style="list-style-type: none"> <li>• Monitor frequency measurement of existing BESS PMU meter every 200 msec.</li> </ul>





Under APRISES15 support, HNEI will continue its work with the utility to develop and refine an effective load bank control and monitoring system to automate the desired use case functions and evaluate operational performance, with the goal to cost-effectively provide grid security and reliability benefits with increased levels of renewable energy integration in an isolated microgrid environment.

### **Coconut Island DC Microgrid**

Coconut Island (Moku O Lo‘e) is a 28-acre (113,000 m<sup>2</sup>) island in Kaneohe Bay off the island of Oahu that is home to the Hawaii Institute of Marine Biology (HIMB) of the University of Hawaii. Among the goals of HIMB is for the island and its research facilities there to be a model for sustainable systems. As such, it is an ideal site for a renewable energy technology-based test bed, particularly representative of in an isolated location vulnerable to energy disruption, yet serving critical power needs essential to the research and educational mission of HIMB. This island is an inherent microgrid served via an undersea electrical connection tied to a single distribution circuit owned and operated by the local utility on Oahu. The tropical marine features of the island further its attractiveness as a unique microgrid test bed. Its exposure to persistent on-shore winds and highly corrosive salt spray allow for material and technology testing in a micro-climate representative of those potentially encountered in coastal installations of Navy interest.

The project objective is to demonstrate the performance and resilience of a DC microgrid designed to serve loads within two buildings on Coconut Island, including reliable power to critical loads during interruptions of grid supplied power, and provide the island with clean electrified transportation options powered primarily by the sun. The project has the following goals:

- Demonstrate innovative new clean energy technologies.
- Reduce island energy dependence upon the local utility and the existing aged undersea electrical service tie, enhancing energy resilience for select critical loads.
- Provide a research platform to study DC microgrid resources and loads, e.g. energy storage and supporting technology and DC power appliances, in a tropical coastal environment.
- Increase island energy sustainability.
- Provide solar electric powered land and sea based transportation options for HIMB.

Initiated under previous APRISES funding, the Coconut Island DC Microgrid Project integrates a DC distribution system into two existing buildings on the island, the Marine Mammal Research Project (MMRP) building and the adjacent Boat House, both depicted in Figure 5.7 below. The energy needs of the two buildings are currently served by AC power through one of the utility owned electric service transformers located on island.



Figure 5.7. Location of Coconut Island and the DC Microgrid Project site.

Major project activities earlier completed through the support of prior APRISES funds include project planning and permitting, baseline energy use data metering and collection, design of the DC microgrid architecture to be integrated with the existing AC building infrastructure, energy use and economic modeling to appropriately scope and size a new rooftop PV system for installation on the MMRP building and a stationary battery energy storage system (BESS), and the specification, design and procurement of an electric E-car and E-boat powered by swappable BESS units charged via a swap battery charging station fed by the DC microgrid.

Under APRISES14, HNEI's major activities included: (1) identification, due diligence assessment and partnering with Sion Electric Co., Ltd. (Sion), a Japan corporation with innovative DC microgrid controller technology that has been integrated with stationary BESS and DC powered lighting and air conditioning loads in the course of prior technology development work in Japan; (2) in close collaboration with Sion, conducting further DC microgrid system design refinements, sizing analysis and detailed specification development for various DC microgrid components and balance of system elements to prepare for equipment procurement; (3) initiating competitive procurement of the materials and services for the MMRP building rooftop PV system to serve as the primary source of renewable energy for the DC microgrid; and (4) conducting test and commissioning of the E-Boat, including operational sea trials.

Working in partnership with Sion, HNEI refined the DC microgrid design resulting in an updated single line diagram with sub-system component selection as shown in Figure 5.8, and described in further detail below:

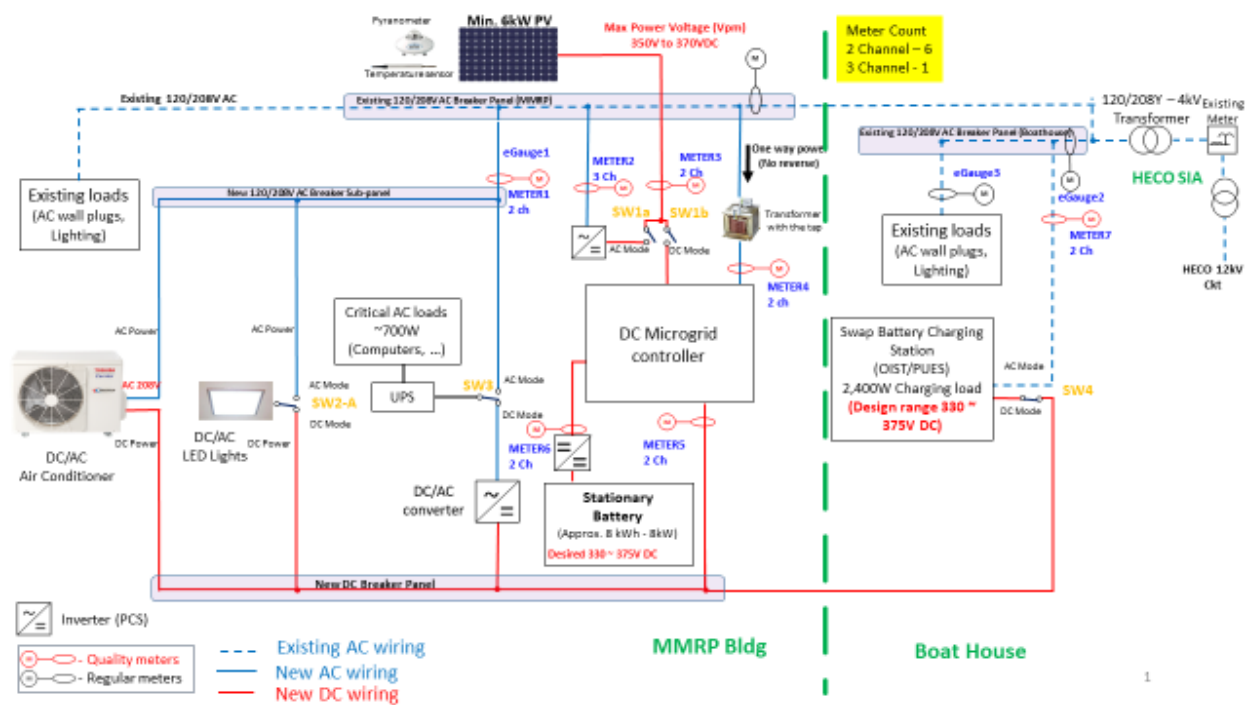


Figure 5.8. DC microgrid description.

- 1) PV modules installed on the MMRP rooftop as the primary source of renewable energy for the microgrid. The PV system capacity was sized at approximately 6 kW DC, which will generate enough energy to support the buildings' targeted loads. PV panels were specified and designed to provide the necessary input DC voltage for effective integration with the Sion DC microgrid controller.
- 2) A stationary BESS used to store excess PV energy production and export that energy to the DC microgrid when needed to minimize the use of utility supplied power during normal operation, and to maintain service to specified critical loads in the event of utility service disruption.
- 3) A Sion DC microgrid controller to manage and optimize energy use and flow among components in the DC microgrid and the utility grid tie, while providing operational status and performance data via local dashboard display and data archiving.
- 4) Inverter(s) with a capacity appropriate to supply designated AC end-use loads within the MMRP building served by the DC microgrid (e.g., computers, Wi-Fi network, etc.).
- 5) An air conditioning unit with appropriate modifications to allow operation with either a DC or AC power source. Its operating performance and efficiency under both DC and AC modes of operation will be assessed and compared.
- 6) A swap battery charging station, designed and manufactured by PUES Corporation (PUES), Japan, will charge the swappable BESS units used interchangeably in both E-boat and E-car and portable power "suitcase battery" system. This station is capable of charging

twelve (12) portable BESS units through the microgrid DC bus, with the capacity of each BESS unit rated at 1.4 KW and 1.4 KWh.

- 7) Interior LED lighting for the MMRP building that will be modified to allow operation with either a DC or AC power source.
- 8) A nominal 330 ~ 375 Vdc bus that transmits power between energy resources (PV, stationary BESS) and loads (LED lighting, air conditioning, inverter for critical AC loads, and swap battery charging station) within the microgrid.
- 9) Metering for performance data capture and analysis.
- 10) Balance of system components, such as wiring, breaker panels, switches and the like.

Notably, HNEI prepared and issued a request for proposal to procure a rooftop PV system sized at approximately 6kW DC. A key system design specification was that the PV modules must meet a  $V_{oc}$  in range of 350 to 370 VDC in each string; a requirement for effective integration of the PV system with the selected DC microgrid controller. Figure 5.9 illustrates the proposed PV system layout by the selected contractor. Depending on the desired operational mode selected in the course of executing the overall system test and research plan, the PV system output can be flexibly directed via switch to connect to either the DC microgrid controller, or to the AC grid through a single-phase inverter.

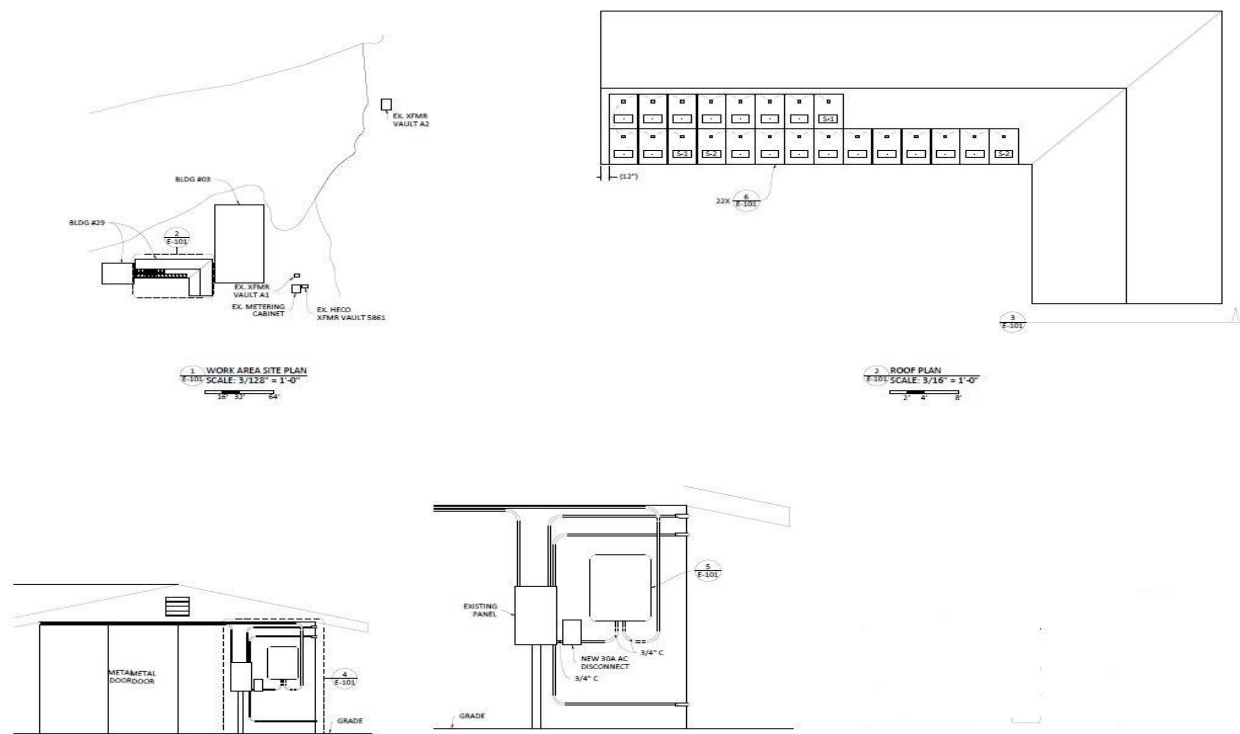


Figure 5.9. PV system layout at the MMRP building.

As previously noted, HNEI worked closely with PUES, a key collaborative research partner on this project, to adapt, improve upon and install their swap battery charging station and associated E-car and E-boat. Figures 5.10 and 5.11 depict the installed battery charging station, portable swappable BESS units, and the commissioned E-Boat in sea trials.



Figure 5.10. Swap battery charging station and portable BESS units.





Figure 5.11. E-Boat in operation in Kaneohe Bay, Hawaii.

Under APRISES14, the E-boat shown in Figure 5.11 underwent final preparations and was transferred to the project site and launched for initial sea test trials. The E-Boat all electric power train is powered by 8 swappable BESS units. These batteries can be charged either in the swap battery charging station connected to the microgrid on island, or through PV panels installed on a custom E-Boat canopy. These 4 PV panels on the boat canopy, connected in a 2-series, 2-parallel configuration, can fully charge all 8 of the E-Boat swappable BESS units in approximately 16 hours (~two days). During E-Boat operation, the canopy mounted PV panels continuously charge the swappable BESS units, extending its operating range as a function of available solar resource. Based on initial sea trials, the E-Boat consumes in the range of 40% to 60% of its BESS state of charge at or near full engine power in the course of an hour of run time.

Under APRISES15 support, HNEI will continue its work to procure and commission remaining equipment for the DC microgrid and progress with implementation of microgrid control functions, monitoring of performance and characterization of perceived energy efficiency benefits (and identified limitations) of DC operation versus legacy AC supply of loads, and the sustainability and resiliency benefits associated with the renewable energy powered DC microgrid operation and electrified transportation alternatives.

## 5c Load and PV Synthesis

Initially funded under APRISES13, methods to synthesize load and PV data based on nearby field measurements were developed. The overall objective of this project is to synthesize PV and load data from a limited number of field measurements in order to enable realistic distribution feeder modeling with high distributed PV penetration.

Prior foundational work was extended under APRISES14 to validate the synthesized load and PV data by injecting it along with field measurements into a simulated electrical model of the Maui Meadows feeder which serves approximately 800 customers. The total installed rooftop PV capacity on this feeder is approximately 2 MW, and the daytime minimum load on the feeder is 976 kW. A utility owned transformer load tap changer (LTC) located at the Maui Electric Company, Ltd. Wailea Substation manages the voltage at the Maui Meadows 12.47 kV feeder head-end and along the length of the entire feeder. Figure 5.12 depicts the Maui Meadows residential subdivision and distribution feeder serving customer loads (red circles) and grid-tied rooftop PV systems (green circles).

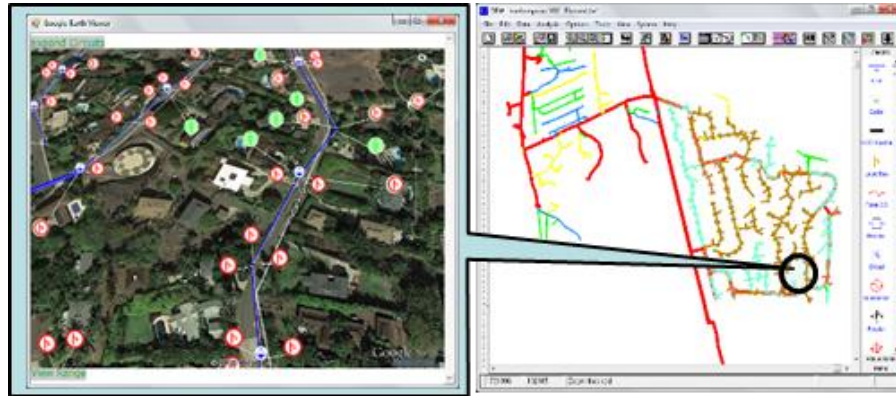


Figure 5.12. Maui Meadows subdivision and distribution circuit.

To validate the synthesized data, the node voltage profiles obtained from time-series power flow results from the OpenDSS power system modeling software are compared against actual measurements collected from the field. The inputs for the power flow simulation includes the electrical model, synthesized load and PV data, field measurements at distribution service transformers, and substation SCADA data.

The power flow is calculated at each time point. The node voltage error is defined as:

$$\%Error = \frac{PowerFlowOutput - Measurement}{Measurement} \times 100\%$$

There are 28 service transformers with power monitoring sensors installed at the secondary side. The node voltages calculated from the power flow model are compared with the actual voltage measurements. For each transformer, the minimum error, maximum error and mean error are reported in Table 5.2.

Table 5.2. Distribution Transformer Node Voltage Error

No.	Trans ID	Min Error (%)	Max Error (%)	Mean Error (%)
1	627	4.18e-4	3.15	0.99
2	583	1.32e-6	1.50	0.23
3	630	4.16e-6	1.71	0.20
4	631	0	1.41	0.16
5	599	0.0025	2.98	1.06
6	632	8.31e-4	2.81	0.75
7	584	0.0021	2.80	0.92
8	585	0.0013	2.76	0.88
9	601	8.39e-4	2.86	0.94
10	641	1.28e-6	1.88	0.34
11	639	2.58e-6	2.26	0.63
12	638	4.19e-4	2.28	0.68
13	640	0	1.88	0.41
14	648	0.0021	2.26	0.71
15	651	0.0010	2.57	0.76
16	662	1.28e-6	1.46	0.17
17	615	3.82e-6	3.11	1.07
18	83287	1.30e-6	1.50	0.27
19	669	8.41e-4	2.21	0.64
20	695	3.83e-6	2.90	0.95
21	83688	8.22e-4	2.97	0.99
22	677	2.55e-6	2.90	0.95
23	687	6.34e-4	3.20	1.30
24	676	0.0010	1.63	0.38
25	678	0.0050	3.00	1.04
26	671	0.0013	2.93	1.05
27	665	4.1592e-4	3.95	1.47
28	659	0.0033	2.94	0.98



As shown in Table 5.2, the voltage errors are within 4%. As expected, the maximum errors are found at the end of the feeder (transformer 665). As a worst-case analysis, Figure 5.13 compares the actual field measured voltage profile at transformer 665 against the power flow calculation, and Figure 5.14 provides a histogram of the node voltage errors at transformer 665.

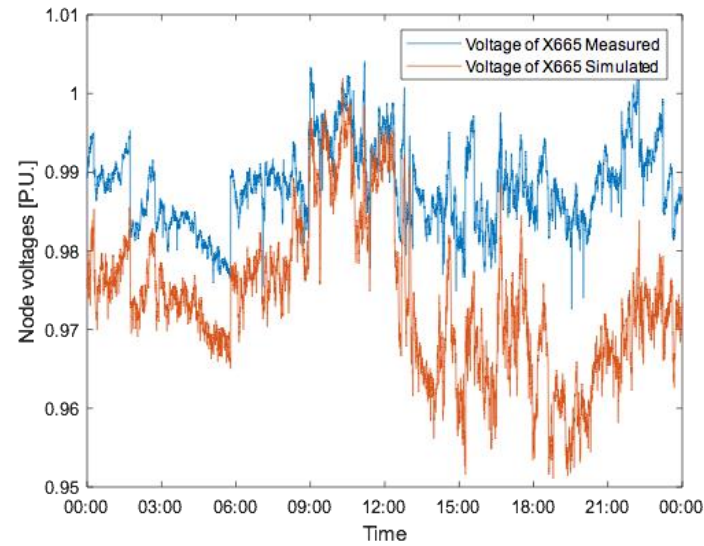


Figure 5.13. Node voltages comparison between the simulated results and real measurements

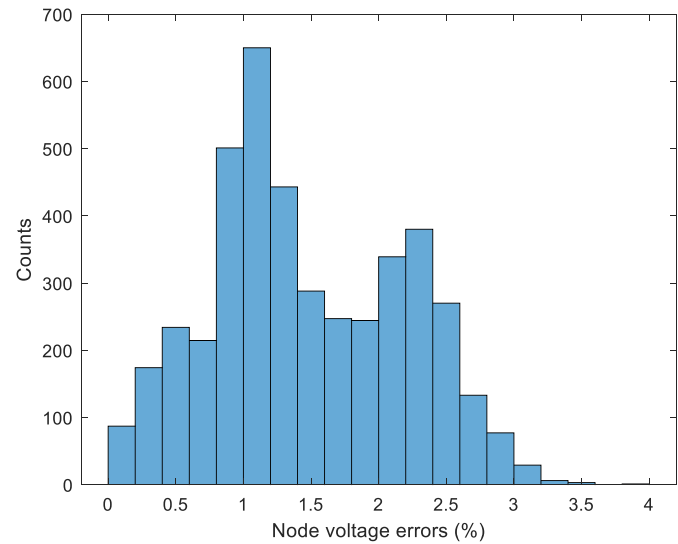


Figure 5.14. Histogram of the percentage error at Transformer 665 node voltages

From Figures 5.13 and 5.14, we find that even in the worst case, the voltage errors are concentrated around 1%. In conclusion, it's determined that the methods for synthesizing unobservable data using measured data provide a reasonably accurate representation of the conditions in the field. This work was leveraged in a collaborative DOE funded project with the University of Central Florida (UCF) in which HNEI was funded to test and validate the performance of a voltage control algorithm developed by researchers at UCF using a model that represents actual field conditions.

Under APRISES15, HNEI will work on developing methods to disaggregate the load and PV data to estimate the gross load data at each distribution service transformer. This will allow for the testing of distributed control algorithms that utilize the distributed resources at customer locations located behind the meter for various use-case scenarios.

### **Power Grid Monitoring and Controls**

The objective of this project is to help solve grid operational issues with high penetrations of distributed energy resources (DER) such as photovoltaic (PV) by offering utilities and distribution system operators (DSOs) greater situational awareness and control capabilities near the edge of the grid. Under this project, HNEI has developed a low-cost, fully integrated, and highly flexible device and system for distributed electrical measurement, real-time analysis, and controls. It provides high-fidelity, low-latency measurement by utilizing carefully selected technology at the intersection of internet of things (IoT), RF mesh communications, open source software, single board computers, and off-the-shelf integrated circuits (ICs) for the smart meter analog front end (AFE), field programmable gate array (FPGA), GPS, and power management. The device is being used to support HNEI's ongoing research and demonstrations on the distribution grid. The device has reached a level of refinement and capability where it is now being shared with external research partners and considered for commercialization.

In order to improve the resiliency of the electric grid and allow high penetrations of distributed PV, utilities need better real-time situational awareness of the distribution circuit. On circuits with very high penetration of PV, power backfeeds from residential customers to the grid. This can introduce issues such as overvoltage and thermal violations on the electrical lines and transformers, which ultimately limits PV hosting capacity. High penetrations of PV can also increase the cost of operations at the system level by requiring additional system operational reserves (and therefore greater fuel consumption) to protect against transient cloud coverage. Better power grid monitoring can help utilities identify and address these issues and ultimately operate the grid more reliably and efficiently with large amounts of distributed PV. It can also potentially detect anomalies that indicate pending equipment failures, revenue loss due to unmetered loads, and cybersecurity intrusions. It could also help utilities improve resiliency by more quickly locating and classifying grid faults.

This project was motivated by HNEI's experience in deploying approximately 60 distribution-level power monitoring devices under the DOE-funded Maui Smart Grid Infrastructure project. That work showed that commercial power monitors are inadequate for measuring the highly variable conditions due to aggregated effect of PV on the distribution grid. Some do not accurately measure reactive power under bi-directional active power flow, which is essential for advanced methods of voltage regulation. Others provide advanced measurement of reactive power, harmonics, and numerous other metrics, but are very expensive (~\$3000/unit) and still require communications equipment with a commercial data plan (~\$80/mo), a power supply, and a weather resistant enclosure. These are designed primarily for event detection and to record power quality data for post-processing rather than to stream data to support increasingly interconnected and controlled networks of DERs.

To fill this gap, HNEI developed a low-cost, fully integrated, and highly flexible solution under this project. Figure 5.15 shows the progression of the design over the course of the project, initiated under previous APRISES funding. The design progression depicted in the (c) to (d) transition (encompassing an enhanced GPS receiver, utility-standard wireless mesh transceiver, improvements to the backup power supply and packaging, and dual connector options for lab or field use) was performed under APRISES14.

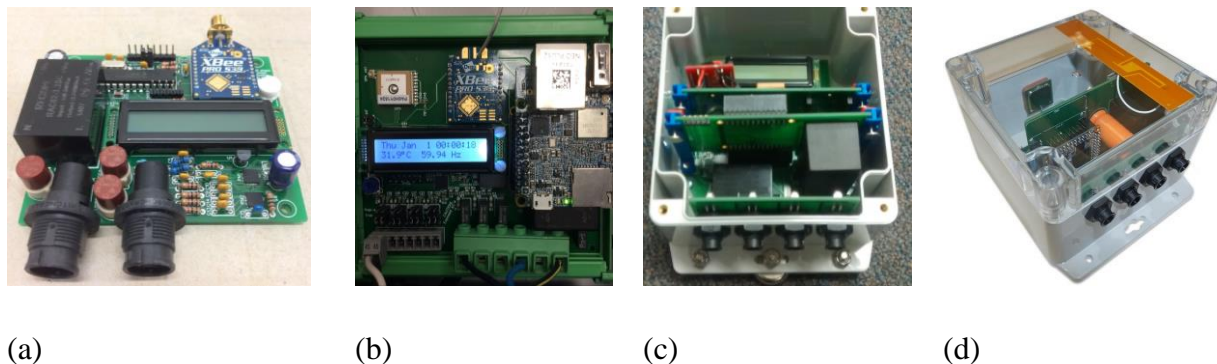


Figure 5.15. Design progression of the power monitor.

The current hardware is final except for minor design maintenance and potential further optimization and cost reductions for commercialization. The key features of the device are:

- Measurement of root mean square (RMS) current, RMS voltage, active and reactive power, and frequency.
- Fundamental and total components reported to indicate harmonic distortion.
- Data reported at 1 Hz or faster (up to 60 Hz), with potential access to raw 32 kHz samples.
- Up to 3 electrical phases.
- Weatherized at IP65 level.

- Self-powered from service lines, with power backup (~20 s) to record grid outage events;
- Automatic onboard data storage (up to a year) in the event of a communications issue.
- Internal electrical isolation for lab use.
- Multiple communication options (Ethernet, WiFi, LTE 4G, and RF Mesh IP) for real-time monitoring and controls.
- Onboard timing-optimized GPS IC for potential synchronization to within 10 ns.
- Quad core 64-bit CPU and FPGA up to 50k logic elements to support future advanced onboard signal processing, data analysis, power flow modeling, and controls.
- Hardware ready for over-the-air programming and configuration.

HNEI has provided educational and employment opportunities to undergraduate students under the project since its inception in 2017. This has included two project courses, an internship, and support for four student employees. Two students are currently working on the project under new lines of funding that have been developed outside of APRISES.

HNEI filed a US patent application through the UH Office of Technology Transfer (OTT) on November 22, 2018. HNEI continues to work with UH OTT to pursue commercialization. HNEI's goal is to transition future research activity to funds outside APRISES, while at the same time licensing the core device to commercial partners. The first tangible step towards commercialization will be to transfer the assembly to a prototyping and production company for better scalability to serve the increasing interest from external parties.

The cost of the device compares favorably with Grid 20/20's approximately \$800 OptaNODE power monitor, the de facto standard for basic distribution transformer power monitoring. With further software development, it would be possible to provide waveform capture and phase measurement unit (PMU) capabilities comparable to Power Standard Lab's approximately \$4000 PQube device and PMU add-on. The hardware parts cost is between \$310 and \$390 at a quantity of 100 (depending on features) and drops as low as \$280 at a quantity of 1000. Assembly costs are still being quantified, but are expected to be less than \$100 at volume. Server operation and shared commercial data communications are estimated at \$50 per year per device plus \$0.34 per device-year of data storage. The field installation time and cost is expected to be minimal due to the compact form factor with integrated mounting flanges and swappable phase and current transducer (CT) leads.

Besides hardware development, APRISES14 funds were used to support development of new software features. In particular, HNEI focused on FPGA firmware and the control capabilities of the device. It can now perform electrical measurement, real-time data analytics, local data storage, data streaming to the server, and low-latency controls concurrently and/or in parallel on separate

processes and threads, while still only utilizing less than 5% of the processing capability of the device.

The system has a web-based graphical user interface (GUI) shown in Figure 5.16, as well as various application programming interfaces that can access both real-time and historical data from the power monitors/controllers. Besides reading from the onboard power monitor, the gateways have software to read from PQube devices and control PV inverters. Over 1 billion scalar data points have been recorded to date among various field deployments.

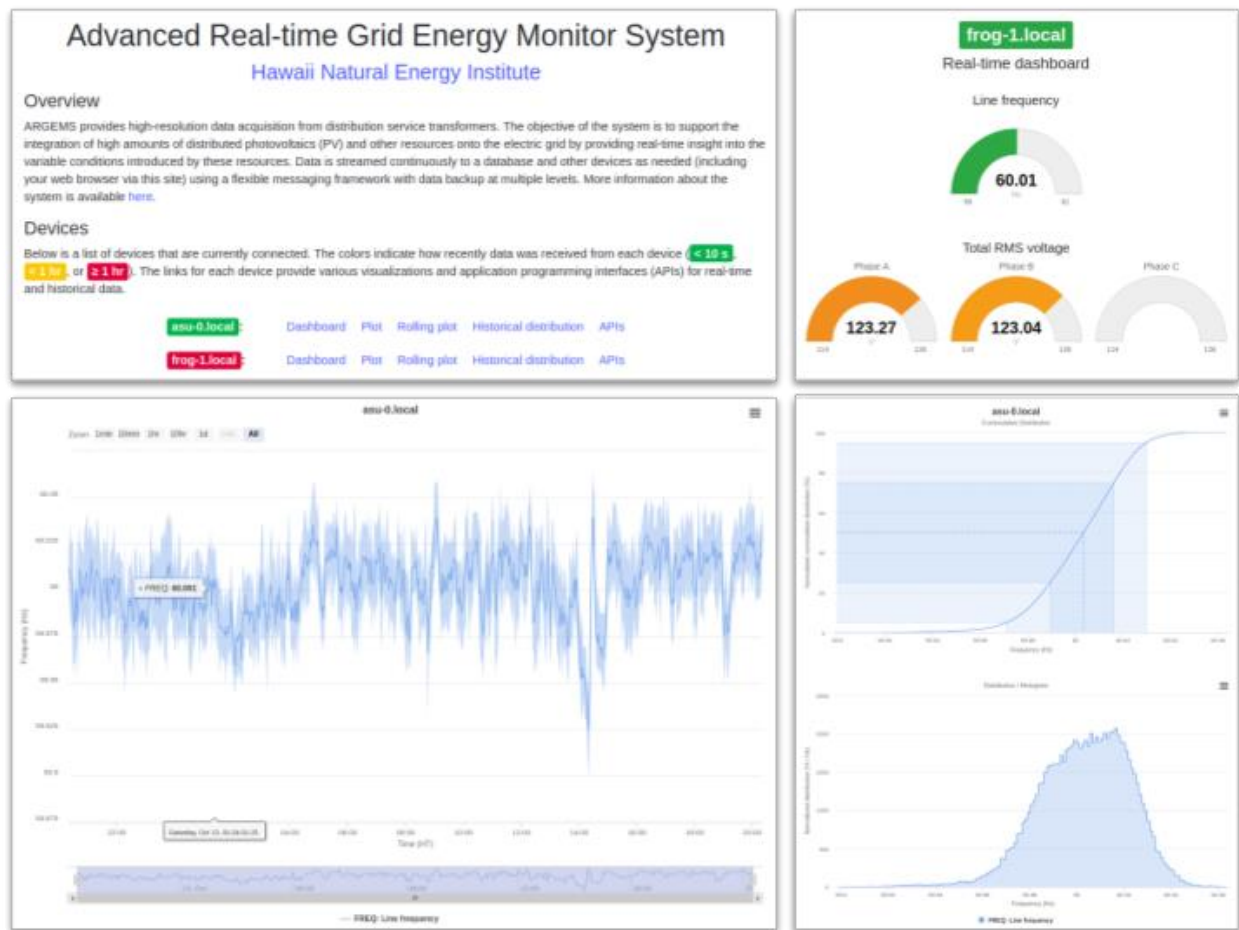


Figure 5.16. Screenshots from the web-based graphical user interface (GUI).

The APIs provide strong capabilities for distributed analytics and controls. For example, using the publish/subscribe paradigm, data can be transferred as needed among devices or to a web browser in less than 10 ms from the time of actual measurement. During testing and demonstration at the Alaska Center for Energy and Power (ACEP) in July 2019, data transfer to Hawaii was found to be only 58 ms, approaching the latency of internet communications itself. This offers the potential

for applications that involve enhanced coordination at the grid edge in combination with high-fidelity electrical measurement, precise GPS timing, high-speed data analytics (e.g. implemented at the logic level on the FPGA), and DER controls. For example, under ONR Defense University Research-to-Adoption (DURA) funding HNEI is currently collaborating with Arizona State University to develop an advanced voltage control application that is shared and coordinated between their devices.

Another application concept, which has been explored with the Hawaiian Electric Company (HECO), Electric Distribution Design, Varentec, Enphase, and EPRI, is shown in Figure 5.17.

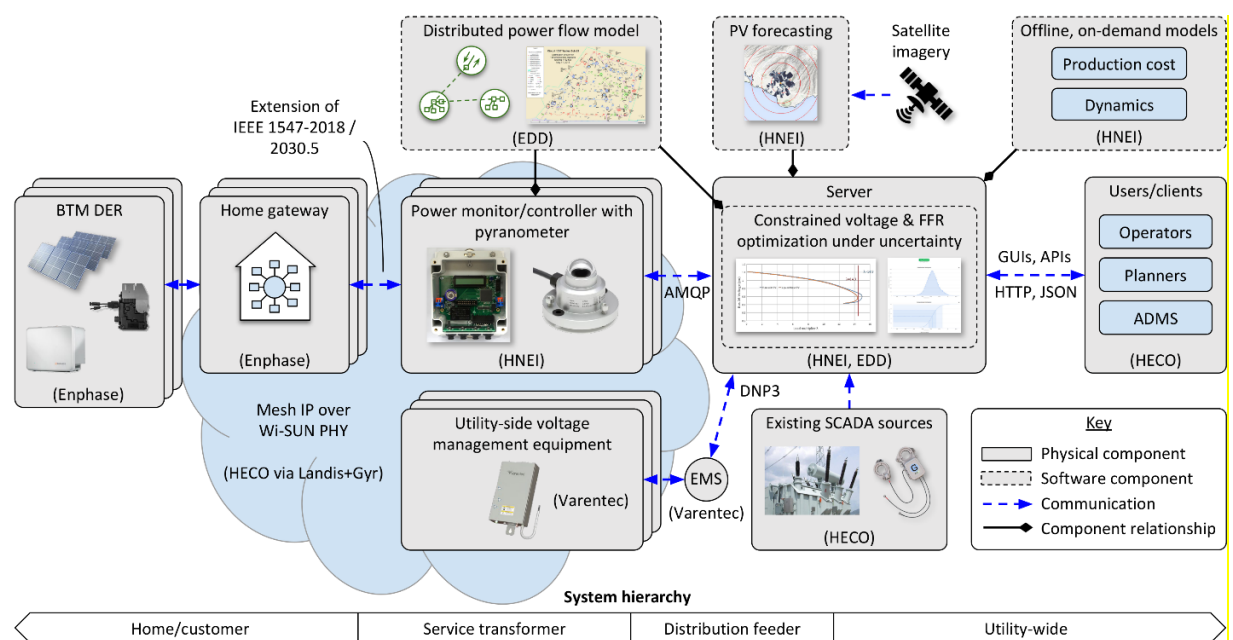


Figure 5.17. Concept for advanced analytics and controls at the grid edge.

Particular applications and use cases which are being considered include:

- Utility asset monitoring and management;
  - transformer health monitoring.
  - remote transformer loading assessment by operating as a PMU.
  - impedance estimation using time-synchronized harmonic measurement.
  - enhanced non-wires alternatives (NWA) through distributed power flow modeling and DER controls.

- Grid robustness and resiliency;
  - fault location and classification using time-synchronized harmonic measurement.
  - near real-time distribution voltage stability assessment and PV hosting capacity analyses through enhanced data collection and distributed power flow modeling.

More information on the project is available at the following sites:

- HNEI project page with links to a project summary sheet and a datasheet: <https://www.hnei.hawaii.edu/projects/argems>
- HNEI announcement of recent demonstrations and deployments: <https://www.hnei.hawaii.edu/news/hnei-demonstrates-low-cost-grid-monitoring-and-controls-platform>
- ACEP announcement: <http://acep.uaf.edu/acep-news/2019/22-july-acep-this-week/hawaii-researcher-demonstrates-grid-monitoring-system-in-psi-lab.aspx>
- Listing as UH OTT technology available for licensing: <http://universityofhawaii.technologypublisher.com/technology/31200>

## **Conservation Voltage Reduction Demonstration**

Initially funded under the Navy Hawaii Infrastructure Modernization and Renewable Integration Project (an ONR-funded microgrid/resilience analysis and planning project performed for joint-base Pearl Harbor-Hickam under the Applied Research Laboratory (ARL) at the University of Hawaii), the primary goal of the project is to demonstrate energy efficiency through Conservation Voltage Reduction (CVR) on a section of the distribution circuit supplying the Plaza Housing complex at USMC Camp Foster in Okinawa, Japan. This project involves technology development, field implementation, test and evaluation of grid improvement technologies.

Specifically, seven (7) distribution service transformers (five of which had existing Advanced Metering Infrastructure (AMI) meters and communications already installed) located on a branch end of the 13.8 kV distribution circuit serving the Plaza Housing complex (Feeder F6A) were identified for CVR demonstration. A new distribution pad mounted Voltage Regulator (VR), in conjunction with near real-time voltage recordings taken at the transformers and communicated back to the VR controller, will regulate the primary voltage of these seven (7) transformers, in turn managing the customer services voltages to the lower limit of the +/- 5% acceptable ANSI voltage range. We expect a reduction in energy consumption in the range of 0.7% to 0.9% for every 1% reduction in voltage. This is the primary value proposition of effective CVR implementation – reduced energy use by more effective management of customer service voltage.



Working in close collaboration with Marine Corps Facilities personnel in Okinawa, Feeder F6A was selected for the CVR demonstration project. This single feeder has approximately fifty-six (56) distribution service transformers and is fed by a large substation transformer providing power to a total of ten (10) feeders. To achieve the project objectives within the scope, budget and implementation scale of an effective field demonstration project, only a section of the entire Feeder F6A was identified for CVR control. The CVR controlled feeder section was isolated with the VR to manage/control the voltage at “downstream” service transformers, essentially behaving like a substation transformer LTC for the limited section of the feeder under test.

Figure 5.18 below is an electrical one-line schematic of the project area. The existing electrical infrastructure integrated with new technology deployment under this project include the new VR and its HNEI developed controls (with associated by-pass switch) located at GS32, seven distribution service transformers powering an array of loads representative of those normally found on a military base (e.g., officer’s club commercial load, troop barracks, residential housing, etc.), metering at service transformers and AMI radio network connections, an HNEI developed reactive power voltage management source and controller installed at TH415, and a 5 kW rooftop PV system located on a building served from TH415.

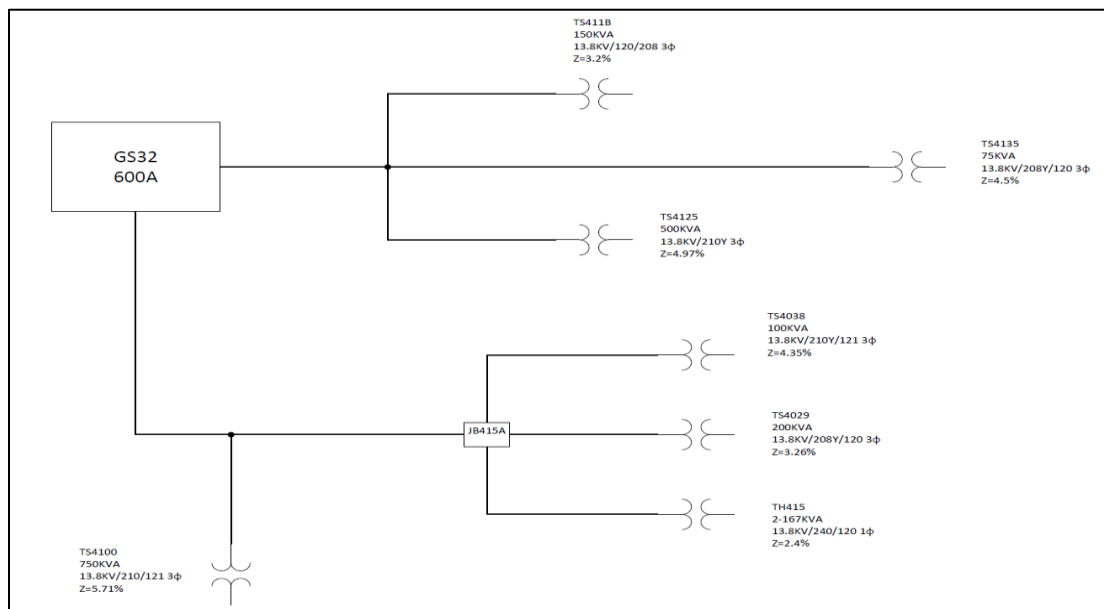


Figure 5.18. Project demonstration area electrical one-line schematic.

Utilizing the hardware-in-the-loop platform in HNEI Grid**START**’s technology development laboratory, testing was performed to validate the proposed CVR control algorithm and the associated communications between the field meters and the CVR controller. Figure 5.19 is a diagram depicting the major components of the HIL test set-up.



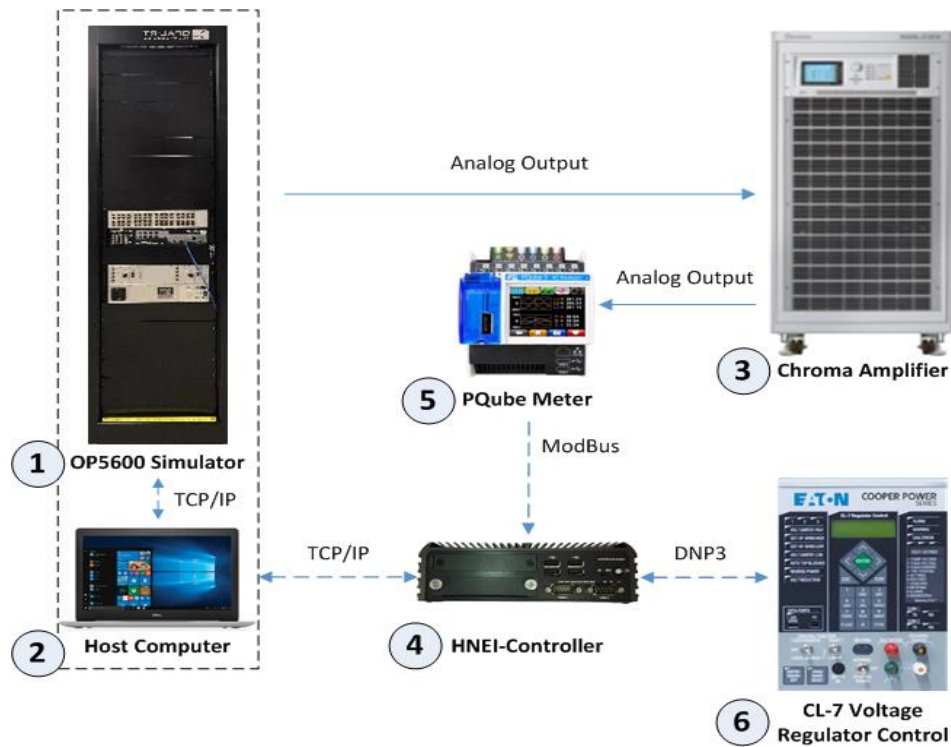


Figure 5.19. Real-time co-simulation platform for CVR test.

The primary piece of hardware and software under test was the HNEI-controller shown in Figure 5.19. Other hardware elements, such as a PQube power monitoring meter and the CL-7 VR controller, are used as ‘stand-ins’ for HIL testing. An OPAL-RT grid simulator and Chroma power amplifier are used to simulate the project area distribution grid. OPAL-RT can simulate power networks in real-time and provide measurements through its I/O boards. The measurements are from earlier recorded field collected data from the project area service transformers and were reproduced and repeatable for testing purposes. The analog output range of the OPAL-RT is  $[-16V, +16V]$ , while the field recorded voltage measurements have a 120V base. Thus, the OPAL-RT measurements are first sent to the Chroma power amplifier and then to the PQube power meter (Process 2-1-3-5), before transmission to the HNEI-controller.

The communication between the OPAL-RT and HNEI-controller (Process 2-1-4) is tested as shown in Figure 5.19. The OPAL-RT simulator works as a TCP/IP master, and it waits for the controller to setup the connection and ask for the measurements. The HNEI-controller receives the measurements and through the exercise of the HNEI developed control algorithm, determines the new VR tap position, the tap position is sent back to the OPAL-RT and updated in each time step.

Due to the way the CL-7 VR controller works with the voltage regulator, the output of the CL-7 does not loop-back into the HIL test. Instead, control commands initiated by the HNEI-controller are sent to both the OPAL-RT simulator and the CL-7 and the commands are verified visually on the front panel of the CL-7. The hardware and associated control software is tested across 6 major categories of operational scenarios:

1. Normal operation
  - Communication with remote PQubes are okay.
  - All voltages are within ANSI limits.
2. Communication dropouts
  - One or more PQubes (at service transformers) lose communication with the HNEI-controller.
  - If two or more PQubes lose communication for more than 2 minutes, return the VR to a neutral tap position.
  - Normal operation resumes when enough PQubes have established communication.
3. Critical low or high voltage sensed
  - If any sensed voltage is outside of the ANSI limit for more than 5 seconds, return the voltage regulator to neutral.
  - Normal operation resumes when voltages return to within ANSI limits.
4. Configuration changes
  - Certain control parameters of the HNEI-controller can be changed while the program is running (no reboot required).
5. Tap limits
  - The VR will be restricted to operate between neutral and the lowest tap position.
6. Power loss or controller reboot
  - CL-7 and VR returns to neutral if it loses communication with the HNEI-controller due to power loss, controller reboot, software or hardware failure.
  - Normal operation resumes after recovery from a power loss or after the HNEI-controller reboots.

Under APRISES14, Grid**START** also developed a user-interface to provide USMC Okinawa personnel with information regarding the status of the VR and HNEI-controller. Webpages hosted on the HNEI-controller allow remote monitoring of the system. A simple ‘snapshot’ page shown in Figure 5.20 shows all data being recorded by the controller at that time. A ‘dashboard’ page shown in Figure 5. 21 depicts the latest 3-minutes of real-time data plotted on time-series graphs.

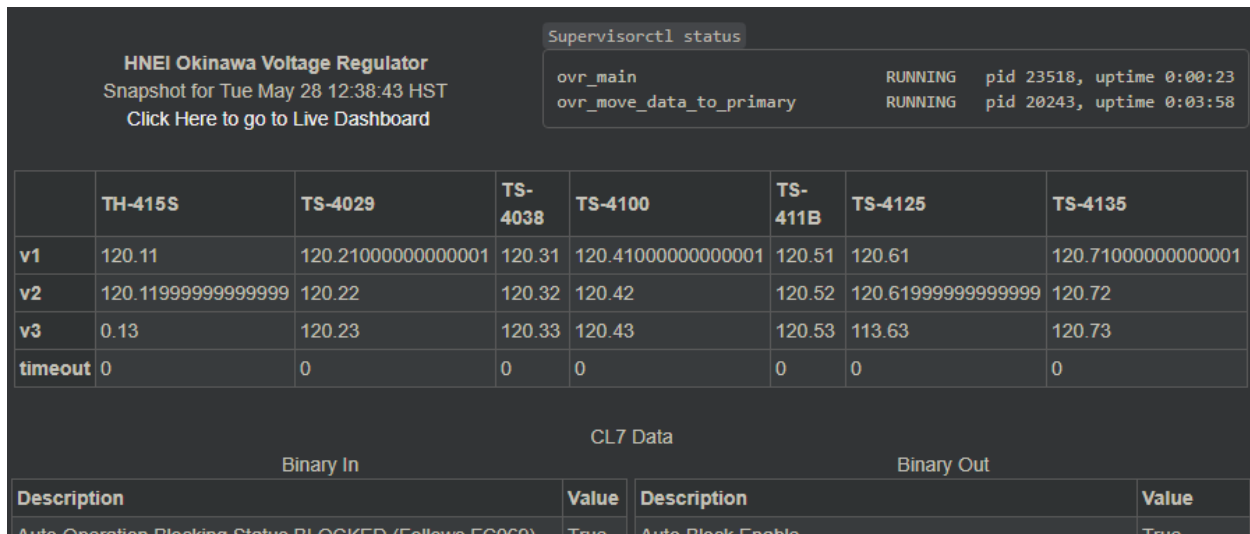


Figure 5.20. Snapshot webpage of HNEI-controller.

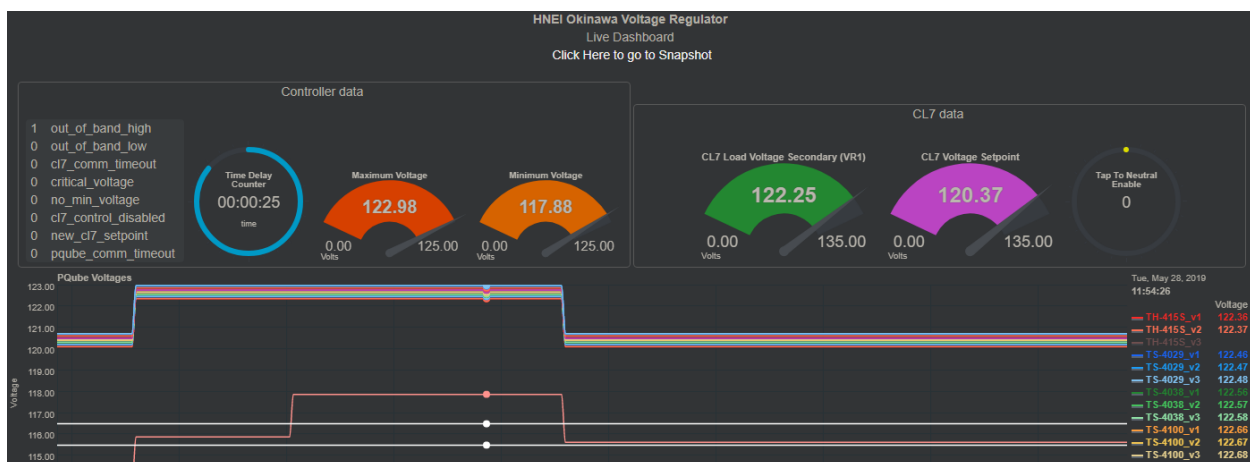


Figure 5.21. Live Dashboard webpage of HNEI-controller.

Multiday real-time HIL simulations were performed to ensure the algorithm and HNEI-controller is robust and reliable under various load conditions. Figure 5.22 is an example of a 24-hour period with and without the CVR algorithm in operation. As indicated in the figure, the normal operating voltage on the distribution feeder is significantly and consistently reduced over the entire 24-hour test period. This reduction in operating voltage, while still maintaining voltage within the ANSI performance limits, is anticipated to deliver significant reduction in energy consumption for the loads in service.

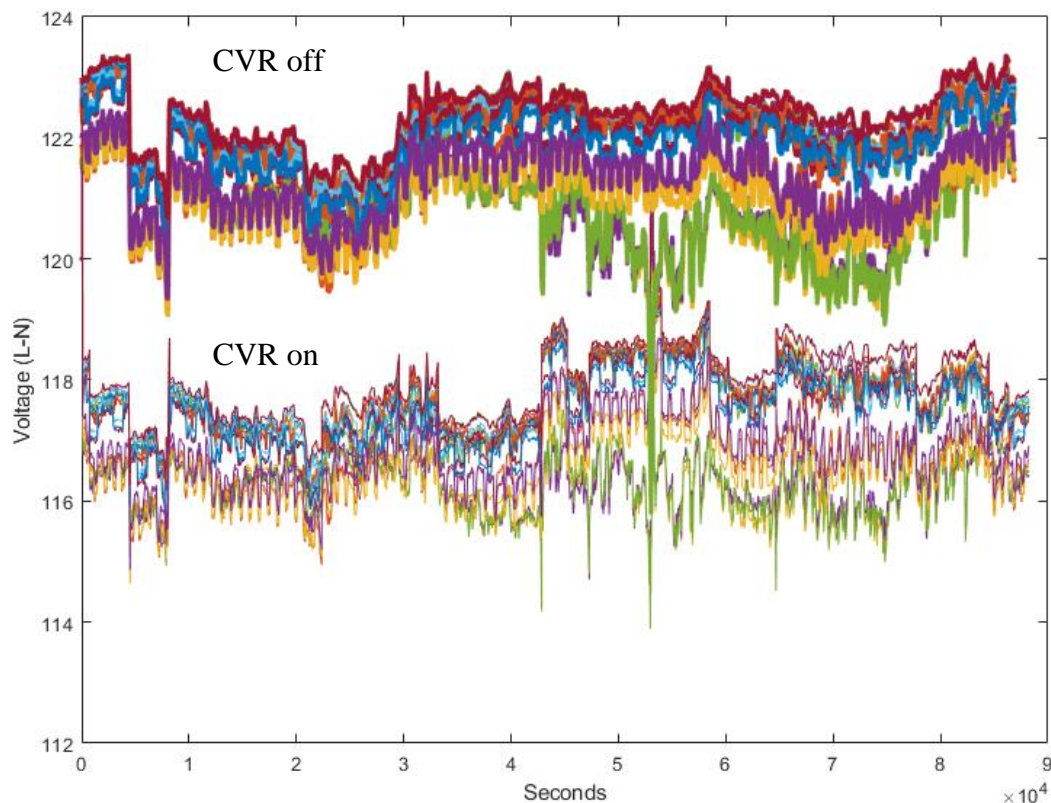


Figure 5.22. Voltage Profiles with CVR on and off

HNEI also worked closely with USMC Okinawa base personnel and the design engineering team to develop the bid package for the final construction and field installation work required to install the VR and by-pass switch, and all associated electrical connection work. The bid package was issues and a construction contract has been awarded. To ensure the VR is installed properly, perform site acceptance testing and equipment commissioning, HNEI has worked in close collaboration with Eaton (manufacturer of the VR and by-pass switch) to define the scope of work for this element of project execution. Both the contracts for construction and VR acceptance test and commissioning will completed under APRISES15 funding support.

### Solar Forecasting

Power output from PV systems is directly related to the power of the sunlight striking the panel, which is measured in irradiance ( $\text{W}/\text{m}^2$ ). Extraterrestrial, or top of the atmosphere irradiance varies with Sun-Earth geometry. Ground-level irradiance is further modulated by the absorption and scattering of sunlight by water and ice particles in clouds, fog and haze, and other particulates

such as dust, ash, and smog. Complex, nonlinear and dynamic atmospheric processes affect these particles, causing large and erratic fluctuations in irradiance and solar power generation. At high penetration levels, PV generation variability and the accompanying uncertainty of future PV generation can cause a range of challenging issues for electric grid operations.

The goal of this project is to develop and employ methods to capture and characterize irradiance variability and to forecast irradiance and PV generation on timescales from minutes to days ahead. The HNEI solar forecasting system combines separate forecasting methods that focus on, and are more accurate at different forecast horizons. Regional, day-ahead (DA) forecasts are generated using numerical weather prediction (NWP) models. Regional, hour-ahead (HA) forecasts are generated using satellite image-based algorithms. Local, minute-ahead (MA) forecasts are generated using sky image-based algorithms.

The observation database described will have several applications for this project: (i) to characterize irradiance patterns and variability in Hawaii; (ii) to evaluate, calibrate and validate the models and algorithms used by the solar forecasting system; and (iii) to develop climatology products for the solar forecasting system.

Under previous APRISES funding, HNEI began development of a long-term observation database to study regional irradiance patterns and variability, and for calibration and validation of methods and models related to solar forecasting. Under APRISES14 funding, we have significantly expanded this database. We have also utilized the observations within the database to calibrate and validate several components of the solar forecasting system, generate a new regional turbidity product for clear sky irradiance modeling, and evaluate the effects of the new turbidity product on the accuracy of satellite image derived irradiance. We introduce and briefly present results from this work below.

We have expanded the observation database to contain a combination of satellite irradiance maps and ground-based irradiance and PV power time-series and have developed software to quickly add to, search, and recall observations within the database. Under previous APRISES funding, a long-term (2006-2016) irradiance dataset for the island of Oahu was generated using imagery from Geostationary Operational Environmental Satellites (GOES) [1]. The observation database contains this dataset; however, we expanded the satellite domain to now cover all of the Hawaiian Islands. The database includes over 123,000, 1 km resolution irradiance maps and the associated raw imagery. The database also includes irradiance observations from ground-based pyranometer instruments from over 40 test sites on the islands of Oahu, Maui, Lanai and Hawaii, and observations of PV power output from 18 monitored PV systems on the islands of Oahu and Maui. Pyranometer and PV power observations were quality checked and homogenized following methodology developed by Longman et al., where data are compared and calibrated using output from a clear sky model.

Figure 5.23 shows the temporal coverage of the observations within the database. The satellite derived irradiance maps have a nominal resolution of 15 minutes and span from 2006 to the end of 2018. A majority of pyranometer and all of the PV power data is at 1-minute resolution. A lesser number of older pyranometer datasets were only available at 1-hour resolution (indicated as “Low-Res Irradiance”). The pyranometer and power observations within the database span from 2003 through 2019, and 2015 through 2019, respectively. The site locations of the pyranometer and power observations are shown in Figure 5.24.

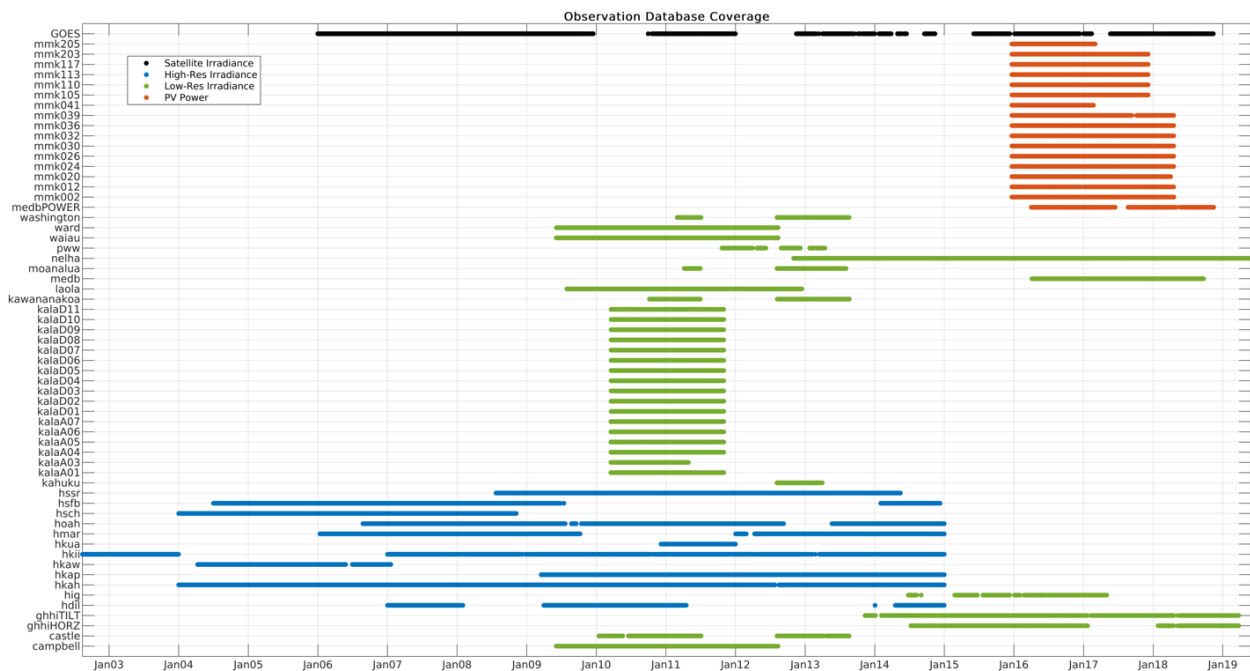


Figure 5.23. Temporal coverage of the observation database.

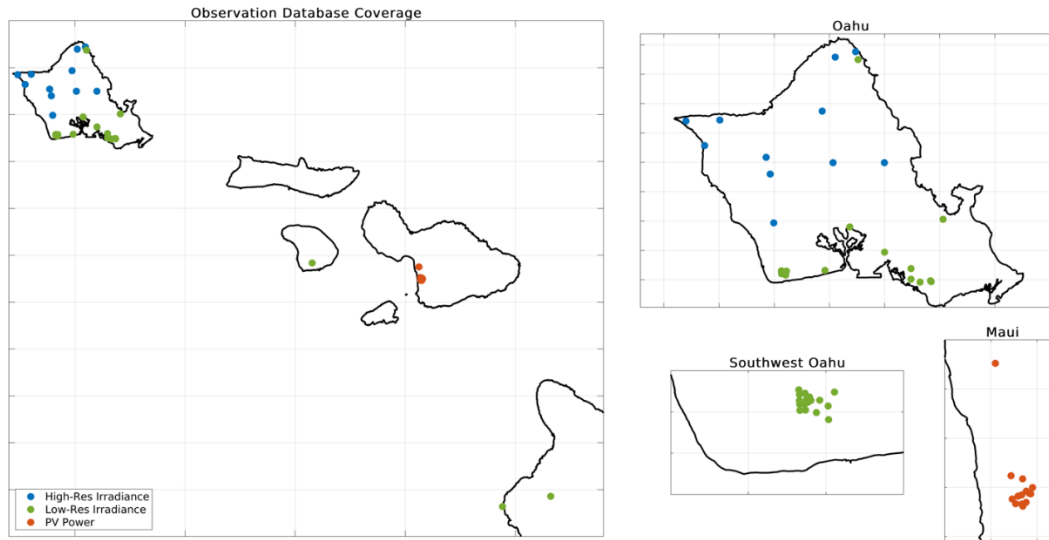


Figure 5.24. Locations of pyranometer and PV power data within the observation database.

Within the database, associated metadata accompanies each observation, as well as solar geometry and clear sky atmosphere information. For ground-based observations, we have also included a binary indicator that identifies clear sky data. The clear sky detection method, which is based on methodology developed by Reno et al. [2], compares the smoothness, shape, and magnitude of observation time-series with coincident output from a clear sky model, applying multiple statistical threshold tests to classify observations. Figure 5.25 shows an example time-series of irradiance observations from the Natural Energy Laboratory of Hawaii Authority (NELHA) test site near the town of Kailua-Kona, on the island of Hawaii. Observations that were classified as clear sky are shown in red, and the clear sky irradiance is shown in orange.

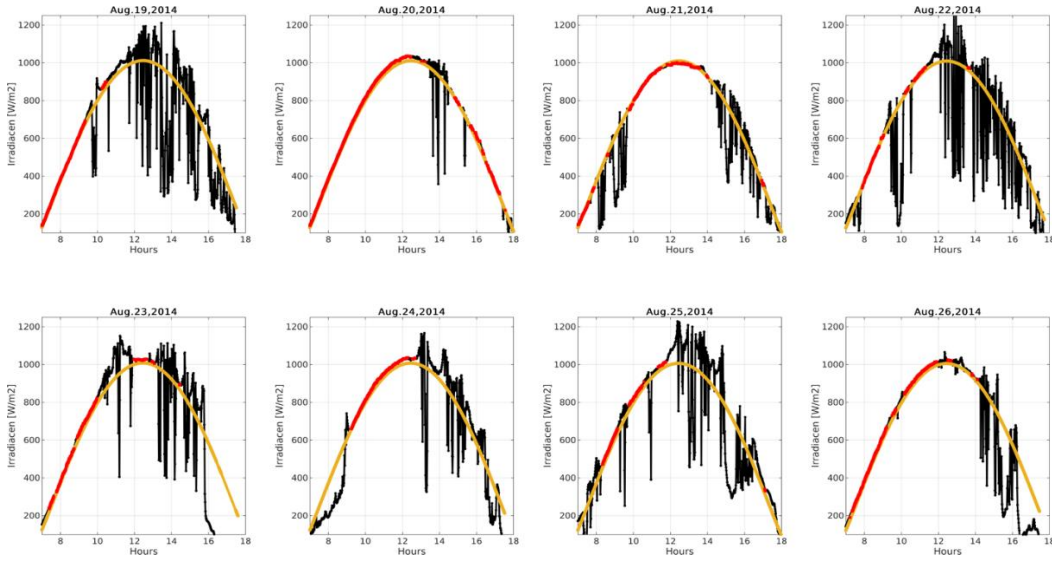


Figure 5.25. Example time series of irradiance observations (black line), with observations identified as clear sky indicated in red and the clear sky irradiance is shown in orange.

In the following, we evaluate the accuracy of the clear sky model, which plays a key role in the solar forecasting system. The clear sky model estimates irradiance conditions under cloudless skies, providing the baseline signal that is modulated by cloud effects determined from satellite or sky image data. So, the accuracy of the clear sky model will set the lower limit of the forecasting error for the HA and MA solar forecasting components.

Our clear sky model is constructed from the formulation proposed by Ineichen and Perez [3]. The model estimates atmospheric transmittance as the product of two terms: the optical thickness of a clean and dry atmosphere, i.e. water and aerosol free; and the Linke turbidity factor (TL), which accounts for the scattering and absorption by water vapor and aerosols. TL is unitless, ranging in value from 1 to 8. Higher TL values indicate, wetter, warmer, and/or more polluted air. In the original setup of our clear sky model, turbidity estimates were extracted from a widely used global turbidity product made available via the Solar Radiation Data (SoDa) Service. The SoDa turbidity product is comprised of global, monthly turbidity maps at  $\sim 10$  km.

The model accuracy is quantified using five metrics: root mean square error (RMSE); mean absolute percent error (MAPE); mean absolute error (MAE); correlation coefficient (CC); and bias. Figure 5.26 shows the accuracy metrics from comparing model output to pyranometer observations classified as clear sky. More specifically, metrics are derived from clear sky model output driven by the SoDa and HNEI turbidity products, compared to irradiance observations identified as clear sky.



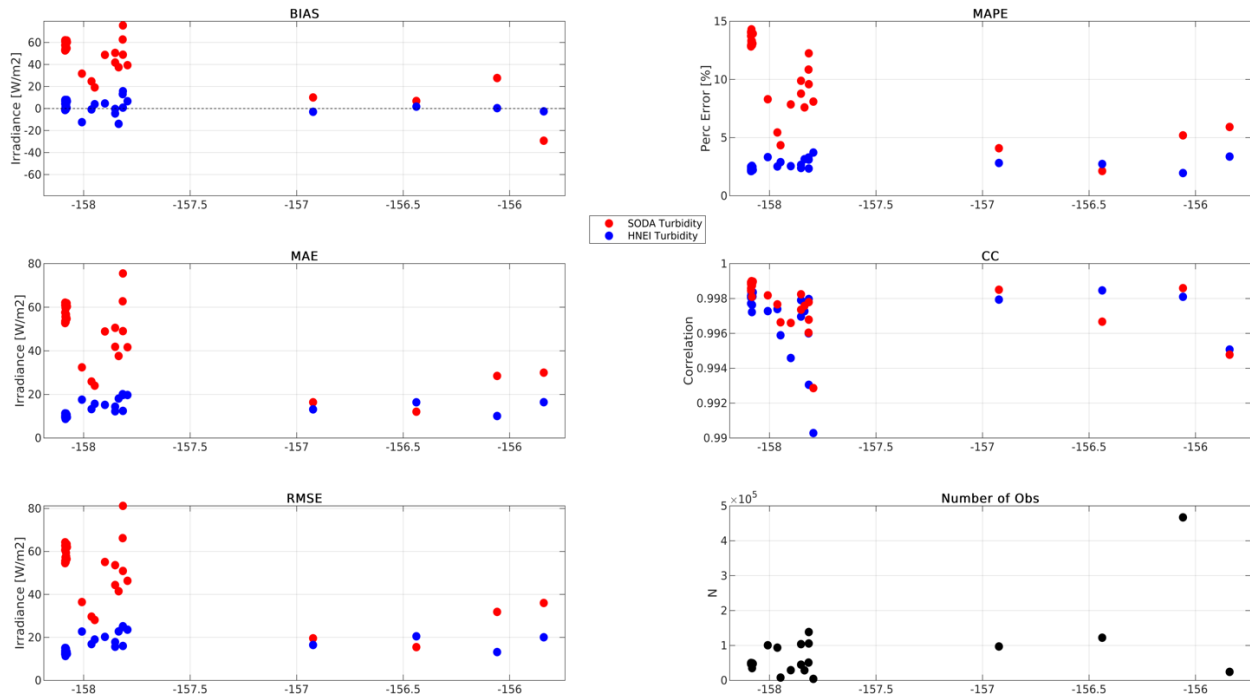


Figure 5.26. Test site clear sky irradiance accuracy metrics with 1-minute resolution data.

Using the SoDa turbidity product, we found significantly higher RMSE and MAE at the test sites on the island of Oahu and that the increased error was primarily a function of model bias due to spatial patterns in the SoDa product. We believe these patterns to be unrealistic, likely due to a lack of regional data and interpolation errors.

Motivated by this result, we constructed algorithms to estimate turbidity from irradiance observations, in order to characterize regional turbidity patterns and variability and generate a new turbidity product for Hawaii. Expressions for turbidity were found by inverting the Ineichen and Perez formulation for direct normal irradiance (DNI) and global horizontal irradiance (GHI) and extracting the turbidity factor. A climatological turbidity time-series was created at each test site using all pyranometer data (over 2.2 million observations) identified as clear sky within the observation database, and dominate length and time scales were estimated using the semi-variogram method [4]. Starting with 10 km SoDa maps, we applied a Laplacian diffuser to propagate the turbidity time-series climatology information across the region onto a 1 km grid and generate 26 bi-weekly turbidity maps, covering a full year. Figure 5.27 shows an example turbidity map from the SoDa product and a coincident map from the new HNEI regional product.

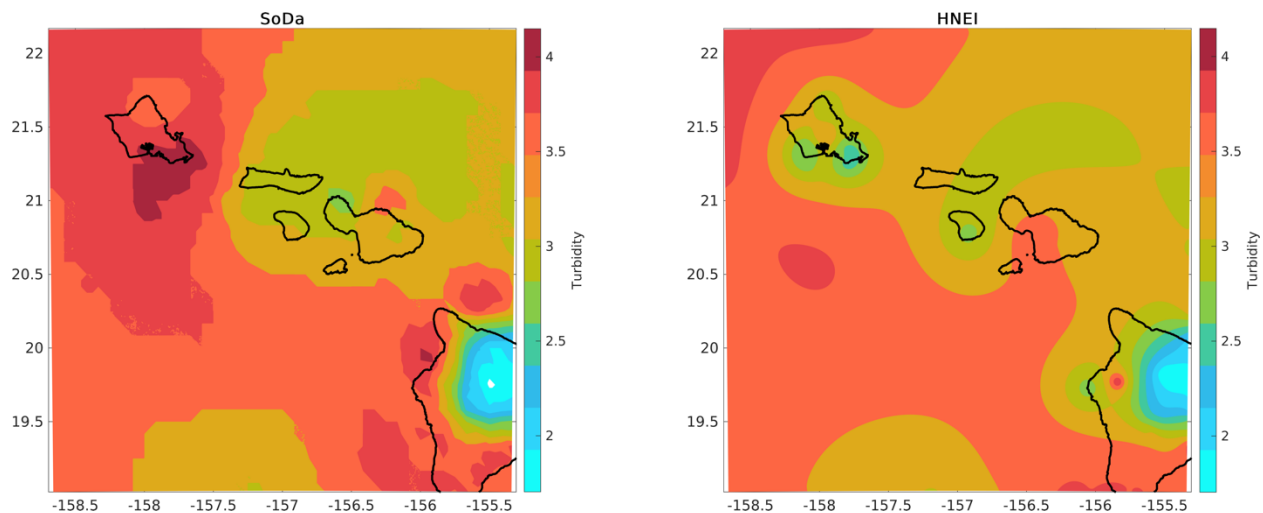


Figure 5.27. Example turbidity maps from the SoDa product (left) and from the new HNEI regional product (right).

The clear sky model accuracy metrics shown in Figure 5.26 were recomputed using the new HNEI regional product. Relative to the initial results using the SoDa turbidity, model error is consistent between test sites at significantly reduced levels, with RMSE ranging from 11 to 26 W/m<sup>2</sup>, MAE from 8 to 21 W/m<sup>2</sup>, and MAPE of 1.8 to 3.7%.

We further evaluated the new turbidity product by testing its effects on the accuracy of satellite derived irradiance estimates. Employing the new turbidity, we generated irradiance nowcasts from all archived GOES images, which span from 2006 to 2018. As a baseline, irradiance nowcasts were also generated using the original SoDa turbidity. Satellite irradiance accuracy was quantified using the same five metrics as above, comparing against coincident (in time and space) pyranometer observations. Relative to the initial evaluation described above, this comparison includes both clear and cloud covered observations, as well as the lower resolution pyranometer that was not used in the generation of the new turbidity product. Overall results, per test site, are shown in Figure 5.28.

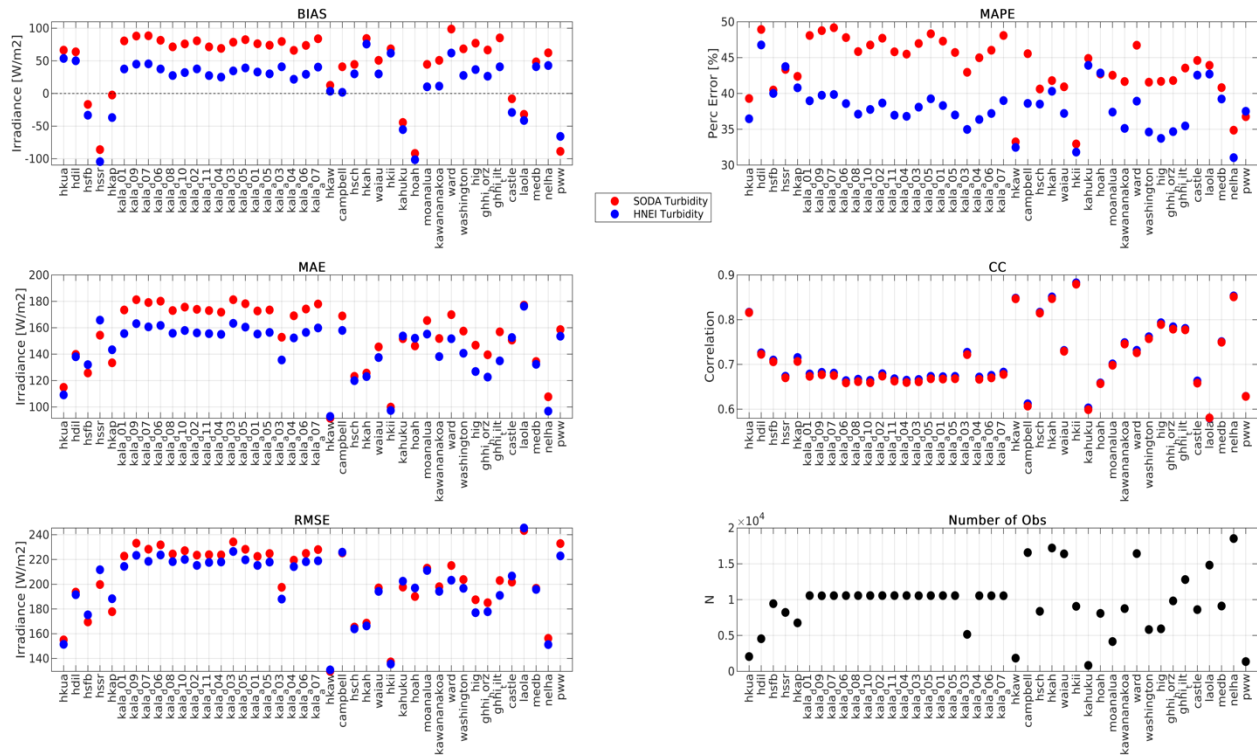


Figure 5.28. Satellite-based irradiance accuracy metrics per test site. Test sites are ordered per longitude, left to right along the x-axis, corresponds to west to east.

Almost all sites show increased accuracy using the new turbidity product. The change in accuracy of satellite derived irradiance estimates using the new turbidity product relative to estimates from SoDa turbidity are as follows:

- Bias was reduced by 32.2 W/m<sup>2</sup>;
- MAPE was reduced by 6%;
- MAE was reduced by 11.5 W/m<sup>2</sup>;
- RMSE was reduced by 4.6 W/m<sup>2</sup>; and
- CC was increased by 0.02.

More testing is required, but these initial results suggest that the new turbidity product will provide significant benefit for the HNEI solar forecasting system, as the reductions in error will propagate through the HA and MA solar forecasting components.

## References

[1] Williamson, S., Businger, S., and Matthews, D. 2018. Development of a solar irradiance dataset for Oahu, Hawai'i. Renewable Energy, Elsevier, vol. 128(PA), pages 432-443.

- [2] Reno, J. and Hansen. C. 2016. Identification of periods of clear sky irradiance in time series of GHI measurements. *Renewable Energy*, Volume 90, pages 520-531.
- [3] Ineichen, P. and Perez, R. 2002. A new airmass independent formulation for the Linke turbidity coefficient. *Solar Energy*, vol. 73, no. 3, pages 151-157.
- [4] Matthews, D., Powell, B., and Milliff, R. 2011. Dominant spatial variability scales from observations around the Hawaiian Islands. *Deep Sea Research Part I: Oceanographic Research Papers*, 58(10), 979–987, doi:10.1016/j.dsr.2011.07.004.

### **Advanced Power Systems Laboratory**

HNEI Grid**START** is equipping a laboratory to facilitate its ongoing research activities across several active projects under Task 5 of APRISES14, and to extend its forward capabilities to research, develop, test and evaluate new technologies in support of electric power systems modernization and renewable energy integration initiatives. Under APRISES14, HNEI developed a conceptual design for its new Advanced Power System Laboratory (APSL) and collaborated with a local electrical engineering firm to produce design drawings necessary for laboratory build-out based on a highly flexible architecture incorporating state-of-the-art grid test and simulation equipment.

Major elements of the lab architecture include a 35.3 kW rooftop PV system fed into the lab room connected to four (4) advanced PV inverters equipped with grid support functions serving three (3) equipment test bays. The architecture also includes a real-time grid simulator connected to a 30 kVA power amplifier. This system is known as a power hardware-in-the-loop (PHIL) configuration because it can evaluate electrical power equipment as units under test (UUTs) in a real-time simulated grid environment. Figure 5.29 illustrates the main components of the lab architecture.

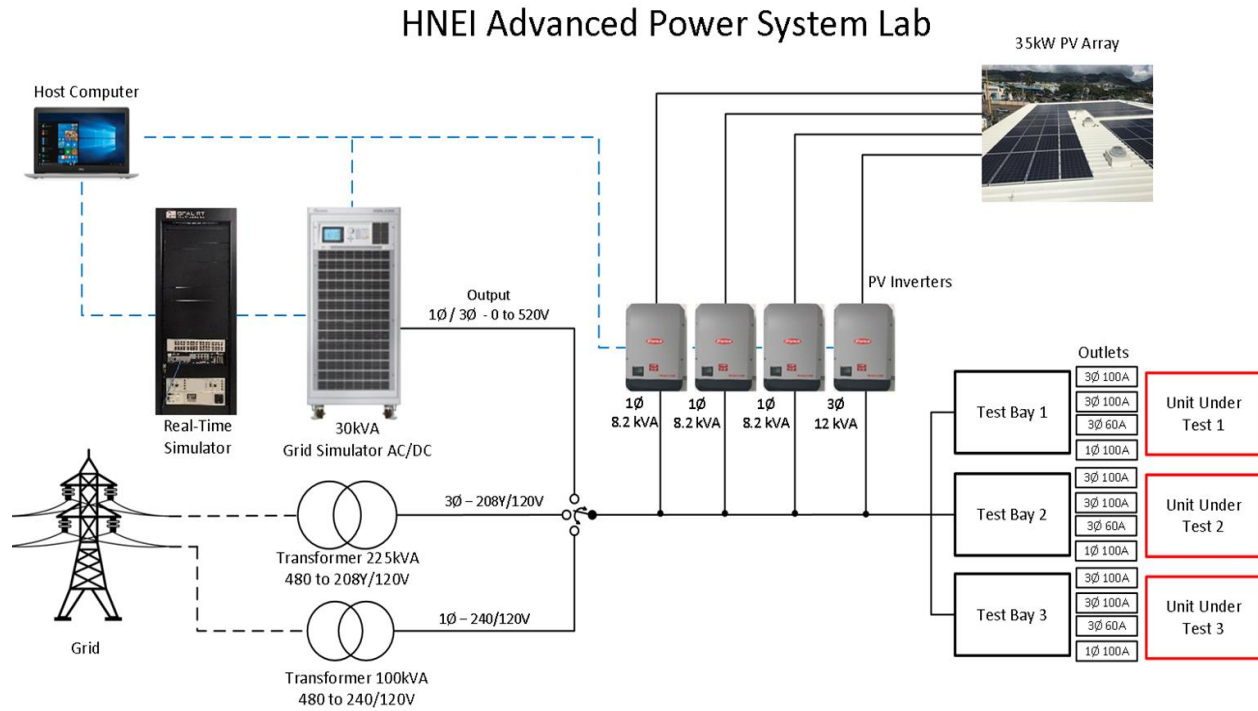


Figure 5.29. HNEI Grid**START** Advanced Power System Lab architecture.

The lab architecture includes three modular test bays that can be used to evaluate the advanced functions, communications and controls of various UUTs including by way of example, equipment such as:

- Advanced function PV inverters.
- EV chargers, including vehicle-to-grid (V2G), vehicle-to-home (V2H) enabled chargers.
- Battery energy storage systems (BESS).
- Power monitoring and edge computing device.
- AC or DC loads/appliances and load control devices.
- Voltage management devices.

Each of the three APSL test bays will be equipped with outlets rated at different voltages (3 $\Phi$  208Y/120 V grid-tied, 1 $\Phi$  240/120 V grid-tied, 3 $\Phi$  0~520 VLL Grid Simulator, 600 VDC off-grid) and currents as shown in Figure 5.30.

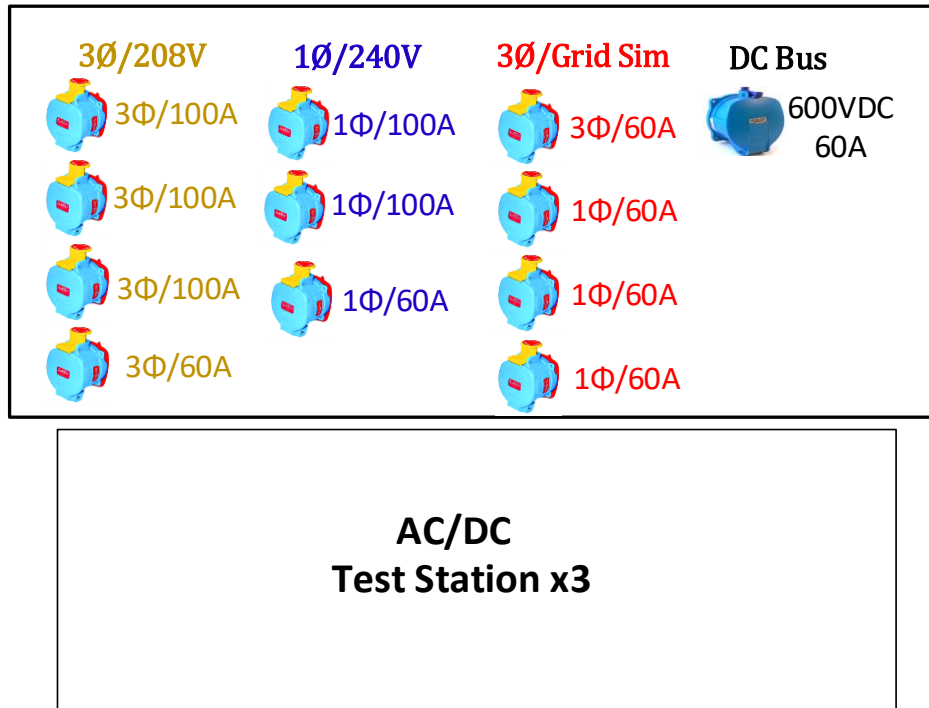


Figure 5.30. AC/DC test bay.

The lab architecture includes an off-grid DC test bed rated at 600 VDC that is accessible at each of the three APSL test bays. The DC test bed can be powered either by the direct output of the rooftop PV array or by the 30 kVA grid simulator configured for DC operation. The DC outlets on the workbenches can be used to evaluate DC loads, inverters, batteries, etc. The DC test bed is shown in Figure 5.31.

## DC Test Bed (off-grid)

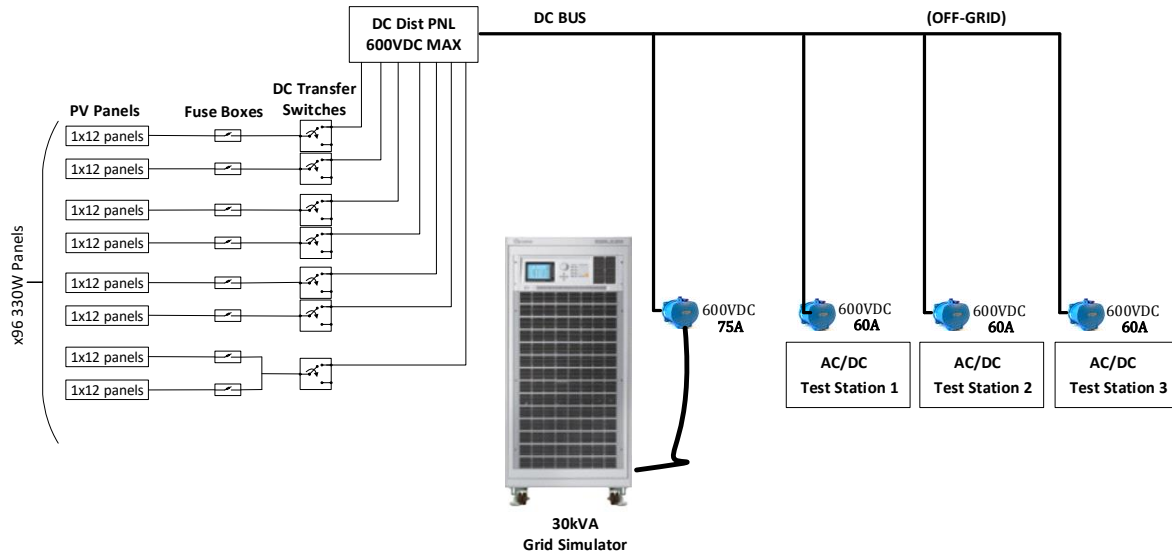


Figure 5.31. DC test bed (off-grid).

The lab architecture also includes an AC test bed comprised of the following three AC test buses:

- 1 $\Phi$ /3 $\Phi$  0~520 VLL AC grid simulator bus served by the Chroma 61830 grid simulator.
- 3 $\Phi$  208Y/120 V AC bus served by a 225kVA transformer.
- 1 $\Phi$  240/120 V AC Bus served by a 100kVA transformer.

The 1 $\Phi$ /3 $\Phi$  0~520VLL AC grid simulator bus is shown in Figure 5.32.

## AC Test Bed – Grid Simulator Bus (off-grid)

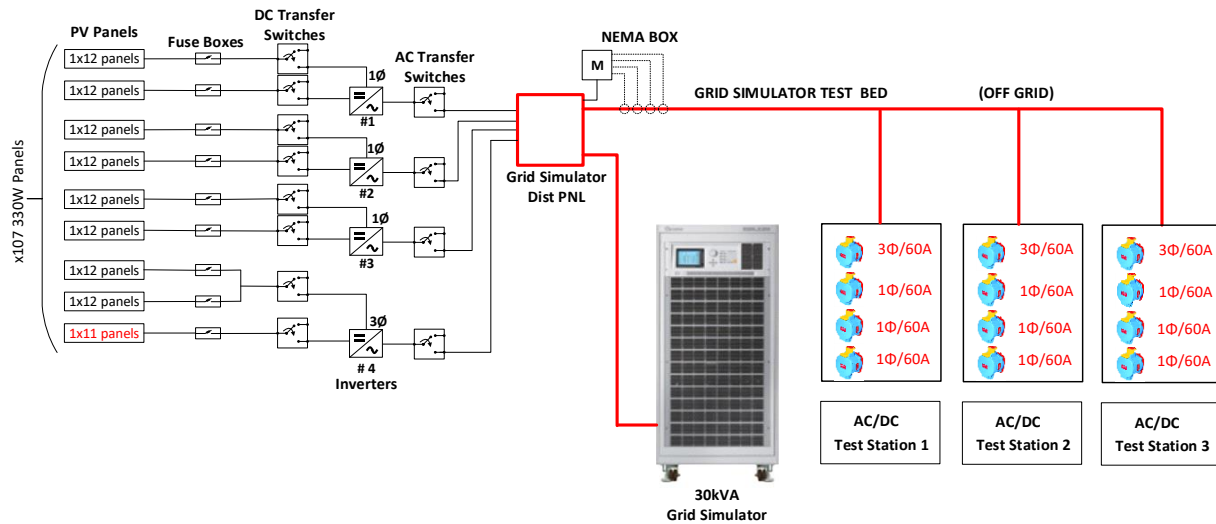


Figure 5.32. AC test bed – Grid simulator (off-grid).

The 3Φ 208Y/120 V AC bus is shown in Figure 5.33.

## AC Test Bed – 3Φ 208Y/120 V AC Bus (grid-tied)

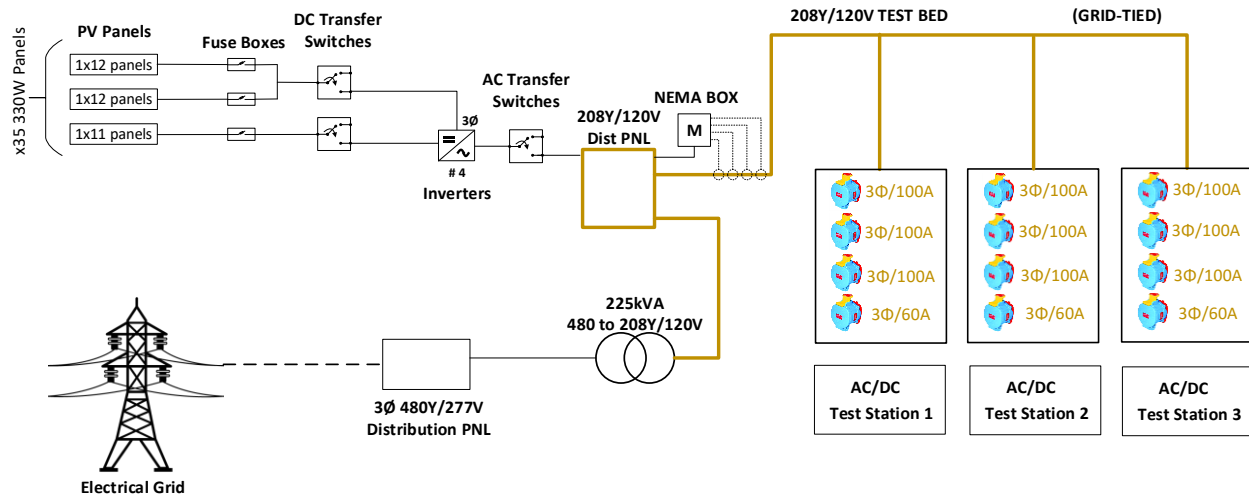


Figure 5.33. AC test bed – 208V (grid-tied).

The 1Φ 240/120 V AC bus is shown in Figure 5.34.



## AC Test Bed – 1Φ 240/120 VAC (grid-tied)

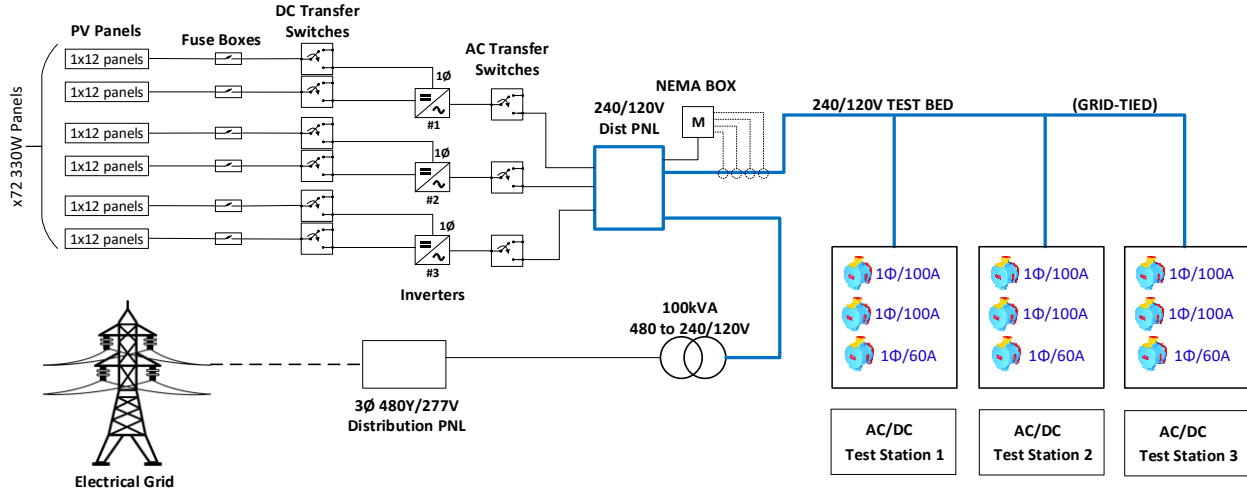


Figure 5.34. AC test bed – 240V (grid-tied).

Under APRISES15, HNEI will contract a highly qualified electrical lab safety consultant to perform a design review. Upon design review completion, the consultant will make necessary recommendations for laboratory design revisions as may be needed and develop appropriate administrative and safe work practices controls to ensure the safe operation of the laboratory and all activities performed therein. In collaboration with HNEI, the consultant will develop the laboratory electrical safety program and associated safety standard operating procedures for laboratory use. Once all recommendations from the safety design review have been fully addressed and incorporated into the design drawings, HNEI will issue the bid package for the electrical work to complete the laboratory build-out. The APSL is expected to enable valuable and productive research, development, test and evaluation of new technologies by HNEI Grid**START** for years to come.

## TASK 6: OCEAN ENERGY

Ocean Energy focused on development of Ocean Thermal Energy Conversion (OTEC). Under a subaward to Makai Ocean Engineering, development of OTEC for both US Navy and commercial applications continued at the Ocean Energy Research Center (OERC), located within the Natural Energy Lab of Hawaii Authority (NELHA) in Kailua Kona, Hawaii.

Makai's work has focused on developing, fabricating, and testing Thin-Foil Heat Exchangers (TFHX) and corrosion testing. Complete detail of the work can be found in the report on HNEI's website.

Makai continues to conduct corrosion testing of aluminum alloys in 915-m cold seawater (DSW), 674-m cold seawater (CSW), and surface seawater (WSW). Previously, 5-year box beam samples were removed from DSW, CSW, and WSW. DSW and CSW samples had pits on nearly all samples. Pitting was most severe in DSW. Although some samples in CSW only had a few pits, alloy performance has been unpredictable; Makai does not recommend the use of untreated aluminum alloys for use in condensers. WSW samples had little to no pitting.

Biofouling has become a problem for warm seawater samples. Any missed or reduced hypochlorite dosages lead to formation of a biofilm. Once the biofilm is formed, hypochlorination becomes less effective. Previous studies on ozone and iodine treatment were unsuccessful at preventing biofouling; consistent, reliable hypochlorination treatment with dosages based on the oxidation reduction potential (ORP) has been most effective at preventing biofouling.

Foil-Fin Heat Exchanger (FFHX) and TFHX samples have also been tested in the cold seawater MCIR. As expected, FFHX samples have failed at burnthroughs where aluminum is in contact with seawater. TFHX samples are being tested in order to observe biofouling growth and fatigue response due to fluctuations in flow.

Makai's TFHX is fabricated using a Makai-developed proprietary process. The TFHX offers several advantages over Makai's previous heat exchanger concepts, the Epoxy-Bonded Heat Exchanger (EBHX) and FFHX (Table 6.1). Primarily, the manufacturing reliability made FFHX unfavorable while ammonia incompatibility and issues with epoxy creep and absorption eliminated the EBHX.

In parallel with TFHX fabrication, Makai designed, constructed, and commissioned the 100-kW testing station to test TFHXs. The 100-kW testing station is scaled at 100 kW nominal duty to allow for rapid fabrication times (fewer plates) while maintaining adequate instrument accuracy. The testing station has been designed with four "slots" for heat exchangers, but the ability to easily expand to include future stations was incorporated into the design concept. Minor issues during construction and commissioning were overcome and the 100-kW testing station was operational by March 2018.

Makai fabricated and successfully pressure-tested the first 1.2-m long TFHX plate in November 2017 and continued on to fabricate twelve 1.2-m TFHX plates (6 plates per configuration) for

performance testing. Each configuration was tested as both a condenser and an evaporator. TFHX2 performed better than TFHX1, driven by higher ammonia-side heat transfer coefficients even though the seawater convective coefficient was higher for TFHX1.

Table 6.1. Comparison of TFHX, FFHX, and EBHX.

	Working Fluid Compatibility	Manufacturing Reliability	Tine to Fabricate	Pressure Rating	Compactness
TFHX	No restrictions	High success rate	1 <sup>st</sup> single plate, 5.5 man-hours*	Max tested pressure = 503 psi but pressure rating depends on fabrication parameters, >2100 psi possible	Currently ~400 m <sup>2</sup> of heat transfer area per m <sup>3</sup> , goal is >1000 m <sup>2</sup> / m <sup>3</sup>
FFHX	No restrictions	~ 60% of weld lines had defects	N/A	Max tested pressure = 185 psi	< 300 m <sup>2</sup> of heat transfer area per m <sup>3</sup>
EBHX	Incompatible with ammonia	High success rate	2 plates, 8.25 man-hours	Max tested pressure = 800 psi	< 300 m <sup>2</sup> of heat transfer area per m <sup>3</sup>

\* Fabrication time for the first plate from start to finish, not including cleaning time. Future plates will utilize assemblyline style process and is expected to significantly reduce average fabrication time per plate.

In order to compare the TFHXs to the previously tested heat exchangers at the OERC, the TFHXs had to be scaled up (by adding plates in parallel) so the duties were matched. Due to the compactness (i.e., high heat transfer area to volume ratio) of the TFHX, a 2 MW TFHX is 4-8X smaller in volume than the heat exchangers previously tested at the OERC (Figure 6.1).

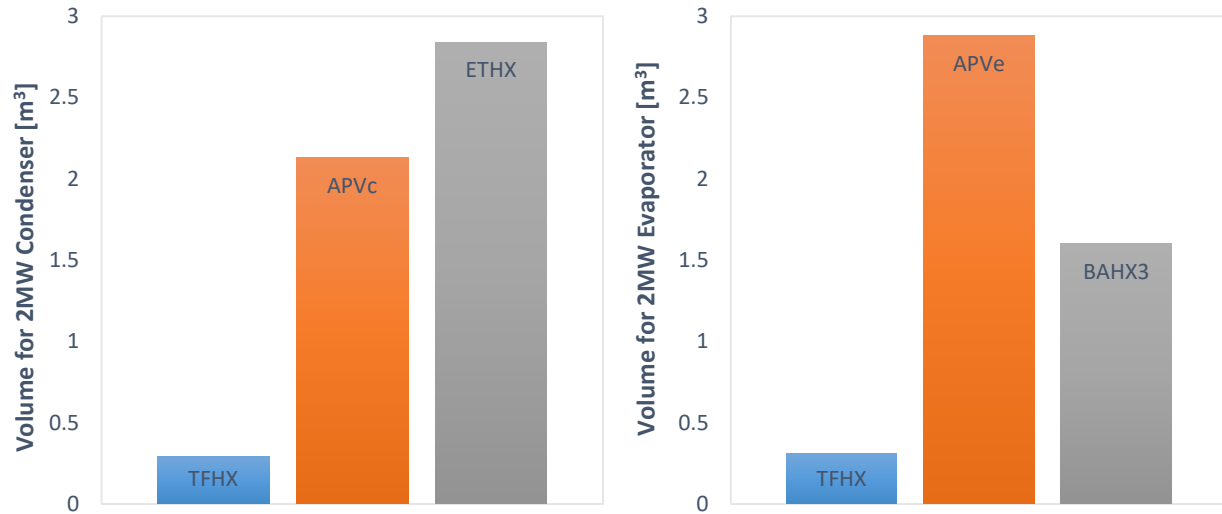


Figure 6.1. Comparison of required volume for 2 MW heat exchanger.

It was also important to compare results based on seawater pumping power (vice the seawater pressure drop) because it accounts for the volume of water flow required for the duty. Compared to previously tested condensers, TFHXs had higher U-values for the same seawater pumping power (through the heat exchanger only). TFHX, as an evaporator, had higher U-values compared to APVe but lower than BAHX3.

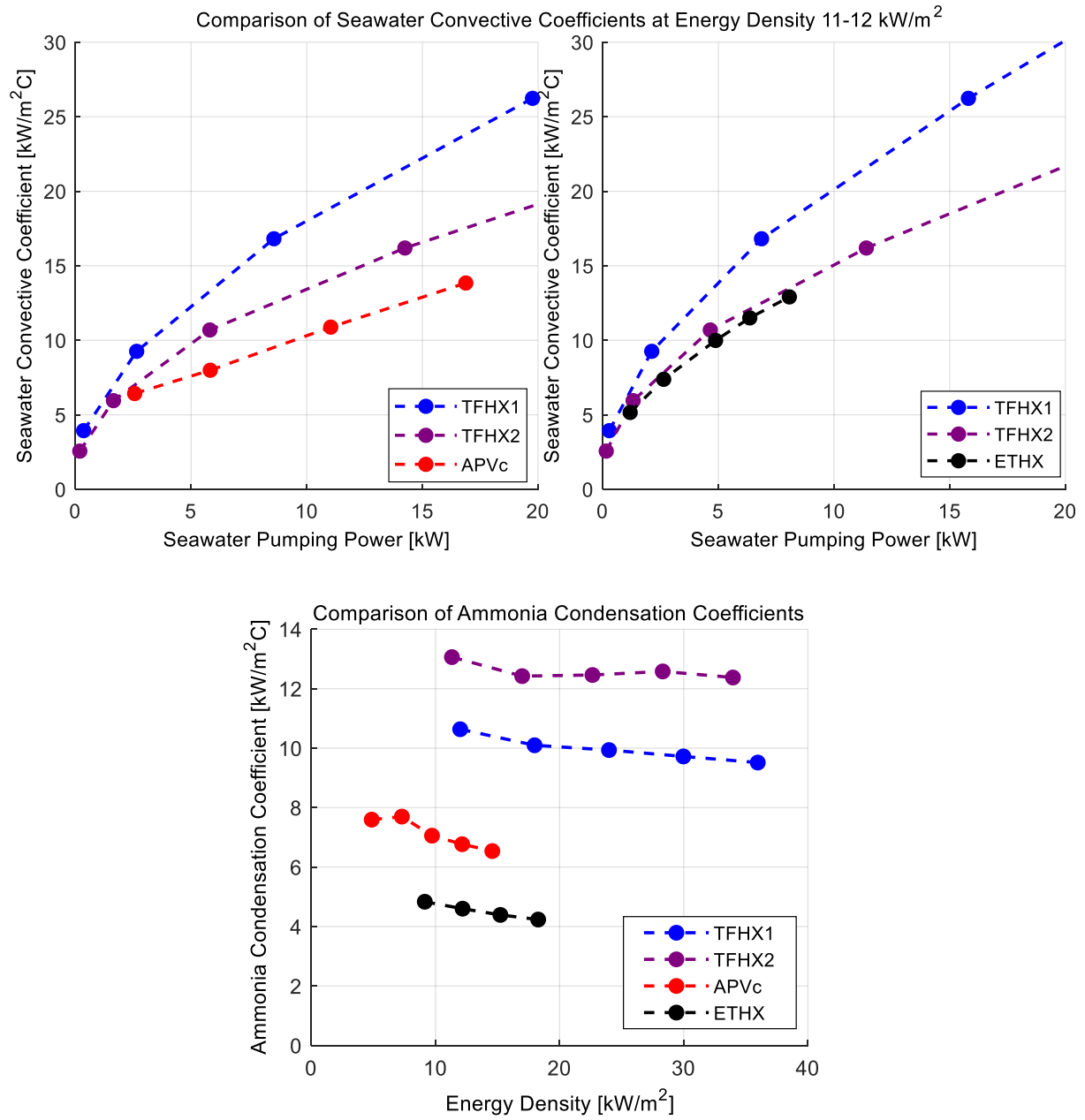


Figure 6.2. Comparison of condenser seawater (top) and ammonia (bottom) convective coefficients.

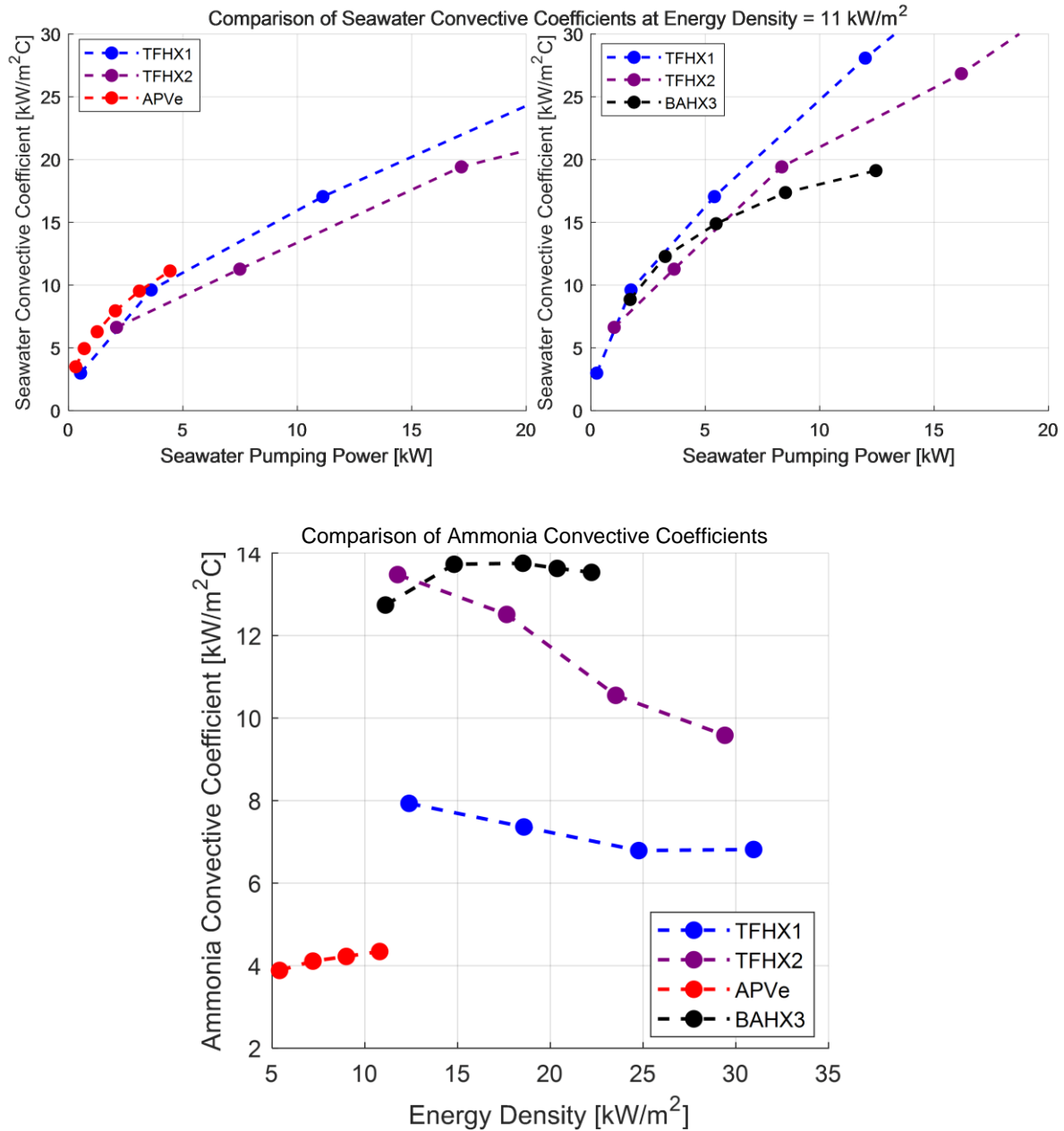


Figure 6.3. Comparison of evaporator seawater (top) and ammonia (bottom) convective coefficients.

In terms of an OTEC heat exchanger, the highest U-value may not always mean the best heat exchanger. An OTEC plant with the highest pressure drop across the turbine and the lowest seawater pumping power (for a fixed ammonia vapor flow rate, i.e., duty) will have a higher net power. When evaluated in terms of heat exchanger operating pressure, at 2MW duty, the TFHXs have a better operating pressure at the same seawater pumping power *and* higher energy density compared to the previously tested heat exchangers.

However, using current fabrication methods, at the 2MW scale, the TFHX is 2-3X more expensive than competitor heat exchangers. Makai identified materials and labor (time) as the two major contributors to TFHX cost. With additional development, the cost to produce the current components could likely be reduced significantly (as much as 6X) when using high quantity fabrication techniques rather than prototyping. Along with design changes to further improve performance and compactness, Makai's next TFHX also utilizes smaller, less costly components and is anticipated to require less time to fabricate. These improvements are targeted at making TFHX the obvious choice for not only OTEC, but many other heat exchanger applications.

For more detailed information, see the complete report on HNEI's website.

## **TASK 7: ENERGY EFFICIENCY**

Under this task, HNEI resumed monitoring of the first generation Project Frog buildings, installed under previous ONR funding, in order to compare performance to second generation FROGs installed at UH Manoa. A more detailed analysis of the data collected under APRISES 14 will be completed and reported under APRISES15.

A second effort was to install, test, and report on performance of a novel "High Wind Energy Generator" concept developed by HEWS Technology, Inc. The installation and data collection was conducted by HEWS Technology under contract to HNEI. HNEI participated in the analysis of the performance.

### **7.1 Data Collection First Generation Project Frog Buildings**

HNEI contracted with consultant MKThink to recommission the environmental monitoring instrumentation on three Project Frog buildings located in Ewa Beach (Ilima Intermediate) and Lihue, Kauai (Kawaikini Charter School, East and West Buildings). These FROGs were installed under HEET 2009 and 2010 ONR funding. Data collection from these original structures had ended in 2015. In 2017, with the instrumentation already in place, HNEI and MKThink recommissioned the instrumentation to collect more current data for comparison to recently collected data from the second generation FROGs on University of Hawaii at Manoa campus (referred to as UH Frog1 and UH Frog2). Comparisons of interest were overall energy consumption relative to generation and interior conditions, including temperature, humidity, and CO2 levels.

Under APRISES14, data collection began on August 1, 2017 and ended September 30, 2018. Over 9 million data points were collected from 147 sensors. Variables that were monitored are shown in Table 7.1.1.

Table 7.1.1 Variables monitored in first generation Project FROGs.

Location	Data Points	Unit
Outdoor Weather	Temperature Relative humidity Dew point Rain Pressure Wind Direction Speed Gust speed Solar Radiation	deg. F percent deg. F inches lbs Hg compass degrees m/s m/s
Indoor Environment	Air Temperature Relative humidity Room air CO2 Room air speed Wall surface temperature Wall and ceiling illuminance	deg. F Percent ppm m/s deg. F lumens
Energy / Elec. Panel	Net energy consumption Net power Total energy consumption Total power Ceiling fans Condensing unit Fan coil unit Exterior lighting Interior lighting Other	kWh kW kWh kW kW and kWh kW and kWh kW and kWh kW and kWh kW and kWh kW and kWh
Energy Generation: Exterior rooftop	Photovoltaic production	kW and kWh

The data was stored and archived on a web server platform operated by MKThink. HNEI had full access to the data using the 4Dapt data visualization tool from MKThink. The 4Dapt visualization



tool can be viewed at <http://ts.4dapt.com/frog>. Figure 7.1.1 is a sample screenshot of the 4Dapt menu of data point categories, with the categories expanded for illustrative purposes:

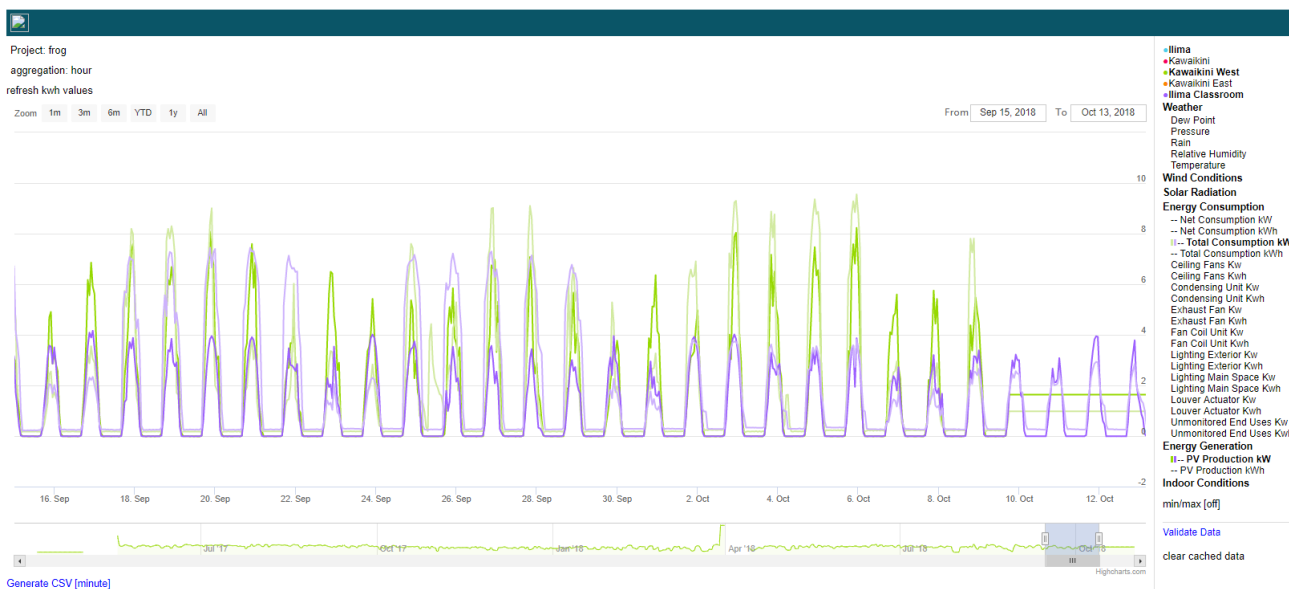


Figure 7.1.1. Sample screen shot of 4Daptive data visualization tool. The right hand column indicates available data. This chart shows total energy consumption (kW) and PV production (kW) for Ilima and Kawaikini West. Variables in bold are visualized.

The hardware that remained on-site from previous monitoring efforts by HNEI and MKThink, was used for this project. Some of the sensors, originally installed in March of 2013, were no longer functioning. MKThink coordinated with HNEI to determine which malfunctioning sensors to replace. Sensors not deemed necessary for the comparisons were not replaced.

Upon re-commissioning, MKThink developed algorithms for each sensor to detect errors and validate the data. A sample of the data validation is found in Table 7.1.2, showing an Error Summary table that identified the sensor, errors detected, missing data, and high/low flags.

Table 7.1.2. Sample monthly error summary table for collected data points.

<b>Error Summary</b>		<b>Current Performance Period (September)</b>					
		<b>Total Data Errors</b>	<b>% of Data Set</b>	<b>Error Types</b>			
<b>Location</b>	<b>Sensor Type</b>			<b>Missing</b>	<b>Bad</b>	<b>Too High</b>	<b>Too Low</b>
Kawaikini West	Air Temperature: East	4	0.1%	4			
Kawaikini West	Air Temperature: West	17	0.4%	17			
Kawaikini West	Floor Surface Temperature: SE	27	0.6%	18		9	
Kawaikini West	Floor Surface Temperature: Center	8	0.2%	8			
Kawaikini West	Floor Surface Temperature: NW	-	-				
Kawaikini West	Plenum Temperature: SE	71	1.6%	37		34	
Kawaikini West	Plenum Temperature: Center	6	0.1%	6			
Kawaikini West	Plenum Temperature: NW	14	0.3%	14			
Kawaikini West	Wall Surface Temperature: East	17	0.4%	17			
Kawaikini West	Wall Surface Temperature: West	4	0.1%	4			
Kawaikini West	Room Air CO <sub>2</sub>	9	0.2%	9			
Kawaikini West	Room Air Humidity	16	0.4%	16			
Kawaikini West	Room Illuminance: Ceiling	21	0.5%	21			
Kawaikini West	Room Illuminance: West Wall	16	0.4%	16			
Kawaikini West	Supply Air Humidity	12	0.3%	12			
Kawaikini West	Supply Air Temperature (°C)	14	0.3%	14			
Kawaikini West	Ceiling Fans (kW)	-	-				
Kawaikini West	Ceiling Fans (kWh)	-	-				
Kawaikini West	Condensing Unit (kW)	-	-				
Kawaikini West	Condensing Unit (kWh)	-	-				
Kawaikini West	Exhaust Fan (kW)	-	-				
Kawaikini West	Exhaust Fan (kWh)	-	-				
Kawaikini West	Fan Coil Unit (kW)	-	-				
Kawaikini West	Fan Coil Unit (kWh)	-	-				
Kawaikini West	Lighting: Main Space (kW)	-	-				
Kawaikini West	Lighting: Main Space (kWh)	-	-				
Kawaikini West	Lighting: Wall & Exterior (kW)	-	-				
Kawaikini West	Lighting: Wall & Exterior (kWh)	-	-				
Kawaikini West	Louver Actuator (kW)	-	-				
Kawaikini West	Louver Actuator (kWh)	-	-				
Kawaikini West	PV Inverter 1: neg (kW)	-	-				
Kawaikini West	PV Inverter 1: neg (kWh)	-	-				

\*Flagged Errors are sensors that are being watched for systemic errors

## CO2 Analysis of First Generation Frogs

Under this task analyses focused on CO2 concentration levels in mixed mode buildings. Users in these structures have the option of opening windows to take advantage of natural trade winds and

localized air movement or manually turning on the air conditioning. In general, when the air conditioning is on, the users tend to close the windows, thereby reducing or eliminating fresh air ventilation other than what is introduced by the mechanical air systems.

This focus on CO<sub>2</sub> was triggered by higher CO<sub>2</sub> concentrations observed in the second generation UH FROGs. The intent was to determine whether these FROGs experience levels that might warrant an awareness intervention. The American Society of Heating and Air Conditioning Engineers (ASHRAE) recommend levels no greater than 1,100 ppm for classrooms. Fresh outside air is typically 350-400 ppm. The effects of high CO<sub>2</sub> concentrations have been shown to correlate to higher absenteeism and student illness. Higher levels of CO<sub>2</sub> in enclosed areas result in sleepiness, reduced cognitive function and poor performance due to the reduced flow of oxygen to the brain [1]. The Occupational Health & Safety has stated that levels above 1000 ppm are associated with complaints of drowsiness and levels above 2,000 ppm are associated with headaches, sleepiness, and loss of attention.

The Kawaikini FROGs had the lowest average concentrations of CO<sub>2</sub>, averaging 391 and 398 ppm. Figure 7.1.2 shows the daily average CO<sub>2</sub> levels of the three first generation FROGs, Kawaikini East and West, and Ilima Intermediate over the 14 months of testing under APRISES 14. While Kawaikini East experienced the highest peak at 1,561 ppm, the Ilima classroom experienced higher concentrations over more prolonged periods than either of the Kawaikini classrooms as illustrated in Figure 7.1.3.

## CO2

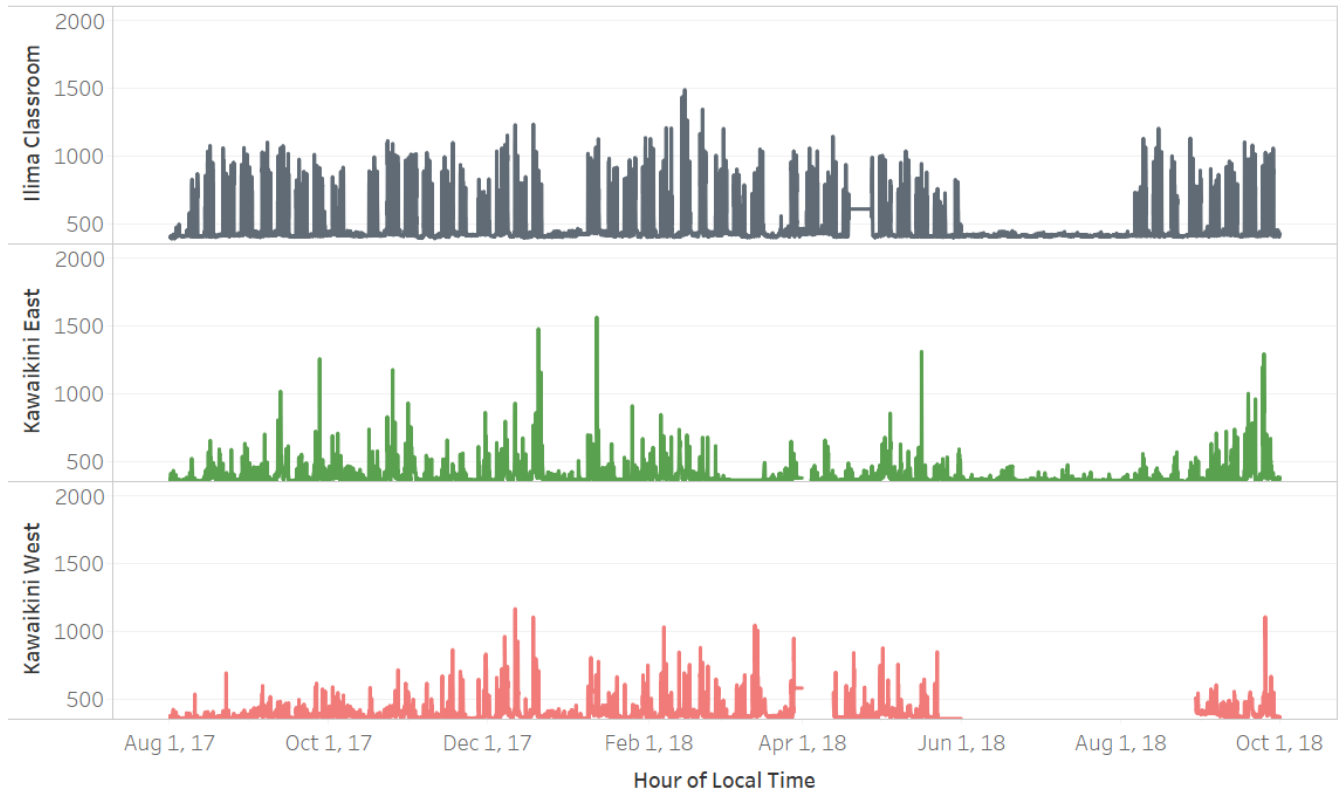
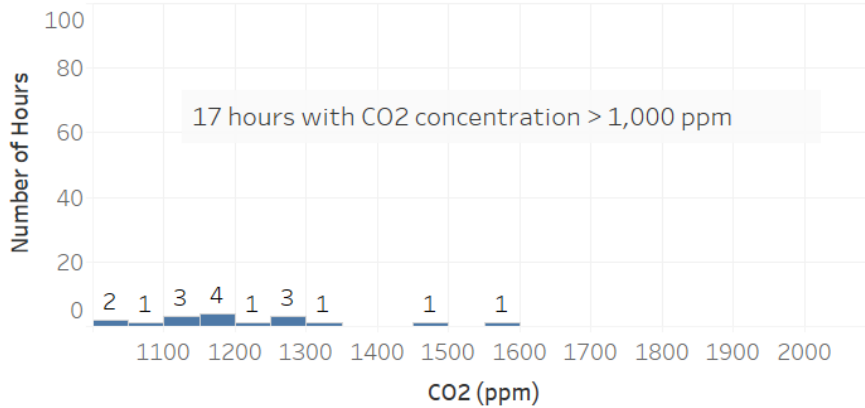


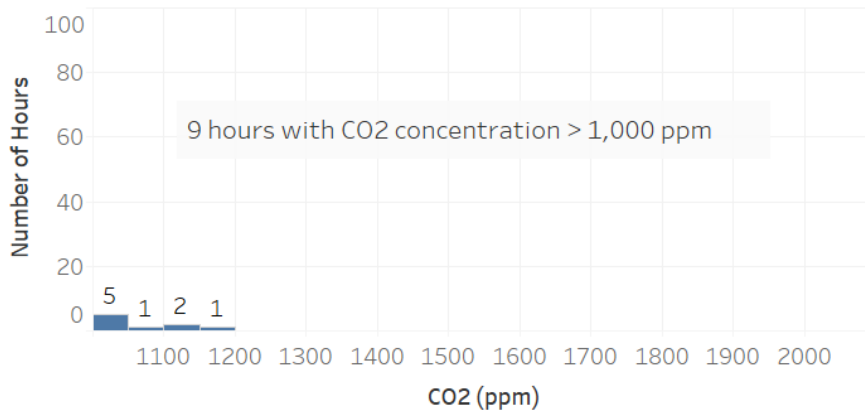
Figure 7.1.2. Average hourly CO2 concentrations (ppm) over 14 month period, 2017-2018.

### Kawaikini East



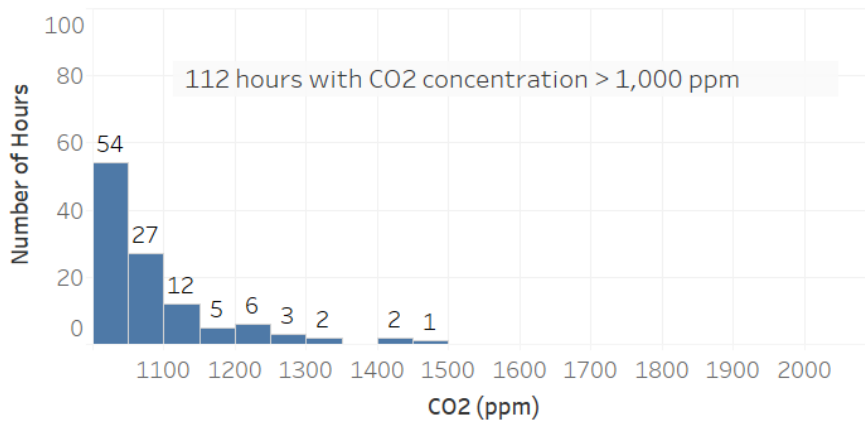
KWE CO2 average	391
KWE CO2 median	366
KWE CO2 stdev.	69
KWE CO2 min.	344
KWE CO2 max.	1,561

### Kawaikini West



KWW CO2 avera..	398
KWW CO2 median	375
KWW CO2 stdev.	70
KWW CO2 min.	345
KWW CO2 max.	1,163

### Ilima



Ilima CO2 average	467
Ilima CO2 median	417
Ilima CO2 Stdev.	129
Ilima CO2 min.	389
Ilima CO2 max.	1,486

Figure 7.1.3. Hours that exceeded 1,000ppm CO2 for first generation FROGs.

Over the course of a year, Ilima experienced 112 hours during which CO<sub>2</sub> levels exceeded 1,000ppm, whereas Kawaikini East and West averaged 17 and 9 hours respectively.

The operation of Kawaikini contrasts with Ilima. At the Kawaikini charter school, users are more aware of the operating costs of using air conditioning and are motivated to keep electricity costs down for the school, despite a tolerable sacrifice of comfort. The classes were observed keeping their lights off much of the time, using natural daylight. While air conditioning is available to them, through either self-directed or school guidance, they use the air conditioning sparingly, relying on open doors and windows for fresh outside air and natural ventilation. The Ilima classroom uses significantly more air conditioning than Kawaikini classrooms, operating the mechanical system about 12 hours per day each school day, while turning off at night and on weekends. Figure 7.1.4 represents a typical weekly profile for the use of air conditioning in the Ilima classroom.

### Ilima AC 1 week

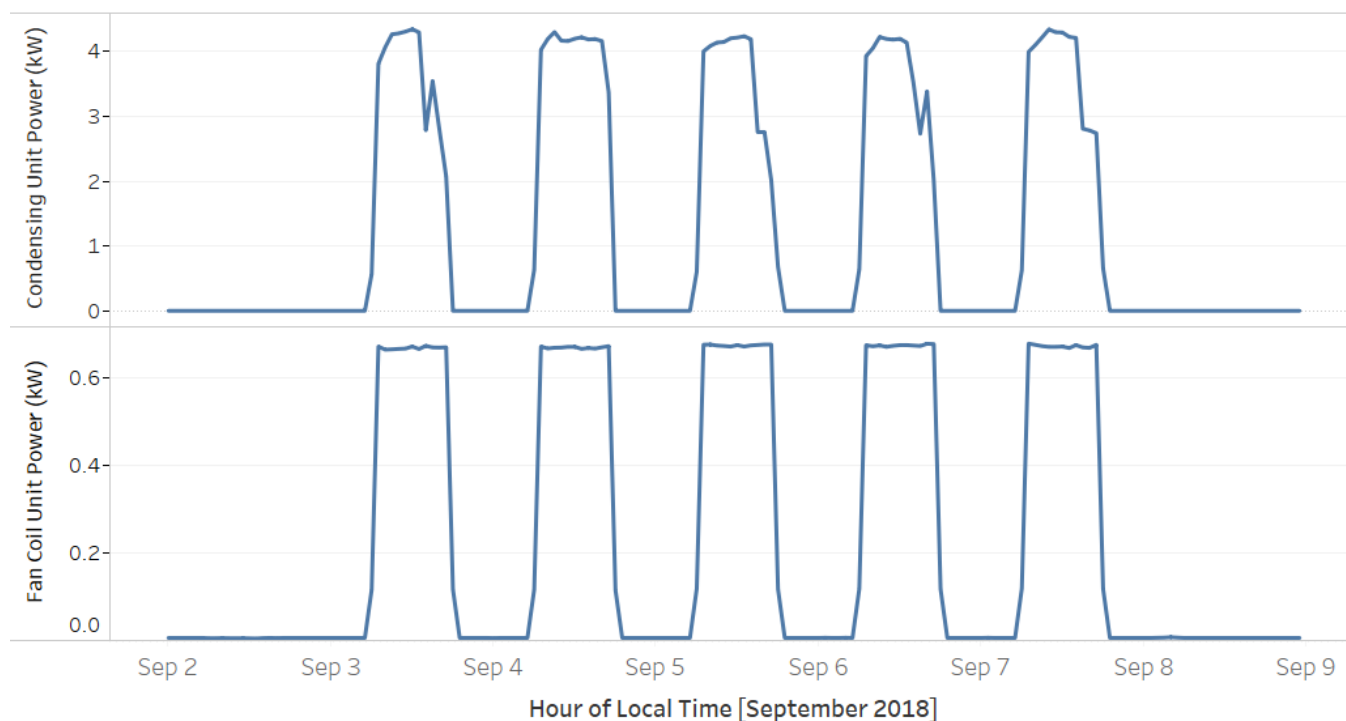


Figure 7.1.4. Typical weekly air conditioning energy profile for Ilima classroom.

Figure 7.1.5 shows the relative air conditioning energy consumed by each of the three classrooms. Ilima used nearly 7 times the average air conditioning energy than the average of the other two FROGs.

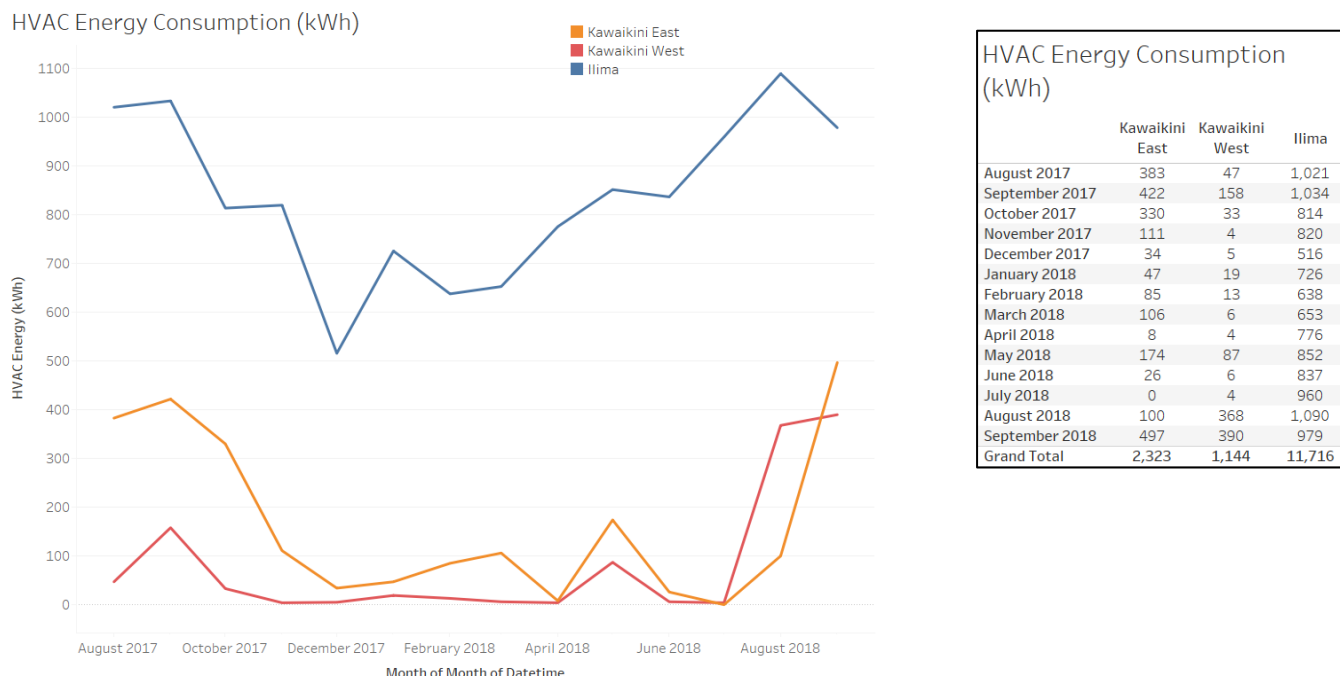


Figure 7.1.5. Monthly energy consumed by air conditioning, first generation FROGs.

Overall, CO<sub>2</sub> levels within all three first generation buildings were found to be in an acceptable range except for a few hours in the Ilima classroom. Even that was not enough to warrant concern. The Kawaikini classrooms seldom exceeded 1,000 ppm indicating good air exchange. While the Ilima CO<sub>2</sub> concentration exceeded 1,000 ppm approximately 10% of classroom time, it never exceeded 1500 ppm. Additionally, approximately half of the values above 1,000 were below 1,100, very near normal. The dependence on air conditioning suggests that the windows are not likely being opened to allow the natural ventilation that the buildings were designed for. While additional outside air intake would improve air quality during mechanical cooling, overall the first generation of FROGs have acceptable air quality.

### Comparison of Gen 1 and Gen 2 (UH) FROGS

Comparisons were also made between the first generation and second generation FROGs, the latter located on the UH Manoa campus, for temperature, relative humidity, CO<sub>2</sub>, energy consumption and energy generation.

The two UH Manoa FROGs are used by intermediate and high school classes from 7:30 AM to 12:30 PM, Monday through Friday, on a consistent, fixed schedule basis; and also by the UH College of Education during the afternoon and evenings, with occupancy schedules that vary every day of the week. We have observed that the UH Manoa FROGs experience significant differences

in CO<sub>2</sub> concentrations levels from one another and as a result of operation. Instructor awareness of how to operate a mixed mode building is a factor in utilizing natural ventilation.

As shown in Figure 7.1.6 the UH Manoa FROGs experienced a wide range of CO<sub>2</sub> values between August 2017 and May 2018. FROG 2 showed significantly lower CO<sub>2</sub> than FROG 1 during this time likely as a result of a difference in preference about whether to open the windows, and/or use the air conditioning. In later months, both FROGs exhibited significantly lower CO<sub>2</sub> levels corresponding to active training for the UH and high school staff on how the mixed mode building is intended to be operated and emphasizing the importance of opening windows for ventilation.

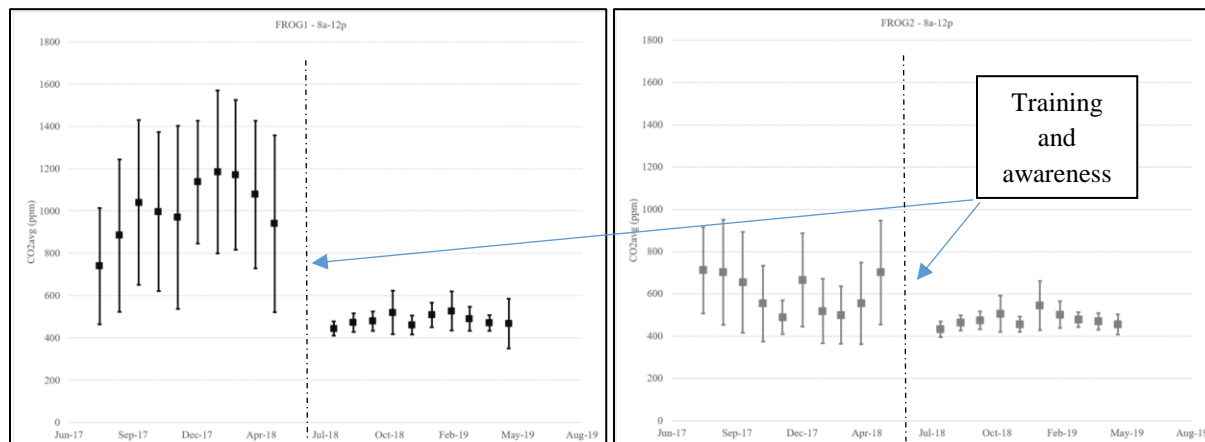


Figure 7.1.6. UHM FROG 1&2 Variability of CO<sub>2</sub> concentration over time.

Figure 7.1.7 reflects the range of daily average values over the course of a year for the second generation UH FROGs. The relatively flat area between June and August 2018 are indicative of very little use during the summer. Overall, the second generation FROGs experience higher CO<sub>2</sub> levels than first generation (Fig 7.1.3). While FROG 2 slightly exceeds the average of the first generation FROGs with an average of 446 ppm, FROG 1 exhibits significantly higher levels, averaging 547 ppm, but with individual readings that exceed 2,000 ppm.



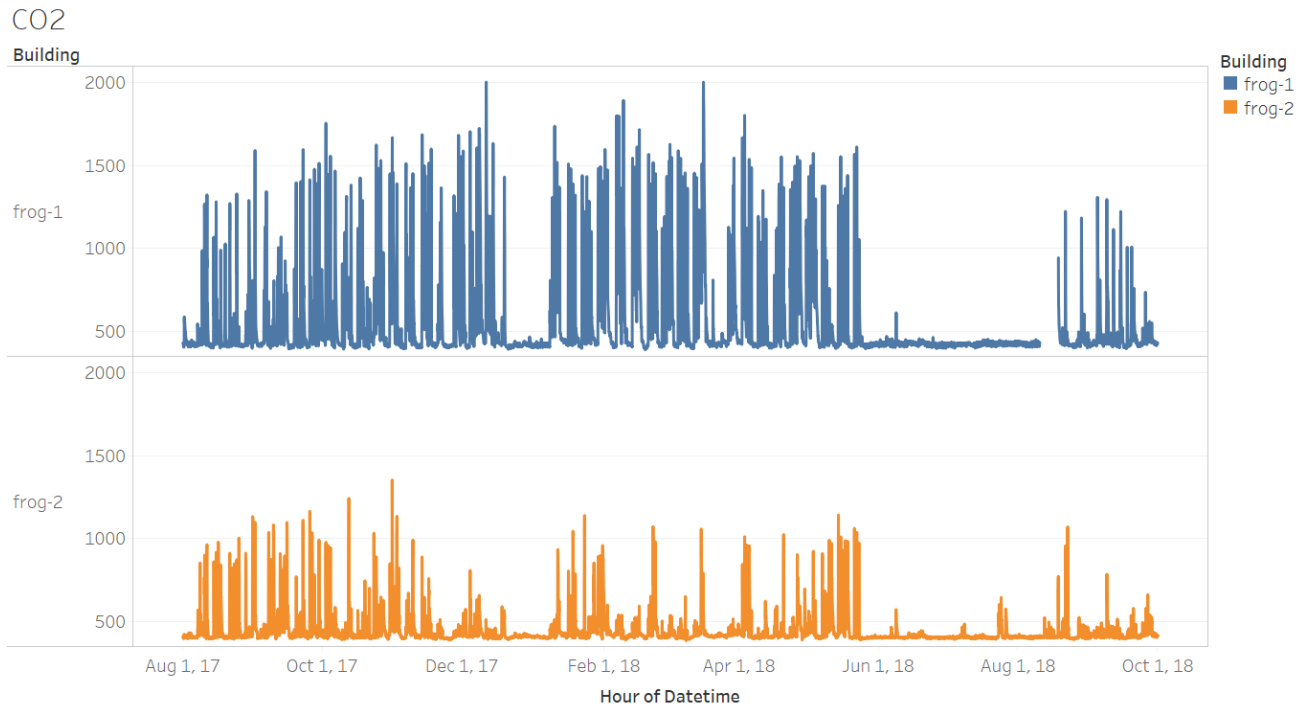
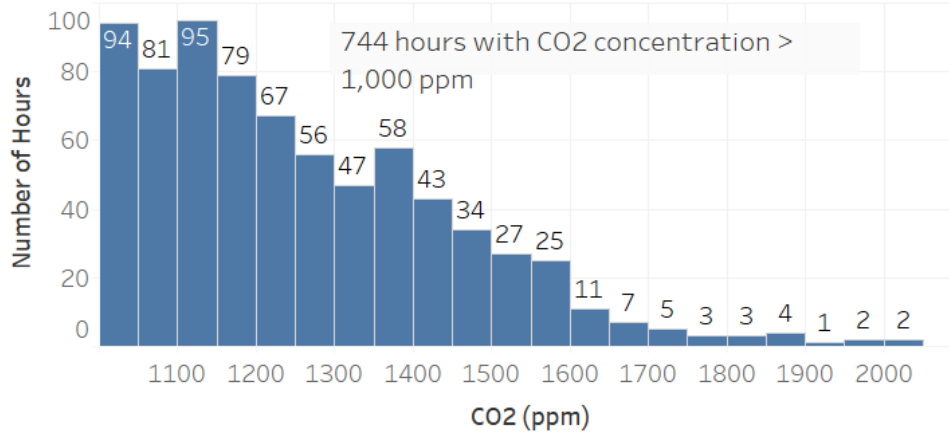


Figure 7.1.7. Average hourly CO2 concentrations (ppm) in both second generation FROGs.

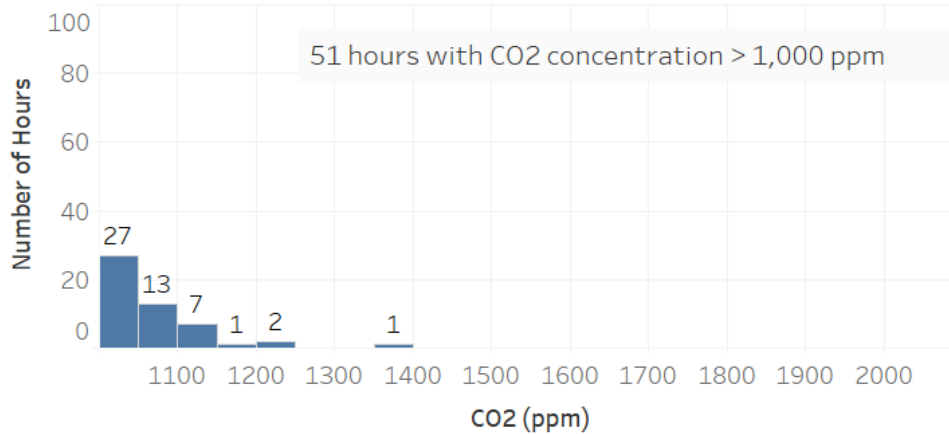
Figure 7.1.8 shows the number of hours that the UH FROGs exceed the 1,000 ppm threshold for CO2. FROG 1 operated 744 hours above 1,000 ppm, with the highest levels over 2,000 ppm. FROG 2 operated 51 hours over the threshold, with a high of 1,354 ppm CO2.

### Frog 1 CO2



Avg. CO2 (ppm)	547
Median CO2 (ppm)	436
Std. dev. of CO2 (p..	243
Min. CO2 (ppm)	390
Max. CO2 (ppm)	2,004

### Frog 2 CO2



Avg. CO2 (ppm)	446
Median CO2 (ppm)	414
Std. dev. of CO2 (p..	95
Min. CO2 (ppm)	386
Max. CO2 (ppm)	1,354

Figure 7.1.8. Number of Hours that exceeded 1,000 ppm CO2 for second generation FROGs.

Comparing the two histograms in Figure 7.1.8, it is evident that the difference in awareness of how the buildings are designed to be operated can make a difference in CO2 concentrations. Experienced and trained users, as reflected in the FROG2 histogram, understand mixed mode buildings and the appropriate operational steps, as compared to the FROG 1. Intuitively, natural ventilation is tied to air conditioning use and closed windows. Other factors contributing to the broad range of CO2 levels have been identified and will be reported under APRISES 15.

The linkage between air conditioning energy consumption and natural ventilation seen in the first generation FROGs is also shown in the UH Manoa FROGs. From the plots below in Figure 7.1.9 it can be seen that FROG 1 uses 21% more energy for air conditioning than FROG 2. Excluding Ilima which is considered air conditioned, the two mixed mode second generation air conditioning energy average is 5% less than the two mixed mode Kawaikini. The lower energy of the second generation is a function of mechanical efficiency, discussed in a later section.

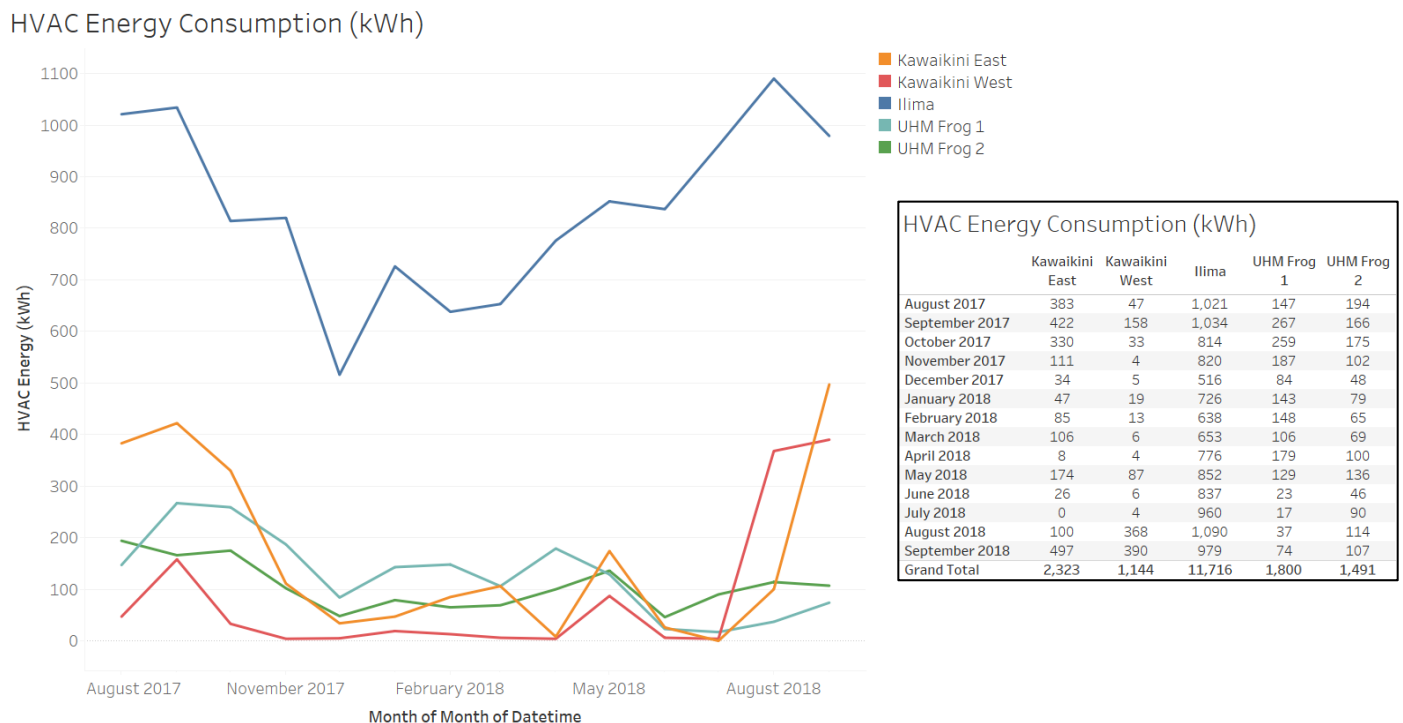


Figure 7.1.9. Energy associated with air conditioning for the first and second generation FROGs.

One of the early design intentions for all the FROG buildings was to be energy efficient and energy neutral in that they generate at least as much energy as they consume. Tables 7.1.3a-e below, show total energy consumption and energy production for the year. All FROGs incorporated energy efficient features, including high performance glazing, insulation, ceiling fans, natural daylighting and natural ventilation. However, the second generation FROGs are more efficient than the first generation, using less annual energy on average. The two Kawaikini and the two second generation FROGs generated more energy than they consumed over the year. Because of Ilima's daily use of

air conditioning, its consumption was far higher than planned, using 28% more energy than they generated, and 5 times more than FROG 2, the lowest energy consumer of all five buildings.

Tables 7.1.3a-e. Energy Consumption and Production first and second generation FROGs.

### 7.1.3a

Ilima Energy Consumption vs Production (kWh)

Month of Month of Datetime	Total consumption (kWh)	PV Production (kWh)	Net consumption (kWh)
August 2017	1,980	-1,631	349
September 2017	1,980	-1,558	422
October 2017	1,644	-1,303	340
November 2017	1,576	-1,172	404
December 2017	1,237	-1,057	180
January 2018	1,581	-1,282	299
February 2018	1,342	-1,054	288
March 2018	1,517	-1,296	220
April 2018	1,653	-1,367	286
May 2018	1,783	-1,482	300
June 2018	1,772	-1,574	198
July 2018	1,890	-1,555	335
August 2018	1,805	-1,085	719
September 2018	1,529	-713	816
Grand Total	23,289	-18,129	5,160

### 7.1.3b

Kaiwaikini West Energy Consumption vs Production (kWh)

Month of Month of Datetime	Total consumption (kWh)	PV Production (kWh)	Net consumption (kWh)
August 2017	985	-1,567	-582
September 2017	990	-1,375	-384
October 2017	772	-1,168	-395
November 2017	614	-956	-341
December 2017	583	-967	-385
January 2018	649	-1,012	-364
February 2018	571	-871	-299
March 2018	591	-1,450	-859
April 2018	727	-664	63
May 2018	933	-1,239	-306
June 2018	810	-1,394	-583
July 2018	719	-1,121	-402
August 2018	1,186	-1,217	-31
September 2018	1,160	-1,153	7
Grand Total	11,291	-16,152	-4,862

### 7.1.3c

Kawaikini East Energy Consumption vs Production (kWh)

Month of Local Time	Kawaikini East Total Consumpt..	Kawaikini East PV Production (...)	Kawaikini Net Consumption (k..)
August 2017	1,398	1,440	-42
September ..	1,235	1,126	109
October 2017	969	821	147
November 2..	596	552	44
December 2..	484	491	-7
January 2018	579	552	26
February 20..	572	537	35
March 2018	561	549	12
April 2018	574	750	-176
May 2018	920	1,062	-142
June 2018	799	1,238	-439
July 2018	801	957	-156
August 2018	900	973	-72
September ..	1,193	898	295
Grand Total	11,582	11,948	-366

### 7.1.3d

UHM Frog 1 Energy Consumption vs Production (kWh)

Month of Month of Datetime	Total consumption (kWh)	PV Production (kWh)	Net consumption (kWh)
August 2017	377		377
September 2017	524		524
October 2017	573		573
November 2017	419		419
December 2017	341		341
January 2018	413	-326	87
February 2018	387	-849	-462
March 2018	342	-657	-315
April 2018	404	-540	-136
May 2018	320	-1,220	-901
June 2018	189	-1,354	-1,165
July 2018	174	-1,352	-1,178
August 2018	223	-1,162	-939
September 2018	338	-1,188	-849
Grand Total	5,025	-8,649	-3,625

### 7.1.3e

UHM Frog 2 Energy Consumption vs Production (kWh)

Month of Month of Datetime	Total consumption (kWh)	PV Production (kWh)	Net consumption (kWh)
August 2017	423		423
September 2017	422		422
October 2017	415		415
November 2017	333		333
December 2017	247		247
January 2018	359	-329	30
February 2018	293	-860	-568
March 2018	293	-667	-374
April 2018	322	-550	-228
May 2018	343	-1,236	-893
June 2018	208	-1,372	-1,164
July 2018	251	-1,369	-1,118
August 2018	410	-1,272	-862
September 2018	418	-1,203	-785
Grand Total	4,737	-8,858	-4,122

While the FROGs at UH Manoa had higher overall average concentrations of CO<sub>2</sub>, the buildings proved to be more energy efficient, using 33% as much energy as the average of the first generation FROGs. In Figure 7.10 the plot of monthly energy consumption is shown for all five FROGs, with the UHM FROG 1 and 2, averaging 358 kWh and 338 kWh per month respectively. Kawaikini East and West averaged 843 and 806 kWh per month respectively. Ilima averaged 1,663 kWh per month.

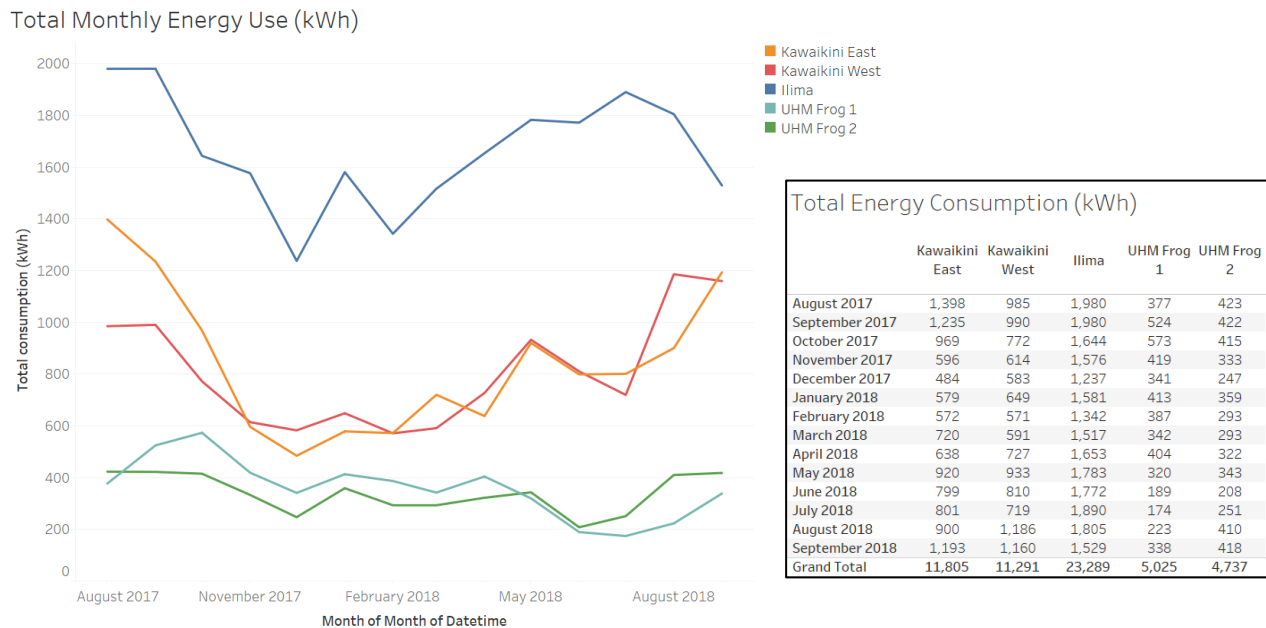


Figure 7.1.10. Overall monthly energy consumption first and second generation FROGs.

Temperature and humidity, indicators of comfort, were also plotted for comparison between the first and second generation buildings. Figure 7.1.11 plots the monthly average temperature and relative humidity for the first generation. The embedded tables show the annual monthly averages as well as the maximum and minimum temperatures observed on the sites. Figure 7.1.12 is the corresponding plot and data table for the second generation FROGs.

The second generation FROGs are on average warmer and slightly less humid than the first generation. The second generation FROG interior temperatures average 6.7°F higher than the first generation FROGs. Relative humidity and temperature are inversely related. Relative humidity in the second generation is 2.3% lower than the first generation.

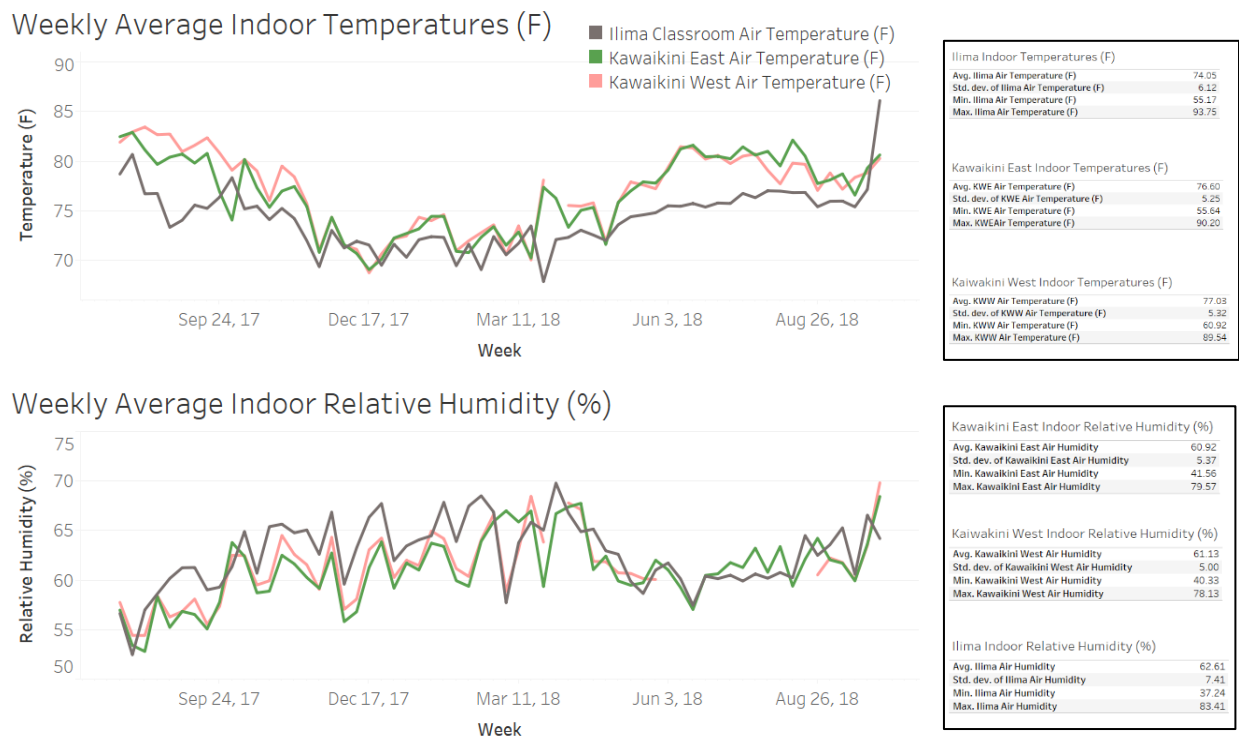


Figure 7.1.11. Average monthly interior temperature and humidity, first generation FROGS.

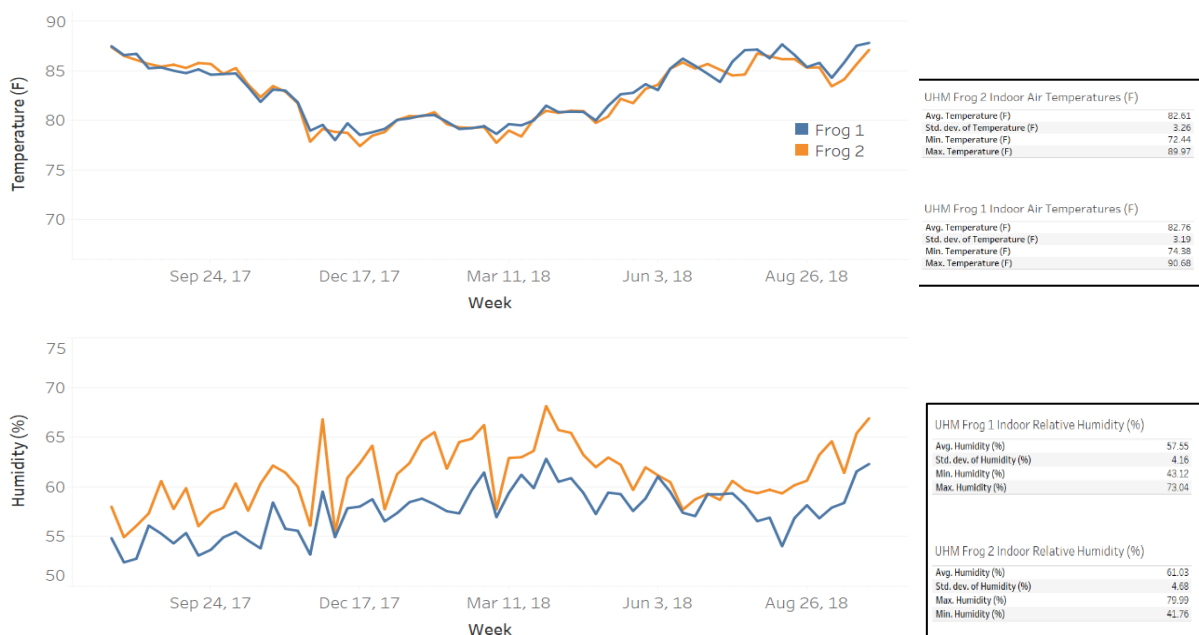


Figure 7.1.12. Average monthly interior temperature and humidity, second generation FROGS.

This project was largely a data collection project, with the results to be used in a detailed comparative analysis between these first generation of FROGs and the second generation in APRISES15. As such the data presented is largely descriptive of findings. There was no attempt to mine data with more granularity at this time for causality or to filter for microclimate, weekdays/holidays and other intervening circumstances that would have a minor effect on the outcome, nor to describe and quantitatively compare comfort conditions. The data is presented at a very high level, in monthly averages, to identify trends that will help inform additional research.

Some of the key findings of this Task 7.1 include:

- Mixed mode buildings, designed for natural ventilation that requires user intervention, can experience increased concentrations of CO<sub>2</sub>.
- During the period studied, the first generation FROGs have overall 16% lower average concentrations of CO<sub>2</sub> than the second generation FROGs.
- Interior temperatures were 6.7°F higher in the second generation FROGs.
- Relative humidity was lower in the second generation of FROGs. Although FROG 2, with more natural ventilation experienced higher average humidity than FROG 1.
- In spite of the daily use of air conditioning and being in a drier zone, Ilima generally was more humid inside than the others.
- The second generation FROGs used 33% as much energy as the first generation, apparently linked to the efficiency of the air conditioning units and lighting systems.

## 7.2 High Wind Energy Generator Testing

The second subtask was to test the durability and performance of a novel 5kW High Wind Energy Generator Testing (HEWS) project under development by HEWS Technology. In a collaboration with HEWS Technology, HNEI was to evaluate the performance of the wind generator installed at a real-world test site, to determine if actual performance approached that predicted from models.

As per the Service Agreement with HNEI, HEWS Technology, Inc. manufactured, delivered, installed, calibrated and completed the initial evaluation. The HEWS 20/5kW wind generator was installed at a private location, outside Fort Collins, CO by HEWS Technology. Power data was collected from December 30, 2018 through February 4, 2019. Testing and system evaluation was performed in two stages with a 9-channel Data Acquisition System (DAS) logging data every one millisecond.



The HEWS wind generator is a unique design that attempts to extract more energy from a moving airstream than conventional vertical and horizontal axis wind turbines. Figure 7.2.1 is an image of the generator at the testing site.

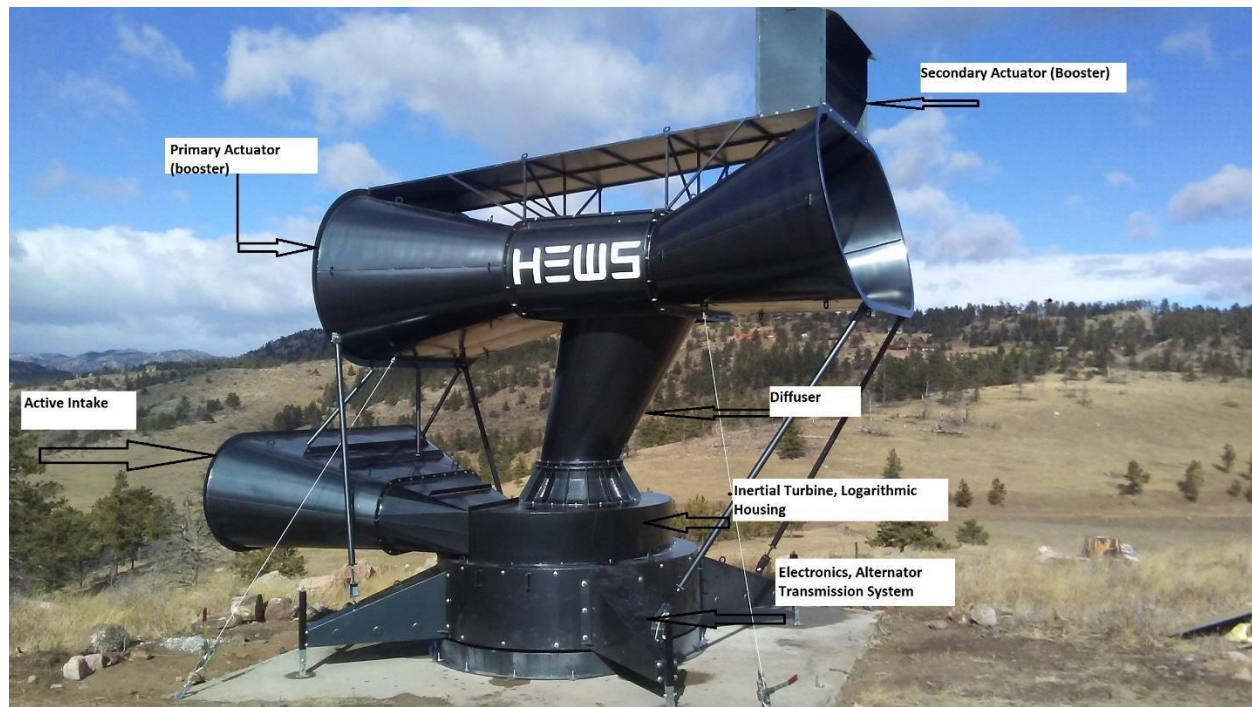


Figure 7.2.1. Components of the HEWS high wind generator.

The key elements include:

1. Secondary Actuator (Booster): accelerates airflow as per a venturi effect to produces lower pressure at the exhaust area of the Primary Actuator causing an inducement (acceleration) and evacuation of combined airflow in the Primary Actuator (Booster) - as a result, effectively evacuates air from the turbine itself.
2. Primary Actuator (Booster): acts as a secondary source of (wind) power by accelerating upstream airflow as per venturi effect through its constriction e.g. coupling section with the Diffuser. This results in a production of low pressure over the Diffuser area to induce an evacuation and acceleration of the upstream Active Intake airflow through the Turbine to the Diffuser.
3. Diffuser: coupled with the Turbine exhaust area to create a channel for evacuating induced Active Intake airflow and to yield effective turbine power production.



4. Active Intake: a venturi (duct) channel designed to deliver upstream open-flow wind to the Turbine.
5. Powertrain: robust power production element consisting of;
  - a) A heavy-duty inertial inverted Francis-type turbine which effectively diverts horizontal upstream airflow received from the Active Intake to a vertical airflow evacuated through the Diffuser and ultimately the Primary Actuator.
  - b) Logarithmic “golden section” spiral housing designed to produce 360-degree airflow torque on the turbine blades.
6. Electronics, transmission, DAS, Alternator compartment: houses elements of control, data acquisition and conversion of mechanical power to electrical power.

From the HEWS February 21, 2019 report, Table 7.2.1 highlights the parameters upon which the evaluation was based.

Table 7.2.1. HEWS 20/5 kW testing parameters.

Data log parameters			
Data collection period		December 30, 2018 – February 4, 2019	
Data collection days		37	
Data log frequency		1/10 of a second	
Total data points logged		31,968,000	

	Test Parameter	Expectation	Reference
1	Structural Integrity	Up to 140 mi/hour wind	PE report
2.	Cut-in Wind Speed	6-7m/sec	PASS
3.	Rated wind speed	25 m/sec	70%
4.	Cut-off wind speed	110 mi/hour	70%
5.	Power Curve (Mechanical) (factual)		PASS (Up to 16m/sec)
	Predicted		Reasonable
6.	Actuator's effect	Pressure differential, Power	PASS
7.	Electromagnetic Power Curve		Reasonable
8	Turbine inertia effect		PASS
9.	Ducting system loses		Reasonable
10.	System effectiveness		PASS
11.	Comparison with conventional HAWT		PASS
12.	Analysis, predictions, conclusions, Possible improvements		

## Results

The HEWS wind turbine is a unique form from other small wind turbines in the high inertia of the turbine. Per the HEWS report “The turbine operates as a Fly Wheel (Energy Storage) producing continuous power even when wind velocity drops and acts as a gear box (transmission) to protect the alternator during wind gusts.

The following graph Figure 7.2.2 illustrates turbine stability due to its inertia in a rapidly changing wind environment. Specifically, with wind (gust) deviation of 200% within a 2-second interval, the turbine RPM changes only 2%, thereby protecting the transmission and producing power consistently” [3].

HEWS concludes that “turbine inertia and flywheel characteristics yields a stabilization in power produced even in rapidly changing wind regime, resulting in a smooth and stable power output [4].

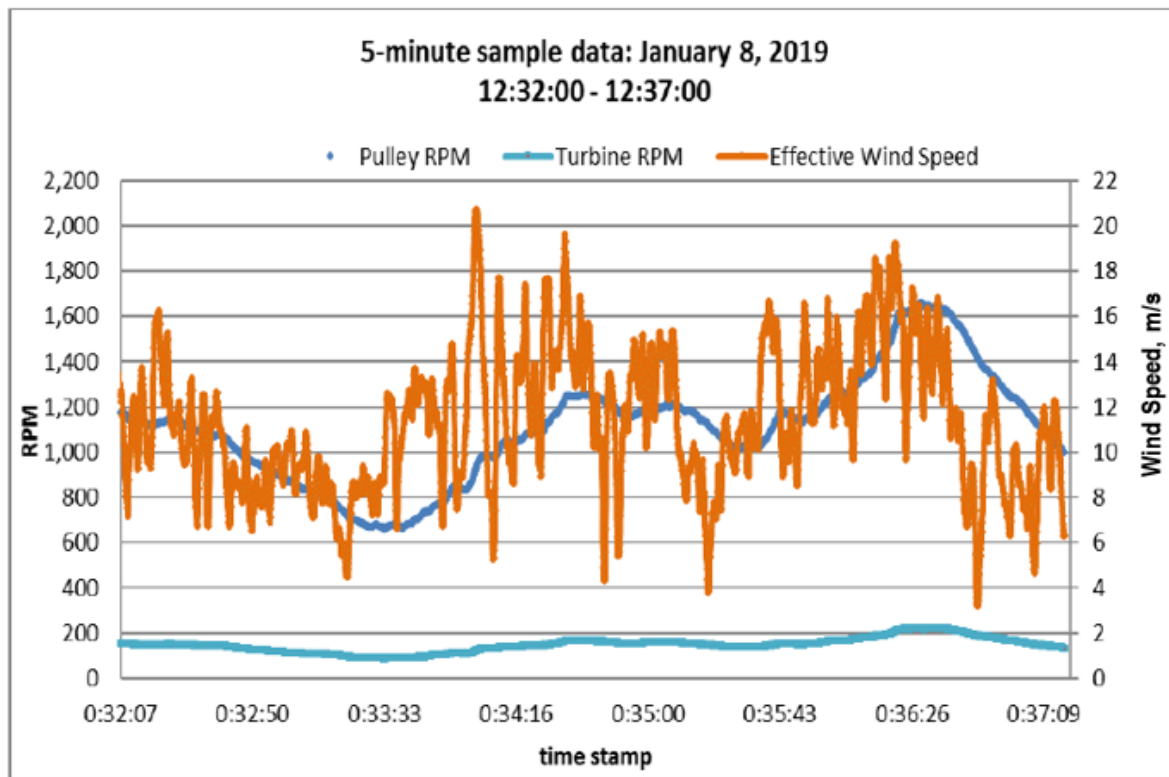


Figure 7.2.2. Turbine and pulley stability under highly variable wind conditions.

Twelve physical and performance parameters were evaluated either in field conditions or through engineering analysis but not all of the test results are conclusive, particularly with actual power generation. Although, the benefits of the high inertia appear to be positive and the HEWS wind generator is a robust, structurally solid, high inertia machine, there are limitations. For example,

the cut-in speed was relatively high at about 6.7 m/s, relegating it to very high wind regimes. Unfortunately, during the test period, the lack of very high wind regimes during the testing period and technical issues connecting the power generation modules to the turbine led to inconclusive results in regard to power generation and efficiency of the wind system. HEWS is continuing testing via other funding.

Details of wind distribution, powertrain configuration, data collection and interface, and evaluated test parameters are found in the *HEWS Interim Report* dated February 21, 2019. This report is available by request from HNEI. HNEI did not feel that we could validate all of the report's conclusions and therefore chose to not publish it on the HNEI website. HNEI will continue to monitor progress of the HEWS high wind generator, but currently has no plans to support further development of this technology.

## References

- [1] Berkeley Lab, undated, Ventilation with Outdoor Air, Berkeley Lab website: <https://iaqscience.lbl.gov/topic/ventilation-outdoor-air>
- [2] Bonino, S. 2016 Carbon Dioxide Detection and Indoor Air Quality, Occupational Health & Safety, April: <https://ohsonline.com/articles/2016/04/01/carbon-dioxide-detection-and-indoor-air-quality-control.aspx>
- [3] HEWS Technology, Draft Interim Report, February 2019, p22.
- [4] *ibid.*